

Single-crystal X-ray diffraction at extreme conditions in mineral physics and material sciences

DISSERTATION

zur Erlangung des akademischen Grades eines
Doktors der Naturwissenschaften (Dr. rer. nat.)
an der Bayreuther Graduiertenschule für Mathematik und
Naturwissenschaften (BayNAT) der Universität Bayreuth

vorgelegt von

Elena Bykova
aus Amursk (Russland)

Bayreuth, 2015

This doctoral thesis was prepared at the Bavarian Research Institute of Experimental Geochemistry and Geophysics and the Laboratory of Crystallography of the University of Bayreuth from 03/2011 until 12/2014 and was supervised by Prof. Dr. Leonid Dubrovinsky and Prof. Dr. Natalia Dubrovinskaia.

This is a full reprint of the dissertation submitted to obtain academic degree of Doctor of Natural Sciences (Dr. rer. nat.) and approved by the Bayreuth Graduate School of Mathematical and Natural Sciences (BayNAT) of the University of Bayreuth.

Date of submission: 23.01.2015

Date of defense: 29.05.2015

Acting director: Prof. Dr. Franz Xaver Schmid

Doctoral committee:

Prof. Dr. Leonid Dubrovinsky (1st reviewer)

Prof. Dr. Sander van Smaalen (2nd reviewer)

Prof. Dr. Daniel Frost (chairman)

Prof. Dr. Jürgen Senker

Zusammenfassung

Die Einkristallröntgenstrahlbeugung (X-ray diffraction, XRD) ist eine leistungsfähige und zerstörungsfreie Methode zur eindeutigen Identifizierung kristalliner Phasen, zur Bestimmung ihrer Kristallstrukturen (Gitterparameter, Raumgruppe, fraktionelle Koordinaten und Besetzung der Atome), sowie, falls notwendig, ihrer Phasenzusammensetzung. Die vorliegende Arbeit behandelt die Anwendung der Einkristallröntgenstrahlbeugung in der Hochdruck-Hochtemperatur-Forschung (high pressure high temperature, HPHT) unter Verwendung von laserbeheizten Diamantstempelzellen (diamond anvil cells, DACs), wobei hier auch die methodologischen Aspekte und Arbeitsschritte der Einkristallröntgenstrahlbeugungsexperimente beschrieben werden, also Kristall- bzw. Probenauswahl, Befüllung und Montage der DACs, Durchführung der eigentlichen Experimente, Datenverarbeitung und zuletzt Strukturbestimmung und/oder Strukturverfeinerung. Das große Potential und neuen Anwendungsmöglichkeiten der Hochdruckkristallographie für die Material- und Geowissenschaften werden an verschiedenen Beispielen diskutiert, an Übergangsmetallboriden, Metall-dotierten Borphasen, Silikaten und Oxiden. Im Einzelnen wurden dafür die Kristallstrukturen von Co_5B_{16} , MnB_4 , Al-dotiertem β -Bor, Knorringit und Fe^{3+} -haltigem Bridgmanit verfeinert und das Hochdruckverhalten von FeB_4 , Fe_2B_7 , Fe_xB_{50} und FeOOH untersucht. Des Weiteren wurden detaillierte strukturelle Untersuchungen an einer Reihe von Hochdruck-Eisenoxiden durchgeführt, die es erlaubten, eine jahrzehntelange Kontroverse zu klären. Die vorliegende Arbeit führte auch zur Entdeckung neuer Phasen, einschließlich dem gemischten Eisenoxid Fe_5O_7 mit einer sehr ungewöhnlichen Stöchiometrie.

Ein Schwerpunkt der hier vorgestellten Arbeit liegt in der Bestimmung der Kristallstrukturen von Al-dotierten, rhomboedrischen β -Bor ($\text{AlB}_{44.8(5)}$ oder $\text{AlB}_{37.8(5)}$) und von Fe_xB_{50} . Für Erstere wurden die Positionen und Besetzungen der Zwischengitter-Al- und B-Atome bestimmt. Das Modell von Al-dotiertem β -Bor zur Beschreibung der Fehlordnung ist dem Modell des bekannten $\text{SiB}_{30.17}\text{C}_{0.35}$ ähnlich. In Fe_xB_{50} besetzt das Metall die tetraedrische Position, wobei die Besetzung zwischen 50 und 65% variiert.

Ein nächster Themenbereich sind die Kristallstrukturen neuer Übergangsmetallboride, nämlich MnB_4 , FeB_4 , Co_5B_{16} und Fe_2B_7 . Die Tetraboride werden allgemein aus Säulen von kantenverknüpften MB₁₂-Polyedern aufgebaut, in denen die Metallatome eindimensionale Ketten bilden. Während die Metall-Metall-Abstände im orthorhombischen FeB_4 einheitlich sind,

führt in MnB_4 die Peierlsverzerrung zur Paarbildung der Mn-Atome und dies zu einer Verringerung der Kristallstruktursymmetrie nach monoklin. Wenn das Metall-Bor-Verhältnis größer ist als 1:4, dann enthalten die Boride nicht nur 12-fach koordinierte Metallatome MB_{12} , sondern auch 10- und 9-fach koordinierte Metallatome (CoB_9 in Co_5B_{16} , FeB_{10} in Fe_2B_7). Aufgrund des Bormangels wird die "Metall"-Packung dichter, was sich nun in gemeinsamen Flächen der Koordinationspolyeder widerspiegelt.

Die für diese Arbeit untersuchten Übergangsmetallboride zeigen kurze B–B Bindungen, welche ihre mechanischen Eigenschaften beeinflussen: das FeB_4 und Fe_2B_7 sind entlang bestimmter kristallographischer Richtungen genauso fest und starr wie Diamant. Die Analyse der Hochdruck-Einkristallröntgenstrahlbeugungsdaten lässt vermuten, dass die Ursache dieser Inkompressibilität in der Steifigkeit der orientierten kurzen B–B Bindungen liegt. Diese einzigartige räumliche Anordnung der Atome befördert FeB_4 in die Klasse der superharten Materialien mit einer Nanoindruckshärte von 62(5) GPa.

Die Struktur von Fe_xB_{50} ist aus B12-Ikosaedern aufgebaut und hat große Hohlräume, wodurch sie effektiver schrumpfen kann als die Bor-Polymorphe (α -, β - und γ -Bor), die ebenfalls chemisch gebundene B12-Ikosaeder enthalten. Die hier gemessenen Daten bestätigen die früheren Beobachtungen zur Komprimierung der Bor-Phasen, dass die intra-ikosaedrischen Bindungen steifer sind als die inter-ikosaedrischen Bindungen.

Genau strukturelle Untersuchungen am Granat Knorringit, der bei 26 GPa und 1800 °C in einem Multitempelapparat synthetisiert wurde, zeigen, dass die Zusammensetzung als $\text{Mg}_3(\text{Cr}_{1.58}\text{Mg}_{0.21}\text{Si}_{0.21})\text{Si}_3\text{O}_{12}$ beschrieben werden kann und Knorringit dadurch 21 mol-% von Majorit, dem MgSiO_3 -Endglied der Mischkristallreihe enthält.

Die Verteilung von Eisen im Al-freien, Fe^{3+} -haltigem Mg-Perovskit (Bridgmanit) wurde mittels Einkristallröntgenstrahlbeugung kombiniert mit Mößbauer Spektroskopie bestimmt, die chemische Zusammensetzung ist $(\text{Mg}_{0.946(17)}\text{Fe}^{2+}_{0.045(4)}\text{Fe}^{3+}_{0.011(1)})\text{Si}_{0.997(16)}\text{O}_3$. Aus der Einkristallröntgenstrahlbeugung konnte gezeigt werden, dass Eisen nicht die Si-Position (die sogenannten B-Sites) besetzt.

Die Methode der Hochdruck-Einkristallröntgenstrahlbeugung wurde auch herangezogen, um das Verhalten von FeOOH bei Drücken oberhalb von 70 GPa zu untersuchen. Unter Normalbedingungen besitzt diese Verbindung eine Wasserstoffbrückenbindung entlang von

Kanälen, die von verzerrten $\text{FeO}_3(\text{OH})_3$ -Oktaedern gebildet werden. Unterhalb 16 GPa schrumpfen diese Kanäle (und als Folge auch die Wasserstoffbrückenbindung) stärker als die einzelnen Fe–O Bindungen in den Oktaedern; oberhalb 16 GPa schrumpfen beide Bindungen einheitlich. Bei etwa 45 GPa reduziert eine Spin-Überkreuzung in Fe^{3+} das Elementarzellvolumen drastisch (um etwa 11%) und verursacht eine Symmetrisierung der Wasserstoffbrückenbindungen, was aus der Analyse der interatomaren Abstände in den $\text{Fe}(\text{O}\dots\text{H})_3(\text{OH})_3$ -Gruppen abgeleitet wurde. Eine Symmetrisierung der Wasserstoffbrückenbindungen in Verbindung mit der High-Spin zu Low-Spin Überkreuzung in Fe^{3+} wurde hier zum ersten Mal mittels Hochdruck-Einkristallröntgenstrahlbeugung nachgewiesen.

Die Hochdruck-Hochtemperatur-Einkristallröntgenstrahlbeugung wurde eingesetzt, um nach HPHT-Polymorphen von Fe_2O_3 und Fe_3O_4 im Megabar-Druckbereich zu suchen und um das Verhalten der Eisenoxide in plattentektonisch abgetauchten Bändererzen (banded iron formations, BIFs) im unteren Erdmantel zu studieren. Es konnte gezeigt werden, dass oberhalb 29 GPa Fe_3O_4 die Kristallstruktur von CaTi_2O_4 annimmt, die bis mindestens 70(1) GPa und 2400(100) K stabil bleibt. Dadurch wurde eine 50-jährige Kontroverse über die Struktur des Fe_2O_3 -Polymorphs, das oberhalb von etwa 50 GPa stabil ist, geklärt. Im Speziellen wurde gezeigt, dass diese Phase eine Doppelperovskit-Typ Struktur in trikliner Symmetrie hat. Darüber hinaus erzwingt die Kompression oberhalb 67 GPa eine Umwandlung zu einer anderen Hochdruckphase mit orthorhombischer Zelle (Raumgruppe $Aba2$). Diese Phase geht bei Temperaturerhöhung bei etwa 67 GPa in ein HPHT- Fe_2O_3 -Polymorph mit CaIrO_3 -Struktur (Postperovskit, $\eta\text{-Fe}_2\text{O}_3$) über. Bei Druckentlastung zu 41 GPa und weiterer Temperaturerhöhung bis 1800 K wandelt sich diese Phase dann in die Rh_2O_3 -II Struktur um. Die faszinierendste Beobachtung ist, dass bei Bedingungen des unteren Erdmantels das $\eta\text{-Fe}_2\text{O}_3$ Sauerstoff freigibt und sich weiter zu einer neuen Fe_5O_7 -Verbindung zersetzt. Fe_2O_3 und Fe_3O_4 bilden bis zu 85 Gewichts-% der BIFs, die aufgrund der Subduktion lithosphärischer Platten bis in den unteren Erdmantel transportiert werden können. Deshalb kann das Fe_2O_3 der abgetauchten BIFs als Quelle für ein sauerstoffreiches Fluid im tiefen Erdinneren dienen, mit einer erheblicher Menge an Sauerstoff (bis zu acht Mal die Sauerstoffmenge in der heutiger Atmosphäre!), was zu einer deutlichen Heterogenität in der Sauerstoffkonzentration in unterschiedlichen Teilen des Erdmantels führt.

Summary

Single crystal X-ray diffraction (XRD) is a powerful non-destructive method which allows unambiguously identify crystalline phases, determine a crystal structure (unit cell parameters, a space group, atomic coordinates and atomic occupancies) and, if required, a phase composition. This thesis deals with applications of single-crystal XRD in high pressure and high temperature (HPHT) research using laser-heated diamond anvil cells (DACs). The thesis describes methodological aspects of our single-crystal XRD experiments which involve crystals selection, DACs preparation, maintaining experiments, data processing, and structure solutions and/or refinements. We demonstrate a great potential and novel opportunities provided by high-pressure crystallography in materials- and geo-sciences on the examples of studies of transition metal borides, a metal-doped boron phase, silicates, and oxides. Particularly, we solved and refined crystal structures of Co_5B_{16} , MnB_4 , Al-doped β -boron, knorringite, and Fe^{3+} -bearing bridgmanite, investigated the high-pressure behaviour of FeB_4 , Fe_2B_7 , Fe_xB_{50} , and FeOOH . We also undertook detailed structural studies of a number of high-pressure iron oxides, which allowed us to resolve some of decade-long controversies. This work has led to discovery of new phases including a mixed iron oxide Fe_5O_7 with an unusual stoichiometry.

One of the focuses of my research was investigation of the crystal structures of Al-doped rhombohedral β -boron ($\text{AlB}_{44.8(5)}$ or $\text{AlB}_{37.8(5)}$) and Fe_xB_{50} . For the first compound we determined positions of interstitial Al- and B-atoms and their occupancies. We found that the disordering model of Al-doped β -boron is similar to one observed in $\text{SiB}_{30.17}\text{C}_{0.35}$. In Fe_xB_{50} the metal fills the tetrahedral positions with the occupancy varying from 50 to 65%.

We also studied crystal structures of novel transition metal borides, namely MnB_4 , FeB_4 , Co_5B_{16} , and Fe_2B_7 . Tetraborides are composed of edge-shared columns of MB₁₂ polyhedra, inside which the metal atoms form one-dimensional chains. While in the orthorhombic FeB_4 the metal-metal distances are uniform, in MnB_4 Peierls distortion leads to a pairing of Mn atoms accompanied with a lowering of the crystal structure symmetry to monoclinic. If a metal to boron ratio is higher than 1:4, the borides contain not only 12-coordinated metal atoms MB₁₂, but also 10- and 9- coordinated ones (CoB₉ in Co_5B_{16} , FeB₁₀ in Fe_2B_7). Due to boron deficiency “metals”

packing becomes denser that is reflected in a sharing of common faces between the coordination polyhedra.

We found that studied transition metal borides possess short B-B bonds which influence their mechanical properties. In the FeB_4 and Fe_2B_7 we found certain crystallographic directions in which the borides are as stiff as a diamond. The analysis of high-pressure single-crystal XRD data suggests that such incompressibility originates from the stiffness of the oriented short B-B bonds. A unique atomic arrangement in the FeB_4 brings it to a class of superhard materials with a nanoindentation hardness of 62(5) GPa.

We found that the structure of Fe_xB_{50} composed of B12 icosahedra has large cavities, so it can contract more effectively than boron polymorphs (α -, β - and γ -boron), also containing chemically bonded B12 icosahedra. Our data confirm previous experimental observations on compression of boron phases that intraicosahedral bonds are stiffer than intericosahedral ones.

Detailed structural studies of garnet knorringite synthesized at 26 GPa and 1800 °C in multianvil apparatus reveal that it has $\text{Mg}_3(\text{Cr}_{1.58}\text{Mg}_{0.21}\text{Si}_{0.21})\text{Si}_3\text{O}_{12}$ composition and thus contains 21 mol % of a majorite MgSiO_3 end-member.

The distribution of iron in Al-free, Fe^{3+} -bearing Mg-perovskite (bridgmanite) was derived from single-crystal XRD combined with Mössbauer spectroscopy. We found that the compound has the composition $(\text{Mg}_{0.946(17)}\text{Fe}^{2+}_{0.045(4)}\text{Fe}^{3+}_{0.011(1)})\text{Si}_{0.997(16)}\text{O}_3$. The important result from single-crystal XRD was that iron does not occupy Si-position (so called B-site).

We applied methods of high-pressure single-crystal XRD to study the behaviour of FeOOH at pressures over 70 GPa. At ambient conditions the compound has a hydrogen bond located in channels created by irregular $\text{FeO}_3(\text{OH})_3$ octahedra. Below 16 GPa the channels (and consequently hydrogen bonds) contract more effectively than individual Fe-O bonds in octahedra; above 16 GPa both kinds of bonds contract uniformly. At ~45 GPa a spin crossover in Fe^{3+} drastically decreases the unit cell volume (by ~ 11%) and provokes symmetrization of the hydrogen bonds that was deduced from the analysis of the interatomic distances in the $\text{Fe}(\text{O}\dots\text{H})_3(\text{OH})_3$ moiety. The hydrogen bond symmetrization linked with the high-spin to low-spin crossover in Fe^{3+} was detected for the first time from high-pressure single-crystal XRD.

High-pressure and high-temperature (HPHT) single-crystal XRD was used to search for HPHT polymorphs of Fe_2O_3 and Fe_3O_4 in a megabar pressure range and to uncover the fate of the iron oxide in subducted banded iron formations (BIFs) in the Earth's lower mantle. We confirmed that above 29 GPa Fe_3O_4 adopts the crystal structure of CaTi_2O_4 which is stable to at least 70(1) GPa and 2400(100) K. We have resolved the over 50-year old controversy regarding the structure of the Fe_2O_3 polymorph stable above ~ 50 GPa. Particularly, we demonstrate that the phase has a double perovskite-type structure and triclinic symmetry. Moreover we found that the compression above 67 GPa provokes the transition to another high-pressure phase with the orthorhombic unit cell (space group $Aba2$). This phase does not sustain heating and transforms to a HPHT Fe_2O_3 polymorph with a CaIrO_3 (post-perovskite, $\eta\text{-Fe}_2\text{O}_3$) structure at ~ 67 GPa. Under decompression to 41 GPa and heating to 1800 K this phase transforms to a polymorph with a $\text{Rh}_2\text{O}_3\text{-II}$ structure. Our most intriguing finding is the observation that at the conditions of the Earth's lower mantle, the $\eta\text{-Fe}_2\text{O}_3$ releases oxygen and can even decompose to form a novel Fe_5O_7 compound. Fe_2O_3 and Fe_3O_4 constitute up to 85 wt.% of BIFs that can be transported into the lower mantle due to subduction with lithospheric plates. Thus, the Fe_2O_3 from subducted BIFs may be a source of an oxygen-rich fluid to the deep Earth's interior with significant amount of oxygen (up to 8 times the amount of oxygen in the modern atmosphere), leading to significant heterogeneity in oxygen fugacity in different parts of the mantle.

Acknowledgments

I would like to thank my supervisors, Prof. Dr. Leonid Dubrovinsky and Prof. Dr. Natalia Dubrovinskaia for their guidance, the encouraging optimism and patience with me. I am grateful for that great working atmosphere when the new exciting scientific problems are generated almost every day.

This work would not have been possible without help of the collaborators. Special thanks to Dr. Sergey Ovsyannikov, Dr. Huiyang Gou, Prof. Andrei Bobrov, Dr. Ryosuke Sinmyo, Dr. Tiziana Boffa-Ballaran and Dr. Catherine McCammon. It was a great pleasure for me to work with you. I highly appreciate to the staff of IDD-13 (APS), BM01A, ID09A, ID18 (ESRF) and P02.2 (Petra III) beamlines for the invaluable help in conduction X-ray diffraction and Mössbauer experiments: Dr. Vitali Prakapenka, Dr. Sergey Tkachev, Dr. Clemens Prescher, Dr. Dmitry Chernyshov, Dr. Marco Merlini, Dr. Michael Hanfland, Dr. Aleksandr Chumakov, Dr. Rudolf Rüffer, Dr. Hanns-Peter Liermann, Dr. Konstantin Glazyrin and Dr. Zuzana Konôpková.

I would like to thank the BGI stuff, Petra Buchert, Lydia Kison-Herzing, Detlef Krausse and Dr. Stefan Keyssner, and the secretary of the Laboratory of Crystallography, Denis Kelk-Huth, for their help and support in administrative issues.

Ein besonderer Dank to PD Dr. Andreas Schönleber who kindly agreed to translate the Summary of this thesis into German.

Many thanks to my friends Leila Ismailova, Dr. Gleb Parakhonskiy, Dr. Svyatoslav Scheka, Valerio Cerantola, Dr. Ilya Kупenko, Dr. Kirill Yusenko, Dr. Vasily Potapkin, Natalia Solopova, Dr. Alexander Kurnosov, Dr. Martha Pamato and Eran Greenberg for the help and support, and for the fruitful discussions during the lunch and coffee-breaks.

I am grateful to my husband, Maxim Bykov, for every moment we spend together. Thank you for your silent patience, your help and your love.

I would like to thank my parents, Svetlana Shusharina and Alexander Shusharin for their constant love, moral support and numerous useful advices throughout my study.

Table of Contents

Zusammenfassung.....	4
Summary.....	7
Acknowledgments.....	10
Table of Contents	11
I. Introduction	16
1.1. Generation of the extreme conditions	16
1.2. X-ray diffraction in studies of materials recovered after HPHT synthesis.....	17
1.3. Study of crystal structures of materials important for materials science	19
1.4. Single-crystal XRD for characterization of minerals and Earth-related compounds.....	21
II. Motivation	22
2.1. Binary compounds in the metal-boron system	22
2.2. High pressure minerals and Earth-related materials.....	24
2.2.1. Knorringite	24
2.2.2. Fe ³⁺ bearing (Mg,Fe)-perovskite	24
2.2.3. FeOOH as a model compound for studying a hydrogen bond.....	26
2.2.4. Fe ₂ O ₃ and Fe ₃ O ₄ as components of subducted into lower mantle banded iron formations	27
III. Methods and instruments	29
3.1. Generation of the extreme conditions in diamond anvil cells (DACs).....	29
3.1.1. Working principle and various designs of DACs	29
3.1.2. Pressure transmitting media	31
3.1.3. Pressure determination.....	31
3.1.4. Temperature generation in DACs.....	32
3.2. X-ray diffraction	34
3.2.1. Selection of crystals	35
3.2.2. Conversion of the XRD images with CrysAlisPro software	42

3.2.3.	Calibration of a diffractometer	46
3.3.	XRD data collection strategy on synchrotron facilities	48
3.3.1.	DAC preparation.....	50
3.3.2.	Alignment of a DAC on the goniometer.....	51
3.3.3.	Selection of the proper data collection mode and data collection	51
3.4.	Processing of high-pressure XRD data	55
3.4.1.	Initial preparation	55
3.4.2.	Peak hunting	55
3.4.3.	Indexing of the reflections	56
3.4.4.	Data reduction	61
3.4.5.	Data finalization	64
3.4.6.	Structure solution and refinement	71
IV.	Scope of thesis.....	73
4.1.	Study of the materials synthesized under HPHT conditions.....	73
4.1.1.	Crystal structure of aluminum doped β -boron.....	73
4.1.2.	Crystal structure of MnB_4	75
4.1.3.	Crystal structure of Co_5B_{16}	76
4.1.4.	Crystal structure of knorringite, $\text{Mg}_3(\text{Cr}_{1.58}\text{Mg}_{0.21}\text{Si}_{0.21})\text{Si}_3\text{O}_{12}$	78
4.1.5.	Crystal structure of Fe^{3+} -bearing $(\text{Mg},\text{Fe})\text{SiO}_3$ perovskite (bridgmanite)	78
4.2.	Application of single crystal XRD for studies transition metal borides.....	80
4.2.1.	Crystal structure and high-pressure behavior of FeB_4	80
4.2.2.	Crystal structure and high-pressure behavior of Fe_2B_7 and Fe_xB_{50}	82
4.3.	Application for studies of materials at the conditions of the Earth's lower mantle	86
4.3.1.	High-pressure behavior of FeOOH	86
4.3.2.	High-pressure high-temperature behavior of Fe_2O_3 and Fe_3O_4	88
4.4.	List of manuscripts and statement of author's contribution	92
V.	Results	96

5.1.	The crystal structure of aluminum doped β -rhombohedral boron.....	96
5.1.1.	Abstract	96
5.1.2.	Introduction.....	96
5.1.3.	Experimental.....	100
5.1.4.	Results and discussion	101
5.1.5.	Conclusion	107
5.2.	Peierls distortion, magnetism, and high hardness of manganese tetraboride	108
5.2.1.	Abstract	108
5.2.2.	Introduction.....	109
5.2.3.	Materials and methods	110
5.2.4.	Results.....	114
5.2.5.	Discussion	126
5.2.6.	Conclusion	127
5.2.7.	Aknowledgments.....	128
5.3.	Novel non-magnetic hard boride Co_5B_{16} synthesized under high pressure.....	129
5.3.1.	Abstract	129
5.3.2.	Introduction.....	129
5.3.3.	Material and methods	130
5.3.4.	Results and discussion	134
5.3.5.	Conclusions.....	138
5.3.6.	Acknowledgements	138
5.4.	X-ray single-crystal and Raman study of knorringite, $\text{Mg}_3(\text{Cr}_{1.58}\text{Mg}_{0.21}\text{Si}_{0.21})\text{Si}_3\text{O}_{12}$, synthesized at 16 GPa and 1600 °C	139
5.4.1.	Abstract	139
5.4.2.	Introduction.....	140
5.4.3.	Experimental methods	141
5.4.4.	Results and discussion	145
5.4.5.	Acknowledgments	147

5.5. Crystal chemistry of Fe^{3+} -bearing $(\text{Mg}, \text{Fe})\text{SiO}_3$ perovskite: a single-crystal X-ray diffraction study	148
5.5.1. Abstract	148
5.5.2. Introduction	149
5.5.3. Experimental procedure	150
5.5.4. Results	152
5.5.5. Discussion.....	156
5.5.6. Conclusions	161
5.5.7. Acknowledgements.....	162
5.5.8. Supplementary material	162
5.6. Discovery of a superhard iron tetraboride superconductor	163
5.6.1. Abstract	163
5.6.2. Manuscript	164
5.6.3. Acknowledgements.....	172
5.6.4. Supplementary material	173
5.7. Crystal structures and compressibility of novel iron borides Fe_2B_7 and Fe_xB_{50} synthesized at high pressure and high temperature	188
5.7.1. Abstract	188
5.7.2. Introduction	188
5.7.3. Materials and methods.....	189
5.7.4. Results	191
5.7.5. Discussion.....	198
5.7.6. Conclusions	200
5.7.7. Acknowledgments.....	201
5.8. Pressure-induced hydrogen bond symmetrization in iron oxyhydroxide	202
5.8.1. Abstract	202
5.8.2. Manuscript	203
5.8.3. Supporting Materials	212

5.9. Novel high pressure monoclinic Fe ₂ O ₃ polymorph revealed by single-crystal synchrotron X-ray diffraction studies	222
5.9.1. Abstract	222
5.9.2. Introduction	223
5.9.3. Experimental	224
5.9.4. Results and discussion	225
5.9.5. Conclusions	236
5.9.6. Acknowledgments	237
5.10. Fate of banded iron formations subducted into the lower mantle	238
5.10.1. Abstract	238
5.10.2. Manuscript	239
5.10.3. Methods	246
5.10.4. Acknowledgements	247
5.10.5. Extended data	248
5.10.6. Supplementary text	255
VI. Bibliography	257
(Eidesstattliche) Versicherungen und Erklärungen	283

I. Introduction

Many scientific disciplines including geophysics, geochemistry, mineralogy, material sciences and engineering are interested in study of materials exposed to extreme conditions as high pressures and high temperatures (HPHT). External stimuli can trigger structural, electronic and magnetic changes in a matter; chemical reactions conducted at HPHT can demonstrate unexpected behavior totally different from that at ambient conditions.

1.1. Generation of the extreme conditions

The pressure generated in a body under applying mechanical force F is expressed by a simple formula:

$$P = \frac{F}{S}$$

where S is an area to which a normal force F is applied.

To generate a high pressure on a sample one can either decrease the area to which the external force is applied, or increase the value of the external force. The first option follows the path of the sample size minimization and pressure is generated by squeezing the sample between anvils made of ultra-hard materials. The technique introduced in the late 1950s is realized in miniature devices called diamond anvil cells where the sample is pressurized by two diamonds. The sample size may vary from the order of hundred microns to just several microns in ultra-high pressure studies. DAC technique coupled with heating or cooling devices provides broad range of possible P - T conditions, while the temperature can vary from ~ 4 K to over 7000 K, the highest possible pressure reached of 640 GPa [1] leaves the pressure in the center of the Earth far behind. DAC provides possibility to measure structural, elastic, electric and magnetic properties of the materials *in situ*.

Large volume presses (LVP, piston cylinder and multianvil apparatuses) work with millimeter and centimeter-scale samples and are mostly oriented on a synthesis. The synthesized sample is then examined *ex situ*, although several possibilities for *in situ* LVP studies exist (see below). Piston cylinder devices can routinely reach up to 4 GPa that corresponds to the under crustal and upper mantle conditions. In multianvil apparatus the sample loaded in pressure media is

compressed by hard anvils often produced from sintered fine-grained tungsten carbide, WC with small amount of Co as a binding agency. Application of the larger force in large volume presses to the sample allows achieving ~28 GPa and temperatures of 2500 K in the routine multianvil laboratory experiments. Experiments in multianvil apparatuses are widely used to study physical and chemical transformations on the geologically important materials under conditions of the upper and uppermost lower mantle. Sophisticated sample assemblies, use of superhard anvils and extreme applied forces recently allowed extending the pressure achievable in multi-anvil devices to 90 GPa [2]. It is believed that in routine experiments in large volume apparatuses pressure and temperature conditions of the experiment can be determined and controlled more accurately than in DACs. Compression of the sample in multianvil apparatuses can be coupled with *in situ* electrical resistivity measurements especially important for geological applications. Attaching acoustic emission system to the anvils gives a possibility to examine the sound velocity in the pressurized material. But unlike in DACs the access to the *in situ* structural characterization is limited to powder XRD. Construction of the multianvil assembly allows a fine focused X-ray beam produced by a synchrotron radiation source to illuminate the sample through anvil gaps but the X-ray flux should be rather high to obtain decent diffraction patterns.

1.2. X-ray diffraction in studies of materials recovered after HPHT synthesis

A small amount of the sample, a close intergrowth of the products, and a miniature size of the crystals after HPHT synthesis in large volume presses above 10 GPa are the factors that hinder the phase analysis and the structural characterization (Figure 1.2-1). Widely used multianvil apparatuses provide millimeter-size samples, so that the amount of the material is rather small for conventional powder X-ray diffractometers with Bragg-Brentano geometry. One option is to analyze the small sample in the capsule containing all products of HPHT synthesis: the top of the capsule has to be removed and the sample section, still in the capsule, should be polished. Then the section is mounted on a powder diffractometer with a highly collimated beam of 50–100 μm . Moving the sample and focusing the X-ray beam on a particular sample area allow

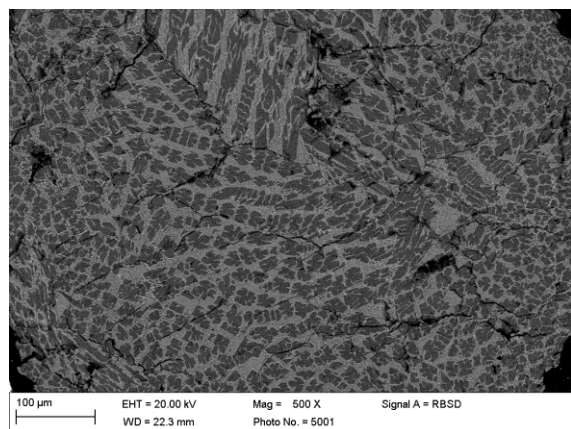


Figure 1.2-1 The SEM image of the polished surface of a sample after a multi-anvil synthesis experiment showing the microstructure typical for crystallization from a melt. Micro-size crystals of FeB_4 are embedded into a matrix of FeB formed after melting of the precursor (Fe and B) materials.

measuring the diffraction using a 2-dimensional (2D)-detector. The other possibility is to grind the sample and make spherical slurry in a highly viscous liquid like a nail polish or a epoxy resin. Then the slurry is placed on a glass fiber and mounted on a diffractometer and measured in a transmission (Debye-Scherrer) geometry, when the X-ray beam passes through the sample and the diffraction pattern is recorded by a 2D-detector. This method also allows investigation of bulky particles, not exceeding in dimensions the size of the X-ray beam (typically of 200–500 μm) without any grinding, but then the diffraction intensities would be likely spoiled due to a strong preferred orientation of crystallites. In small and/or weakly-scattering samples the reflection intensities may be insufficiently accurate for the structure solution. If the sample contains several phases (often not known) then even a search for the unit cell parameters (*indexing* procedure) becomes a non-trivial task.

The phase analysis is performed by matching the *d*-spacings (related to the angle of diffraction) and relative intensities of observable diffraction peaks with those attributed to the known phases. Each crystalline compound has its unique set of *d*-spacings. For many of them that data is recoded in specific databases, like the ICDD Powder Diffraction File (PDF) containing 799,700+ unique material data sets. The method is usually insensitive to minor phases which are present in a mixture in an amount below ~ 1 wt.%. Structure solution for a material with unknown chemical composition is challenging for powder XRD.

Unlike to powder XRD, single-crystal XRD requires small quantities of a sample for the analysis and has many advantages in studying materials with unknown structures. Crystals of a few tens

of micrometers in size may be investigated routinely using *in-house* equipment and the use of an optical microscope and/or SEM for the sample preparation allows separating pure phases. The indexing procedure for single crystal data of a reasonable quality is unambiguous and often can be performed even by a non-expert user automatically by means of the software provided with the diffractometer. In some simple cases (a full dataset of the reflections' intensities from a good-quality crystal without twinning and/or modulation) the structure solution can also be done in an automatic mode. For other cases many standard procedures are developed that lead at the end to *one* unique reliable structural model. Naturally, single-crystal XRD has its own limitations. The first one is that quantity of phase(s) in the sample cannot be derived from single crystal XRD and therefore it is often used in a combination with powder XRD to perform reliable quantitative phase analysis. The second problem is that single-crystal XRD is sensitive to the sample quality, and ideally the sample should not contain any admixtures, give sharp diffraction peaks, and have sufficiently large size (a couple of tens of microns for *in-house* studies, and a few microns for synchrotron facilities). All these requirements however are not too strict nowadays. Modern software for XRD applications allows one to detect many crystalline domains in one sample, index diffraction patterns of each of them separately, and *integrate* reflection intensities independently. In case of strong reflection overlap the simultaneous integration of several domains is also possible. Note, that a routine phase identification based on single crystal data does not demand high crystal quality.

1.3. Study of crystal structures of materials important for materials science

Extreme conditions are often used in a synthesis of new materials with valuable mechanical properties, like high hardness and low compressibility. Crystal structure of such materials would give insight into mechanisms responsible for these properties, may open way to further improve them, help in design of new materials, and enhance prediction power of the modern computational methods.

Hardness indicates how a solid material resists a deformation under an applied load. In the current thesis we used the Vickers hardness test for the characterization of the hardness of

materials. In the Vickers test a polished surface of a material is indented by a diamond square pyramid. Then one can measure the diagonals of the indentation and using known value of the applied load derive the hardness value (H_v).

The hardest known material is diamond with a rigid 3-dimensional framework of carbon atoms interconnected by sp^3 -hybridized bonds. Single-crystal diamond has the Vickers hardness above 100 GPa [3]. Cubic boron nitride c-BN being isoelectronic and isostructural to the diamond possesses $H_v \sim 45\text{--}50$ GPa [4]. Other binary compounds composed of elements from the p -block of the periodic table, which are able to create strong covalent bonds, may also demonstrate the high hardness (ex. $H_v(\text{B}_6\text{O}) \sim 38\text{--}45$ GPa [5–7]; $H_v(\text{B}_4\text{C}) \sim 35\text{--}40$ GPa [6,8]). Metal borides and carbides are another group of hard materials. Tungsten carbide with $H_v \sim 24$ GPa [3] is widely used as anvils material in multianvil apparatuses. Some believe that for tungsten tetraboride, WB_4 , the H_v is even higher, ~ 43 GPa [9]. Moreover metal borides are known for low compressibility (OsB_2 , WB_4 [10,11]) and superconductivity (MgB_2 , [12]). Therefore synthesis of novel metal borides and investigation of their properties have a great interest for material science and technology.

Compressibility of a solid is a measure of its relative volume change in response to a pressure (or mean stress) change. Its inverse value is known as a *bulk modulus* of the solid. The isothermal bulk modulus is derived by the following formula:

$$K_T = -V \left(\frac{\partial P}{\partial V} \right)_T$$

where V is the volume, $\frac{\partial P}{\partial V}$ is the partial derivative of pressure with respect to the volume. In the thesis we operate with the value of the bulk modulus determined at zero pressure, K_{T0} .

Incompressible materials do not always possess the high hardness, however hard materials always have rather high bulk moduli. Using single-crystal XRD under compression one can follow structural changes in the material and link its structure and properties. More specifically, it allows characterization of individual bond compressibilities that can give a clue to understanding the real nature of the material's resistance to the pressure and help to reveal the

specific bonds responsible for incompressibility. Such information is highly valuable for materials design and the analysis of theoretical calculations.

1.4. Single-crystal XRD for characterization of minerals and Earth-related compounds

High-pressure and high-temperature experiments using large volume presses are widely used in geo- and planetary sciences in a study of the minerals and materials related to the deep Earth's interiors, their stability fields and a chemical behavior in various solid state reactions, investigations of melting curves and elements partitioning, etc. Single-crystal XRD can serve as an ultimate probe in the characterization of the products of HPHT synthesis. It makes possible phase analysis, characterization of structures of the new materials, and the refinement of atomic occupancies that gives elements distribution between the crystallographic positions and thus defines a proper crystal-chemical formula. For Fe-bearing materials a combination of single crystal diffraction with Mössbauer spectroscopy allows defining Fe^{2+} and Fe^{3+} distribution in the atomic positions.

In situ high-pressure high-temperature studies in DACs of minerals and Earth-related compounds give direct information on the behavior of corresponding samples at the conditions of the deep Earth's interiors. High-pressure single crystal XRD experiments provide the data on a change of the volume/density of the material under pressure and thus its volume compressibility which characterizes elastic properties of this material at corresponding thermodynamic conditions. This information is valuable for explaining some seismic phenomena and seismic observations since changes in the density and the bulk modulus under compression influence the velocity of seismic waves propagating through the Earth. Structural changes in a matter also can be characterized by means of single-crystal XRD providing information about the phase transitions in the deep Earth's interiors. Material exposed to the HPHT is able not only to undergo phase transitions but also to exhibit unexpected chemistry, like decomposition and chemical reactions. Estimation of the atomic occupancies after phase transitions *in situ* gives direct information about element partitioning for unquenchable materials.

II. Motivation

Single-crystal XRD is a powerful non-destructive method which makes possible to unambiguously identify crystalline phases, determine a crystal structure and a phase composition. The first aim of the thesis was to apply methods of single-crystal XRD to materials synthesized at high-pressures and high-temperatures. Minerals, Earth-related compounds and materials with remarkable mechanical properties were studied at ambient conditions. The second aim was to apply single-crystal XRD *in situ* at HPHT conditions. The materials listed above were studied using laser-heated DACs. Particular attention was paid to the development of the technique of the single-crystal XRD in DACs at the 3rd generation synchrotron radiation facilities.

2.1. Binary compounds in the metal-boron system

Metal borides are an important class of compounds having a number of remarkable properties like superconductivity (MgB_2 , [12]), low compressibility (OsB_2 , WB_4 [10,11]), and high hardness (tungsten borides [9]). Therefore synthesis of novel metal borides and investigation of their properties have a great interest for material science and technology.

The Fe–B phase diagram [13] experimentally established at ambient pressure is very poor in compounds. So far they were represented by Fe_2B with a tetragonal structure and orthorhombic FeB [14], although hexagonal FeB_2 [15] and rhombohedral $\text{FeB}_{\sim 4.9}$ [16] have been reported in literature. Additionally to the earlier calculated orthorhombic Fe_3B phase [17], recently two new orthorhombic phases were theoretically predicted in the Fe–B system [18], FeB_2 as the ground state for FeB₂ and previously unknown compound, FeB_4 [18]. It was suggested that FeB_4 , should be stable under normal conditions in a never-seen-before orthorhombic crystal structure. The material was predicted to have naturally electron-doped bands and a large electron-phonon coupling that might render FeB_4 the first *conventional* Fe-based superconductor [18], as opposed to the recently discovered family of *unconventional* Fe-based superconductors [19,20]. Bialon *et al.* [21] suggested that the predicted FeB_4 phase could be synthesized under pressure. We have undertaken a series of high-pressure experiments aimed at the synthesis of the predicted Fe–B phases, we investigated the crystal structures of obtained phases and studied their high-pressure behavior.

Cobalt borides share many similarities with the Fe–B compounds. Co_2B and CoB are isostructural to Fe_2B and FeB , respectively, but they show a somewhat weaker magnetism. Co_2B becomes ferromagnetic below $T_C = 433$ K, whereas CoB is a paramagnetic metal [22]. Remarkably, no cobalt borides with the Co:B ratio below 1:1 have been reported. Therefore our aim was to synthesize boron-rich cobalt borides and to study their structural and magnetic properties.

Mn–B binary system is represented by Mn_4B , Mn_2B , MnB , Mn_3B_4 , MnB_2 , MnB_4 and MnB_{23} [23]. Investigations on a detailed structure of MnB_4 are still missing – the ICSD provides information about the monoclinic crystal structure of MnB_4 (space group $C2/m$), ICSD#15079, based on powder X-ray diffraction data of Andersson [24] and Andersson & Carlsson [25] obtained in late 1960s. So far MnB_4 has never been synthesized in a quantity sufficient for the investigation of its electronic and magnetic properties. Therefore our goal was to synthesize MnB_4 in a quality and a quantity sufficient for single-crystal XRD, and to study its mechanical (compressibility and hardness) and magnetic properties.

Numerous boron-rich compounds adopt structures of pure crystalline boron polymorphs, α - and β - rhombohedral boron [26,27]. As noted in [27], binary compounds of B with elements of main groups (C, Si, N, P, As, O, S, Se) usually have structures based on that of α -B. The structure of β -B, having many voids of various kinds and sizes, can adopt different dopants, such as elements of main groups (Li, Mg, Al, Si, Ge) and transition metals (Cr, Cu, Fe, Mn, Ni, Sc, V, Zn, Zr). The dependence of the atomic size of a possible dopant on a type of the occupied void was previously reviewed in [28,29]. It was shown that doping of β -B by transition metals and some other elements, such as Al, Si, and Ge, leads to increase microhardness of β -B [29] and change of its electrical properties [30].

According to the Al–B phase diagram, the maximal Al solubility in β -B is 3 at. % and it is temperature independent between 600 and 2100 K [31]. Our goal was to determine positions of interstitial Al- and B-atoms and their occupancies in the crystal structure of Al-doped β -B.

2.2. High pressure minerals and Earth-related materials

2.2.1. Knorringite

Garnet is an important constituent of the upper mantle rocks being stable over a wide range of pressures. Knorringite, $\text{Mg}_3\text{Cr}_2\text{Si}_3\text{O}_{12}$, is the chromium end-member and it is usually found either in rocks from the lowermost upper mantle or as inclusions in diamonds and constituents of ultramafic mantle xenoliths [32–34]. It was established that incorporation of knorringite in garnet does occur from 3 GPa (beyond the diamond depth facies), and the concentration of chromium achieves significant values (5–10 wt. % Cr_2O_3 and more) in the pressure range of stability of most of natural diamonds (i.e. 4–7 GPa) [35], which is an indicative feature of diamondiferous dunite–harzburgite paragenesis of the lithospheric mantle.

Despite the importance of the knorringite component in garnets in the lowermost upper mantle, the stability and high-pressure phase relations of knorringite are still controversial. Its stability field has been investigated in several studies [36–41]. More recently it was demonstrated that knorringitic garnet synthesized in high-pressure experiments always contained admixture of majorite, which resulted in the appearance of eskolaite in run products [40,42].

The paucity of structural studies on Cr-rich garnets does not allow a complete understanding of the changes of thermodynamic properties and the structure as a function of Cr incorporation in high-pressure garnets. Thus a synthesis and a detailed structural investigation of knorringite may help significantly to improve our knowledge about processes in the upper mantle and the transition zone.

2.2.2. Fe^{3+} bearing (Mg,Fe)-perovskite

It is widely accepted that MgSiO_3 -dominant perovskite (bridgmanite, referred to below as MgPv) is the most abundant phase in the Earth's lower mantle, and that this phase can accommodate a substantial amount of Fe, which is the third most abundant cation in the Earth's mantle. Many studies have attempted to understand details of the crystal structure of Fe-bearing MgPv, because changes in this structure can have strong effects on its elastic and rheological properties as well as electrical/thermal conductivity [43–49]. MgPv has two cation sites, one that

is a distorted 8- to 12-fold site (A-site, illustrated as a grey sphere in Figure 2.2.2-1) and another that is a 6-fold site (B-site, illustrated as BO_6 octahedra in Figure 2.2.2-1). The structural position (i.e., A- or B-site) and oxidation state ($2+$ or $3+$) of a cation have a strong influence on whether or not iron spin transitions occur in MgPv under lower mantle pressure and temperature conditions [50–52]. For example, theoretical calculations predict that Fe^{3+} in the B-site of Al-free MgPv should undergo high-spin to low-spin crossover at 40–70 GPa, while Fe^{3+} in the A-site should be in the high-spin state at all mantle pressures [52]. The transition to the post-perovskite structure may also be linked to the nature of cation substitution in MgPv, since the transition can be related to the degree of octahedral tilting [53,54] which has been observed to depend on MgPv composition [44,46,55].

Fe^{2+} in MgPv has been shown to occupy the A-site using single-crystal X-ray diffraction and/or Mössbauer spectroscopy [56–60]. In contrast, the site preference of Fe^{3+} is not so unequivocal. Fe^{3+} in Al-free MgPv has been assigned to the B-site [58] or both the A- and B-sites [59] on the basis of Mössbauer spectroscopy. More recently, Hummer and Fei [61] suggested that Fe^{3+} substitutes on both the A- and B-sites in Al-free MgPv with 100 % $Fe^{3+}/\Sigma Fe$. Jephcoat *et al.* [62] reported that all iron (both Fe^{2+} and Fe^{3+}) occupied the A-site based on the results of Mössbauer spectroscopy and Rietveld refinement of powder X-ray diffraction data. Catalli *et al.* [50] reported that Fe^{3+} substitutes equally on both the A- and B-sites in Al-free MgPv with 100 % $Fe^{3+}/\Sigma Fe$ above 50 GPa based on a combination of time-domain synchrotron Mössbauer spectroscopy (also known as nuclear forward scattering), X-ray emission spectroscopy and powder X-ray diffraction measurements. The detailed crystal structure of, and site preference of Fe in, MgPv have been examined using single-crystal X-ray diffraction [56,60,63,64]; however

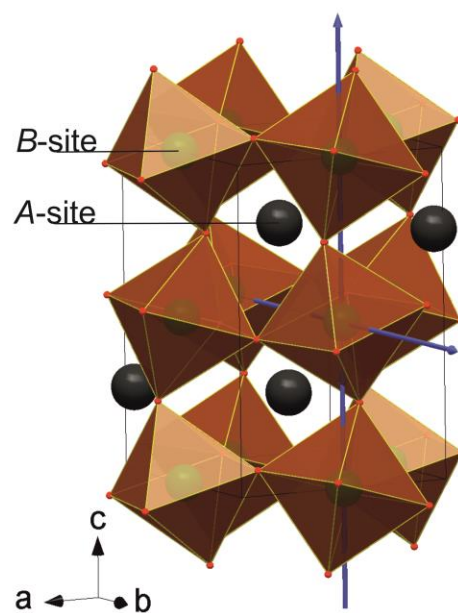


Figure 2.2.2-1 Crystal structure of $(Mg,Fe)SiO_3$ perovskite composed of corner-shared SiO_6^{4-} octahedra and Mg^{2+} , Fe^{2+} , Fe^{3+} ions filling 8-fold void. Blue arrows are directions of octahedra tilt from positions in an ideal cubic perovskite structure.

the valence state of Fe was not determined in these studies. In order to characterize the effect of Fe substitution on the crystal structure of MgPv, it is important to determine both its valence state and site preference simultaneously.

2.2.3. FeOOH as a model compound for studying a hydrogen bond

The hydrogen bond in oxyhydroxides and hydroxides is an attractive interaction between a hydrogen atom from a hydroxyl (O–H) group and a near neighbor oxygen atom or a group of atoms [5]. In contrast to other interacting atoms, H-bonds undergo large variations of their energetic and geometrical parameters under pressure [66–69]. At ambient pressure the O–H···O configuration is highly asymmetric. For example, in goethite, α -FeOOH, a common mineral in soils, sediments, and ore deposits, the angle formed by the (O–H) and the adjacent O is $161(3)^\circ$, the O–H length is $0.88(4)$ Å, and H···O is $1.90(4)$ Å [70]. As observed by Holzapfel [66] even moderate compression reduces the H···O distances, barely affecting the hydroxyl bond length, which leads to the strengthening of the hydrogen bond at high pressure [69]. Benoit *et al.* [67] and Lin *et al.* [68] predicted that higher compression will also lead to linearization of the O–H···O bond and eventually the formation of a symmetric O–H–O hydrogen species of equal O–H distances.

Symmetrization of hydrogen bonds is expected to have a significant effect on crystal structure and the behavior of materials [69]. Suggestions that the phenomena may occur under compression were reported for a number of compounds, namely, the hydrogen halides [71], δ -AlOOH(D), $\text{MgSi}_2\text{O}_4(\text{OH})_2$, δ -Al(OH)₃, CrOOH(D), GaOOH, InOOH, and formic acid [72–76], but only in H₂O ice-X, at pressures approaching 100 GPa, the elusive symmetrization has been unambiguously demonstrated [77–80]. High-pressure structural studies of goethite up to ~ 29 GPa have been performed by several groups [81,82] but no signs of the symmetrization was observed as any other changes as well. In principle high-spin Fe^{3+} in FeOOH may undergo a spin crossover to low-spin state under compression but theoretical calculations could not resolve this question unambiguously [83].

Experimental studies of hydrogen bond properties at pressures exceeding 20 GPa are difficult. The reason is that the ordinary direct and indirect structural methods such as powder X-ray

diffraction (XRD), and vibration spectroscopy, Raman or Infra-Red, are unable to locate the position of hydrogen [73–79]. Neutron diffraction, the perfect method for this purpose, is currently limited to pressures of < 20 GPa [75]. Yet the combination of single crystal XRD and vibrational spectroscopy, as demonstrated in the example of ice-X [80], may be adequate to resolve the geometry of the hydrogen bond as a function of pressure. We studied high-pressure behavior of FeOOH in order to trace the geometry of the hydrogen bond by its effect on the shape of atomic groups or polyhedrons forming FeOOH crystal structure.

2.2.4. Fe₂O₃ and Fe₃O₄ as components of subducted into lower mantle banded iron formations

Banded Iron Formations and ironstones formed starting from the late Precambrian (between 2.8 and 1.8 billion years ago) until the Pliocene [84]. Typical BIFs consist of distinctly separated alternating iron-rich (magnetite, Fe₃O₄, and hematite, α -Fe₂O₃) and amorphous silica-rich layers. Together with downwelling lithosphere BIFs are expected to penetrate deep into the mantle [85,86]. Available experimental data [85,87,88] suggest that iron oxides melt above the geotherm in the entire mantle and thus remain solid in slabs that are colder than the surrounding mantle. Thus the fate of iron oxides, a major component of subducted BIFs, depends on the pressures and temperatures (*P-T*) to which they are exposed.

Previously based on powder XRD and Moessbauer spectroscopy experiments in DACs, magnetite (Fe₃O₄) was shown to transform into a high-pressure phase above 19 GPa [89,90]. Many candidates have been proposed for high-pressure polymorph of Fe₃O₄, among them monoclinic structure with octahedrally coordinated iron atoms [91], CaMn₂O₄-type (space group *Pbcm*, No. #57) [92] and CaTi₂O₄-type (space group *Bbmm*, No. #63) structures [89,93]. We applied methods of single-crystal XRD in laser-heated DACs to follow the HPHT behavior of Fe₃O₄ to conditions of the Earth's lower mantle.

Due to its significance in condensed matter and mineral physics, the high-pressure behavior of hematite, α -Fe₂O₃, has been investigated even more intensively than that of Fe₃O₄. Particular attention has been focused on elucidating the nature of phase transition(s) and the structure of the high-pressure phase of hematite observed above ~50 GPa [94–103]. For this phase two

structures have been proposed by different groups: Rh_2O_3 -II-type (space group $Pbcn$, No. #60) and GdFeO_3 -perovskite-type (space group $Pbnm$, No. #62) structures [94,97]. While Mössbauer spectroscopic and resistivity measurements clearly demonstrate the importance of electronic changes in Fe^{3+} and seem to support the Rh_2O_3 -II-type structure [95], powder diffraction data collected by various groups over several decades did not allow an unambiguous assignment of the structural type (see Refs. [94,95,97,98] and references therein). Experiments in laser-heated DACs revealed the formation of a CaIrO_3 -type phase (“post-perovskite”, PPv $\eta\text{-Fe}_2\text{O}_3$) at pressures above ~ 60 GPa [88,99,100,103]. However, the behavior of this phase under compression is not well studied. The phase diagram of Fe_2O_3 at megabar pressure range is incomplete and the data are often conflicting [88,99–101]. Therefore, in order to study the behavior of ferric iron (Fe^{3+}) in subducting BIFs, we applied the complementary methods of single crystal XRD in laser-heated DACs and SMS spectroscopy.

III. Methods and instruments

3.1. Generation of the extreme conditions in diamond anvil cells (DACs)

3.1.1. Working principle and various designs of DACs

The DAC technique was introduced in the late 1950s and since then became the most successful method for generating high-pressure conditions providing the opportunity for *in situ* study of matter at pressures above 300 GPa using a wide range of diffraction, spectroscopic, elastic and inelastic scattering methods.

The heart of the device is a pair of polished diamonds (often according to the (100)-crystal orientation for the highest strength). A metal (Re or steel) gasket with an indentation and a hole is placed between the two opposing diamond anvils forming a sample chamber (Figure 3.1.1-1). The diamonds are mounted on a hard (tungsten carbide, for example) seats and the latter are placed inside a mechanically driven metallic cell (Figure 3.1.1-2).

For XRD many DACs' designs are available. There are both commercial (by Diacell, Almax easyLab, Syntek) and academic research solutions (Merrill-Basset 3-pin DAC [104], BX90 and BX90mini [105], Mao-Bell-type DAC [106], Le Toullec type DAC [107], ETH-type DAC [108], Heidelberg HPHT-DAC [109]). In the current thesis we used DACs of the BX90 type designed and machined in the BGI [105]. Such DAC provides an easy alignment, a stable pressurization, and maintains the pressure constant for a long time. For several synchrotron studies at the ESRF we used a membrane driven Le Toullec type DAC [107] modified for Boehler-Almax anvils.

To use a DAC in a single-crystal XRD experiment, both the diamonds and the DAC should have a large optical aperture because metallic parts of the DAC and WC seats shadow the major part of the diffracted reflections. In the current work we used specially designed BX90 cells with a large opening angle together with commercial diamonds of Boehler-Almax design [110] produced by Almax easyLab which provide the highest opening angle of $4\theta = 80^\circ$.

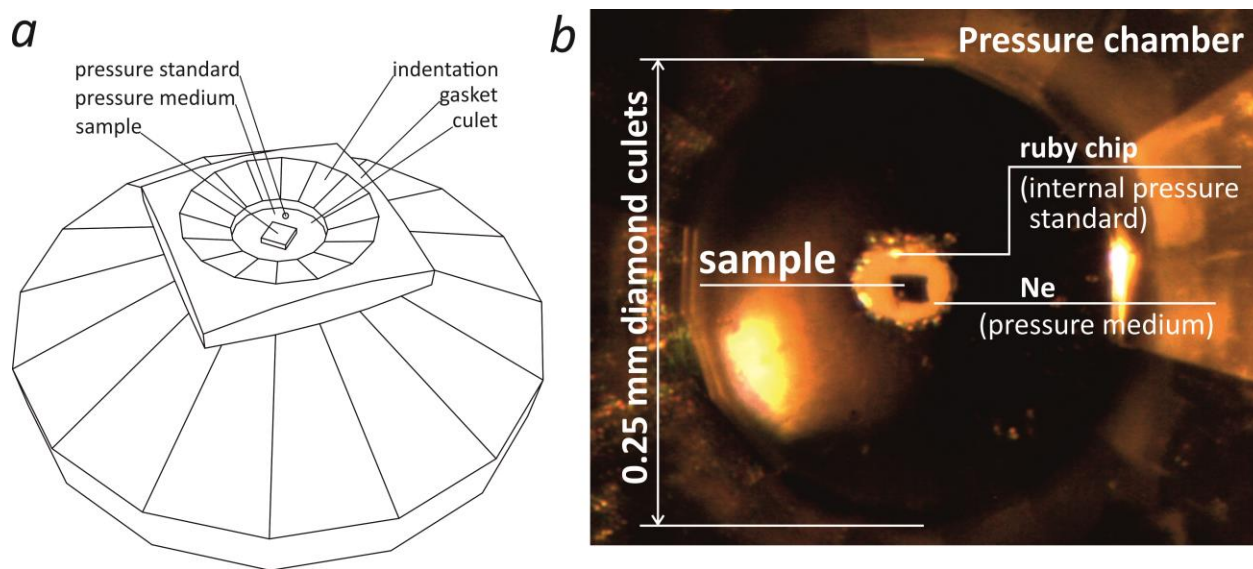


Figure 3.1.1-1 Images of the pressure chamber: *a* – a schematic representation of the Boehler-Almax diamond with a gasket on it and a sample in the hole; *b* – a photograph of the pressure chamber taken under an optical microscope through the diamond anvil (top view).

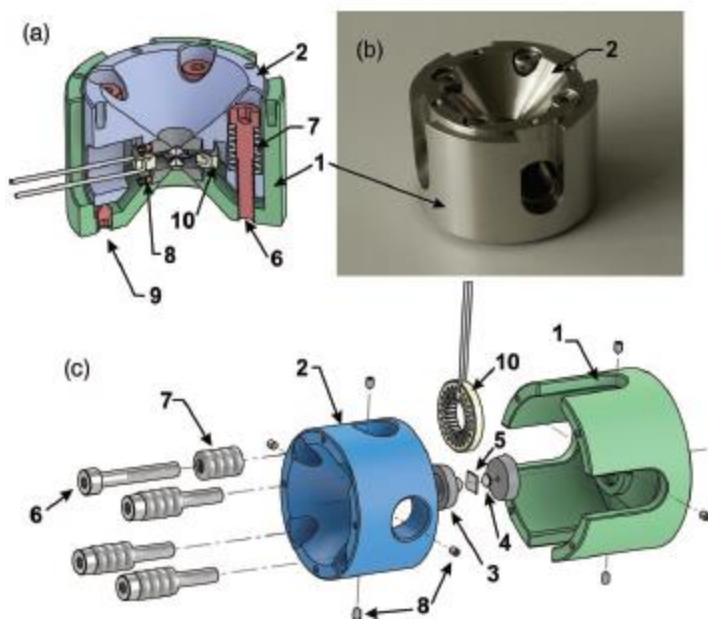


Figure 3.1.1-2 BX90 diamond anvil cell design. *a* – Section view, *b* – photograph of a loaded cell, *c* – exploded view. 1 – Outer cylinder part, 2 – inner piston part, 3 – diamond supporting plates, 4 – diamond anvils, 5 – metallic gasket, 6 – M4 (#8-32) screws for generating loading force, 7 – pack of conical spring washers (Belleville springs), 8 – setscrews for diamond anvils alignment, 9 – safety setscrews, 10 – optional miniature resistive heater [105].

3.1.2. Pressure transmitting media

Pressure transmitting medium is used to transmit the pressure from squeezing diamonds to the sample. Without the pressure transmitting medium a single-crystal in the pressure chamber would be smashed by the contracting gasket and diamonds. The construction of the DAC assumes a uniaxial compression and the pressure medium also serves to make it isotropic, i.e. *hydrostatic*. Otherwise, the uniaxial stress would cause shear strains in the sample that would lead to the broadening of the diffraction reflections. Nevertheless, the true hydrostaticity above 15 GPa and ambient temperature is not possible, since no compounds are known to be in a liquid state at these conditions. Inert gases loaded into the pressure chamber are the best substitutes; they create a quasi-hydrostatic environment and can preserve the single crystal of decent quality to at least 150 GPa [111].

In the current work the pressure medium (Ne or He) was loaded with a gas-loading system developed and installed in Bayerisches Geoinstitut. A DAC was placed inside the pressure vessel and then the gas was pumped in up to ~1.5 kbar. Then the DAC was closed by the piston-driving mechanism [112]. Afterwards one released the pressure, tightened the DAC's screws and removed the DAC from the pressure vessel. Several loadings were done using similar gas-loading systems installed on synchrotron facilities (ESRF, APS).

3.1.3. Pressure determination

Measurements in DACs require proper *in situ* determination of the pressure inside the pressure chamber. For these purposes one loads a pressure standard together with the sample. The pressure can be measured utilizing one of two (or both) methods based on:

1. laser-induced fluorescence, where one measures positions of particular spectral lines of pressure standards: R_1 line of ruby, Cr-doped Al_2O_3 (Figure 3.1.3-1a) [113,114] or Y_1 line of in Sm-doped yttrium aluminum garnet $\text{Y}_3\text{Al}_5\text{O}_{12}$ (Sm:YAG) [115] (Figure 3.1.3-1b).
2. XRD, where the unit cell parameters of the pressure standard are obtained (Figure 3.1.3-1c). The pressure is calculated using the known equation of state of the standard material. Commonly used pressure standards are inert, relatively compressible

compounds with simple crystal structures, namely: metals (Au, Pt, Mo) or simple binary compounds (MgO, NaCl, KCl, KBr) [116–119]. Pressure transmitting media, as Ne (after solidification above 10 GPa) and NaCl are widely used as the standards as well since they have demonstrated excellent agreement with ruby, Au and Pt pressure standards in high-pressure and high-temperature experiments [117].

In the thesis we used pressure standards of both types, often simultaneously. The first method typically was used for preliminary pressure estimations (for instance, during an increase of the pressure in the DAC), while powder XRD on Ne was used for the pressure determination in cold compression studies and laser-heating experiments as well.

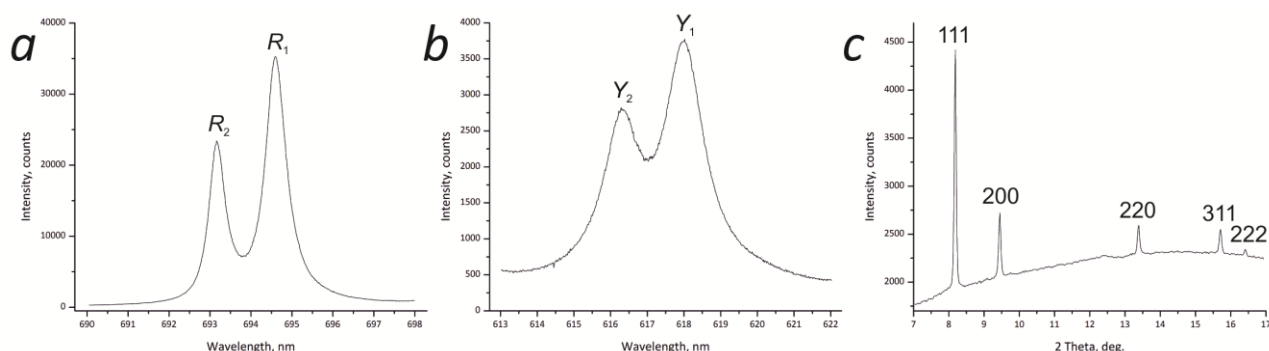


Figure 3.1.3-1 Fluorescence spectra of ruby (a) and Sm:YAG (b). For pressure estimation one measures a position of the lines R_1 and Y_1 , respectively. Powder XRD pattern of solid Ne at 12.3 GPa (c) with indexed reflections used for calculation of the unit cell volume. The pressure is determined from Ne equation of state.

3.1.4. Temperature generation in DACs

Heating is an important part of high-pressure experiments, especially if studies are dedicated to modelling processes in deep Earth's interiors. There are two possibilities to generate high temperatures in DACs, an external electrical resistive heating and a heating with a laser.

External electrical resistive heating provides accurate temperature determination (using a thermocouple), allows one to avoid thermal gradients, is very stable over a long duration of the experiments, however, it can be used only below ~ 1100 K. Already above 800 K the diamonds start to oxidize and the pressure inside the pressure chamber is not stable anymore.

The temperatures above 1200 K can be generated by the laser heating. The maximal temperature may reach that of the Earth's inner core. The method, however, suffers from the significant uncertainties in the temperature determination (~ 50 – 100 K) and large thermal gradients within the sample, especially when only one side of the DAC is heated. A double-sided laser-heating system was introduced to eliminate the latter problem (Figure 3.1.4-1) [120]. With certain modifications it is widely applied at synchrotron facilities. Until recently all existing systems were stationary and it did not allow the DAC rotation during the heating, i.e. *in situ* HPHT single-crystal XRD was impossible. A portable laser-heating system developed in BGI [121] is mounted directly on a goniometer stage. During the measurement it rotates together with the DAC that provides an opportunity to collect single-crystal XRD simultaneously with the laser heating (Figure 3.1.4-2).

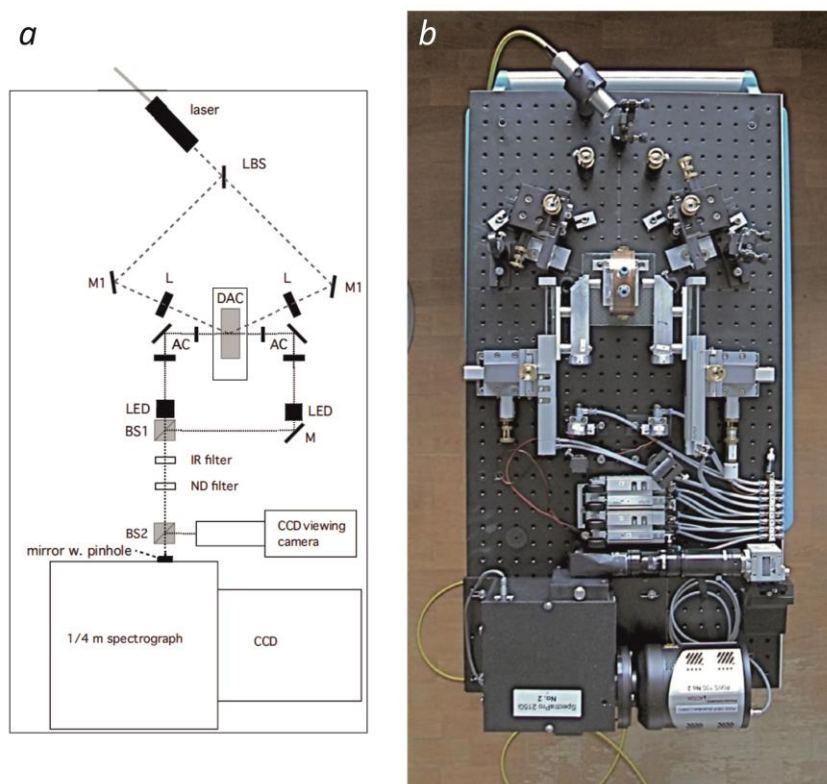


Figure 3.1.4-1 Double-sided laser-heating system introduced by Boehler *et al.* [120], schematics of the layout (a) and a photograph (b). LBS – laser beam splitter; M – mirrors; L – focusing lenses; AC – collecting achromats; DAC – diamond anvil cell; LED – light-emitting diode; BS – beam splitters; IR – infrared; ND – neutral density.

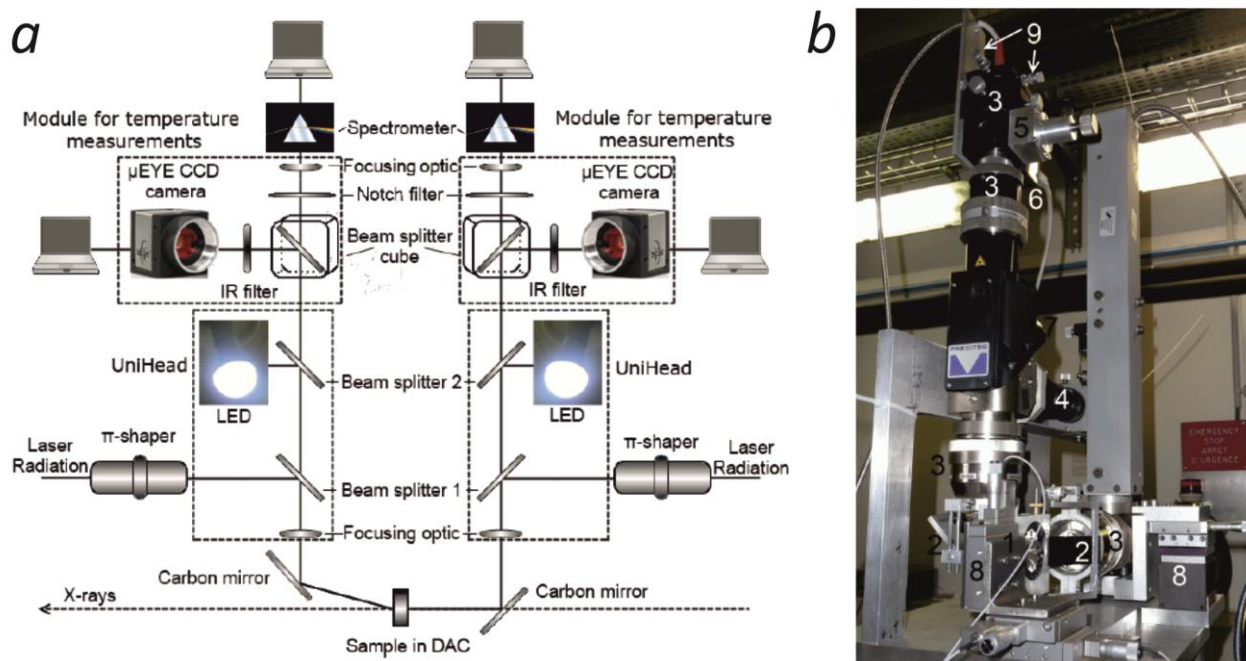


Figure 3.1.4-2 Portable double-sided laser-heating system developed in BGI: schematics of the layout (a) and a photograph [121]. 1 – holder with a diamond anvil cell; 2 – carbon mirrors; 3 – focusing optics; 4 – π -shaper; 5 – beam-splitter cube; 6 – CCD camera; 7 – LED; 8 – 3-axis translation stages; 9 – adjustable screws for spectrometer focusing.

3.2. X-ray diffraction

Diffraction occurs when the light encounters an obstacle with repeating features that is comparable in size to the wavelength of the light. As a result a complex picture of the light scattering with varying intensities appears (*diffraction pattern*). A crystalline material can be considered as an object with a 3-dimensional periodic structure, and when it is exposed to X-rays with the wavelength close to interatomic distances in the material, that causes a diffraction of the X-rays (Bragg diffraction). The diffraction condition is defined according to Bragg law:

$$2d \sin \theta = n\lambda$$

where d – is a distance between family of hkl crystallographic planes (i.e. the lattice spacing), θ – the angle of incidence of X-rays with the wavelength λ to the planes, n is the order of the reflection (integer number) (Figure 3.2-1).

In a routine *in-house* X-ray diffraction experiment the crystal mounted on a goniometer is illuminated by a collimated monochromatic X-ray beam and the positions and intensities of the diffraction reflections are measured. Using information about reflections' positions one can derive an orientation of the crystal with respect to the goniometer axis, unit cell parameters and a lattice symmetry, while from reflections intensities a space group and atomic coordinates can be calculated.

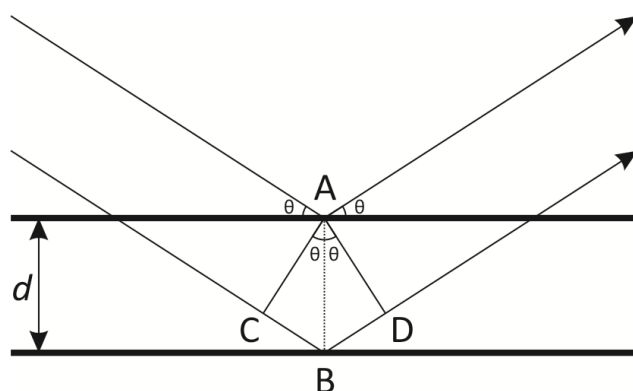


Figure 3.2-1 Diffraction condition for the family of *hkl*-planes. When coherent waves meet the family of lattice planes with *hkl* indices, they interfere each other if the difference between those pathways ($CB + BD$) is equal to integer number of wavelengths. Mathematically it is expressed by Bragg's law: $2d \sin \theta = n\lambda$.

3.2.1. Selection of crystals

Selection of an appropriate single crystal for XRD is the most crucial stage of the experiment. Single crystals are composed of smaller fragments, *mosaic blocks*, which are not perfectly aligned with one another. The degree of the orientation divergence of the blocks called as *mosaic spread* or *mosaicity* is a major characteristic of the crystal quality. High-quality crystals with the low mosaicity are required for the collection of accurate crystallographic data, for the structure solution and the reliable refinement of atomic positions and thermal parameters. In a high-pressure experiment the crystal is affected by stresses that cause strains propagating through the sample and deteriorating it. Empirically, high-quality crystals deteriorate slower, and the structural information can be obtained for a larger pressure range. Therefore high-pressure studies demand for nearly perfect quality single crystals.

Initial selection of the crystals is performed using an optical microscope. The crystal is placed inside a drop of an epoxy resin located on a glass slide, and then it is mounted on a top of a glass fiber which is attached to a cylindrical metal holder with wax (Figure 3.2.1-1a). The holder with the crystal is mounted on a *goniometer head* (Figure 3.2.1-1a) serving for the precise alignment of

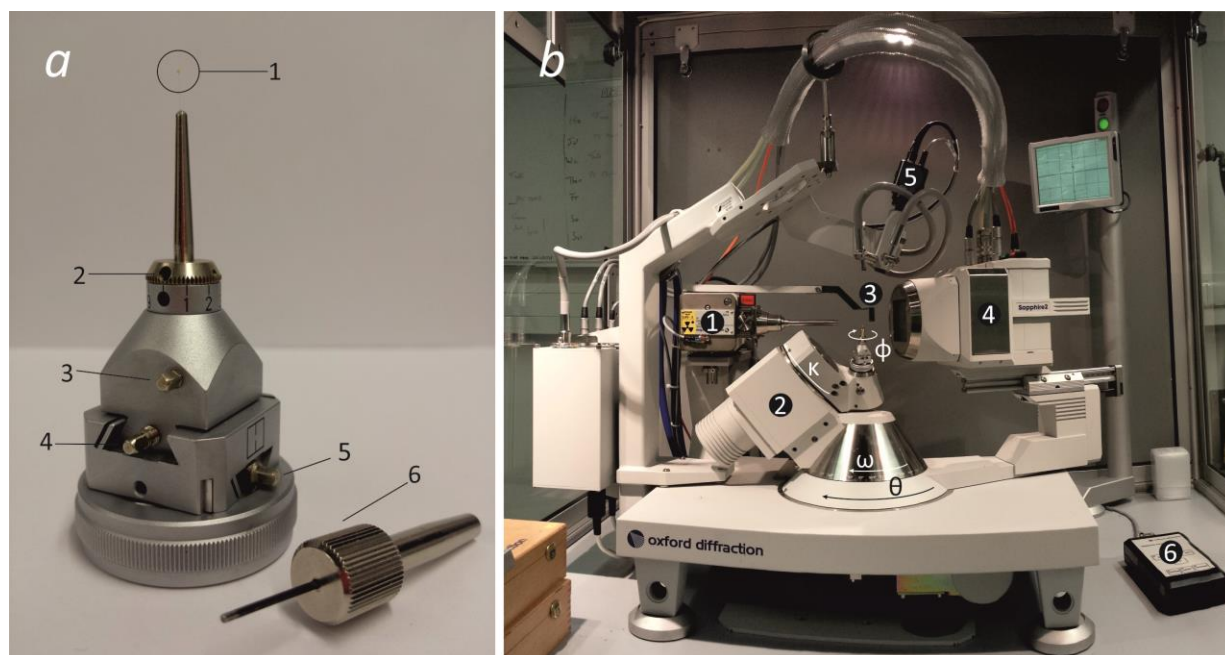


Figure 3.2.1-1 Crystal mounted on a goniometer head (a): 1 – crystal on a glass fiber, 2 – pin lock, 3, 4, 5 – positioning screws along z, x and y, respectively, 6 – screwdriver for sample adjustment. four-circle single-crystal diffractometer (b): 1 – X-ray source (Mo-tube); 2 – goniometer with labeled rotation axis (ω -, θ -, κ -, φ); 3 – beamstop; 4 – CCD detector; 5 – video camera for optical alignment; 6 – remote control device.

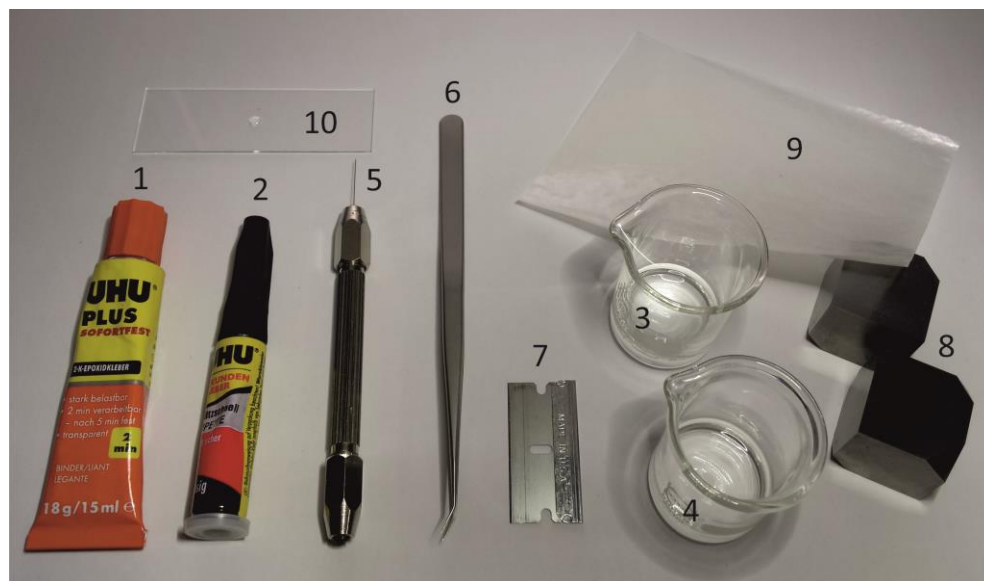


Figure 3.2.1-2 Auxiliary instruments for selection of single crystals: 1 – epoxy (binder component) and 2 – instant adhesives, with correspondent solvents, 3 – ethanol and 4 – acetone; 5 – a holder with 2 μ m tungsten needle for sample selection, 6 – tweezers, 7 – a steel blade; 8 – two tungsten carbide cubes and 9 – weighing paper; 10 – a glass slide with an epoxy resin drop and a sample inside it.

the crystal on a diffractometer (Figure 3.2.1-1*b*). For the routine selection of the crystals and a preliminary phase identification one can use the liquid epoxy resin to hold the sample on the glass fiber. Then after the XRD analysis the sample is returned back into the drop of the epoxy resin directly without use of any additional dismounting agents. If necessary the epoxy resin is easily washed out with ethanol. For the full data collection the crystal has to be fixed firmly, for example with instant (cyanoacrylate) adhesive or nail polish. Afterwards the crystal is dismounted by acetone.

Figure 3.2.1-2 shows auxiliary instruments for selection of single crystals. The epoxy resin is used not only for the sample mounting but also as a viscous medium that holds the particles. A cylindrical holder with 2 μm top tungsten needle is used to extract the sample from the capsule and manipulate with the sample inside the medium. With a steel blade one can simply decrease the size of the single crystal or separate several crystals assembled in one large particle (Figure 3.2.1-3). The separation is performed inside the epoxy resin to prevent the loss of the crystals. XRD experiments in DACs require relatively small crystals. Ideally for standard 250 μm diamonds the crystal should not exceed 10 μm in thickness and ~15–30 μm in diameter (see below for

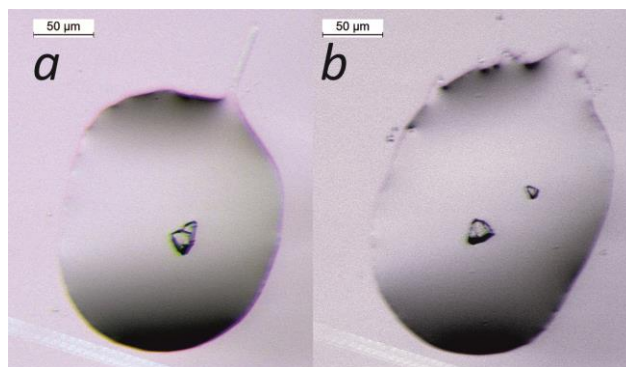


Figure 3.2.1-3 A separation of optically detectable twins in ~20 μm sample with a steel blade: a view before (*a*) and after (*b*).

details). When the material is very hard (like metal borides or perovskites) it is not always possible to extract the sample from the capsule using the needle or the steel blade, and instead the capsule packaged in a sheet of weighing paper is smashed between two tungsten carbide cubes and the sample is selected from the resulted particles. Hard large pieces can also be crashed in the same way when the steel blade is too soft to cut the material, or when the cutting provokes the sample deterioration (for example, in some iron oxides).

Once the sample is mounted on a diffractometer (Figure 3.2.1-1*b*), the center of the sample should be aligned by moving positioning screws on the goniometer head (Figure 3.2.1-1*a*), so

that the center is brought into the point where the rotation axis of the goniometer crosses with the incident X-ray beam. This point is usually viewed at the center of the video camera.

Afterwards in order to estimate the quality of the sample one runs a pre-experiment: a set of ~ 100 XRD-images (*frames*) that can be collected for a relatively short time (~ 30 minutes). The pre-experiment as well as an ordinary full data collection are done in an *oscillation* (= *narrow slicing*) *mode*, i.e. when the diffraction is recorded while rotating the sample about a single (usually ω -) axis in small steps of $0.1\text{--}2^\circ$. During the pre-experiment the frames are measured in narrow ranges of ω ($\sim 10\text{--}20^\circ$) in three different orientations of the sample with respect to the X-ray primary beam. The decision on the crystal (and the diffraction data) quality is taken after the inspection of the shape of the diffraction peaks which is an indicator of the crystal mosaicity (see Table 3.2.1-1 for details).

For this thesis research the selection of single crystals was usually performed on a three-circle Bruker diffractometer equipped with a SMART APEX CCD detector and a high-brilliance Rigaku rotating anode (Rotor Flex FR-D, Mo- $K\alpha$ radiation) with Osmic focusing X-ray optics. The finely focused high brilliance X-ray beam makes possible a selection of even $10\text{ }\mu\text{m}$ -sized samples with a medium scattering power.

In some cases the selection of crystals was not possible on the *in-house* diffractometer - when the crystals were too small, or weakly scattered, or their quality strongly varied within the same batch. Then a fast and effective selection procedure was realized on the synchrotron XRD beamlines where the diffractometers were equipped with remotely controlled positioning motors and a video camera aligned with the X-ray beam. Several studied crystals were placed into a DAC where diamonds had large culets ($500\text{--}900\text{ }\mu\text{m}$). Then we performed a fast scanning through the diamond anvils, collection of single-crystal XRD for each individual crystal, and evaluation of the crystal quality. For example, the surface of $900\text{ }\mu\text{m}$ diamond can in principle accommodate up to 70 crystals of $5\text{--}10\text{ }\mu\text{m}$ (Figure 3.2.1-4), and screening of such a cell at ID09A beamline at ESRF takes ~ 4 hours. The procedure, for instance, was used for selection of Mg, Al-perovskite single crystal; only 3 crystals out of 113 had proper quality.

For high-pressure experiments the size of the investigated sample plays a significant role. To prevent bridging of the crystal between diamonds that causes its destruction, the thickness of the crystal should be less than the thickness of the pressure chamber under the highest expected pressure. For standard 250 μm -culet diamonds it is $\sim 10\text{--}15\text{ }\mu\text{m}$, for 120 μm beveled diamonds it is less than 10 μm . The gasket hole shrinks almost twice in the diameter upon a noble gas loading and compression; therefore diameter of the sample should not exceed 30 μm for 250 μm diamonds and 10-15 μm for 120 μm diamonds. An additional constrain is the beam size – the diffraction volume should be constant or vary predictably during the measurement to provide correct intensities for symmetry-equivalent reflections. Therefore situations when the crystal is comparable with the beam in size should be avoided, and crystals should be either significantly larger or smaller than the beam.

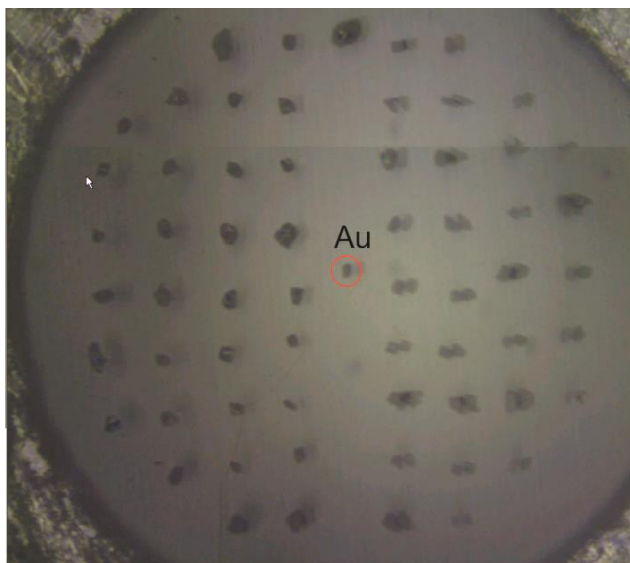


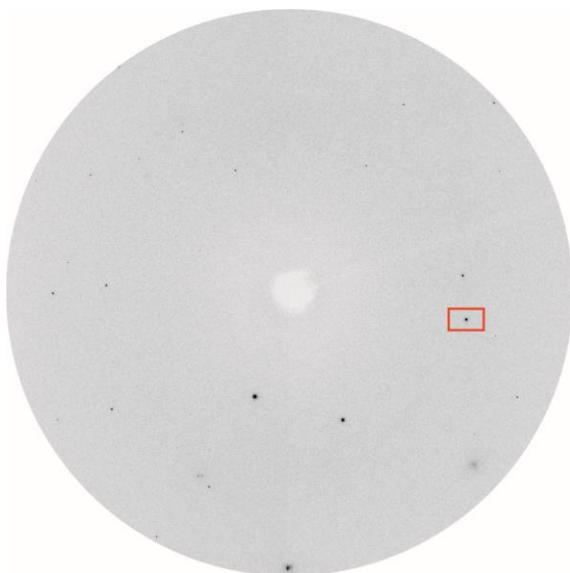
Figure 3.2.1-4 Sample screening on synchrotron. 61 crystals with the average diameter of 5–10 μm size are placed inside a 500- μm hole in the steel gasket located between a pair of diamonds with 900- μm culets. Gold particle in the center is used for an accurate DAC positioning.

III. Methods and instruments

Table 3.2.1-1 2D XRD frames (left) measured from various crystals along with judgments of the crystal (and the corresponding diffraction data) quality. The frames were taken during narrow (0.3 or 0.5°) ω -scanning. Figures of the right show areas-of-interest on the detector around specific reflections (highlighted as red rectangles) as a function of ω .

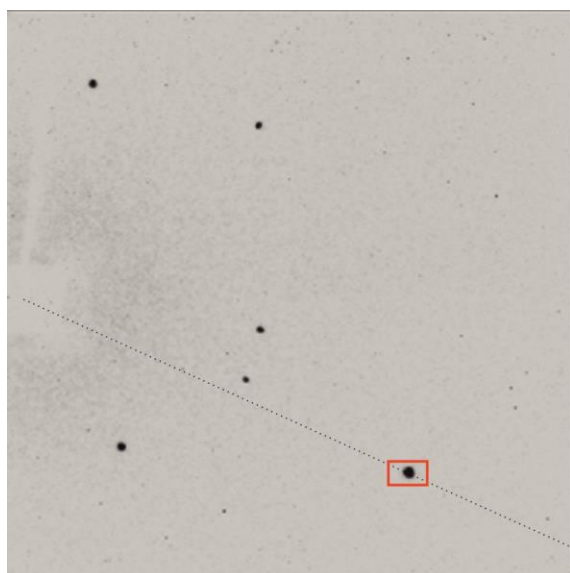
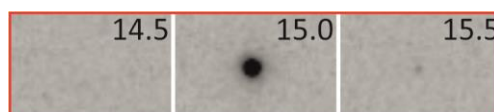
2D XRD frames

Selected peak profiles and judgments of the data quality



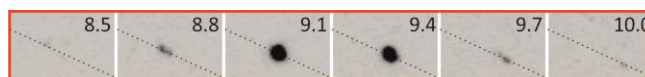
Perfect synchrotron data.

The peaks are rather sharp and mostly not splitted up over several frames.



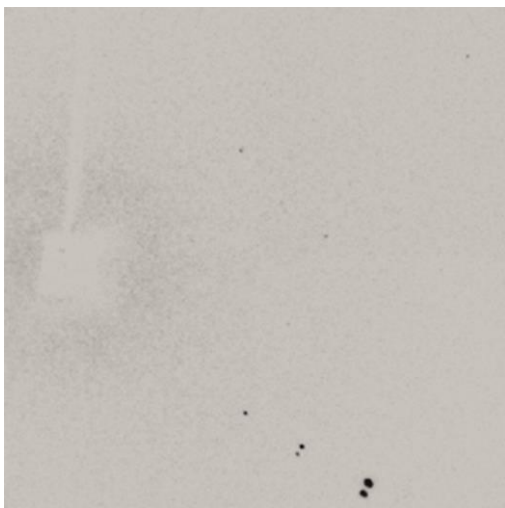
Perfect data (here and below *in-house* data are displayed).

The peaks are intense and relatively sharp. No visible movement of the reflection's profile along the detector plane (i.e. no movement from the dotted line connecting a detector origin and the diffraction spot). No apparent twinning.



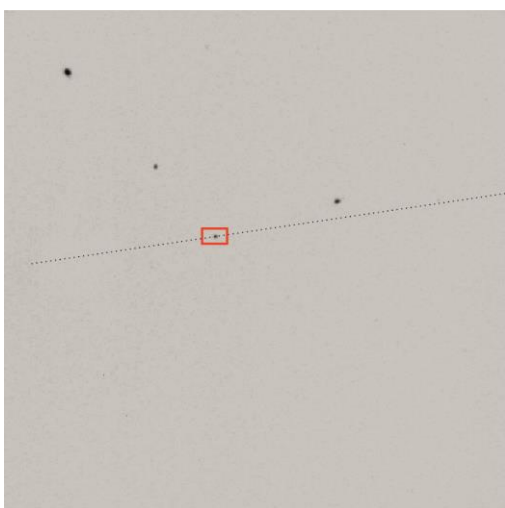
2D XRD frames

Selected peak profiles and judgments of the data quality



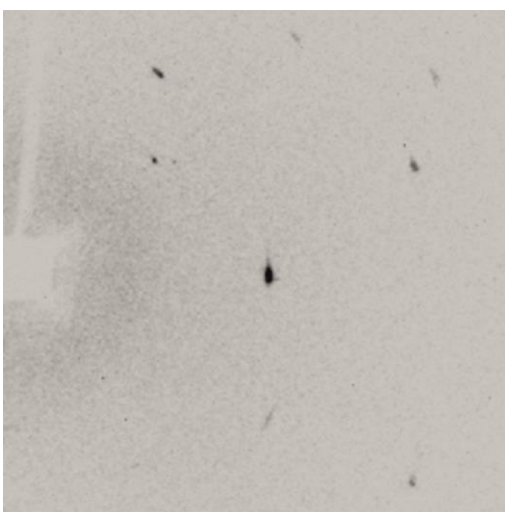
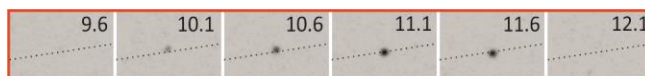
Good data.

The peaks are intense and relatively sharp. No visible movement of the reflection's profile along the detector plane but apparent twinning exists. The degree of the reflection overlap seems to be rather small and the twins can be deconvoluted during the data reduction.



Bad data (in a sense that the crystal is not suitable for high-pressure XRD).

The peaks are intense but there is an obvious movement of the reflection along the detector plane (an apparent movement from a dotted line connecting a detector origin and the diffraction spot).



Bad data (in a sense that the crystal is not suitable for high-pressure XRD).

The reflections broaden along the detector plane.

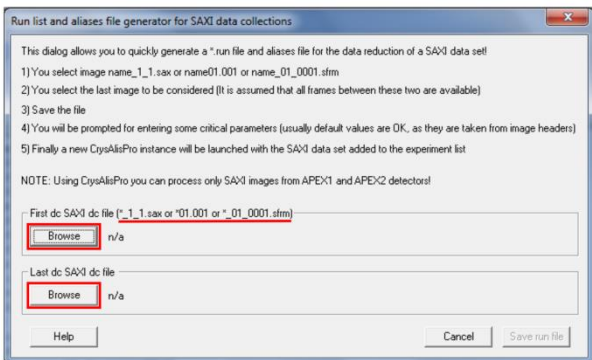
3.2.2. Conversion of the XRD images with CrysAlisPro software

CrysAlisPro is a user-friendly software created to operate Agilent technologies diffractometers and perform a XRD data reduction. In the current thesis CrysAlisPro was used in various applications for the analysis of the XRD data as preliminary identification of the phase composition, selection of the appropriate sample for X-ray (including synchrotron-based) diffraction, and single-crystal XRD data processing.

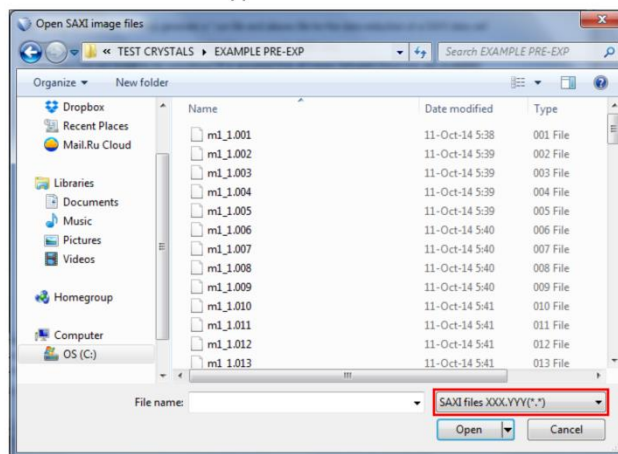
A very helpful feature of the software is a support of geometries and XRD images of third-party diffractometers. All XRD data presented in the current thesis were converted to the formats supported by CrysAlisPro if it was necessary. The majority of the *in-house* experiments on the selection of the crystals and identification of the phases were performed on three-circle Bruker diffractometer. CrysAlisPro directly works with Bruker SAXI frames, but before the data processing one has to *create an experiment* using these frames (the procedure is demonstrated on Figure 3.2.2-1).

The studies under extreme conditions were carried out on three synchrotron XRD beamlines: 13-IDD beamline at Advanced Photon Source (APS) in Argonne, USA; ID09A beamline at European Synchrotron Radiation Source (ESRF) in Grenoble, France; P02.2 Extreme Conditions beamline at Petra III in Hamburg, Germany. In order to create the CrysAlisPro experiment one has to convert the images to the native CrysAlisPro format called ESPERANTO [122]. The dialog is started by `dc rit` command called from the command line (can be invoked by F5 button). In the opened window one provides information referred to diffraction image, instrument model and data collection features (see Figure 3.2.2-2 for details). The typical values attributed to the synchrotron single-crystal XRD studies are shown in Table 3.2.2-1.

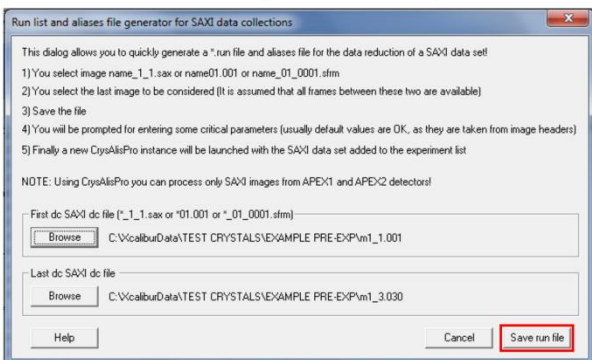
1. Select the first and the last frames of the experiment by 'Browse' button. Pay attention to the image numbering, the first frame should be written in format <Name>_1.001



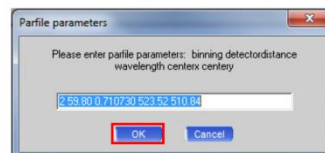
2. The first and the last frames should have SAXI XXX.YYY file type.



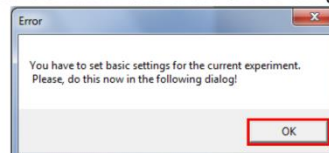
3. Save the created experiment in CrysAlisPro.



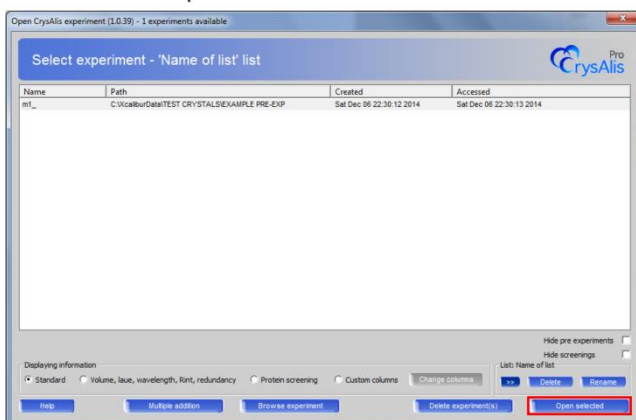
4. Confirm preliminary calibration parameters.



6. Confirm the default settings of the experiment.



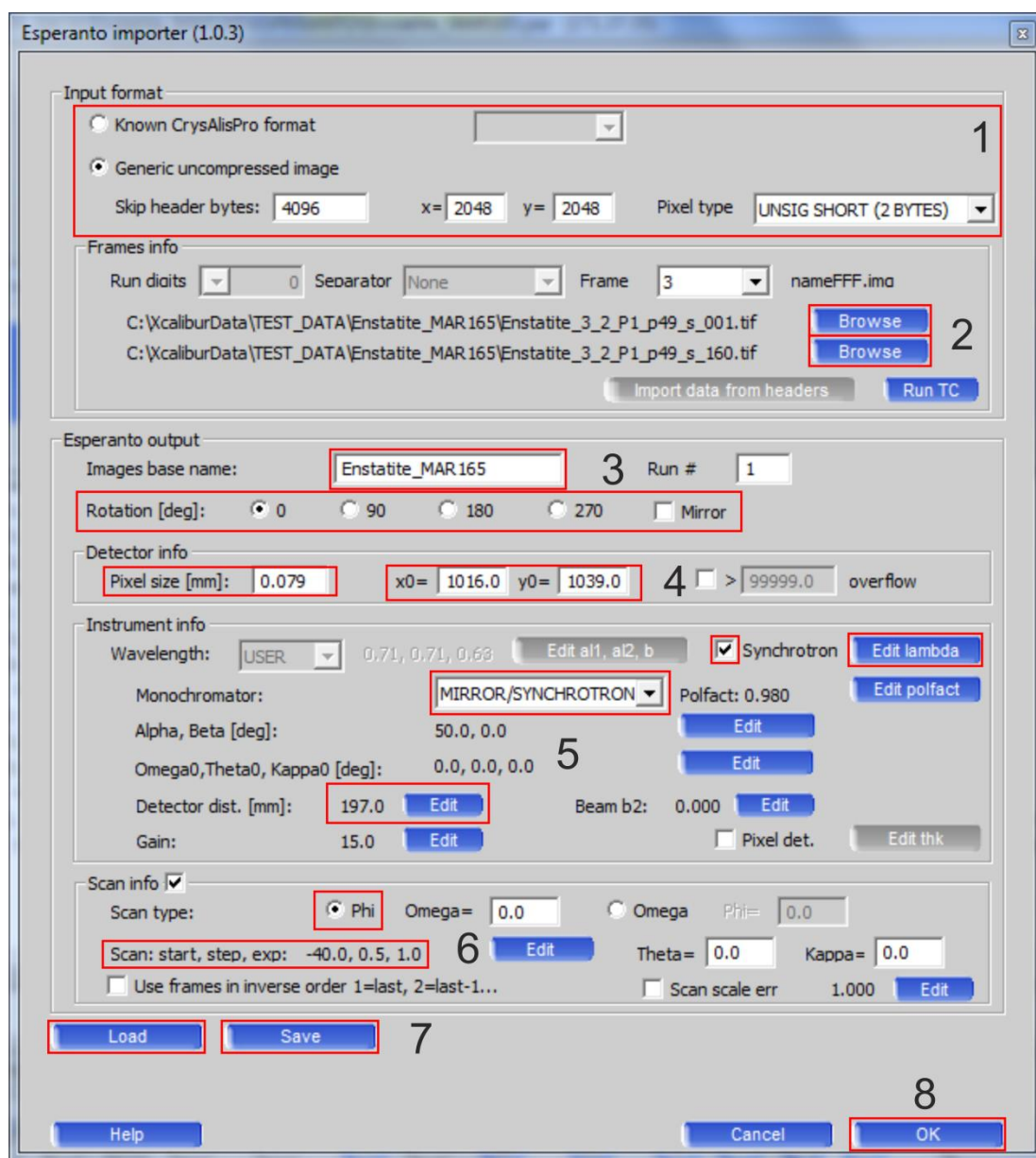
5. Select the experiment from the list.



7. Call command line (F5 button) and open calibration file with *.par extension using `rd p` command, ignore appeared lattice reduction dialog (press "OK" button).

8. Follow standard procedures of data reduction.

Figure 3.2.2-1 Interactive dialog for creation CrysAlisPro experiment using Bruker SAXI images.



1. Select a format of input images. It can be either an image format supported by CrysAlisPro (certain MAR images, Bruker SAXI, ESPERANTO, etc.) or a generic image. In latter case provide the byte length of a header, the image size and the pixel type.
2. Provide the location of the first and the last frame of the experiment.
3. Provide a base name for the output images and rotate and/or flip to the input images if necessary.
4. Provide the detector's pixel size (in mm) and origin (in pixels).
5. Enable 'Synchrotron' for the instrument type and provide the X-ray wavelength and the sample-to-detector distance.
6. Enable 'Scan info' and use 'phi' scan type. Provide the starting angle, the step size and the exposure time of the scan.
7. Save the input parameters as *.at_rit file for the later use in other conversion procedures.
8. Start the conversion procedure.

Figure 3.2.2-2 A dialog for conversion XRD images collected on a synchrotron facility to ESPERANTO CrysAlisPro format. Red rectangles show the parameters which one has to set up for the proper conversion. The numerical values specific for certain synchrotron XRD beamlines are given in Table 3.2.2-1. After the conversion process finishes one should create the corresponding experiment in CrysAlisPro (steps 5–7 in Figure 3.2.2-1).

Table 3.2.2-1 Parameters for the conversion XRD images collected at the synchrotron facilities to ESPERANTO CrysAlisPro image format.

	MAR555		Perkin Elmer		MAR165 CCD	
	flat panel detector		flat panel detector		13-IDD, APS	
	ID09A, ESRF		P02.2, Petra III			
Input format	Known	CrysAlisPro	Generic	uncompressed	Generic	uncompressed
	format – MAR		image ^a :		image:	
			- skip header bytes = 1024;		- skip header bytes = 4096;	
			- x, y = 2048;		- x, y = 2048;	
			- pixel type = LONG		- pixel type = UNSIG SHORT	
			(4BYTES)		(2BYTES)	
Rotation, ° / Mirror	180 / enabled		90 / disabled		0 / disabled	
Detector info:						
- pixel size, mm	0.139		0.200		0.079	
- origin, x ₀ , y ₀ (roughly) ^b	1570, 1530		1030, 1080		1020, 1040	
Instrument info:						
-synchrotron / lambda, Å ^c	enabled / ~0.41		enabled / ~0.29		enabled /	
					typically 0.3100 or 0.3344	
-monochromator	MIRROR/SYNCHROTRON		MIRROR/SYNCHROTRON		MIRROR/SYNCHROTRON	
-detector distance, mm	~300 (for routine HP)		~400 (for routine HP)		~200 (for routine HP)	
(roughly) ^b	~ 400 (for laser heating)					
Scan info:	enabled		enabled		enabled	
- scan type	phi		phi		phi	
- use frames in inverse	disabled		disabled		disabled	
order						

^a raw *.tiff images created by the PerkinElmer detector are not supported by CrysAlisPro. Therefore prior the conversion procedure one have to transform the images into European Data Format, *.edf, using `petra2EDF.py` script implemented in Fable package [123].

^b defined after the calibration on the powder standard (LaB₆, CeO₂).

^c provided by beamline scientist; the value has to be exactly defined.

3.2.3. Calibration of a diffractometer

X-ray diffraction diffractometers have a number of mechanical parts affected by a continuous movement/rotation that results in their shifts from the proper positions. For an accurate data processing it is necessary to carefully evaluate the shifts first (refine an *instrument model*). For this purpose one performs a data collection on a standard crystal (Figure 3.2.3-1) and using its pre-defined symmetry and unit cell parameters accurately determines the sample-to-detector distance, the detector's origin, offsets of the goniometer angles and rotation of the X-ray beam and the detector around the instrument axis. For Agilent technologies diffractometers calibration process can be run in an automatic mode, for other machines (customized diffractometers on synchrotrons, third-party commercial diffractometers) the model has to be refined manually (see Figure 3.2.3-2 for details). In the current thesis we used Ylid standard crystals (2-dimethylsulfuranylidene-1,3-indandione, $C_{11}H_{10}SO_2$, $P2_12_12_1$, $a = 5.9552(4)$, $b = 9.0294(4)$, $c = 18.3719(13)$ Å, Figure 3.2.3-1a) to refine the instrument model of the Bruker and Oxford Diffraction Xcalibur diffractometers. For high-pressure studies we used a specially prepared DAC with an orthoenstatite calibration crystal ($(Mg_{1.93}, Fe_{0.06})(Si_{1.93}, Al_{0.06})O_6$, $Pbca$, $a = 8.8117(2)$, $b = 5.18320(10)$, $c = 18.2391(3)$ Å, provided by Prof. Dr. H. Keppler) placed into the center of the 125 µm gasket hole (Figure 3.2.3-1b).

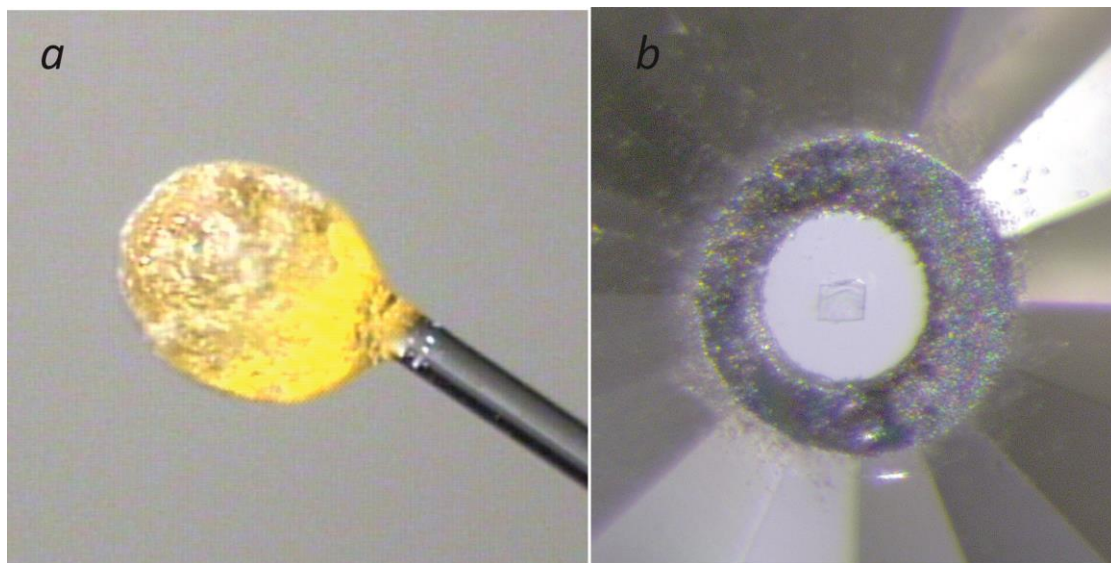
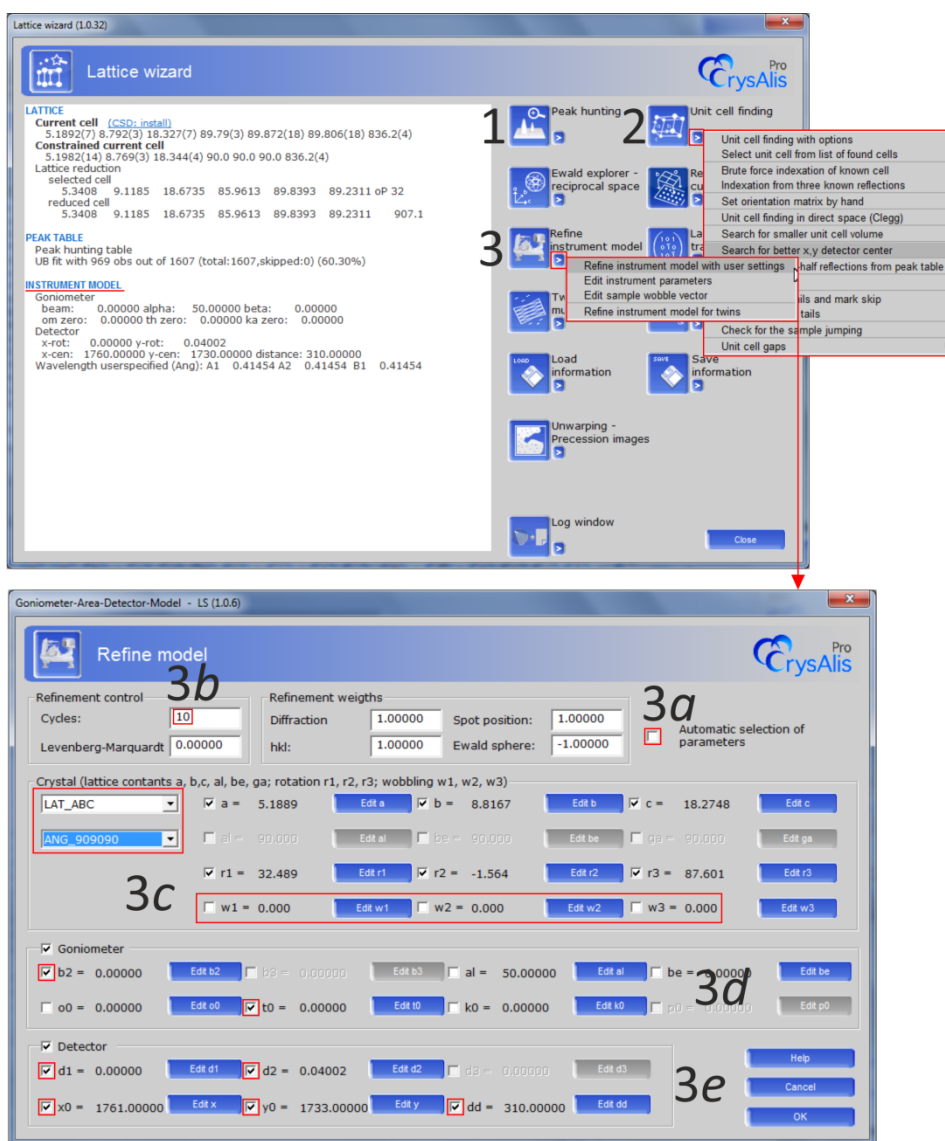


Figure 3.2.3-1 Calibration crystals for refinement of the diffractometer instrument model with CrysAlisPro: ylid, $C_{11}H_{10}SO_2$, for *in-house* XRD (a); enstatite, $(Mg_{0.98}Fe_{0.02})SiO_3$, in a DAC for high-pressure synchrotron XRD (b).



1. Create the experiment with preliminary instrument model using CrysAlisPro conversion tool. Harvest the reflections with `ph s` command.
 2. Find the unit cell and search for x , y detector origin. Remember to refine the unit cell after each change in the instrument model (`um i`).
 3. Refine instrument model with user-defined settings.
 4. Perform the data reduction.
 5. Check if the parameters of the instrument model have changed and repeat steps 3, 4 until the model converges.
- 3a. Disable automatic selection of the refinement parameters.
 - 3b. Increase the number of refinement cycles to ~20.
 - 3c. Add constraints on the lattice symmetry (ex. for orthorhombic enstatite fix α , β , and γ angles to 90°). Disable refinement of the sample wobbling (w_1 , w_2 , w_3).
 - 3d. Check the refinement of the beam rotation (b_2) and the θ -position.
 - 3e. Check the refinement of the detector rotation (d_1 , d_2), the detector origin (x_0 , y_0) and the sample-to-detector-distance (dd).

Figure 3.2.3-2 Refinement of the instrument model with CrysAlisPro.

3.3. XRD data collection strategy on synchrotron facilities

The 3rd generation synchrotron radiation facilities provide by about billion times higher *brilliance* (the measure of photons that can be concentrated on a spot) of an X-ray beam than laboratory X-ray sources. A small focused X-ray beam of minimum $2 \times 4 \mu\text{m}^2$ is perfect for fast laser heating experiments, when one has to measure diffraction from a small heating spot. A small beam is also essential for ultrahigh-pressure (100+ GPa) experiments, when the pressurized area is very tiny. A parallel beam of 8 to 30 μm in diameter is perfect for a collection of high-quality single-crystal XRD data. X-ray diffraction beamlines we used operate with energies from ~ 30 to 43 keV that corresponds to the wavelengths of $\sim 0.41\text{--}0.29 \text{ \AA}$ that is about two times lower than the X-ray wavelength of conventional Mo-tubes installed on *in-house* single-crystal diffractometers. High energies give access to outermost *d*-shells that may somehow compensate the insufficient redundancy and completeness of XRD data obtained in DACs.

Our synchrotron-based XRD experiments usually started with a calibration of the diffractometer: first using powder standards (LaB_6 or CeO_2) and then with a standard single crystal (enstatite). A sample-to-detector distance and a detector center obtained from powder diffraction data are taken as starting values for a refinement of an instrument model in the CrysAlisPro software. The calibration on the powder standards is also required for an accurate processing Ne powder XRD used for determination of the pressure in DACs.

The photographs of the diffractometer installed at the ID09A beamline, ESRF (Grenoble, France) demonstrate the principle components of the experimental setup common for each high-pressure XRD beamline (Figure 3.3-1). The DAC is fixed in a holder attached to positioning *x*, *y*, *z*-motors and rotation (ω -) stage. In ESRF axis notation the *x*-motor moves the DAC towards/from the X-ray beam, *y*-motor moves the cell in horizontal direction perpendicular to the beam. The *z*-motor moves the whole goniometer in vertical direction. The DAC on the goniometer is rotated about the ω -axis which is parallel to the *z*-axis. The position when the optical axis of a DAC (going through the diamonds) is perpendicular to the incident beam corresponds to the omega $\omega = 0^\circ$. Si-diode is served for a precise alignment of the DAC to the center of rotation of

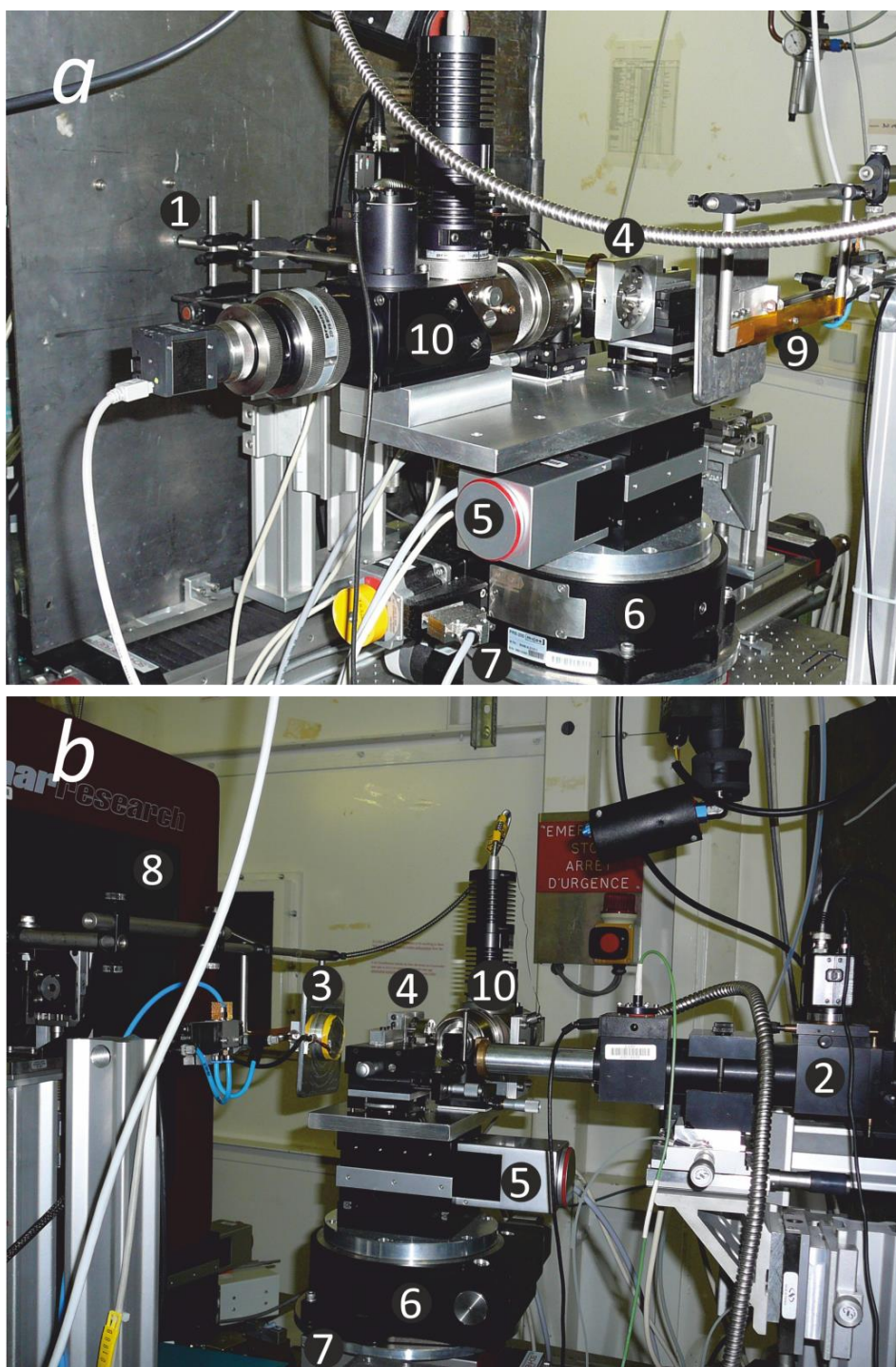


Figure 3.3-1 Photographs of the diffractometer installed at the ID09A beamline, ESRF, Grenoble (*a* - view towards X-ray beam., *b* - towards detector): 1 – incident X-ray beam, 2 – PRL-system combined with video camera, 3 - Si-diode, 4 - DAC fixed on a holder, 5 - x, y-position stages, 6 – rotation (ω -) stage, 7 – z-position stage, 8 – detector, 9 – beamstop, 10 – portable laser heating head (optional).

the goniometer. Ruby Luminescence (PRL) system combined with a video camera is used to determine the pressure and to visualize the position of the sample.

In our synchrotron studies XRD data collection strategy had the following stages which will be considered further in detail:

1. A DAC preparation.
2. Alignment of the DAC to the center of rotation of the goniometer and alignment of the crystal with respect to the X-ray beam.
3. Determination of the proper conditions of the data collection: intensity level (exposure time / primary beam intensity / X-ray filters) and data collection mode (ω scan width, starting and final ω values, single or multiple measurements with different exposure time / DAC orientation).
4. Data collection.
5. Preliminary data reduction and decision if an additional data collection is required.

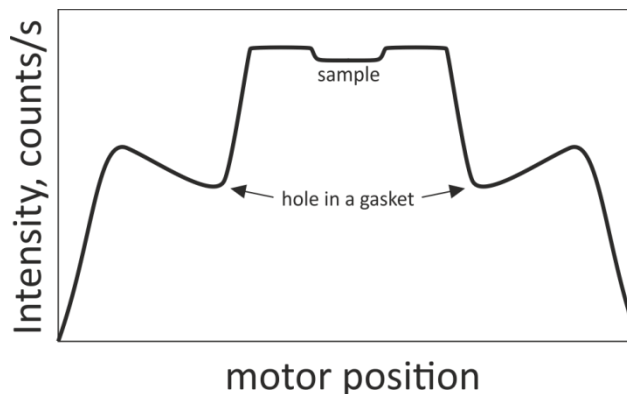
3.3.1. DAC preparation

For high-pressure single-crystal XRD one or several crystals may be loaded into the DAC. If only one crystal is used, then it should be placed strictly in the center of the pressure chamber (the hole in the gasket). This drastically saves time in the further search for the crystal in the course of the experiment and minimizes chances of the crystal's misalignment, which usually has a negative effect on the quality of the collected XRD data. If 2–3 crystals are studied, it is better to build them in one line and mount the DAC so that this line appears on the rotation (ω -) axis thus minimizing the crystals' misalignment. The recommendations to the crystal size are discussed above.

Before the measurements the diamonds' table faces should be thoroughly cleaned. Even a small foreign particle illuminated by the high-brilliance synchrotron X-rays can easily create diffraction spots on the detector that may lead to confusing results.

3.3.2. Alignment of a DAC on the goniometer

Proper alignment of the sample in DAC is essential for collecting high-quality XRD data. The general alignment procedure is based on the absorption of X-rays. The DAC is moved by y - and z -motors and the intensity of the X-ray beam is recorded by Si-diode (Figure 3.3-1). The resulted absorption curve has a



characteristic profile when the beam passes through a gasket and a hole (Figure 3.3.2-1). A center of the gasket is then defined from the absorption curves obtained for y - and z -scans. A position on the rotation axis is defined from a triangulation procedure by scanning the DAC along the y -axis at two omega positions ($+20$ and -20°). Once the beam is aligned to the center of the gasket, one can use an optical (for example, PRL) system to find the sample position by the video-camera.

Figure 3.3.2-1 Characteristic profile of an absorption curve recorded by Si-diode when the X-ray beam passes through a DAC.

Alignment of the sample position is performed after each possible displacement of the DAC, e.g. after a manual pressure increase or after laser heating, when the DAC may move upon cooling. Additionally in HPHT experiments the size of a heated spot on a sample does not exceed $10\text{ }\mu\text{m}$, so the spot can be easily lost after quenching. In order to restore its position, one should measure a series of XRD images across the sample incrementing y and z positions by a small step of $3\text{--}5\text{ }\mu\text{m}$ (*mapping mode*) and inspect the collected XRD images.

3.3.3. Selection of the proper data collection mode and data collection

In synchrotron high-pressure experiment XRD frames are collected in oscillation mode when a DAC is rotated typically from -40 to $+40^\circ$ on ω , through a certain ω steps of $0.1\text{--}2^\circ$. The values of the starting and final ω angles are pre-defined by an X-ray opening angle of the DAC, a selection of the proper ω step is based on a crystal mosaicity and time limits for a single experiment (see below).

The XRD data collected in the DAC usually have worse quality than in the routine *in-house* experiment at ambient conditions. Diamonds, a solidified pressure transmitting medium, and sometimes a gasket exposed to the X-ray give rise to the diffraction spots and rings that may overlap with the diffraction spots belonging to the sample. A metallic body of the DAC shadows a significant portion of XRD reflections belonging to the sample; an available part of a reciprocal space depends on the opening angle of the DAC which does not exceed 80°. The resulted data *completeness* (portion of the reflections collected to a total number of the reflections referred to a certain *d*-spacing shell) is often twice lower than suggested by the International Union of Crystallography value of 99.5 % at the 0.8 Å *d*-shell. The limited number of available reflections creates problems for the solution of low-symmetry structures and the refinement of anisotropic parameters. Therefore certain “tricks” are applied to maximize the number of reflections with reliable intensities. For instance, one may pressurize several differently orientated crystals of the same kind in one DAC, and merge those reflection intensities in specialized software, like XPREP (implemented in SHELXTL package [124]) or Jana2006 [125] (we realized this procedure in studies of Fe₂B₇). The rectangular MAR555 detector installed on ID09A beamline requires two data collections at different DAC orientations (0 and 90°). To complete *Friedel pairs* (the reflections with indices *hkl* and *-h-k-l*) one can collect additional ω -scan from an opposite side of the DAC.

Each detector possesses its own *dynamic range*, i.e. the lowest and the highest intensity values which can be practically measured by the detector. The smaller the dynamic range, the more carefully an exposure time and/or primary X-ray beam intensity have to be selected. We used a two-stage procedure for the estimation of the optimal exposure time. First, an XRD image is taken upon continuous ω -rotation of the DAC from -20 to +20° (*wide-scan* image). On the image a threshold intensity *Tr* for saturated reflections is derived according to the formula:

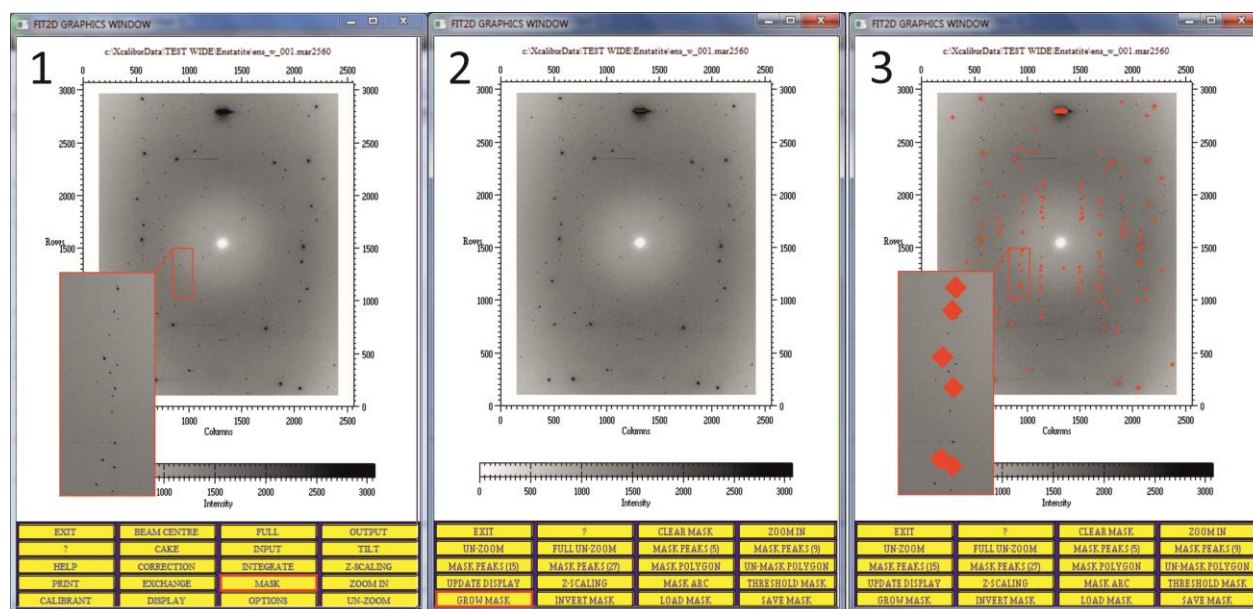
$$Tr = DYN \frac{t_{step}/\Delta w_{step}}{t_{wide}/\Delta w_{wide}}$$

where DYN is the highest intensity which the detector can read linearly, t_{step} , t_{wide} are exposure times for step and wide images, Δw_{step} , Δw_{wide} are scan widths for step and wide

images. For example, if the wide image is taken upon ω -rotation from -20 to $+20^\circ$ with the exposure time of 2s and one is planning to measure step scan images through 0.5° with the exposure time of 1s, and DYN of the detector is 300000 counts (MAR555), then the threshold for saturated intensities on the wide image would be:

$$Tr = 300000 \text{ counts} \cdot \frac{0.5^\circ/1s}{40^\circ/2s} = 7500 \text{ counts}$$

In the FIT2D software one can visualize saturated reflections (Figure 3.3.3-1) and visually estimate a corresponding fraction to the total amount of reflections. Normally the fraction should range from 5 to 10 %, so the exposure time (or intensity of the primary beam) should be adjusted accordingly.



1. Open 'Mask' menu, select 'Threshold mask'. Answer 'No' for the question 'Less than comparison' and then enter the threshold for saturated reflections, Tr (see text for details).
2. To enlarge the size of the created masks, select 'Grow mask' and enter the number of growth cycles (usually 20–30).
3. Visually inspect the number of saturated reflections. Normally, their fraction to the total amount of reflections should be between 5 and 10 %, so the exposure time should be adjusted correspondingly.

Figure 3.3.3-1 Visualization of saturated reflections in the FIT2D software.

The second stage is performed after the data collection and the data reduction in CrysAlisPro. The attention is paid to overall intensity indicators (R_σ and $F_{obs}^2/\sigma_{int}(F_{obs}^2)$) and to the quality of merging intensities of the symmetry-equivalent reflections (R_{int}). The values are derived as follows:

$$R_{int} = \frac{\sum |F_{obs}^2 - \langle F_{obs}^2 \rangle|}{\sum F_{obs}^2}$$

$$R_\sigma = \frac{\sum [\sigma_{int}(F_{obs}^2)]}{\sum F_{obs}^2}$$

$$\sigma_{int}(F_{obs}^2) = \sqrt{\frac{\sum (F_{obs}^2 - \langle F_{obs}^2 \rangle)^2}{n}}$$

where the summations are taken over all input reflections for which more than one symmetry equivalent is averaged; F_{obs}^2 is intensity corrected for Lorentz-polarization, $\langle F_{obs}^2 \rangle$ is its mean value over all measured equivalents; n – is the number of redundant reflections. A dataset with insufficient intensities has poor $F_{obs}^2/\sigma_{int}(F_{obs}^2)$ and high- R_σ values (< 3 for and $> 20\%$, respectively for the outermost resolution d -shells), and as a result, high R_{int} values. A case is more complicated when the number of the saturated intensities is too high, and then the R_{int} value is low and does not anymore indicate the data quality. $F_{obs}^2/\sigma_{int}(F_{obs}^2)$ values are high and R_σ values are low in this case. Thus, the final judgment is based on the quality of the structure refinement.

Instead the selection of the overall intensity level for one experiment it is sometimes better to collect two XRD datasets with different exposure times/primary beam intensity. The resulted intensities except the ones for saturated reflections are merged using the appropriate software (XPREP, Jana2006). The other choice is to collect the data in a fine slice (0.1 – 0.5°) scanning mode where the 3-dimensional profile of the reflection can be obtained. If the saturation happens, it affects only one frame out of several ones on which the reflection occurs, then the overexposed intensity may be ignored, while the true intensity is reconstructed by CrysAlisPro from the calculated 3-dimensional reflection profile. Both approaches, however, drastically increase the measurement duration, which become an important factor during the limited synchrotron beam time. We normally performed a single ω -scan with compromise width of 0.5° , thus the data collection took from 15 minutes to 1 hour.

3.4. Processing of high-pressure XRD data

Processing of XRD data collected under extreme conditions includes the following steps:

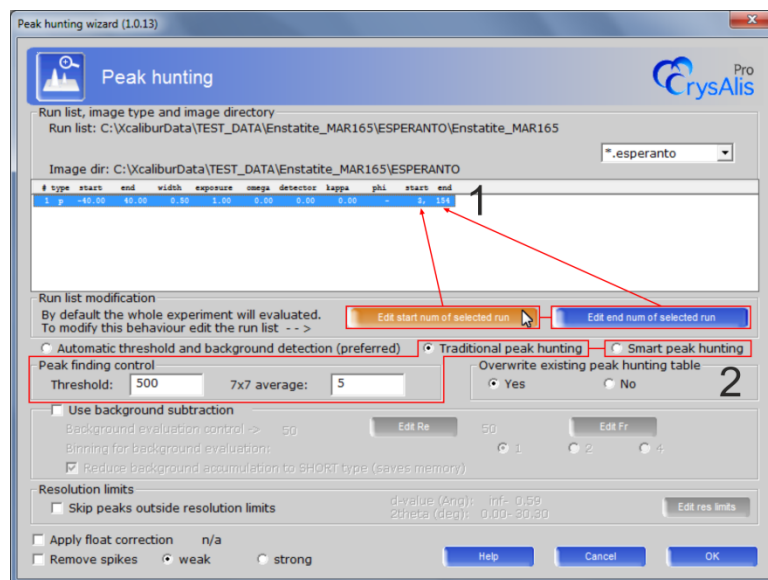
1. Initial preparation.
2. Peak hunting.
3. Indexing of the reflections.
4. Data reduction.
5. Data finalization.
6. Structure solution and refinement.

3.4.1. Initial preparation

An initial preparation involves conversion of the images to the format supported by CrysAlisPro, applying a proper calibration file and applying a correct beamstop mask and additional masks if the detector has unused regions (Mar555, Pilatus).

3.4.2. Peak hunting

A peak hunting procedure is started by `ph s` command which calls a dialog window shown in Figure 3.4.2-1. It is important to check before the procedure starts, if the first and the last



1. Frame range for peak hunting procedure (whole range is used by default). Change the values in case if the first and the last frames contain trash diffraction from tungsten carbide seats or if the diffraction is shadowed by the DAC body.

2. Change the peak hunting mode. 'Traditional' procedure is perfect for images collected with MAR555 detector (threshold ~500–1000 and 7x7 average ~5), while 'Smart peak hunting' is used for the rest cases (PerkinElmer, Bruker SAXI and other MAR frames, and native CrysAlisPro images).

Figure 3.4.2-1 Peak hunting dialog of CrysAlisPro software. For better performance one has to change certain parameters highlighted in red rectangles.

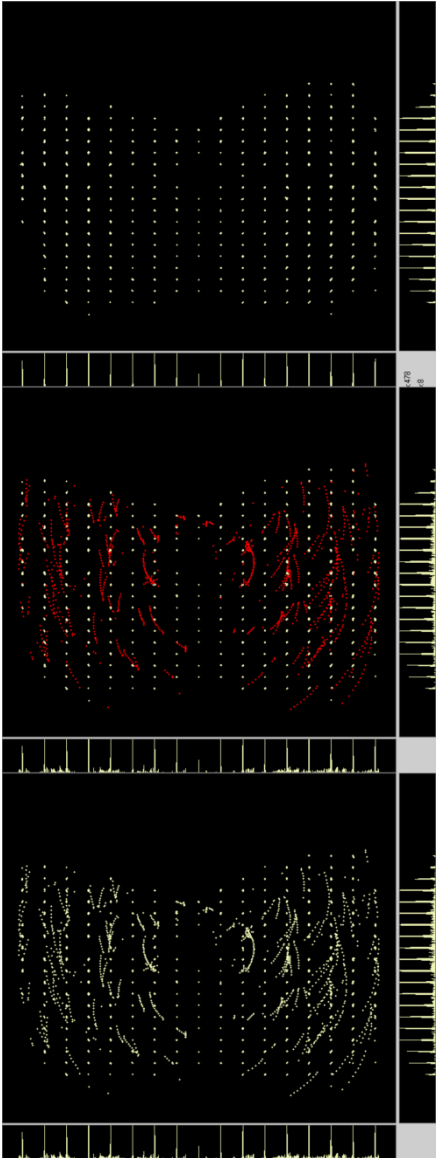
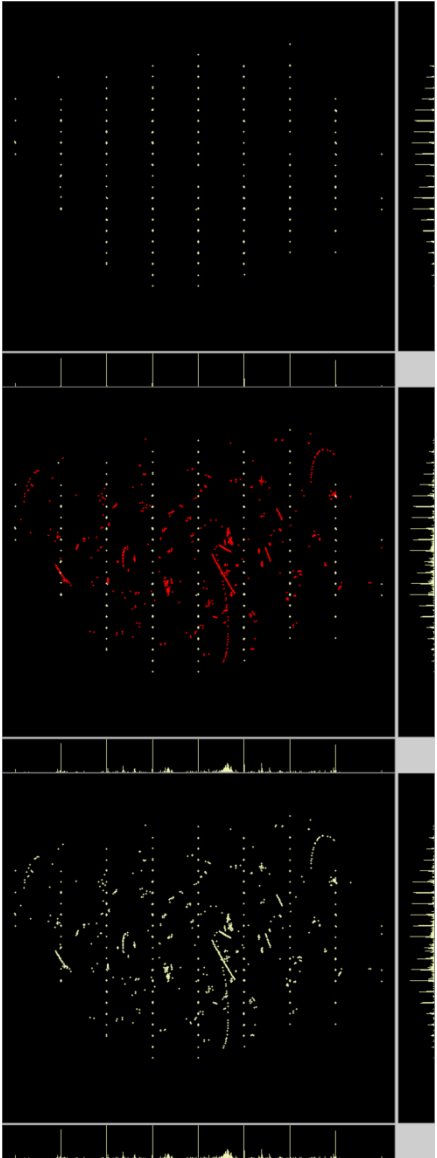
images of an experiment contain trash diffraction rings from tungsten carbide seats, and skip the images from the peak hunting if necessary. Three options for the peak search are offered: *automatic*, with default parameters, *traditional*, when user defines a threshold for peak intensities and a threshold for an average intensity in 7 x 7 pixel area, and a *smart* peak hunting. The smart peak hunting option perfectly worked with the images collected with MAR165 (13-IDD beamline at APS, ID27 beamline at ESRF), Perkin Elmer (P02.2 beamline at Petra III, ID27 beamline at ESRF), and Bruker SMART APEX CCD (*in-house* diffractometer) detectors, while the traditional peak hunting with 500 threshold and 5 for 7 x 7 average was used for MAR555 detector (ID09A beamline at ESRF).

3.4.3. Indexing of the reflections

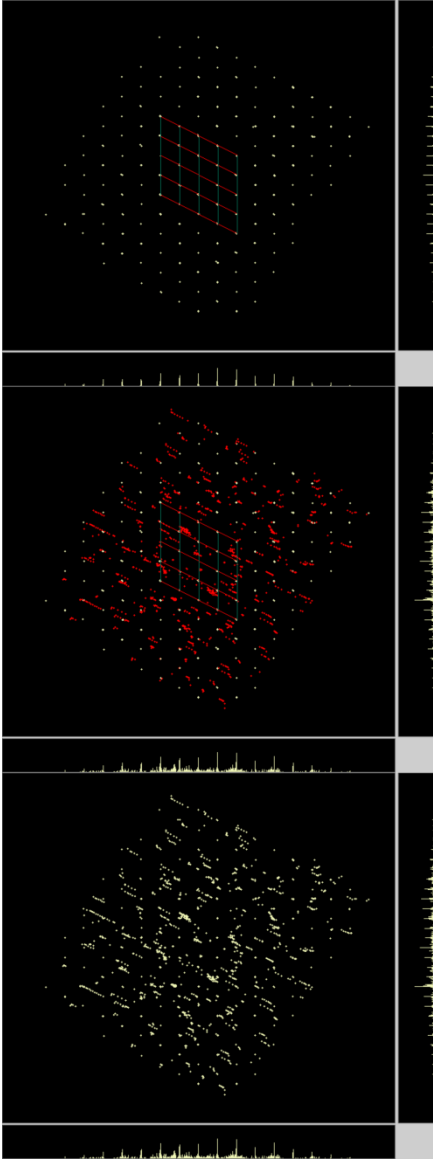
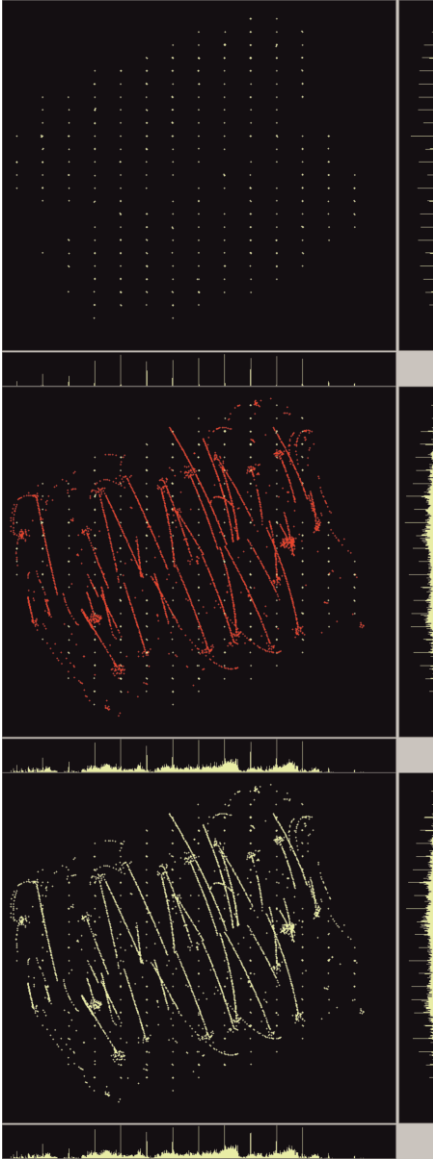
An automatic indexing of the reflections is started in CrysAlisPro with `um ttt` command. To increase chances of the successful indexing one has to exclude diamond reflections, as well as solid Ne and gasket diffraction lines from a peak list. This can be done in a reciprocal space viewer invoked by `pt ewald` command. The reflections can be excluded manually or by applying filters on intensities and *d*-spacings. The best performance of the automatic indexing method can be achieved on a small set of the reflections (~20–30) belonging only to a single crystal. One can manually select those reflections which should build a 3-dimensionall lattice in the reciprocal space (Table 3.4.3-1). The obtained unit cell is refined against the whole batch of the reflections (`um i` command). If a position of a DAC barely changes upon compression then an orientation of the crystal to instrument axes (*UB matrix*) obtained on the first pressure point can be used in the next experiments. To get the UB-matrix one should call `ty u` command and in the appeared report copy the last line which has format of `UM S a1 a2...a9` (*a_i* are float numbers). To apply the orientation matrix one simply executes the copied command.

Laser heated samples as a rule, contain a huge amount of crystallites, that creates problems in the unit cell search (Table 3.4.3-1). The automatic indexing has very low chances to give a meaningful result. If one knows the approximate unit cell parameters of a HPHT phase, those can be searched by `um searchcell` command. More frequently one has to distinguish peaks of the HPHT phase(s) manually that requires a certain experience and patience (Table 3.4.3-1).

Table 3.4.3-1 Indexing process in various single-crystal XRD experiments in DACs (continued on the next page).

Sample,	experiment	conditions,	and	Reciprocal space view before (left) and after indexing. White reflections belong to the target unit cell, red ones are non-indexed reflections
quality of the dataset for indexing				
<i>Enstatite calibration crystal at ambient pressure</i>				
Perfect. Reflections belonging to a target unit cell are clearly visible. Here and below no reflections from the gasket are observed. Diamond reflections (arcs) are rather strong. An automatic indexing finds the correct unit cell without additional actions.				
<i>Fe₂B₇, 12.5 GPa</i>				
Perfect. Reflections belonging to a target unit cell are clearly visible. Ne rings and diamond reflections present but do not affect the automatic indexing. An automatic indexing finds the correct unit cell without additional actions.				

(continued from the previous page).

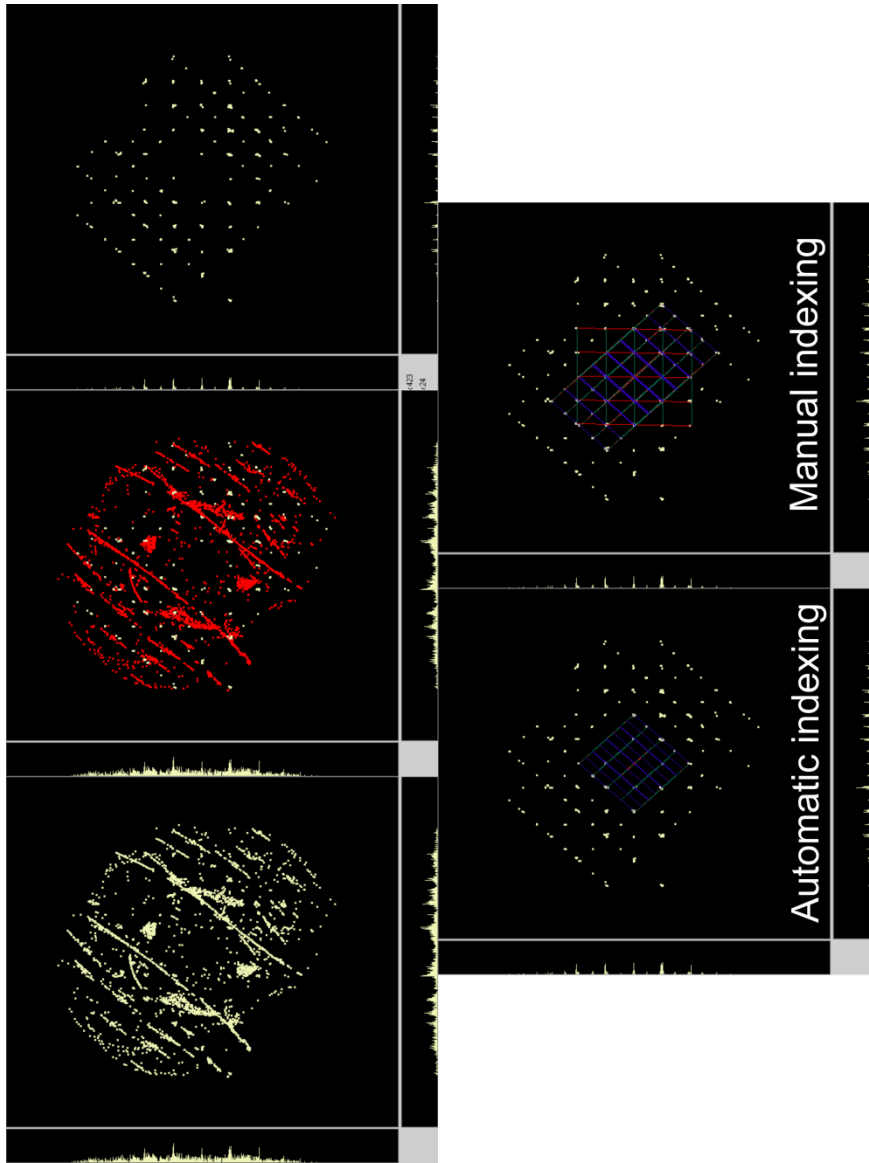
Sample, experiment conditions, and quality of the dataset for indexing	Reciprocal space view before (left) and after indexing. White reflections belong to the target unit cell, red ones are non-indexed reflections
<p><i>Fe₂O₃ 48.2 GPa</i></p> <p>Perfect. Reflections belonging to a target unit cell are clearly visible. Ne rings and diamond reflections present but do not affect the automatic indexing. An automatic indexing finds the correct unit cell without additional actions.</p>	
<p><i>Fe_{1.01}B₅₀ 2.8 GPa</i></p> <p>Good. Reflections belonging to a target unit cell are clearly visible. Ne is in a liquid state and does not produce diffraction reflections. However the diamond reflections are rather strong and an automatic indexing fails.</p>	

(continued from the previous page).

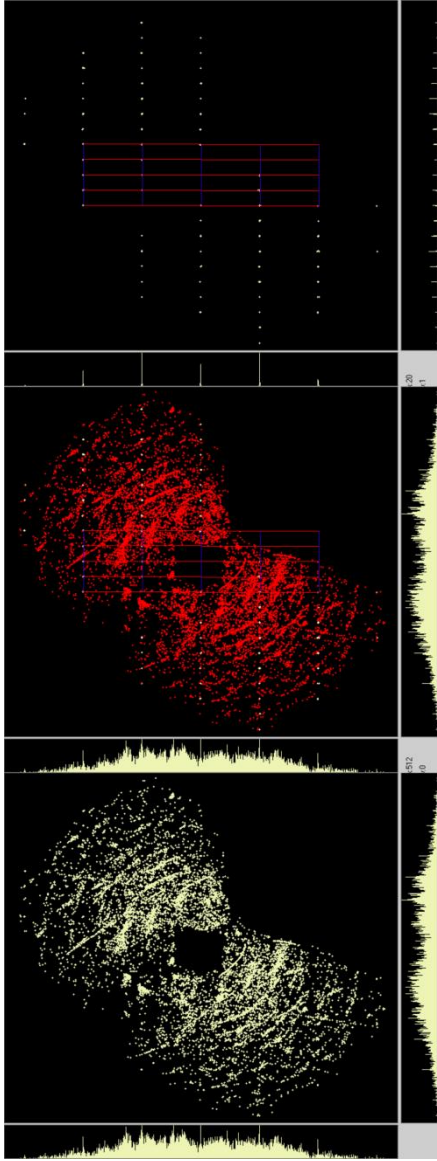
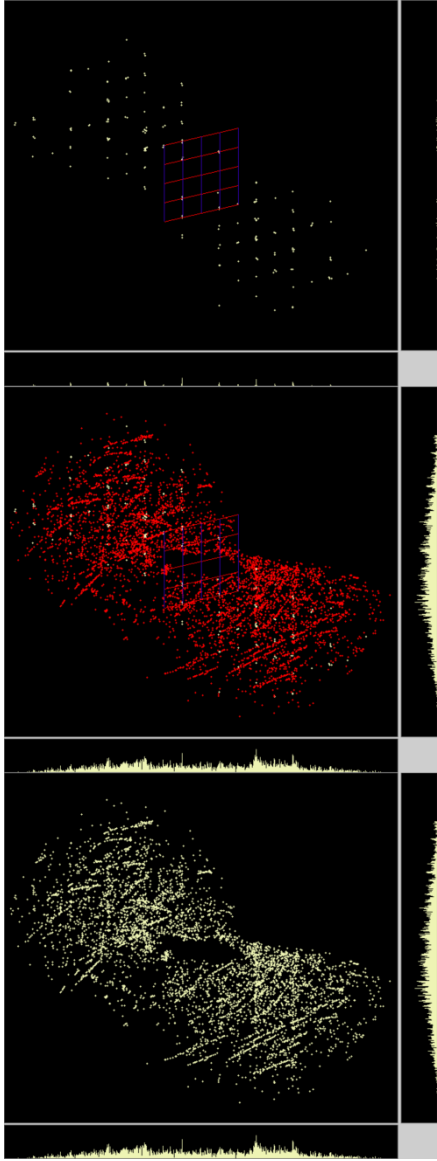
Sample, experiment conditions, and quality of the dataset for indexing	Reciprocal space view before (left) and after indexing. White reflections belong to the target unit cell, red ones are non-indexed reflections
------------------------------------------------------------------------	------------------------------------------------------------------------------------------------------------------------------------------------

Fe_2O_3 , 54 GPa

Medium. Reflections belonging to a target unit cell are hardly recognized. Ne rings and diamond reflections are rather strong and have to be skipped. After a phase transition the sample transformed to two twin domains related by a symmetry law. An automatic indexing finds a misleading unit cell with a larger volume.



(continued from the previous page).

Sample, experiment conditions, and quality of the dataset for indexing	Reciprocal space view before (left) and after indexing. White reflections belong to the target unit cell, red ones are non-indexed reflections
<p><i>Fe₃O₄, 50 GPa, after laser heating</i></p> <p>Bad. Ne rings and diamond reflections are rather strong and have to be skipped. After heating a sample recrystallized and a huge number of crystallites appeared. Many domains were rather intense. For successful indexing reflections from individual domains have to be selected manually.</p>	
<p><i>Fe₅O₇, 41 GPa, after multiple laser heating procedures</i></p> <p>Terrible. Ne rings and diamond reflections are rather strong. Due to high exposure time diamonds create secondary diffraction. After a laser heating a sample disintegrated into huge number of crystallites. The proper unit cell can be found only if to select peaks manually in a reciprocal space viewer or manually harvest peaks from the images.</p>	

3.4.4. Data reduction

Once the unit cell parameters are defined, a procedure of extraction reflection intensities from the images (*data reduction*) can be started. In CrysAlisPro the data reduction is performed in two stages. On the first step the program predicts the positions of the reflections based on the UB-matrix, then it analyses partial reflections (whose profile is split over several frames) and reconstructs the reflection shape in the scanning direction. At the second stage the program collects reflection intensities based upon the reflection shape and the background level. By default after the data reduction the program applies a frame scaling, absorption corrections and searches for a space group by an analysis of systematic absences.

`Dc proffit` command invokes the data reduction assistant that asks a user to provide information related to an XRD experiment and specify parameters of the integration (the process is shown in detail in Figure 3.4.4-1). That includes a correct data ranges (similar to the peak hunting process), an opening angle of the DAC ($\sim 38^\circ$ for a standard BX90 DAC with Boehler-Almax diamonds), an integration box (or mask) size, a reflection profile fitting mode (2D or 3D) and a background evaluation mode. An instrument model refinement is disabled, to follow the behavior of the unit cell parameters without altering the pre-calibrated model that is especially important if one needs accurate compressibility data.

The integration box size defines an area from which the peak intensity is collected. High R_{int} values in apparently good datasets sometimes appear when CrysAlisPro underestimates the box size (observed for MAR165 and PerkinElmer frames). In that case the R_{int} enhances after the re-processing of the data with the larger box size.

The profile fitting mode depends on the crystal mosaicity (a degree of perfection of the lattice translations throughout the crystal) and the ω -slicing mode. To choose the proper fitting mode one has to inspect the behavior of individual reflections in the scanning direction. If the reflection profiles are split over several frames, then 3D profile fitting should be used and 2D option – otherwise (Table 3.2.1-1).

III. Methods and instruments

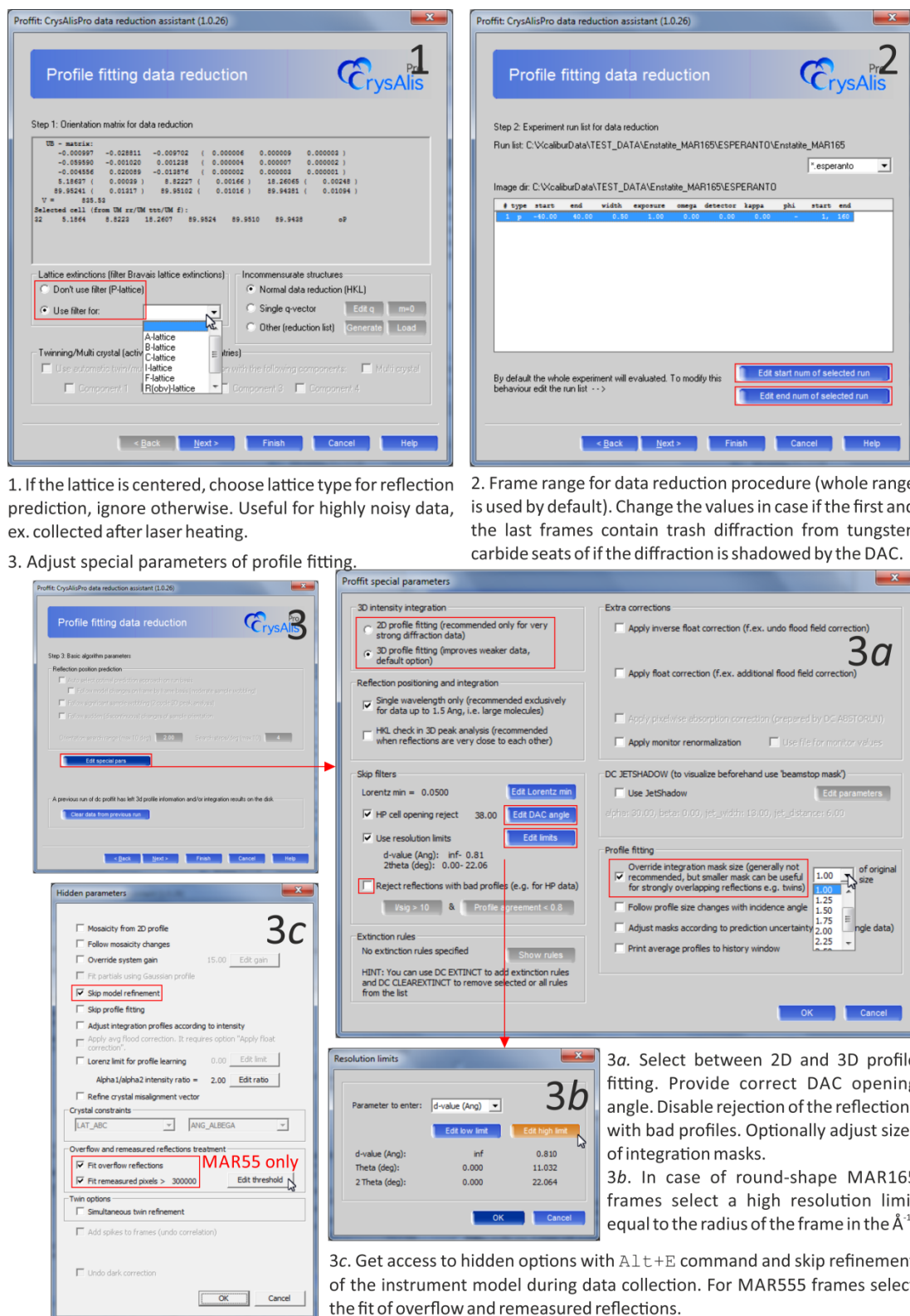
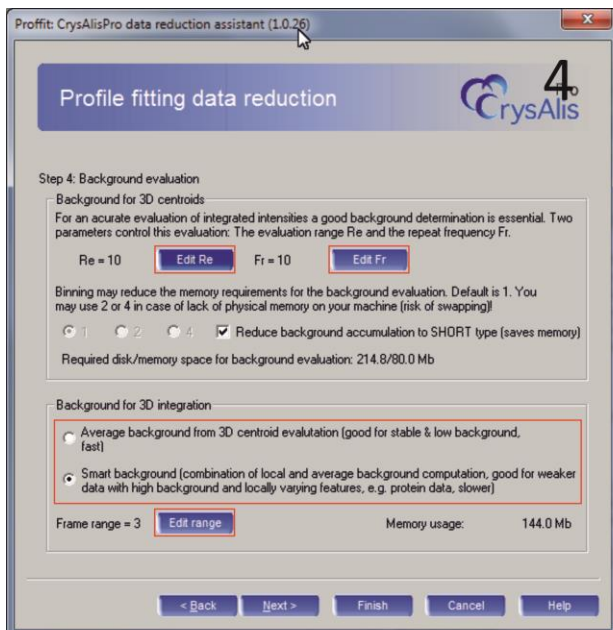
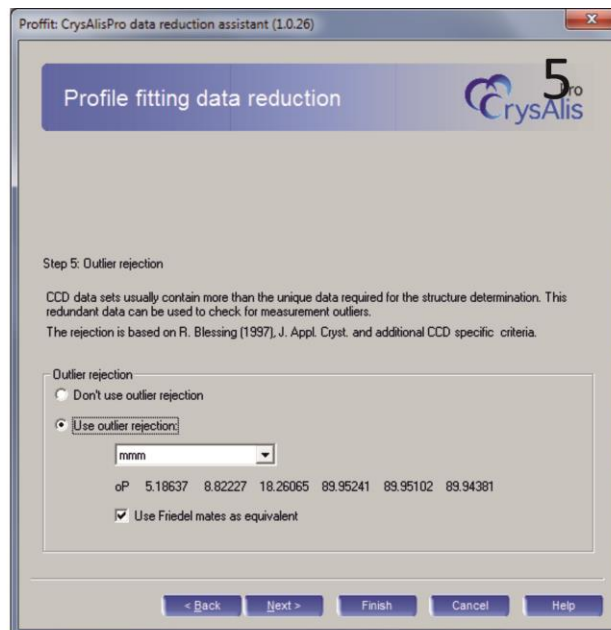


Figure 3.4.4-1 6-stage process of data reduction in CrysAlisPro. For better performance one has to change certain parameters highlighted in red rectangles (*continued on the next page*).

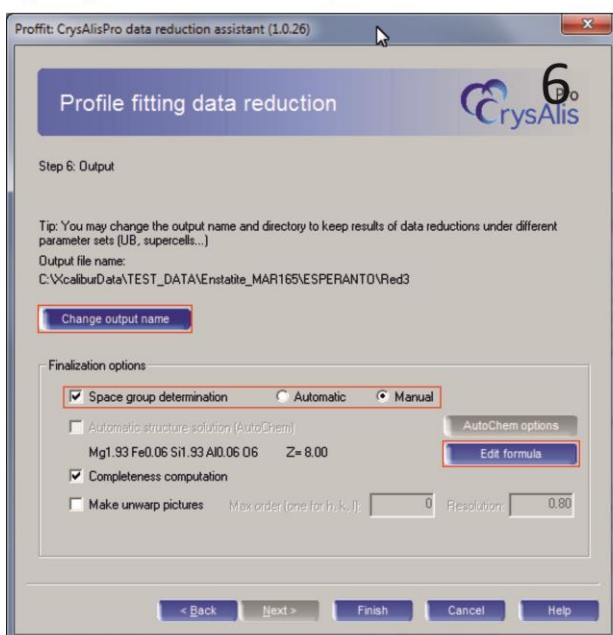
(continued from the previous page)



4. Adjust parameters for 2-stage background evaluation. Typically Re and Fr are both equal to 5-10.



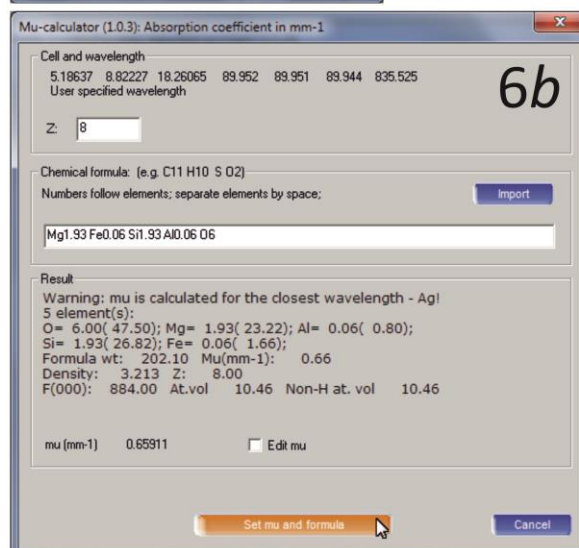
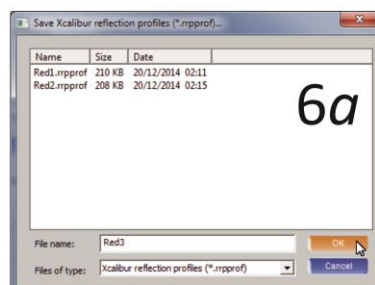
5. Turn on/off the rejection of outliers detected by comparing symmetry equivalent reflections. If turned on then one should provide the Laue group used for the internal consistency comparison.



6. Specify the output. Enable the manual space group determination to define the correct space group with CrysAlisPro build-in tool. Uncheck 'space group determination' to perform the procedure later using the other software.

6a. Provide a new output name (optional).

6b. Provide the chemical composition and number of formula units, Z.



The proper background evaluation is important for the accurate determination of the reflections' intensities. On the first stage of the data reduction it is controlled by a background evaluation range *Re* and a repeat frequency *Fr*. *Re* means how many consecutive frames are used to compute a particular background image, while *Fr* is the frequency with which the procedure is repeated. The typical values for synchrotron high-pressure XRD vary from 5 to 10 for the both parameters. On the second stage of the integration process one selects the background type to use for extraction of reflection intensities. An *average* background pre-computed on the first stage is used for good quality XRD data with high intensity and a low and constant background. Highly noisy data with local features, like laser heated samples, are integrated with a *smart* background option. Then the background will be computed for each individual frame. In that case one has to specify a 'Frame range' parameter, which controls how many adjacent frames will be used for the background computation (the typical values are 1, 3 and 5).

3.4.5. Data finalization

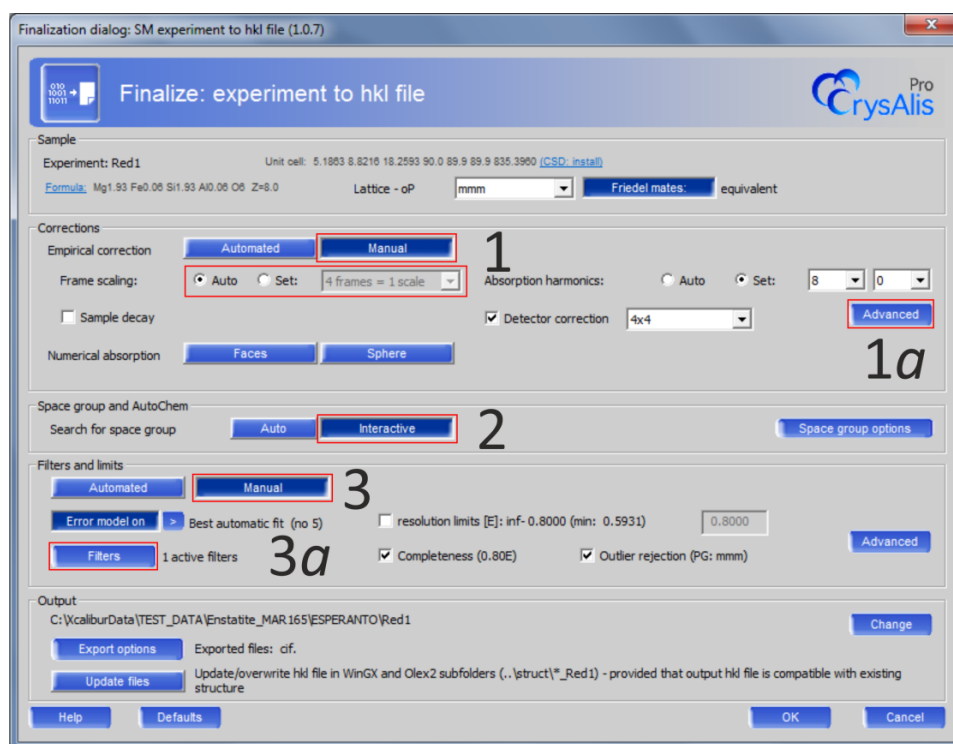
In CrysAlisPro `dc rrp` command runs the data finalization (Figure 3.4.5-1) which applies a frame scaling, absorption corrections to the reflections' intensities and outputs those final values in *.*hkl* file (see below). By default an automatic procedure is performed after each data reduction, but it often works not well on the high-pressure XRD data. A 'Data finalization' button opens a window where one can inspect the data reduction output which includes intensity and resolution statistics and a consistency between intensities of the equivalent reflections. Table 3.4.5-1 shows how the inspection of the such XRD data quality indicators as R_σ , $F_{obs}^2/\sigma_{int}(F_{obs}^2)$ and R_{int} values and a form of frame-by-frame scaling coefficients (*frame scaling curve*) may help in a detection of serious problems during the data collection. In particular, R_σ and $F_{obs}^2/\sigma_{int}(F_{obs}^2)$ values depend on a correct determination of an intensity level (see above), while the problems with a sample misalignment can be detected if one inspects the shape of the frame scaling curve. The R_{int} value indicate the overall quality of the data collection; and if the value is too high (> 15 %) an accurate structural refinement won't be possible.

The default settings in the data reduction and finalization are often not optimal in the treatment of the high-pressure XRD data. Usually one performs several consecutive cycles to find the best set of the integration parameters. If the data is highly damaged due to the crystal misalignment or saturated/too low intensities, then the data collection is repeated after re-alignment of the sample or adjustment the correct intensity level.

After the data collection and finalization, CrysAlisPro outputs several files which are used in a structure solution and refinement:

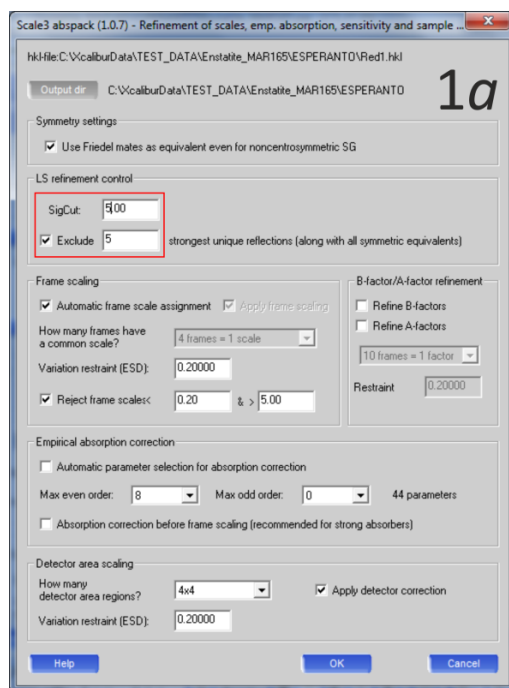
1. *.*hkl* is experimental data essential for the structure solution and refinement. The file contains a list of all observed reflections, namely their Miller indices and corresponding *structural amplitudes* F_{hkl}^2 with the standard deviations.
2. *.*p4p* file contains unit cell parameters with the standard deviations, a chemical composition, a Bravais lattice and a wavelength. Together with *.*hkl* file *.*p4p* can be used for space group tests in the side programs (like XPREP).
3. *.*ins* file is an instruction file for the structure solution in SHELXS and the refinement in SHELXL. The file created by CrysAlisPro contains the space group, the unit cell parameters with standard deviations, the wavelength, the number of formula units, the lattice type, symmetry operators, i.e. coordinates of the general positions, the chemical composition, instructions for the structure solution and instructions for *.*hkl*-file format. After the structure solution and refinement *.*ins* file is supplemented by atomic coordinates and thermal parameters.
4. *.*cif* (and *.*cif_od*) files contain the structural information and a detailed description of the data collection and the integration procedure.
5. *.*sum* file is a log file of the XRD data processing performed by the user. Together with *.*cif_od*, *.*sum* files can be used in Jana2006 to create of the experiment for the structure solution and refinement.

III. Methods and instruments



1. (Optional) Enable calculation of manual empirical corrections. In the expanded dialog one can specify the number of frames for which a single scale should be used.

1a. (Optional) In 'Advanced' options one can skip the strongest (saturated) reflections from the frame scaling and/or change the number of reflections taken for the calculation of the frame scaling.



2. Enable interactive space group determination to define a correct space group with CrysAlisPro build-in tool. Otherwise disable space group determination and perform the procedure later using the other appropriate software.

3, 3a. (Optional) Enable 'manual' filters and in expanded menu select 'Filters'. Apply filters to the reflections based on their intensities, d -spacings, geometrical positions on the frame, appearance on certain frames/runs, corresponding R_{int} values etc.

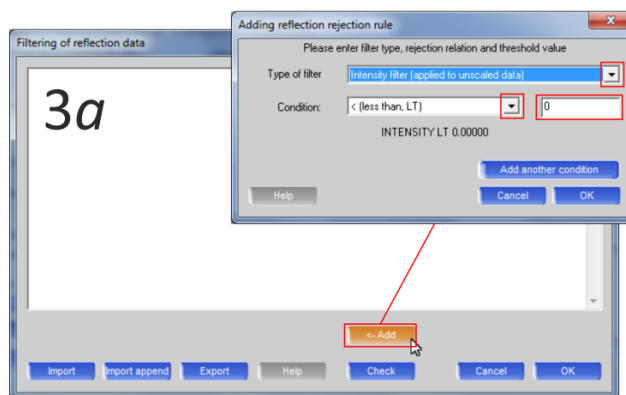


Figure 3.4.5-1 Data finalization dialog of CrysAlisPro software with available options. For better performance one may change certain parameters highlighted in red rectangles.

Table 3.4.5-1 Detection of serious problems occurred during XRD data collection or data reduction. One inspects the output of the CrysAlisPro after the data finalization (*continued on the next page*).

Inspection of the reflection statistics											Possible solutions of problems appeared	
Statistics vs resolution (taking redundancy into account) - point group symmetry: O-3m1											No further corrections are required.	
resolu- tion(Å)	# kept	# theory	# unique	% complete	average redundancy	mean F2	mean F2/sig(F2)	Rint	RsigmaB			
inf-1.05	83	40	25	62.5	3.3	460102.04	34.90	0.044	0.022			
1.05-0.84	93	34	25	73.5	3.7	273553.71	24.28	0.036	0.031			
0.83-0.72	83	37	25	67.6	3.3	156833.00	13.97	0.061	0.048			
0.72-0.64	81	40	25	62.5	3.2	101518.56	11.26	0.061	0.069			
0.64-0.59	79	42	25	59.5	3.2	100258.77	10.11	0.118	0.068			
0.58-0.48	51	147	26	17.7	2.0	44315.04	5.36	0.242	0.109			
inf-0.48	470	341	151	44.3	3.1	202233.23	17.66	0.056	0.038			
inf-0.80	191	82	56	68.3	3.4	345892.19	27.84	0.041	0.026			
<i>Ideal statistics.</i>												
The reflections are intense, but not saturated, the data reach the highest resolution of 0.48 Å.												
Statistics vs resolution (taking redundancy into account) - point group symmetry: Pmmn											a) apply correct skip regions before data reduction (MAR555, MAR165, Pilatus) or apply filters on negative and zero reflections during data finalization (not recommended) and provide correct DAC opening angle;	
resolu- tion(Å)	# kept	# theory	# unique	% complete	average redundancy	mean F2	mean F2/sig(F2)	Rint	RsigmaB			
inf-1.73	212	123	56	45.5	3.8	17830.67	11.32	0.063	0.054			
1.72-1.39	243	107	56	52.3	4.3	16929.21	12.43	0.060	0.057			
1.39-1.22	198	94	56	59.6	3.5	8856.37	9.61	0.076	0.065			
1.22-1.11	241	95	56	58.9	4.3	4522.71	9.02	0.095	0.067			
1.11-1.02	183	100	56	56.0	3.3	5231.01	8.42	0.057	0.075			
1.02-0.97	236	100	56	56.0	4.2	7586.30	10.21	0.092	0.062			
0.97-0.92	211	87	56	64.4	3.8	2377.99	7.41	0.110	0.095			
0.92-0.87	199	106	56	52.8	3.6	3093.67	6.43	0.116	0.081			
0.87-0.84	190	92	56	60.9	3.4	5093.68	7.15	0.095	0.072			
0.84-0.81	234	101	60	59.4	3.9	2699.59	6.51	0.116	0.091			
inf-0.81	2147	1011	564	55.8	3.8	7546.33	8.93	0.076	0.064			
<i>Apparently low-intense data.</i>												
Possible sources of the problem may be following:												
a) reflections' intensities are extracted from shadowed regions or regions with zero/negative intensities;												
b),c),d) reflections' positions on the frames are predicted wrongly (wrong instrument model, strong sample misalignment, wrong unit cell);												
d),e),f) underestimation of the intensities during data reduction or data finalization;												
g) really low-intense data (number of saturated reflections is lower than 3–5%).												
Statistics vs resolution (taking redundancy into account) - point group symmetry: Pmmn											Check the number of reflections with saturated intensities (ph s). Re-collect the data with lower exposure time if necessary.	
resolu- tion(Å)	# kept	# theory	# unique	% complete	average redundancy	mean F2	mean F2/sig(F2)	Rint	RsigmaB			
inf-1.34	63	47	25	53.2	2.5	4035476.08	249.66	0.023	0.003			
1.31-1.03	63	45	25	55.6	2.5	3847254.29	193.58	0.037	0.004			
1.03-0.87	69	48	25	52.1	2.8	4551541.81	216.17	0.024	0.004			
0.87-0.78	66	46	25	54.3	2.6	3410914.43	128.70	0.023	0.005			
0.78-0.70	50	63	25	39.7	2.0	4391242.60	149.96	0.017	0.005			
0.70-0.59	40	167	25	15.0	1.6	1708394.91	71.20	0.023	0.009			
inf-0.59	351	417	150	36.0	2.3	3771187.11	175.73	0.025	0.004			
inf-0.80	253	178	96	53.9	2.6	3960134.63	198.32	0.027	0.004			
<i>Saturated data, number of saturated reflections is higher than 10%. R_{int} values and corresponding frame scaling curve look perfect but accurate structure refinement is not possible (R₁ ~ 20 %).</i>												

(continued from the previous page)

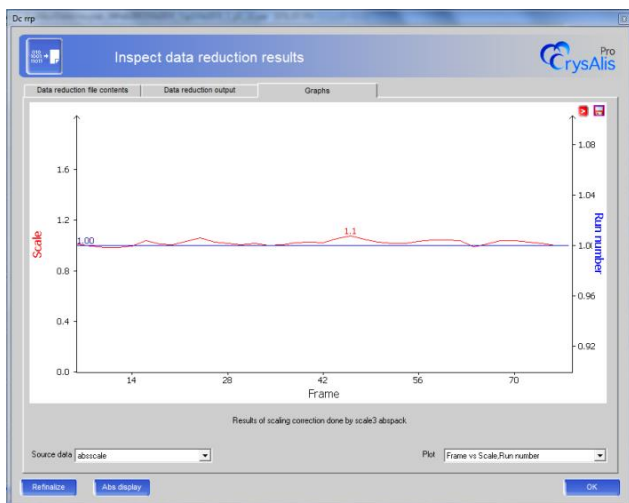
Inspection of the reflection statistics	Possible solutions of problems appeared
<p><i>No apparent problems with intensities, but R_{int} values are unexpectedly high (10 % and higher at 0.8 Å d-shell).</i></p> <p>The other problems may be following:</p> <p>a),b),c),d) wrong determination of crystal mosaicity and shape of the reflections;</p> <p>e) under/overestimation of all the reflection intensities;</p> <p>f),g) intensities of several sample's reflections are overestimated due to overlap with Ne and diamond diffraction spots and diffraction rings from a gasket;</p> <p>h),i),j),k) reflections' positions on a frames are predicted wrongly (moderate and strong sample misalignment, wrong unit cell determination due to missed twinning, wrong determination of the lattice centering).</p> <p>l) the crystal itself has low quality (for example it can deteriorate after the phase transition).</p>	<p>a) for synchrotron data always disable 'Reject reflections with bad profiles' option;</p> <p>b) check the size of the integration mask and increase it if necessary. Sizes of integration masks were often underestimated for XRD data collected with MAR165 and PerkinElmer detectors;</p> <p>c) check the shape of the reflections. Typically during compression the crystal accumulates strains and deteriorates, that reflects in broadening of the reflections. For moderate strains one can change of the size of integration masks. In difficult situations the improvement is not possible;</p> <p>d) try to use 'smart background' option or decrease background evaluation range (1–5 frames);</p> <p>e) for strong diffraction data use 2D profile fitting mode instead of default 3D profile fitting;</p> <p>f) check if Ne diffraction rings or diffraction rings from the gasket material are strong. If yes, use command <code>um skipd <d-spacing></code> to specify omitted regions and re-process the data;</p> <p>g) estimate the number of crystalline domains. On highly spotty frames it may appear difficult to evaluate the correct background. Therefore either apply d) or in rare cases mask the all reflections except those belonging to the sample (<code>dc rejecttrfxy</code>). During data reduction the omission area will be not considered. If the target phase diffraction give spotty rings the data reduction is not possible and it is worth to try powder diffraction or try l);</p> <p>h) check if the lattice has centering and if yes apply corresponding filters (during data reduction);</p> <p>i) in a case of twinning specify orientation matrices of the twin domains; perform data reduction and finalization taking twinning into account;</p> <p>j) inspect frame scaling curve for sample misalignment skip a few first and/or last frames during data reduction if necessary;</p> <p>k) re-align the sample and re-collect the data;</p> <p>l) re-collect the data on a different sample if possible.</p>

(continued on the next page)

(continued from the previous page)

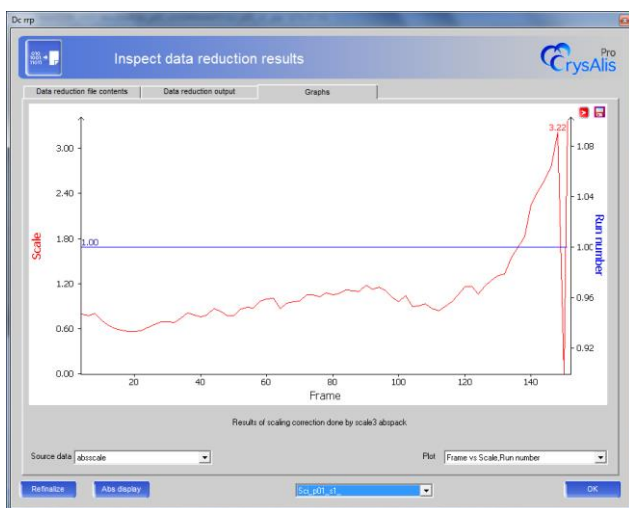
Inspection the shape of the frame scaling curve

Possible solutions of problems appeared



No further corrections are required.

Ideal shape of the frame scaling curve.



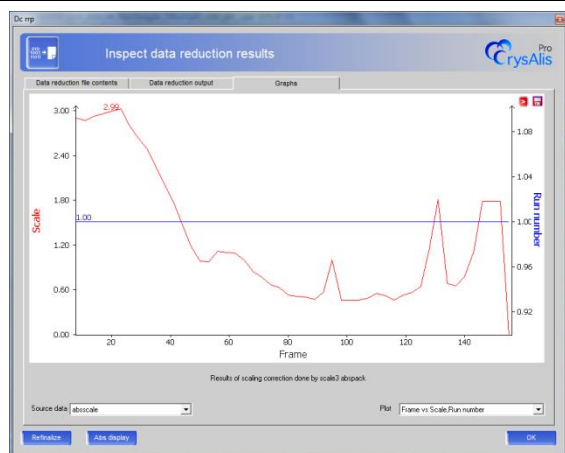
Skip a few first and/or last frames during data reduction. For example the shape of frame scaling curve shown on the left suggest to skip last 35-40 frames.

Moderate sample misalignment. At the starting and/or the final omega positions the sample moves from the incident beam and intensities of the corresponding reflections decrease which create problems for scaling boundary frames.

(continued on the next page)

(continued from the previous page)

Inspection the shape of the frame scaling curve



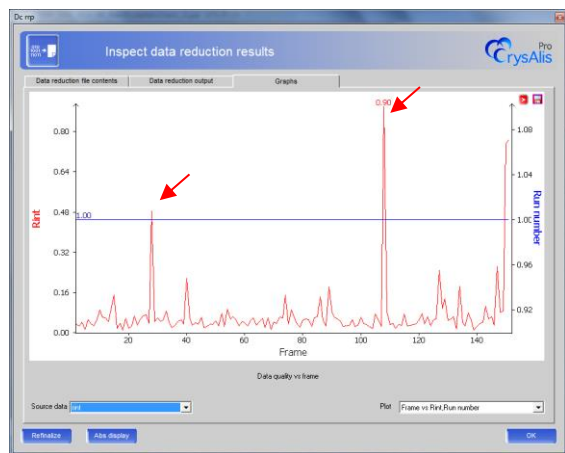
CrysAlisPro fails to calculate correct frame scaling. As a result the shape of the frame scaling curve is rocky or even not presented. Problems may originate from:

- a) strong sample misalignment;
- b) amount of available XRD reflections insufficient for frame scaling.

Possible solutions of problems appeared

- a) Re-align the sample and re-collect the data;
- b) Crystals with cubic unit cell and/or with small unit cell parameters have few number of independent XRD reflections which are not enough for CrysAlisPro to define proper frame scaling. If no apparent problems with data exist (misalignment, intensity level), skip the calculation of the frame scaling.

Inspection of R_{int} behavior



Strong parasite diamond reflections (red arrows) overlap with several reflections from the sample.

Possible solutions of problems appeared

Skip inconsistent reflections during structure refinement.

Final remark

Good statistics, R_{int} values and frame scaling do not 100 % guarantee a correct solution of the structure and an accurate structure refinement.

3.4.6. Structure solution and refinement

The structure solution is a process of calculation of atomic positions and thermal parameters (isotropic or anisotropic displacement parameters) based on a set of squared experimental structural amplitudes, F_{hkl}^2 . The structural amplitudes are defined from reflection intensities after applying special corrections:

$$F_{hkl}^2 = \frac{I_{hkl}}{k \cdot Lp \cdot A}$$

where k is a scale factor, Lp is Lorentz-polarization correction, A is a transmission factor.

F_{hkl} is an amplitude of the wave diffracted from a family of crystal lattice planes in a units of scattering amplitude of a single electron. The wave diffracted from crystal lattice planes is described by the *structure factor*:

$$\mathbf{F}_{hkl} = F_{hkl} \exp(i\alpha_{hkl}) = \sum_j f_j \exp \left[-B_j \left(\frac{\sin\theta}{\lambda} \right)^2 \right] \exp[2\pi i(hx_j + ky_j + lz_j)]$$

where the sum is over all atoms in the unit cell; x_j, y_j, z_j are the coordinates of the j^{th} atom; f_j is the scattering factor of the j^{th} atom; α_{hkl} is the phase of the diffracted beam; B_j is a B -factor directly related to the mean square isotropic displacement of the j^{th} atom; θ is the scattering angle and λ is the X-ray wavelength. The structure factor is a complex number; its amplitude is derived from the diffraction experiment, but phases are unknown that creates a so-called phase problem, the main issue of the structure solution process. A process of elaboration of phases is nowadays automated; there are a number of techniques implemented in different structure solution programs: direct methods, Patterson synthesis, heavy-atom method, charge flipping, etc. However incomplete high-pressure datasets can decrease chances of the structure solution especially for low-symmetry structures (triclinic and monoclinic).

Once the phases for the reflections are somehow derived, then the atomic coordinates can be directly calculated, since an electron density in a position x, y, z of the unit cell ρ_{xyz} is related with the structure factors with an inverse Fourier transform:

$$\rho_{xyz} = \frac{1}{V} \sum_{hkl} F_{hkl} \exp[-2\pi i(hx + ky + lz)]$$

where V is the unit cell volume.

After an initial structural model is obtained, it is refined against experimental data by the least-squares minimization of adjustable parameters. At the first stage missing atoms are found from the reconstruction of residual electron density maps, their positions, and if applicable, atomic occupancies are refined; and finally anisotropic displacement parameters are refined. Due to incomplete data sets the last step is often not performed for the high-pressure data.

An agreement between the model and experimental data is defined by so-called residual R -factors, which represent the quality of the structural model:

$$R_1 = \frac{\sum ||F_{obs}| - |F_{calc}||}{\sum |F_{obs}|}$$

$$wR_2 = \left[\frac{\sum w|F_{obs}^2 - F_{calc}^2|}{\sum wF_{obs}^2} \right]^{1/2}$$

where F_{obs} – is the observed structure factor amplitude, F_{calc} – is the calculated structure factor amplitude based on the model; and w – is a weighting factor individually derived for each measured reflection based on its standard uncertainty.

The high-pressure data suffer from overlapping with a parasite diffraction, mostly created by diamonds and a crystallized pressure medium. Those overlapped reflections have to be omitted from the refinement that usually improves thermal parameters and decreases R -factors. In SHELX-based programs such reflections can be identified in the list of the most disagreeable reflections located in the `*.lst` file. Then one inspects the XRD frames in order to check if the candidate reflections are really corrupted. The rejected reflections are added the `*.ins` file with `OMIT <h k l>` instruction. Jana2006 has its own reflection culling tool, which is more convenient and informative.

IV. Scope of thesis

This part shortly overviews the results presented in Chapter V. In framework of my PhD Project, eight papers were published, one submitted, and one is prepared for submission to a peer-reviewed journal. Subsection 4.1 summarizes the results of single-crystal XRD on materials synthesized at high pressures and high temperatures and studied at ambient conditions. That are compounds important for material sciences (metal borides, namely aluminum doped β -boron, MnB_4 , Co_5B_{16}) and high pressure minerals (knorringite ($\text{Mg}_3(\text{Cr}_{1.58}\text{Mg}_{0.21}\text{Si}_{0.21})\text{Si}_3\text{O}_{12}$) and Fe^{3+} -bearing bridgmanite ((Mg,Fe) SiO_3 perovskite)). Subsection 4.2 describes *in situ* high-pressure single-crystal XRD studies of FeB_4 , Fe_2B_7 , and Fe-doped δ -B. The Subsection 4.3 is devoted to applications of single-crystal XRD in study of materials at conditions of the deep Earth interiors. Particularly it describes compressibility and structural changes in FeOOH and possible symmetrization of hydrogen bond. High-pressure and high-temperature single-crystal XRD was used to establish the crystal structures of Fe_2O_3 and Fe_3O_4 polymorphs, reveal relations between structural and electronic transformations, and discuss implications for behavior of banded iron formations subducted into the Earth lower mantle.

4.1. Study of the materials synthesized under HPHT conditions

4.1.1. Crystal structure of aluminum doped β -boron

The crystals of aluminum-doped β -boron were formed at 3 GPa and 2100 K, in one of our large-volume press experiments on studying pressure-temperature phase diagram of boron [26]. The crystals appeared on the edges of the capsule after an accidental reaction of β -boron with a corundum Al_2O_3 cylinders served as a thermal insulator. Crystals were of the small size ($0.10 \times 0.08 \times 0.01 \text{ mm}^3$), black, and poorly scattered X-rays, and therefore they could be easily misidentified as pure β -boron. However, using single-crystal diffraction we were able to distinguish pure boron and phase containing just about $\sim 2.5 \text{ at.}\% \text{ Al}$.

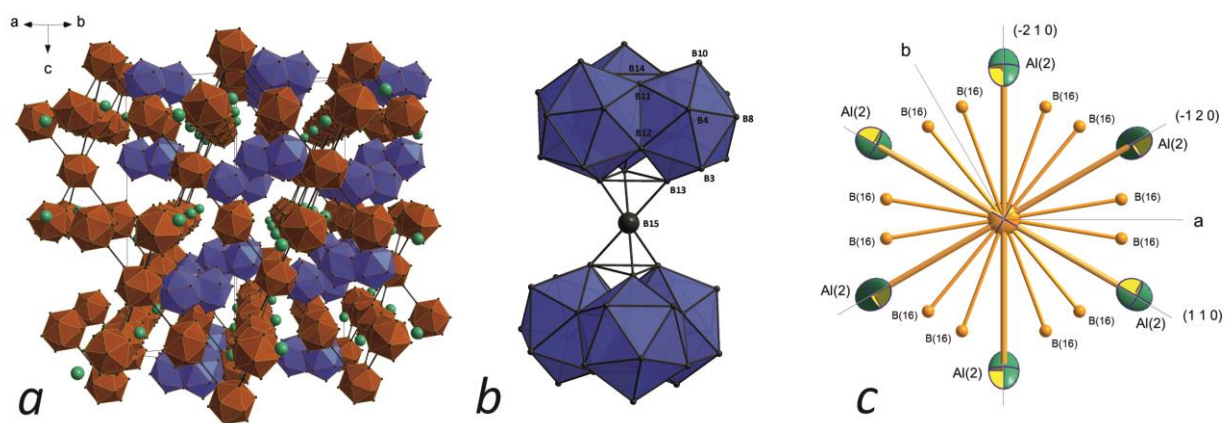


Figure 4.1.1-1 Graphical representation of the Al-doped β -B crystal structure: (a) “porous” three-dimensional framework formed by B₁₂ icosahedra (brown) with Al (green) atoms and B₂₈ units (blue) located in the voids of the framework; (b) enlarged two B₂₈ units connected via the B(15) atom; (c) atomic distribution near the B(15) atom (non-labeled atom in the center of the picture) shown along the c -axis. Al atoms occupy A1- (a) and D-sites (b).

Aluminum-doped β -rhombohedral boron crystallizes in $R\bar{3}m$ space group with $a = 10.9014(3)$, $c = 23.7225(7)$ Å. The structure of β -B was used as a starting model for the solution. Interstitial atoms were identified from the residual electron density maps. The first rather strong residual electron density peak of $28 \text{ e}/\text{\AA}^3$ was assigned as Al atom, other two peaks were less intense, namely of $1.5 \text{ e}/\text{\AA}^3$ and $3.5 \text{ e}/\text{\AA}^3$. Inspection of corresponding interatomic distances allowed to assign the peaks to boron and aluminum atoms, respectively, both atoms occupy those positions by ca. 11 %. As a result the final discrepancy factor R_1 (all data) dropped from 44.3 (for the base β -B structure) to 5.09 %.

The structure is based on the three-dimensional framework made of B₁₂ icosahedra with voids being occupied by the B₂₈–B–B₂₈ units (Figure 4.1.1-1a, b). Aluminum atoms partially fill certain interstitial positions, namely A1- (tetrahedral void formed by four B₁₂ icosahedra) and D-sites (between two B₂₈ units) of 82.7(6) % and 11.3(4) %, respectively (Figure 4.1.1-1a and Figure 4.1.1-1c). We have got two possible models of atomic distribution near the D-site as it was previously reported in literature for aluminum boride [126]. The similar atomic arrangement near the D-site has been revealed in a crystal structure of SiB_{30.17}C_{0.35} [127]. The structure refinement of the two appropriate models results in two possible chemical compositions,

AlB_{44.8(5)} or AlB_{37.8(5)}, which fit well a chemical analysis data obtained by an EDX method using a scanning electron microscopy. These compositions get within a field of limited solubility of Al in β -B (3 at. %) [31] in the Al-B phase diagram.

4.1.2. Crystal structure of MnB₄

Single crystals of MnB₄ were synthesized under high-pressure high-temperature conditions in a multianvil apparatus at 10 and 12 GPa and temperature of 1600 °C. While the compound has been known for decades, details of its crystal structure and its relations with structures of other transition metal borides remained controversial. We found that in contrast to superconducting FeB₄ and metallic CrB₄, which are both orthorhombic, MnB₄ features a monoclinic crystal structure ($P2_1/c$, $a = 5.4759(4)$, $b = 5.3665(4)$, $c = 5.5021(4)$ Å and $\beta = 115.044(9)^\circ$, R_1 (all data) = 6.52 %). Its lower symmetry originates from the Peierls distortion of Mn chains.

In the crystal structure of MnB₄ which we solved and refined each Mn atom is surrounded by 12 boron atoms and the distorted MnB₁₂ polyhedra pack in columns parallel to the $(a + c)$ -direction (Figure 4.1.2-1a), so that the metal atoms form one-dimensional chains with alternating Mn–Mn distances of 2.7006(6) and 3.1953(7) Å. Every column of MnB₁₂ polyhedra is shifted with respect to the four nearest ones by $(a + c)/2$ (Figure 4.1.2-1a, b).

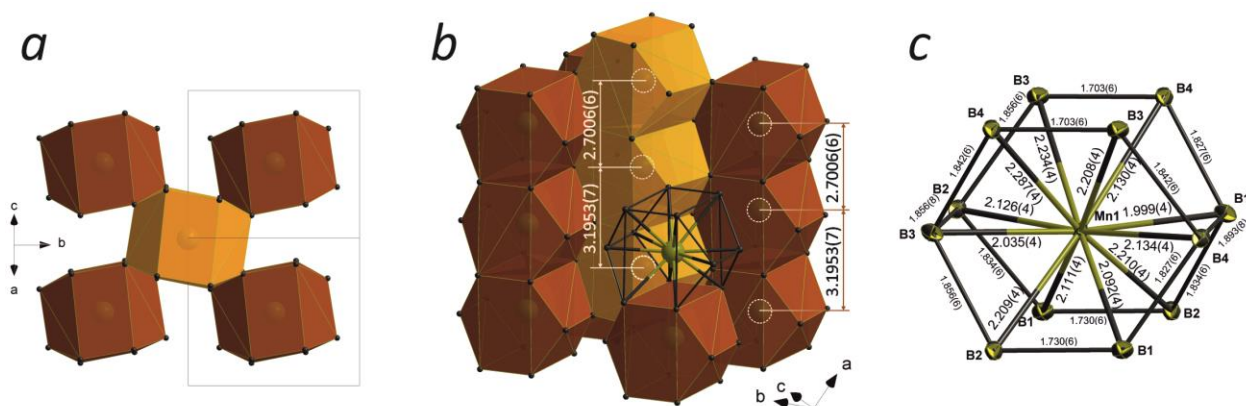


Figure 4.1.2-1 Structure of MnB₄. MnB₁₂ polyhedra pack in columns along [1 0 1] direction with alternating Mn–Mn distances of 2.7006(6) and 3.1953(7) Å through the column (a, b). Interatomic distances (Å) in the MnB₁₂ polyhedron (c). The shortest B–B distance of 1.703(6) Å is directed along b -axis.

Short B–B bonds are responsible for high hardness and low compressibility of CrB₄ and FeB₄. The minimal B–B distance in MnB₄ of 1.703(6) Å (Figure 4.1.2-1c) is comparable with those in CrB₄, FeB₄, Fe₂B₇, and Co₅B₁₆ compounds with similar crystal structures. Indeed, a bulk modulus obtained from high-pressure powder XRD data appeared to be of 254(9) GPa, which is close to that of the superhard FeB₄ (252(5) GPa). A considerable anisotropy of the compressibility is also similar to that observed in FeB₄ [128]. Along the *b* direction MnB₄ is almost as incompressible as diamond [129] that can be linked to the mentioned above very short B–B bond (Figure 4.1.2-1c) oriented along the *b*-axis.

Nanoindentation measurements resulted in the average hardness of 30.7 ± 2.3 GPa and an average indentation modulus of 415 ± 30 GPa. Thus, MnB₄ is a fairly hard, but not superhard material.

4.1.3. Crystal structure of Co₅B₁₆

A first cobalt boride with the Co:B ratio below 1:1, Co₅B₁₆, was synthesized at 15 GPa and 1300-1600 °C in multianvil apparatus. Good quality crystals are quite small (with a maximum linear dimension about 50 μm) and appear in a mixture with other compounds, thus complicating single crystal diffraction studies. Moreover, an exact determination of boron content based on a conventional microprobe analysis is very difficult. The Co₅B₁₆ has a unique orthorhombic structure (space group *Pmma*, *a* = 19.1736(12), *b* = 2.9329(1), and *c* = 5.4886(2) Å, *R*₁ (all data) = 3.70 %). The material is hard, paramagnetic, with a weak temperature dependence of the magnetic susceptibility.

The crystal structure of Co₅B₁₆ is similar to an atomic arrangement in metal tetraborides (FeB₄ [128], MnB₄ [130], CrB₄ [131]) which is based on a rigid network of boron atoms with metal atoms being in interstitial positions. In Co₅B₁₆ one can easily see honeycomb-like stripes (Figure 4.1.3-1) oriented along the *b*-axis and condensed into a complicated ramous structure. Such an arrangement of boron atoms gives rise to the straight, channel-like voids along the *b*-axis. Cobalt atoms occupy these voids creating infinite rows. All metal-metal distances in the rows are equal, but they are larger than the sum of metallic radii of two Co atoms.

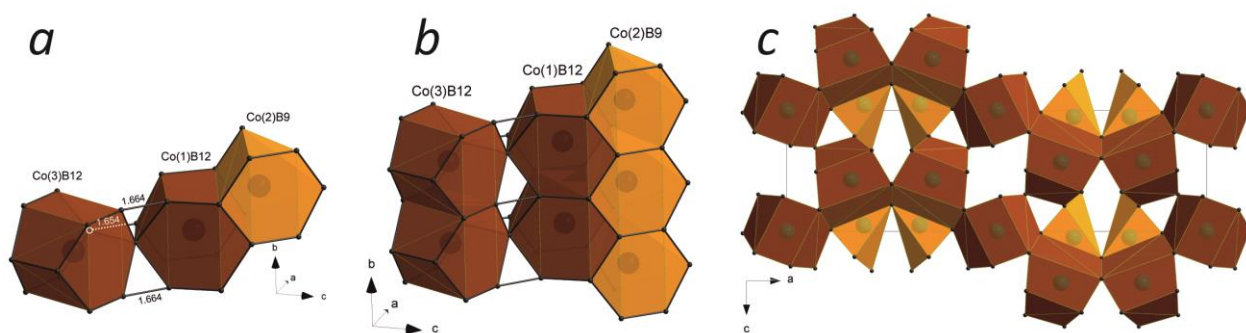


Figure 4.1.3-1 A polyhedral model of the structure of Co_5B_{16} . (a) An asymmetric part of the structure consisting of three units: an irregular Co(3)B_{12} polyhedron, its distorted counterpart Co(1)B_{12} , and a Co(2)B_9 polyhedron. (b, c) Packing of the polyhedra in columns along the b -axis by sharing common fragments. The y coordinates of Co atoms in light and dark polyhedra differ by $1/2$. B-B bonds are highlighted by bold lines, the shortest distances are labeled.

Despite some allusion to the tetraborides structures, the Co polyhedra in Co_5B_{16} are distinctly different. The Co atoms occupy three independent crystallographic sites, Co(1), Co(2) and Co(3). The structure of Co_5B_{16} can be visualized in terms of packing of three kinds of Co-B polyhedra (Figure 4.1.3-1). An asymmetric part of the structure (Figure 4.1.3-1a) consists of three units: an irregular Co(3)B_{12} polyhedron, its distorted counterpart Co(1)B_{12} , and a Co(2)B_9 polyhedron. Polyhedra of each kind (Co(2)B_9 , Co(1)B_{12} and Co(3)B_{12}) pack in columns by sharing common upper and bottom faces and create their own infinite columns parallel to the b -axis (Figure 4.1.3-1b). The columns are connected with each other through common vertices, edges and parallelogram side faces (Figure 4.1.3-1c).

The B-B distances in the structure of Co_5B_{16} vary from 1.654(7) to 1.908(7) Å. The shortest bond located at the ac plane is observed between B atoms of the neighboring Co(3)B_{12} and Co(1)B_{12} polyhedra. This is the shortest B-B bond length among transition metal borides with related structures. The dense atomic packing and short B-B contacts make Co_5B_{16} rather hard with the measured Vickers hardness $H_v = 30 \pm 2$ GPa, the value slightly higher than reported for CrB_4 [131], but lower than that of the superhard FeB_4 [128].

4.1.4. Crystal structure of knorringite, $\text{Mg}_3(\text{Cr}_{1.58}\text{Mg}_{0.21}\text{Si}_{0.21})\text{Si}_3\text{O}_{12}$

Knorringite is a mineral species belonging to the garnet group. Having a nominal composition $\text{Mg}_3\text{Cr}_2(\text{SiO}_4)_3$, it forms a solid solution series with pyrope. It was discovered in 1968 in the Kao kimberlite pipe, and may play a role in the mantle mineralogy. So far information regarding crystal chemistry of the mineral remains limited. A single crystal of knorringite-type compound, $\text{Mg}_3(\text{Cr}_{1.58}\text{Mg}_{0.21}\text{Si}_{0.21})\text{Si}_3\text{O}_{12}$, was synthesized in a multianvil press at $P = 16$ GPa and $T = 1600$ °C. Its crystal structure is composed of corner-shared SiO_4^{4-} tetrahedra and $(\text{Cr,Mg,Si})\text{O}_6^{9-}$ octahedra, and Mg^{2+} ions occupying 8-fold voids (Figure 4.1.4-1). Atomic positions, anisotropic displacement parameters, and occupancies of

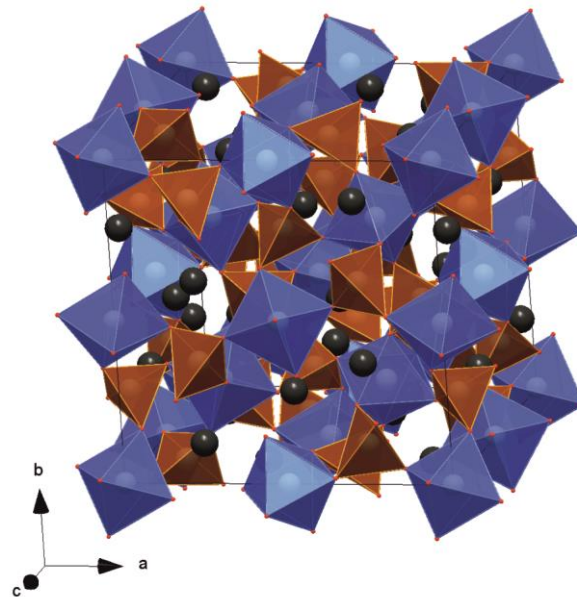


Figure 4.1.4-1 Crystal structure of garnet-like $\text{Mg}_3(\text{Cr}_{1.58}\text{Mg}_{0.21}\text{Si}_{0.21})\text{Si}_3\text{O}_{12}$, composed of corner-shared SiO_4^{4-} tetrahedra (brown) and $(\text{Cr,Mg,Si})\text{O}_6^{9-}$ octahedra (blue), and Mg^{2+} ions (black spheres) occupying 8-fold voids.

Cr, Mg and Si in octahedral site were refined from single-crystal X-ray diffraction data ($Ia\bar{3}d$, $a = 11.5718(1)$ Å, R_1 (all data) = 2.36 %). The occupancies were refined with a constraint on an electroneutrality of the final structure:

$$2\text{Cr}^{3+} = \text{Mg}^{2+} + \text{Si}^{4+}$$

As a result the studied knorringite crystal contains 21 mol. % of the majorite end-member.

The relationship between majorite and knorringite at the high pressure provides an evidence for similarity in their behavior at the conditions of the deep Earth's interiors.

4.1.5. Crystal structure of Fe^{3+} -bearing $(\text{Mg,Fe})\text{SiO}_3$ perovskite (bridgmanite)

Silicate perovskite with a general formula $(\text{Mg,Fe})(\text{Si,Al})\text{O}_3$, recently receiving mineral name “bridgmanite”), is a major component of the Earth's lower mantle. Understanding of its crystal chemistry is a crucial problem of a modern high-pressure mineral physics and highly important

for the interpretation of geophysical and geochemical observations. Iron is the only abundant element in the Earth mantle with variable oxidation states. The structure of bridgmanite has two cation sites, distorted 8-fold (*A*-site), occupied predominantly by Mg, and smaller 6-fold *B*-site (Figure 4.1.5-1) filled mostly by Si and Al. Iron atoms in a form of Fe^{2+} and Fe^{3+} may occupy both *A*- and *B*-sites.

A single crystal of Al-free, Fe^{3+} -bearing Mg-perovskite was synthesized at 26 GPa and 1800 °C in a multianvil apparatus. The compound crystallizes in *Pbnm* space group, $a = 4.7877(18)$, $b = 4.9480(18)$, and $c = 6.915(3)$ Å.

In order to accurately establish structural position and oxidation state of Fe atoms, single-crystal XRD was used in a combination with an electron microprobe analysis and Mössbauer spectroscopy. Results show that the chemical composition of synthesized bridgmanite is $\text{Mg}_{0.946(17)}\text{Fe}^{2+}_{0.045(4)}\text{Fe}^{3+}_{0.011(1)}\text{Si}_{0.997(16)}\text{O}_3$ (R_1 (all data) = 7.9 %) and that both Fe^{2+} and Fe^{3+} occupy the *A*-site of the perovskite structure. The data are consistent with the creation of cation vacancies on either the *A*-site: $(\text{Mg}, \text{Fe}^{2+}, \text{Fe}^{3+})_{1-\delta}\text{SiO}_3$ or the *B*-site: $(\text{Mg}, \text{Fe}^{2+}, \text{Fe}^{3+})\text{Si}_{1-\delta}\text{O}_3$ instead of $\text{Fe}^{3+}\text{--Fe}^{3+}$ coupled substitution or the creation of oxygen vacancies. A comparison of octahedral tilting angles calculated from the unit cell parameters with those

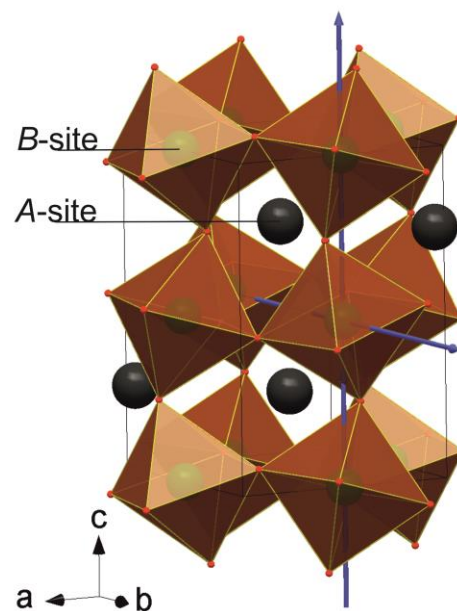


Figure 4.1.5-1 Crystal structure of $(\text{Mg}, \text{Fe})\text{SiO}_3$ perovskite composed of corner-shared SiO_6^{4-} octahedra and Mg^{2+} , Fe^{2+} , Fe^{3+} ions filling 8-fold void. Blue arrows are directions of octahedra tilt from positions in an ideal cubic perovskite structure.

obtained from atomic coordinates indicates that the effect of Fe substitution on the nature of *B*-site octahedra is clearly different between Fe^{3+} and Fe^{2+} . This behavior suggests that the effect of Fe on physical/thermodynamic parameters of MgPv (e.g., bulk modulus, sound velocity and phase boundary between perovskite and post-perovskite) strongly depends on its valence state.

4.2. Application of single crystal XRD for studies transition metal borides

4.2.1. Crystal structure and high-pressure behavior of FeB₄

Experiments in multianvil apparatuses at pressures of 8 GPa to 18 GPa and temperatures of 1250 to 1750 K led to the synthesis of previously unidentified phases with the FeB₄, Fe₂B₇, and Fe_{1+x}B₅₀ ($x \approx 0.01$ – 0.32) compositions (the results for Fe₂B₇, and Fe_{1+x}B₅₀ are given in Section 4.2.2). According to the single crystal X-ray and electron diffraction, FeB₄ adopts an orthorhombic *Pnnm* ($Z = 2$) crystal structure with $a = 4.5786(3)$, $b = 5.2981(3)$, and $c = 2.9991(2)$ Å ($R_1(\text{all data}) = 4.00\%$).

The structure consists of irregular FeB₁₂ polyhedra arranged in columns along the *c*-axis by sharing the parallelogram-shaped faces (Figure 4.2.1-1*a*). The columns are connected with each other by common edges of the neighbouring polyhedra, whose centres (Fe atoms) are shifted with respect to each other on $\frac{1}{2}$ of the body diagonal of the unit cell. If viewed along the *c*-axis, the columns of polyhedra and empty channels alternate in a chess-like order (Figure 4.2.1-1*b*).

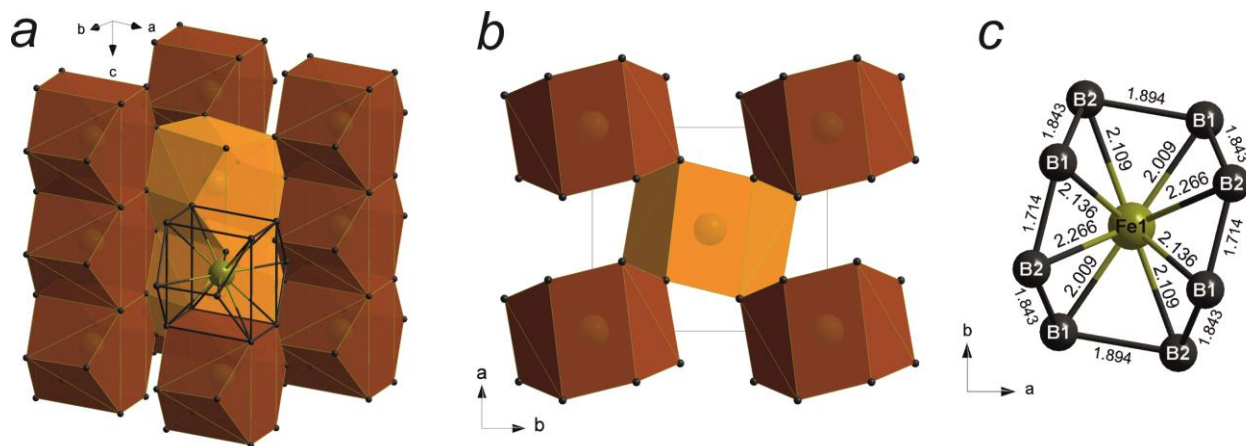


Figure 4.2.1-1 Crystal structure of FeB₄ composed of irregular FeB₁₂ polyhedra arranged in columns parallel to *c*-axis (*a*) and packing of columns viewed down the *c*-axis (*b*). The shortest B–B bond of 1.714(6) Å almost parallel to *b*-axis (*c*) may be responsible for high stiffness along *b*-axis comparable with that of diamond.

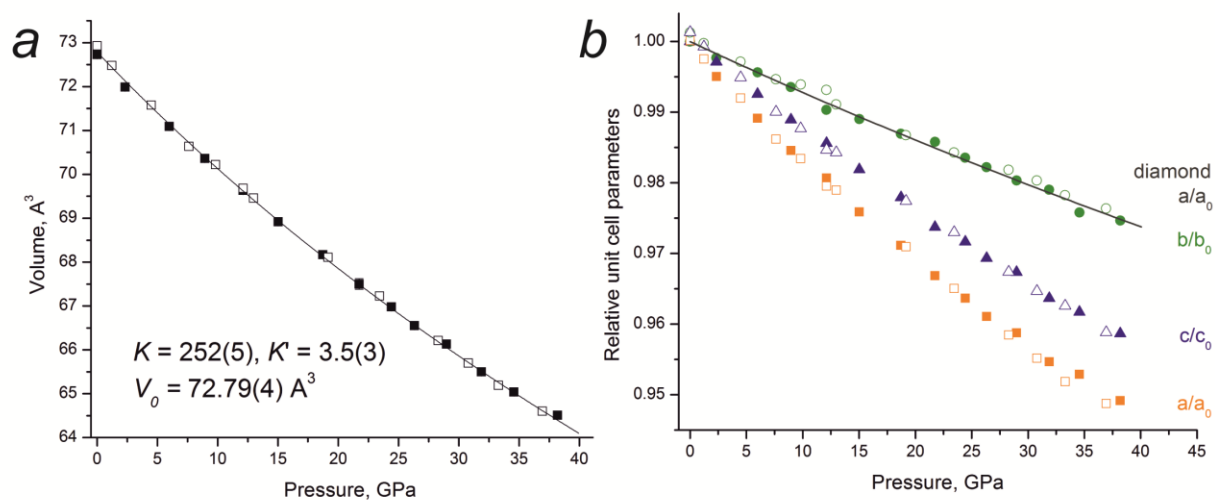


Figure 4.2.1-2 Volume (a) and axial (b) compressibility of FeB_4 based on high-pressure single-crystal XRD data. Filled symbols represent the data points obtained on compression and open ones – on decompression. Continues line (a) shows the fit of the pressure-volume data with the third-order Birch-Murnaghan equation of state. The structure is most compressible along the a -direction and least compressible along the b -direction. The stiffness of the FeB_4 structure along the b -direction is the same as that of diamond (continues line according to [129]) suggesting possible high hardness of the material.

The shortest Fe–B bonds ($2.009(4)$, $2.109(4) \text{\AA}$) are located in the same ab plane, while 8 longer Fe–B bonds ($2.136(3) \text{\AA}$ and $2.266(3) \text{\AA}$) are related to the boron atoms forming parallelogram-shaped faces common for the two neighboring polyhedra (Figure 4.2.1-1c). The distances between boron atoms vary from $1.714(6) \text{\AA}$ to $1.894(6) \text{\AA}$ and are common for pure boron phases. The closest B–B contact is located in the parallelogram-shaped face of the polyhedron (Figure 4.2.1-1c).

Metal borides are known for their high hardness [27] and low compressibility [10], so characterization of the elastic behavior of the newly synthesized boride and its stability under pressure is an important issue. No phase transitions were observed under compression of FeB_4 at ambient temperature in a diamond anvil cell up to ca. 40 GPa (Figure 4.2.1-2a). Compressibility measurements on both compression and decompression revealed the relatively high bulk modulus, $K = 252(5) \text{ GPa}$ ($K' = 3.5(3)$, $V_0 = 72.79(4) \text{\AA}^3$, by fitting the third-order Birch-Murnaghan equation of state) and a significant degree of anisotropy in the elastic behaviour of FeB_4 . The structure of FeB_4 is the most compressible along the a -direction, while it is the stiffest

along the *b*-axis. It may be related to the fact that the shortest (and thus least compressible) B–B contact (1.714(6) Å at ambient conditions) in this structure is nearly parallel to the *b*-axis. The stiffness of the FeB₄ structure along the *b*-direction is the same as that of diamond [129] (Figure 4.2.1-2*b*) suggesting that the iron tetraboride may have remarkable mechanical properties.

Indeed, the nanoindentation hardness approaches an average value of $H = 62 \pm 5$ GPa, while Vickers microhardness values range from 43 to 70 GPa, thus confirming that FeB₄ belongs to the group of superhard materials [132].

4.2.2. Crystal structure and high-pressure behavior of Fe₂B₇ and Fe_xB₅₀

A unit cell of Fe₂B₇ is orthorhombic (*Pbam*, $a = 16.9699(15)$, $b = 10.6520(9)$, $c = 2.8938(3)$ Å, R_1 (all data) = 7.36 %). Similarly to MB₄ ($M = \text{Fe, Mn, Cr}$) and Co₅B₁₆ [128,130,133,134], the crystal structure of Fe₂B₇ contains a rigid boron covalent framework and metal atoms located in its voids. Four crystallographically independent iron atoms in Fe₂B₇ are surrounded by 10 or 12 boron atoms, forming Fe(3)B₁₀, Fe(1)B₁₂, Fe(2)B₁₂, Fe(4)B₁₂ polyhedra (Figure 4.2.2-1*a*). Polyhedra of each kind create its own columns packed along *c*-axis by sharing the common top and bottom parallelogram faces. Eight columns of polyhedra, two columns of each kind assembled together and provide a rod-like “hexagonal” fragment of the structure extended in the *c*-direction (Figure 4.2.2-1*b*); the “rods” share common edges and vertices and create the close packing (Figure 4.2.2-1*c*). Fe₂B₇ was studied by synchrotron single crystal XRD up to 41 GPa. The compound possess a high bulk modulus (Figure 4.2.2-2*a*) and a strong anisotropy upon contraction (Figure 4.2.2-2*b*). In one direction, namely along the *b*-axis, Fe₂B₇ is extremely incompressible (like diamond), but in other crystallographic directions the compressibility is comparable with that along the *a* and *b* axes in γ -B. An inspection of individual bond compressibilities demonstrated that the shorter the B–B or Fe–B bond the easier it contracts. Particularly, the high axial incompressibility along the *b*-axis originates from short and incompressible B–B bonds of 1.647(13), 1.628(14) and 1.691(13) Å oriented along the *b*-axis.

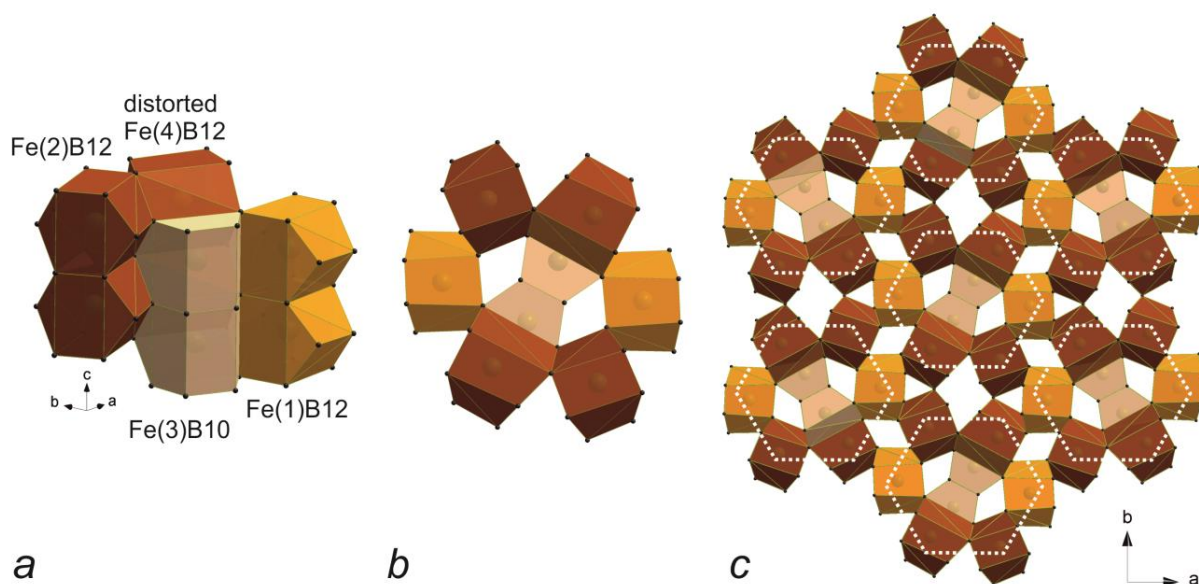


Figure 4.2.2-1 Crystal structure of Fe_2B_7 composed of $\text{Fe}(3)\text{B}_{10}$, $\text{Fe}(1)\text{B}_{12}$, $\text{Fe}(2)\text{B}_{12}$, $\text{Fe}(4)\text{B}_{12}$ polyhedra. Polyhedra of each kind are packed in columns along the c -axis by sharing common top and bottom parallelogram faces (a). The z -coordinates of Fe atoms in light and dark polyhedra differ by $\frac{1}{2}$. Eight columns of polyhedra, two columns of each kind assembled together and provide a rod-like “hexagonal” fragment of the structure extended in the c -direction (b). The “rods” share common edges and vertices and create close packing.

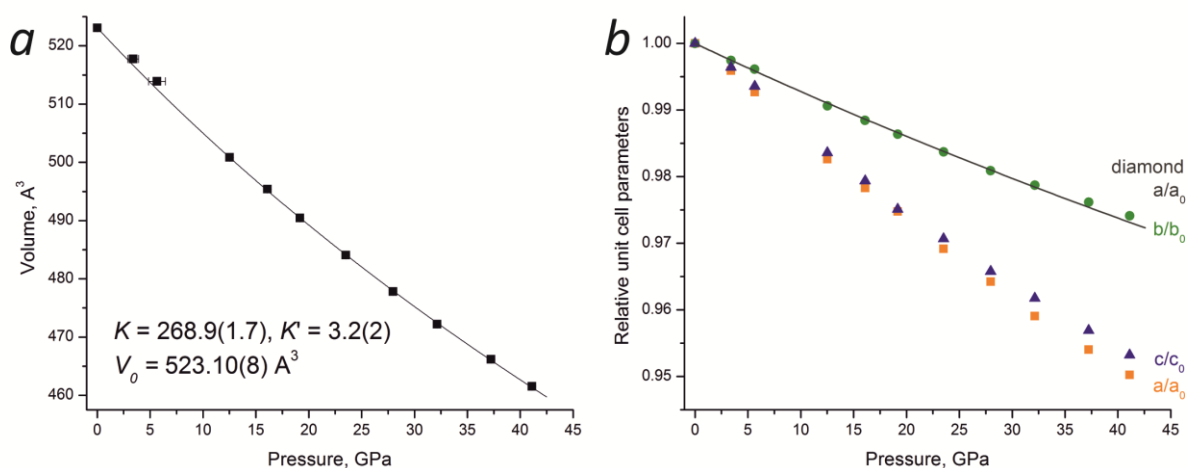


Figure 4.2.2-2 Volume (a) and axial (b) compressibility of Fe_2B_7 based on high-pressure single-crystal XRD data. Continues line (a) shows the fit of the pressure-volume data with the third-order Birch-Murnaghan equation of state. The structure is most compressible along the a - and c -directions and least compressible along the b -direction. The stiffness of the Fe_2B_7 structure along the b -direction is the same as that of diamond (continues line according to [129]) suggesting a possible high hardness of the material.

The crystal structure of Fe_xB_{50} is built on a basis of the structure of a tetragonal boron polymorph, δ -B. In the structure of δ -B ($\text{B}_2\text{B}_{48} = \text{B}_2(\text{B}_{12})_4$) boron icosahedra B12 form a 3-dimensional framework being arranged in the distorted cubic close (*fcc*) packing having 8 distorted tetrahedral cavities per a unit cell. Two of eight cavities are located in the $2a$ Wyckoff position, each one is surrounded by four B(3) atoms belonging to the corners of B12 icosahedra. In the crystal structure of δ -B this cavity is occupied by a boron atom forming covalent bonds with four corners of B12 icosahedra. Other two voids with the geometric centers in the $2b$ Wyckoff position are formed by 4 triangular faces B(3)–B(2)–B(2) of B12 icosahedra.

According to our single-crystal XRD studies Fe atoms occupy a larger cavity in the $2b$ position with an occupation degree of 50–65 % (Figure 4.2.2-3). In our work three Fe-doped boron phases were observed with common formula Fe_xB_{50} ($x = 1.01(1), 1.04(1), 1.32(1)$). Single-crystal XRD for $\text{Fe}_{1.04(1)}\text{B}_{50}$ was measured at ambient conditions ($P4_2/nnm$, $a = 8.9866(4)$, $c = 5.0620(4)$ Å, R_1 (all data) = 6.23 %); while for $\text{Fe}_{1.01(1)}\text{B}_{50}$ and $\text{Fe}_{1.32(1)}\text{B}_{50}$ we studied single-crystal XRD under compression up to ~ 48 GPa. Due to large voids in the structure Fe_xB_{50} are more compressible than boron phases (α -, β -, and γ -B [135–139]), $\text{Fe}_{1.32(1)}\text{B}_{50}$ has a slightly higher bulk modulus than $\text{Fe}_{1.01(1)}\text{B}_{50}$ (Figure 4.2.2-4a). Our data confirm previous experimental observations on a compression of pure boron phases [24,26] that intraicosahedral bonds are stiffer than intericosahedral ones. Fe–B and intraicosahedral B–B bonds contract almost uniformly in all directions that maintain the c/a ratio constant at a pressure increase. (Figure 4.2.2-4b).

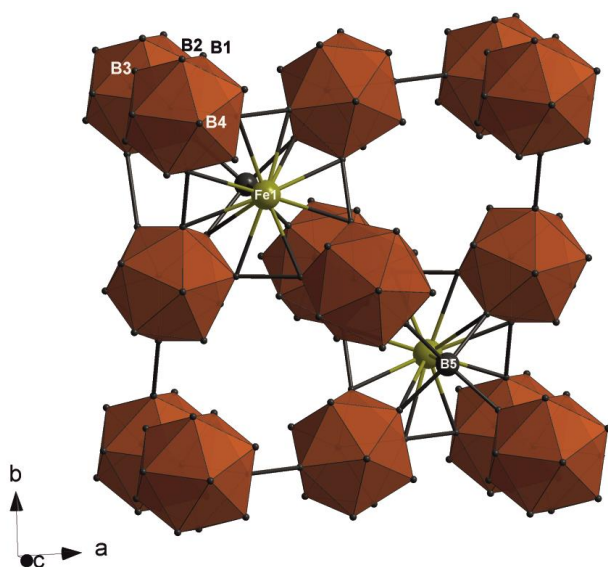


Figure 4.2.2-3 Crystal structure of Fe_xB_{50} ($x = 1.01(1), 1.04(1), 1.32(1)$) built on the basis of the structure of a tetragonal boron polymorph, $\delta\text{-B}$. Boron icosahedra form a 3-dimensional framework being arranged in the distorted *fcc* packing having 8 distorted tetrahedral cavities per unit cell. Two of eight cavities are located in the $2a$ Wyckoff position and occupied by interstitial B(5) atoms forming short covalent bonds with four surrounding B(3) atoms belonging to the corners of B12 icosahedra. Two larger cavities with the geometric centers in the $2b$ Wyckoff position are partially filled by Fe(1) atoms. The B(1)...B(1) interatomic distances in $\text{Fe}_{1.32(1)}\text{B}_{50}$ are shorter than in $\text{Fe}_{1.01(1)}\text{B}_{50}$ that fact probably allows $\text{Fe}_{1.01(1)}\text{B}_{50}$ to contract more effectively during compression.

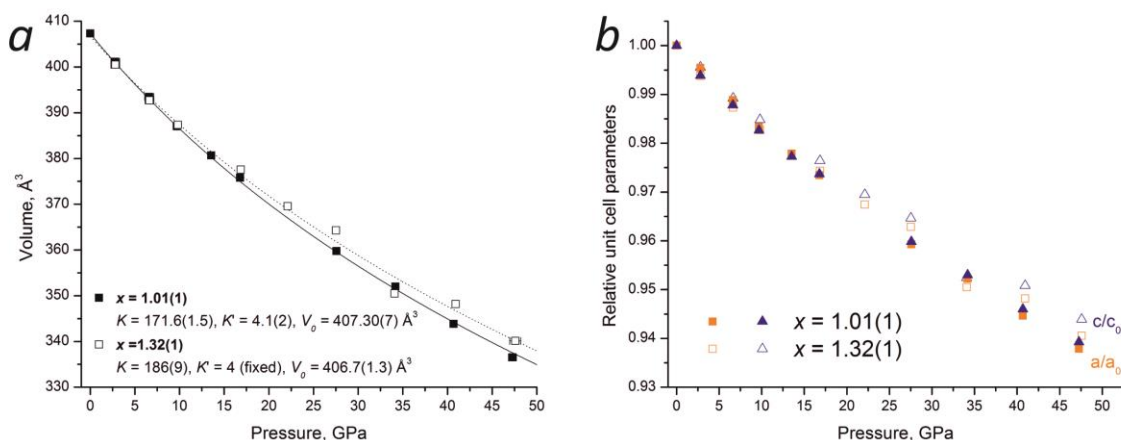


Figure 4.2.2-4 Volume (a) and axial (b) compressibility of Fe_xB_{50} based on high-pressure synchrotron single-crystal XRD data. Filled symbols referred to $\text{Fe}_{1.01(1)}\text{B}_{50}$ and open ones to $\text{Fe}_{1.32(1)}\text{B}_{50}$. Continuous line (a) shows the fit of the pressure-volume data with the Birch-Murnaghan equations of state (of third and second order, respectively). $\text{Fe}_{1.32(1)}\text{B}_{50}$ has slightly higher bulk modulus than $\text{Fe}_{1.01(1)}\text{B}_{50}$. Fe-B and intraicosahedral B-B bonds contract almost uniformly in all directions. That maintains the c/a ratio constant at a pressure increase.

4.3. Application for studies of materials at the conditions of the Earth's lower mantle

4.3.1. High-pressure behavior of FeOOH

Mineral goethite, α -FeOOH, crystallizes in an orthorhombic structure ($Pnma$, $a = 9.9510(5)$, $b = 3.0178(1)$, $c = 4.5979(2)$ Å) and is isostructural with diaspore, AlOOH. At ambient conditions it is composed of highly distorted FeO₆ octahedra linked together by sharing edges to form infinite bands. The bands are connected via shared octahedra vertices that results in infinite channels parallel to the b axis. Hydrogen bonds are located inside the channels (Figure 4.3.1-1a).

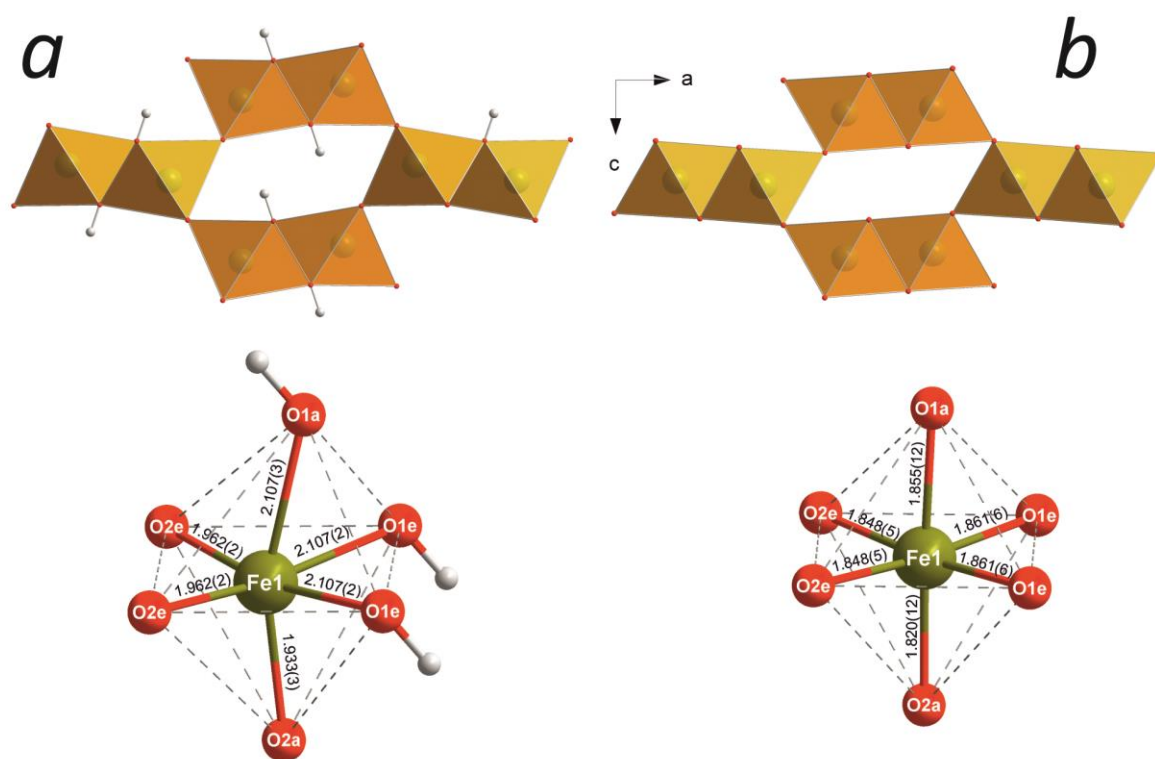


Figure 4.3.1-1 Crystal structure of α -FeOOH as well as FeO₆H₃ octahedra at ambient pressure (a) and at 47.6(2) GPa (b). There are two independent oxygen sites: O1, at ambient conditions covalently bound to hydrogen (O-H bond), and O2, characterized by a weak H...O bond; in the selected octahedron one can distinguish O1a and O2a atoms in the axial position and two O1e and two O2e atoms in the equatorial position. The octahedral FeO₆H₃ moiety is highly distorted at ambient pressure (a); and becomes regular above the transition pressure (b).

We applied methods of single-crystal XRD to study compressibility and follow structural changes in mineral goethite (Figure 4.3.1-2). Upon the compression to 44 GPa, the lattice parameters and the unit cell volume of FeOOH gradually decrease (Figure 4.3.1-2a). A close examination of a dependence of a normalized stress versus Eulerian strain, $P_N(f_E)$ and $V(P)$ shows that at $P > 16$ GPa the elastic properties change. Up to 16 GPa the O1...O2 distances, involved in the hydrogen bond and located across channels formed by octahedra (Figure 4.3.1-1), decrease much more rapidly than the Fe–O distances. At ~16 GPa the compressibility of the O1–H...O2 bond decreases sharply and becomes comparable to the compressibility of the Fe–O bonds (Figure 4.3.1-2b). This indicates that up to 16 GPa, similar to isostructural α -AlOOH [140], bulk compression takes place through contraction of the channels, involving shortening of the hydrogen bonds, rather than slimming down of the FeO₆ octahedra [82]. Distorted FeO₆ octahedra demonstrate a clear trend to symmetrization under compression, which is nevertheless far from complete at ~44 GPa.

At ~45 GPa an isostructural phase transition takes place manifested by a drastic reduction of the molar volume (by ~11 %), and vanishing of the Raman modes. Within the experimental errors the transition is reversible upon decompression with no obvious signs of hysteresis (Figure 4.3.1-2a). Mössbauer spectroscopy detects HS→LS spin crossover which is supported by theoretical

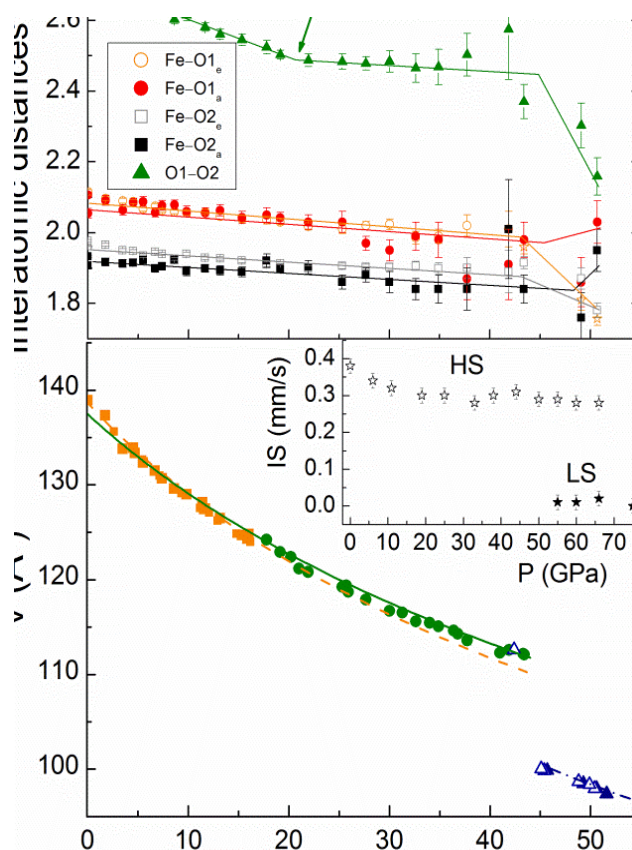


Figure 4.3.1-2 Dependence on pressure of unit cell volume (a) and interatomic distances (b) as revealed by *in situ* single-crystal X-ray diffraction. The arrow (b) marks a change in pressure dependency of the O1-O2 distances at ~20 GPa. The inset (a) shows the pressure dependence of the isomer shift obtained from Mössbauer spectroscopy. Filled are for compression studies, open symbols are for decompression.

calculations and single-crystal XRD. Electrical resistivity drops by 5 orders of magnitude but FeOOH remains a semiconductor.

The high-pressure phase is characterized by significantly shorter O1...O2 distances, the same as measured in ice-X at 145 GPa where the symmetrization of the hydrogen bond has been reported [80]. Furthermore, the distortion of $\text{Fe}(\text{O}\cdots\text{H})_3(\text{O}-\text{H})_3$ moiety is strikingly reduced (Figure 4.3.1-2b) with the O1_a-Fe-O2_a angle approaching 180° and nearly equal $\langle\text{Fe}-\text{O2}\rangle$ and $\langle\text{Fe}-\text{O1}\rangle$ bond lengths. The exact position of the hydrogen atom cannot be directly determined from XRD data, but the interatomic distance of the hydroxyl and the O...H species can be derived using the *valence bond* rule and the experimentally measured atomic positions of iron and oxygen providing a strong evidence for a symmetric hydrogen bond in the high-pressure FeOOH phase. This H-bonds symmetrization is induced by the spin crossover, which converts the largely asymmetric polyhedra of into an axially symmetric orthorhombic octahedra, accompanied by a ~11 % volume collapse.

4.3.2. High-pressure high-temperature behavior of Fe₂O₃ and Fe₃O₄

High-pressure behavior of hematite, $\alpha\text{-Fe}_2\text{O}_3$ and magnetite, Fe_3O_4 , was studied very intensively due to their significance in condensed matter and mineral physics. Despite 50 years of research involving powder XRD, Mössbauer and Raman spectroscopy, electrical resistivity measurements etc. under HPHT conditions many unresolved problems remained. The crystal structures of high-pressure polymorphs of Fe_2O_3 and Fe_3O_4 appearing above 50 and 20 GPa, respectively are subjects of debates [89,91–94,97]. The phase diagram of Fe_2O_3 at megabar pressure range is incomplete and the data are often conflicting [88,99–101].

At ambient conditions magnetite, Fe_3O_4 , has a cubic crystal structure of inverse spinel ($Fm\bar{3}m$). Our single-crystal XRD data allowed us to finally establish the crystal structure of high-pressure polymorph to have CaTi_2O_4 structural type ($Bbmm$, $a = 9.309(3)$, $b = 9.282(2)$, and $c = 2.6944(9)$ Å ($R_1(\text{all data}) = 6.91\%$ at 44.3(5) GPa). The crystal structure is composed of FeO₆ octahedra and trigonal prisms (Figure 4.3.2-1). Laser heating of *HP*- Fe_3O_4 at 2350(100) K and pressures up to 50 GPa does not result in any chemical or structural modifications. In addition, we identified

Building blocks:

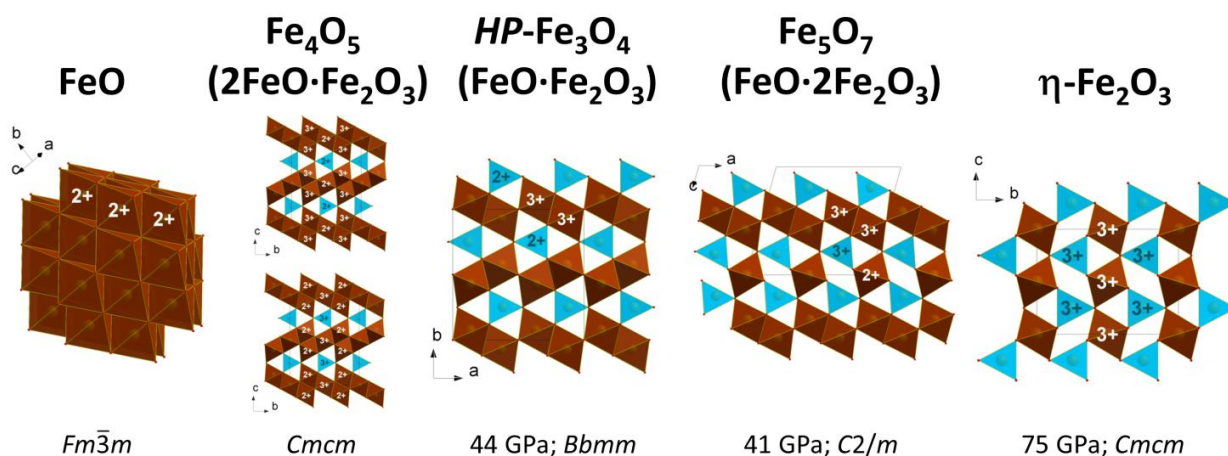
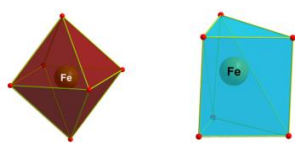


Figure 4.3.2-1 Homological series of iron oxides described by the common formula $nFeO \cdot mFe_2O_3$. The structures may be described as constructed from two building blocks: FeO_6 octahedra and trigonal prisms. “2+” and “3+” represent the charges of iron ions.

reflections belonging to $HP\text{-}Fe_3O_4$ in the products of thermal decomposition of siderite, $FeCO_3$ (70(1) GPa and 2400(100)). Thus, our experimental results show that $HP\text{-}Fe_3O_4$ may exist to depths of at least 2000 km.

Hematite, $\alpha\text{-}Fe_2O_3$ adopts rhombohedral crystal structure of corundum, Al_2O_3 (Figure 4.3.2-2a). In agreement with previous studies [94,95,97,98], our cold compression experiments of hematite single crystals to 54(1) GPa results in a transition to a $\zeta\text{-}Fe_2O_3$ phase manifested by a ~ 8.4 % volume discontinuity. According to single-crystal XRD data $\zeta\text{-}Fe_2O_3$ possess with distorted $GdFeO_3$ perovskite ($Pbnm$) with monoclinic or triclinic unit cell (Figure 4.3.2-2c). At 67(1) GPa a small drop in the unit cell volume (~ 1.7 %) manifests the next transformation to the novel $\theta\text{-}Fe_2O_3$ phase (Figure 4.3.2-2e) with an orthorhombic symmetry ($Aba2$, $a = 4.608(7)$, $b = 4.730(4)$, $c = 6.682(18)$ Å ($R_1(\text{all data}) = 10.55$ % at 73.8(7) GPa). On compression at ambient temperature $\theta\text{-}Fe_2O_3$ can be observed to at least 100 GPa.

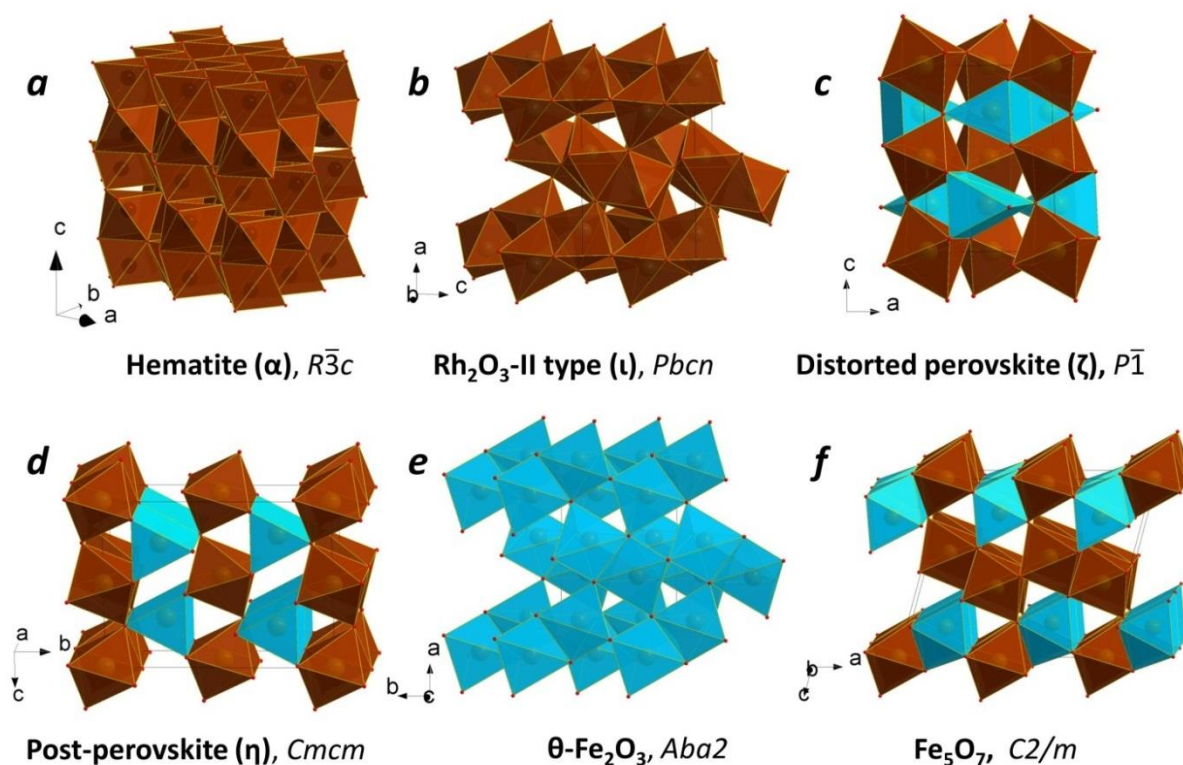


Figure 4.3.2-2 Crystal structures of hematite, HP polymorphs of Fe_2O_3 and a new compound, Fe_5O_7 , studied in the present work by single-crystal XRD. Building blocks are octahedra (brown) and trigonal prisms (blue).

In situ laser heating of $\theta\text{-Fe}_2\text{O}_3$ above 1600(50) K results in the formation of a post-perovskite PPv type $\eta\text{-Fe}_2\text{O}_3$ (Figure 4.3.2-2d). Once synthesized, $\eta\text{-Fe}_2\text{O}_3$ may be preserved at ambient temperature down to at least 26 GPa. At lower pressures it transforms back to hematite. Moderate heating to ~ 2000 K at pressures of about 50 GPa provokes a transition to the dPv $\zeta\text{-Fe}_2\text{O}_3$ phase. Decompression of $\zeta\text{-Fe}_2\text{O}_3$ or $\eta\text{-Fe}_2\text{O}_3$ to 41(1) GPa with heating at 1800(100) K results in a growth of Rh_2O_3 -II type $\iota\text{-Fe}_2\text{O}_3$ (Figure 4.3.2-2b). Interestingly, $\iota\text{-Fe}_2\text{O}_3$ was synthesized earlier [101,102] from hematite, thus bracketing the possible P - T stability field of the phase.

The behavior of $\eta\text{-Fe}_2\text{O}_3$ under heating is rather remarkable. Firstly, we noted that its unit cell volume increases by up to 1 % upon laser heating to about 2000 K at ~ 56 GPa and 64 GPa. Secondly, after heating for a few seconds to 2700–3000 K and 71 GPa we observed a novel mixed-valence iron oxide Fe_5O_7 ($\text{FeO}\cdot 2\text{Fe}_2\text{O}_3$) crystallized in a monoclinic $C2/m$ space group ($a =$

9.208(7), $b = 2.7327(10)$, $c = 8.270(5)$ Å and $\beta = 105.50(8)^\circ$, R_1 (all data) = 6.77 % at 40.7(3) GPa, Figure 4.3.2-2f). Thus, we explain our observations as a continuous loss of oxygen by $\eta\text{-Fe}_2\text{O}_3$ upon heating at moderate temperatures and pressures above ~ 60 GPa, according to the reaction $\eta\text{-Fe}_2\text{O}_3 \rightarrow \eta\text{-Fe}_{2-6}\text{O}_3 + 0.5\delta\text{-O}_2$. The reaction is accompanied by a partial reduction of Fe^{3+} to larger-sized Fe^{2+} that consequently increases the unit cell volume. Upon heating at sufficiently high temperature (above ~ 2700 K), the oxygen deficiency in $\eta\text{-Fe}_2\text{O}_3$ reaches a critical limit and provokes a reconstructive phase transition resulting in the formation of the mixed-valence iron oxide Fe_5O_7 : $5\eta\text{-Fe}_2\text{O}_3 \rightarrow 2\text{Fe}_5\text{O}_7 + 0.5\text{O}_2$.

Similarities in the crystal structures of $\eta\text{-Fe}_2\text{O}_3$, Fe_5O_7 , $HP\text{-Fe}_3\text{O}_4$, and a recently discovered Fe_4O_5 [141] demonstrate [142] that iron oxide phases form a homological series $n\text{FeO} \cdot m\text{Fe}_2\text{O}_3$ (with wüstite, FeO and $\eta\text{-Fe}_2\text{O}_3$ as the end-members), so that potentially other mixed-valence iron oxides may be found under pressure temperature conditions of the lower mantle (Figure 4.3.2-1).

Our results clearly demonstrate the complex experience of iron oxides subjected to high pressures and temperatures (Figure 4.3.2-3). Fe_2O_3 and Fe_3O_4 transferred into the deep Earth's interior by subduction of BIFs [85]. Upon subduction into the lower mantle, hematite undergoes numerous phase transformations. At pressures above ~ 60 GPa the HP phase $\eta\text{-Fe}_2\text{O}_3$ starts to decompose, producing oxygen. Based on estimates of the amount of BIFs subducted into the Earth's mantle [85], the amount of oxygen produced by the formation of Fe_5O_7 can vary from 2 to 8 masses of oxygen in the modern atmosphere.

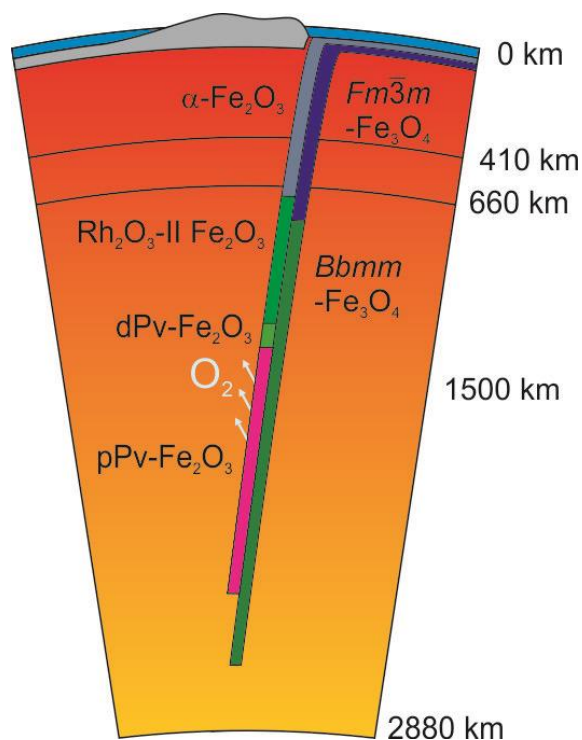


Figure 4.3.2-3 Possible consequence of phase transitions of Fe_2O_3 and Fe_3O_4 in a BIF subducted to the lower mantle.

4.4. List of manuscripts and statement of author's contribution

[1] Bykova, E., Parakhonskiy, G., Dubrovinskaia, N., Chernyshov, D. & Dubrovinsky, L. The crystal structure of aluminum doped β -rhombohedral boron. *J. Solid State Chem.* **194**, 188–193 (2012).

G. Parakhonskiy synthesized the sample and performed chemical analysis. E. Bykova (EB) selected the single-crystal, maintained synchrotron single-crystal XRD experiment (with D. Chernyshov) and analyzed the XRD data. EB, N. Dubrovinskaia (ND) and L. Dubrovinsky (LD) interpreted the results and wrote the manuscript with contributions of all authors. EB made 80% contribution in the paper.

[2] Gou, H., Tsirlin, A. A., Bykova, E., Abakumov, A. M., Van Tendeloo, G., Richter, A., Ovsyannikov, S. V., Kurnosov, A. V., Trots, D. M., Konôpková, Z., Liermann, H.-P., Dubrovinsky, L. & Dubrovinskaia, N. Peierls distortion, magnetism, and high hardness of manganese tetraboride. *Phys. Rev. B* **89**, 064108 (2014).

HG conducted all synthesis experiments, analysed all samples and performed theoretical calculations. A.A. Tsirlin (AAT) performed magnetic susceptibility measurements. A. M. Abakumov (AMA) and G. Van Tendeloo (GVT) performed the TEM analysis. EB selected the single-crystal, collected and analyzed single-crystal XRD at ambient conditions; high-pressure powder XRD was collected by S.V. Ovsyannikov (SVO), A.V. Kurnosov, D.M. Trots (DMT), Z. Konôpková (ZK), H.-P. Liermann (HPL) and analyzed by SVO and DMT. A. Richter (AR) conducted nanoindentation measurements. ND, HG and LD interpreted the results and wrote the manuscript with contributions of all authors. EB contributed 100% in single crystal diffraction studies and 40% in the whole work.

[3] Bykova, E., Tsirlin, A. A., Gou, H., Dubrovinsky, L. & Dubrovinskaia, N. Novel non-magnetic hard boride Co_5B_{16} synthesized under high pressure. *J. Alloys Compd.* **608**, 69–72 (2014).

HG conducted all synthesis experiments, analysed all samples and performed theoretical calculations. EB selected the single-crystal, collected and analyzed the single-crystal XRD data. A.A. Tsirlin performed magnetic susceptibility measurements. ND, EB, and LD interpreted the

results and wrote the manuscript with contributions of all authors. EB made 80% contribution in the paper.

[4] Bykova, E. A., Bobrov, A. V., Sirotkina, E. A., Bindi, L., Ovsyannikov, S. V., Dubrovinsky, L. S. & Litvin, Y. A. X-ray single-crystal and Raman study of knorringite, $\text{Mg}_3(\text{Cr}_{1.58}\text{Mg}_{0.21}\text{Si}_{0.21})\text{Si}_3\text{O}_{12}$, synthesized at 16 GPa and 1,600 °C. *Phys. Chem. Miner.* **41**, 267–272 (2013).

A.V. Bobrov (AVB) and SVO synthesized the sample. AVB collected and analyzed Raman spectra. AVB and E.A. Sirotkina performed chemical analysis. EB maintained the single-crystal XRD experiment; EB, AVB and L. Bindi analyzed the single-crystal XRD data. AVB, EB, LD and Y.A. Litvin interpreted the results and wrote the manuscript with contributions of all authors. EB made 80% contribution in the paper.

[5] Sinmyo, R., Bykova, E., McCammon, C., Kупenko, I., Potapkin, V. & Dubrovinsky, L. Crystal chemistry of Fe^{3+} -bearing (Mg, Fe) SiO_3 perovskite: a single-crystal X-ray diffraction study. *Phys. Chem. Miner.* **41**, 409–417 (2013).

R. Sinmyo (RS) synthesized Fe^{3+} -bearing (Mg, Fe) SiO_3 perovskite and performed chemical analysis. EB maintained the single-crystal XRD experiment; RS, LD and EB analyzed single-crystal XRD data. RS, I. Kупenko (IK), V., Potapkin, C. McCammon (CMC) and LD collected and analyzed synchrotron Mössbauer spectra. RS, CMC and LD interpreted the results and wrote the manuscript with contributions of all authors. EB contributed 80% in single crystal diffraction studies and 40% in the whole work.

[6] Gou, H., Dubrovinskaia, N., Bykova, E., Tsirlin, A. A., Kasinathan, D., Schnelle, W., Richter, A., Merlini, M., Hanfland, M., Abakumov, A. M., Batuk, D., Van Tendeloo, G., Nakajima, Y., Kolmogorov, A. N. & Dubrovinsky, L. Discovery of a superhard iron tetraboride superconductor. *Phys. Rev. Lett.* **111**, 157002 (2013).

LD, ND and A.N. Kolmogorov conceptualized the work. LD and ND planned and coordinated the study. HG conducted all synthesis experiments and analysed all samples; EB analysed all single crystal X-ray diffraction data; AAT and D. Kasinathan performed magnetic susceptibility

measurements; experiments in DAC were carried out by EB, M. Merlini, M. Hanfland (MH), LD and ND; AMA, D. Batuk, GVT performed the TEM analysis; AR conducted nanoindentation measurements. Y. Nakajima took part in multi-anvil synthesis experiments. The paper was prepared by ND with contributions of all authors. EB contributed 80% in single crystal diffraction studies and 40% in the whole work.

[7] Bykova, E., Gou, H, Bykov, M., Hanfland, M., Dubrovinskaia, N., Dubrovinsky, L. Crystal structures and compressibility of novel iron borides Fe_2B_7 and Fe_xB_{50} synthesized at high pressure and high temperature. *Prepared for submission in J. Solid State Chemistry*.

HG conducted all synthesis experiments and analysed all samples. EB selected the single-crystals and analyzed all XRD data. M. Bykov (MB), EB, LD and MH maintained high-pressure single-crystal XRD experiments. EB, ND and LD interpreted the results and wrote the manuscript. EB made 80% contribution in the paper.

[8] Xu, W., Greenberg, E., Rozenberg, G. K., Pasternak, M. P., Bykova, E., Boffa-Ballaran, T., Dubrovinsky, L., Prakapenka, V., Hanfland, M., Vekilova, O. Y., Simak, S. I. & Abrikosov, I. A. Pressure-induced hydrogen bond symmetrization in iron oxyhydroxide. *Phys. Rev. Lett.* **111**, 175501 (2013).

LD provided the crystals. EB selected crystals for high-pressure experiments and collected Raman data under compression; EB and T.Boffa-Ballaran analysed all single crystal X-ray diffraction data; single-crystal XRD experiments in DACs were carried out by EB, LD, MH and V. Prakapenka (VP). W. Xu, E. Greenberg, G.K. Rozenberg (GKR) and M.P. Pasternak (MPP) collected Mössbauer spectra, performed electrical resistivity studies and analyzed the data. O.Y. Vekilova, S. I. Simak and I. A. Abrikosov performed the theoretical calculations. LD, GKR, MPP and EB interpreted the results and wrote the manuscript with contributions of all authors. EB contributed 90% in single crystal diffraction studies and 40% in the whole work.

[9] Bykova, E., Bykov, M., Prakapenka, V., Konôpková, Z., Liermann, H.-P., Dubrovinskaia, N. & Dubrovinsky, L. Novel high pressure monoclinic Fe_2O_3 polymorph revealed by single-crystal synchrotron X-ray diffraction studies. *High Press. Res.* **33**, 534–545 (2013).

[10] Bykova, E., Dubrovinsky, L., Dubrovinskaia, N., Bykov, M., McCammon, C., Ovsyannikov, S.V., Liermann, H.-P., Kuppenko, I., Chumakov, A.I., Rüffer, R., Hanfland, M., Prakapenka, V. Fate of banded iron formations subducted into the lower mantle. *Submitted in Nat. Geosci.*

V. Results

5.1. The crystal structure of aluminum doped β -rhombohedral boron

E. Bykova^{1,2}, G. Parakhonskiy^{1,2}, N. Dubrovinskaia², D. Chernyshov³, L. Dubrovinsky¹

¹*Bayerisches Geoinstitut, Universität Bayreuth, Universitätsstraße 30, D-95440 Bayreuth, Germany*

²*Materialphysik und Technologie, Lehrstuhl für Kristallographie, Physikalisches Institut, Universität Bayreuth, Universitätsstraße 30, D-95440 Bayreuth, Germany*

³*Swiss-Norwegian Beam Line, ESRF, F-38043 Grenoble Cedex, France*

J. Solid State Chem. **194**, 188–193 (2012)

5.1.1. Abstract

A crystal structure of aluminum doped β -rhombohedral boron was studied by single-crystal X-ray diffraction at 80 K. The crystals were synthesized using high-pressure high temperature technique at 3 GPa and 2100 K. The structure is based on three-dimensional framework made of B_{12} icosahedra with voids occupied by the B_{28} –B– B_{28} units, it has the $R\bar{3}m$ space group with $a = 10.9014(3)$, $c = 23.7225(7)$ Å lattice dimensions in hexagonal setting. Aluminum atoms are located in $A1$ and D special positions of the β -B structure with occupancies of 82.7(6) % and 11.3(4) %, respectively. Additional boron atoms are located near the D -site. Their possible distribution is discussed. Finally we have found two appropriate structural models whose refinement suggests two possible chemical compositions, $AlB_{44.8(5)}$ and $AlB_{37.8(5)}$, which are in a good agreement with the chemical analysis data obtained from EDX. The crystal structure of $AlB_{44.8(5)}$ is described in detail.

5.1.2. Introduction

Boron compounds are widely used as engineering materials (dielectrics, B-doped semiconductors), superhard materials (cBN, boron carbide), reinforcing chemical additives, for example, for obtaining special glass or corrosion- or heat-resistant alloys [143], and superconducting materials (ex., MgB_2 [144]). Numerous boron-rich compounds adopt structures of pure crystalline boron polymorphs, α - and β - rhombohedral boron [26,27]. As

noted in [27], binary compounds of B with elements of main groups (C, Si, N, P, As, O, S, Se) usually have structures based on that of α -B. The structure of β -B, having many voids of various kinds and sizes, can adopt different dopants, such as elements of main groups (Li, Mg, Al, Si, Ge) and transition metals (Cr, Cu, Fe, Mn, Ni, Sc, V, Zn, Zr). The dependence of the atomic size of a possible dopant on a type of the occupied void was previously reviewed in [28,29]. It was shown that doping of β -B by transition metals and some other elements, such as Al, Si, and Ge, leads to increase microhardness of β -B [29] and change of its electrical properties [30].

According to the Al-B phase diagram, maximal Al solubility in β -B is 3 at. % and it is temperature independent between 600 and 2100 K [31]. The number of stable stoichiometric Al-borides is still under question. Duschanek *et al.* [31] and later Mirkovic *et al.* [145] supposed only AlB_2 and $\alpha\text{-AlB}_{12}$ to be stable borides. Al_2B_3 , $\beta\text{-AlB}_{12}$, $\gamma\text{-AlB}_{12}$ and AlB_{10} described earlier were believed to be impurity stabilized or metastable. Later it was shown that AlB_2 is non-stoichiometric due to defects in aluminum positions which result in chemical composition close to $\text{Al}_{0.9}\text{B}_2$ [146]. The crystal structure of $\text{Al}_{0.9}\text{B}_2$ is different from that of other aluminum borides: it has the $P6/mmm$ space group and contains layers of boron and aluminum atoms alternating along the c -axis. The crystal structure of AlB_{10} is based on a three-dimensional framework consisting of B_{12} icosahedra and Al atoms located in the voids [147]. The framework of the $\alpha\text{-AlB}_{12}$ structure includes additional B_{19} units formed by two B_{12} icosahedra, each one with a vacant vertex, which share a common triangular face [148]. According to [149], $\gamma\text{-AlB}_{12}$ contains similar B_{20} units in which only one apex is vacant. The Al atoms are located in the vacancies of the boron framework.

Current work presents the refinement of the β -B-type crystal structure of an aluminum boride, $\text{AlB}_{44.8(5)}$. The only one reference to a structural study of an aluminum boride with the similar β -B-type structure, AlB_{31} , we could find was that to Higashi *et al.* [126]. It will be discussed below in detail.

The crystal structure of β -B has been a subject of a long-standing dispute regarding the number of crystallographically independent positions and the occupancies of different boron sites [150–154]. The β -B has the space group $R\text{-}3m$ and the unit cell parameters (in hexagonal setting) of $a = 10.932(2)$ and $c = 23.819(5)$ Å [152]. Modern view on the structure of β -B is based on the

work by Slack *et al.* [152]. They performed the single crystal X-ray diffraction and independent density measurements suggesting 320.1 atoms per a unit cell distributed over 20 independent positions including partially occupied and interstitial ones. The crystal structure consists of B_{12} icosahedra, B_{28} - B - B_{28} units and interstitial B atoms. In our work on studying the crystal structure of an aluminum boride we followed the numbering scheme for B atoms used by several authors [151–153]. Namely, we considered two types of B_{12} icosahedra, distorted due to the Jahn-Teller effect, with different B atoms as asymmetric parts: B(5) and B(6) (type A) and B(1), B(2), B(7), and B(9) (type B) (Figure 5.1.2-1a). Three icosahedra of the B-type and one icosahedron of the A-type tend to form a tetrahedron (Figure 5.1.2-1a) linked with its closest three neighbors that results in a “porous” three-dimensional framework shown in Figure 5.1.2-1b. According to [149], the framework could also be described in terms of Kagomé nets of icosahedra (Figure 5.1.2-1c) stacked along the *c*-direction and shifted in respect of each other by a translation of $1/3(\mathbf{b} - \mathbf{a})$. The opposite triangles of the adjacent Kagomé nets form voids which allocate additional B_{12} icosahedra of the A-type. Other bulky vacancies of the framework include two B_{28} units (Figure 5.1.2-1d) connected via the B(15) atom, while the whole fragment is directed along the *c*-axis. Each B_{28} unit comprised of three B_{12} icosahedra associated by sharing triangular faces has B(3), B(4), B(8), B(10), B(11), B(12), B(13), and B(14) atoms in the asymmetric part (Figure 5.1.2-1e). Possible atomic interstitial positions were first described by Andersson *et al.* [155] and designated as A1, A2, A3, D, E, F1, F2 and G. Later, Slack *et al.* [152] refined these positions and introduced additional ones designated as J1 through J7. According to [152], the interstitial B atoms B(16), B(19) and B(20) filled J2, J3 and J4 sites with respective occupancies of 27.2(2), 6.8(9) and 3.7(4) %. Bonded B(17) and B(18) atoms with occupancies of 8.5(9) and 6.6(6) %, respectively, were both located in the (1 1 0) plane and occupied the sites near B(15) between the two B_{28} units. The presence of interstitial atoms between B_{28} units resulted in the position of the B(13) atom to be usually partially occupied. The occupancy of B(13) in pure β -B and in metal-doped β -B, according to [152], varies from 63 for a Zr-doped compound to 77 % for pure β -B. Therefore composition of the “ B_{28} ” unit is close to B_{27} .

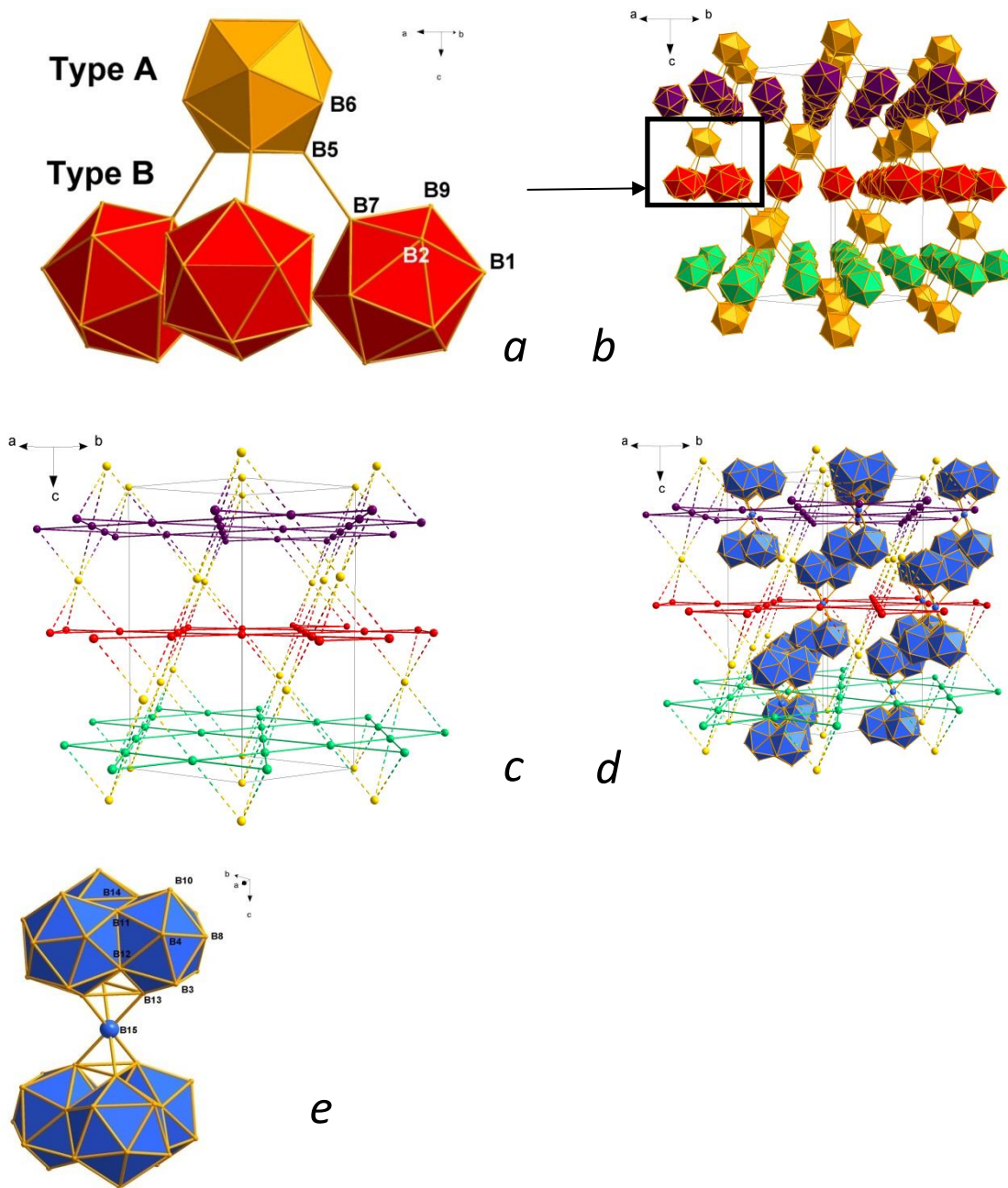


Figure 5.1.2-1 Graphical representation of the rhombohedral β -B crystal structure: (a) two types of B_{12} icosahedra (type A and type B); (b) “porous” three-dimensional framework formed by icosahedra; (c) the same framework visualized as the Kagomé nets of icosahedra stacked along the c direction and shifted in respect of each other by a translation of $1/3(\mathbf{b} - \mathbf{a})$. The nodes of the Kagomé nets given in different colors represent the centers of icosahedra. The opposite triangles of the adjacent Kagomé nets form voids which allocate additional B_{12} icosahedra of the A-type, whose centers are shown as yellow balls. (d) B_{28} units located in the voids of the framework; (e) enlarged two B_{28} units connected via the B(15) atom.

5.1.3. Experimental

Sample preparation and chemical analysis

Aluminum boride crystals formed in one of our experiment on studying pressure-temperature (PT) phase diagram of boron [26]. The experiment was carried out using a piston cylinder apparatus [156]. The pressure was generated by squeezing the cylindrical cell placed inside a WC core of a steel bomb (a cross-section is shown in Figure 5.1.3-1). A pure crystalline β -B powder (Chempur Inc., 99.995 at. % purity, grain size less than 1 mm) was used as an initial material and loaded into a Pt capsule with a diameter of 5 mm and a height of 10

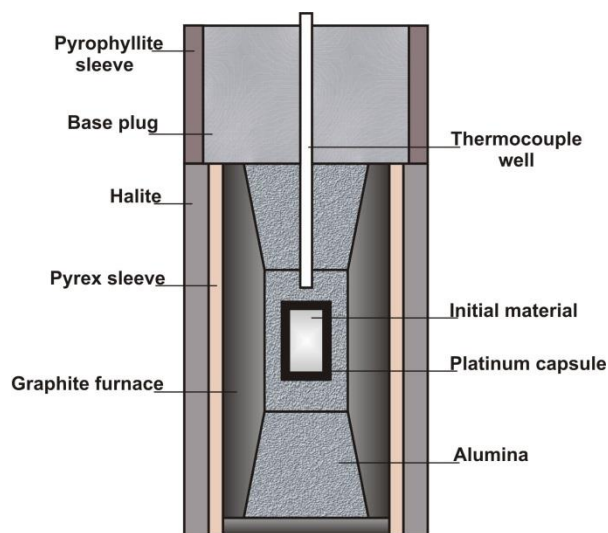


Figure 5.1.3-1 Experimental setup for high-T and high-P synthesis of β -B.

mm. The capsule was placed into a corundum Al_2O_3 cylinder served as a thermal insulator, and the cylinder was surrounded by a graphite heater. Temperature was increased stepwise at a speed of about 100 K/min. The experiment was performed at 3.0(3) GPa and 2100(50) K. The sample was heated during 5 minutes and then quenched by switching off the power supply. Upon heating Pt capsule melted and boron reacted with corundum forming aluminium boride. After extraction from the capsule, the sample was cut into several discs. The crystal selected from an edge of a disc was a black thin plate with dimensions of $0.10 \times 0.08 \times 0.01 \text{ mm}^3$. According to the powder X-ray diffraction data, besides aluminium boride crystals the sample contained not reacted polycrystalline β -B, Pt and PtB.

Examination of the crystal by the electron dispersive X-ray spectroscopy (LEO 1530 VP Gemini scanning electron microscope) gave 3(1) at. % of the aluminum content in the structure, which is in a good agreement with 2.2(1) at. % Al in $\text{AlB}_{44.8(5)}$ or 2.6(1) at. % in $\text{AlB}_{37.84(5)}$, as deduced due to the crystal structure refinement of the appropriate models (see below). According to the Al–B phase diagram [31], the composition obtained appears within the field of limited solubility of Al in β -B.

Single-crystal XRD

Single-crystal X-ray diffraction data of the aluminum boride were collected using a six-circle KUMA6 diffractometer ($\lambda = 0.6953 \text{ \AA}$) equipped with a Titan CCD detector at the Swiss-Norwegian beam line BM01A of the European Synchrotron Radiation Facility (ESRF). The temperature was maintained at 80 K during the experiment with a N_2 -gas stream cooling device (Oxford Cryosystems Cryostream). The reflection intensities were measured by omega-scanning of narrow (0.5°) frames. The data we present were collected only up to $\sin\theta/\lambda = 0.666 \text{ \AA}^{-1}$. As a result, the observed correlations between ADPs and occupancies are 0.750 ($U_{11}(\text{B}(16))$), 0.701 ($U_{11}(\text{Al}(2))$), 0.566 ($U_{11}(\text{Al}(1))$), 0.556 ($U_{22}(\text{Al}(2))$) and 0.518 ($U_{11}(\text{B}(13))$). The data collection and further integration were performed with CrysAlis CCD [157] and CrysAlis RED [158] software, respectively. The software used to process the data also accounts the beam intensity as a function of time, Lorentz, polarization, flat field of the detector, geometrical distortions and oblique correction. The absorption corrections were applied empirically by the SADABS program [159,160]. SADABS scaling and absorption correction was used due to the small size of the inspected crystal that makes difficult the precise face indexing. The structure was solved by the direct method and refined by full matrix least-squares in the anisotropic approximation for all atoms excluding B(16) (see further) using SHELXTL software [161]. The X-ray experiment details and crystallographic characteristics are presented in Table 5.1.4-1 and Table 5.1.4-2. The DIAMOND software [162] was used to create molecular graphics.

5.1.4. Results and discussion

The structure of rhombohedral β -B proposed in [152] (excluding B(16)–B(20) B atoms) was used by us as a starting model for the solution of the aluminum boride crystal structure. After refinement a strong residual electron density peak $Q(1) \sim 28 \text{ e/\AA}^3$ appeared to be in the A1 site (located in the center of the tetrahedron shown in Figure 5.1.2-1a) and further was assigned as Al(1) atom that sharply decreased $R_1(wR_2)$ values. The occupancy of the A1 position by the aluminum atom (82.7(6) %) is slightly lower than 85.7(4) % obtained by Higashi *et al.* [126] for AlB_{31} . The next cycle of refinement also revealed additional two residual electron density peaks.

Table 5.1.4-1 Crystal data and structure refinement for $\text{AlB}_{44.8(5)}$.

Empirical formula	$\text{Al}_7\text{B}_{313.40}$
Formula weight (g/mol)	3576.71
Temperature (K)	80(2)
Wavelength (Å)	0.69530
Crystal system	Trigonal
Space group	$R\bar{3}m$
a (Å)	10.9014(3)
c (Å)	23.7225(7)
V (Å³)	2441.5(1)
Z	1
Calculated density (g/cm³)	2.433
Linear absorption coefficient (mm⁻¹)	0.151
$F(000)$	1658
Crystal size (mm³)	0.10 x 0.06 x 0.01
Theta range for data collection (deg.)	2.27 to 27.59
Completeness to theta = 27.59°	100.0 %
Index ranges	-11 < h < 14, -14 < k < 13, -31 < l < 31
Reflections collected	7796
Independent reflections / R_{int}	788 / 0.0629
Max. and min. transmission	0.9985 and 0.9851
Refinement method	Full matrix least squares on F^2
Data / restraints / parameters	788 / 0 / 113
Goodness of fit on F^2	1.081
Final R indices [$I > 2\sigma(I)$]	$R_1 = 0.0378$, $wR_2 = 0.1021$
R indices (all data)	$R_1 = 0.0509$, $wR_2 = 0.1099$
Largest diff. peak and hole (e / Å³)	0.456 and -0.371

Table 5.1.4-2 Atomic coordinates, positions, occupancy values and equivalent isotropic displacement parameters for $\text{AlB}_{44.8(5)}$.

Atom	Position	Occupancy	<i>x</i>	<i>y</i>	<i>z</i>	$U_{\text{eq}}^a, \text{\AA}^2$
Al(1)	6c	0.827(6)	0	0	0.8653(1)	0.005(1)
Al(2)	18h	0.113(4)	0.2071(5)	0.414(1)	0.1758(3)	0.030(3)
B(1)	36i	1	0.1772(2)	0.1768(2)	0.1773(1)	0.008(1)
B(2)	36i	1	0.3187(2)	0.2953(2)	0.1288(1)	0.008(1)
B(3)	36i	1	0.2617(2)	0.2178(2)	0.4196(1)	0.008(1)
B(4)	36i	1	0.2358(2)	0.2516(2)	0.3469(1)	0.008(1)
B(5)	18h	1	0.0549(1)	0.1097(3)	0.9446(1)	0.007(1)
B(6)	18h	1	0.0861(1)	0.1723(3)	0.0134(1)	0.007(1)
B(7)	18h	1	0.1110(1)	0.2220(3)	0.8875(1)	0.008(1)
B(8)	18h	1	0.1698(1)	0.3396(3)	0.0283(1)	0.008(1)
B(9)	18h	1	0.1291(1)	0.2582(3)	0.7662(1)	0.008(1)
B(10)	18h	1	0.1020(1)	0.2039(3)	0.6981(1)	0.007(1)
B(11)	18h	1	0.0563(1)	0.1126(3)	0.3268(1)	0.008(1)
B(12)	18h	1	0.0900(1)	0.1800(3)	0.3989(1)	0.009(1)
B(13)	18h	0.700(1)	0.0580(2)	0.1160(4)	0.5543(1)	0.009(1)
B(14)	6c	1	0	0	0.3859(2)	0.008(1)
B(15)	3b	1	0	0	0.5	0.020(2)
B(16)	36i	0.106(7)	0.1542(15)	0.1870(16)	0.5000(6)	0.005(4) ^b

^a U_{eq} is defined as one third of the trace of the orthogonalized U^{ij} tensor.

^b B(16) position has been refined in isotropic approximation

The first peak with $Q(3) \sim 1.5 \text{ e/\AA}^3$, located in the vicinity of the *D*-site at the 36i (0.1542(15), 0.1870(16), 0.5000(6)) position, was assigned as partially occupied by the B atom marked as B(16) based on taking into account the interatomic distance $Q(3)\text{--}B(15) = 1.885(15) \text{ \AA}$. The refinement assuming that $Q(3)$ is partly occupied by Al gave approximately the same $R(R_w)$ values of 3.74(10.86) % but was inconsistent with the bond length. The mirror plane which coincides with (1 1 0) and passes through the B(15) atom splits B(16) over two positions (Figure 5.1.4-1). Unfortunately, any attempts to refine B(16) in anisotropic approximation were failed most likely due to the low occupancy of the position (10.6(7) %).

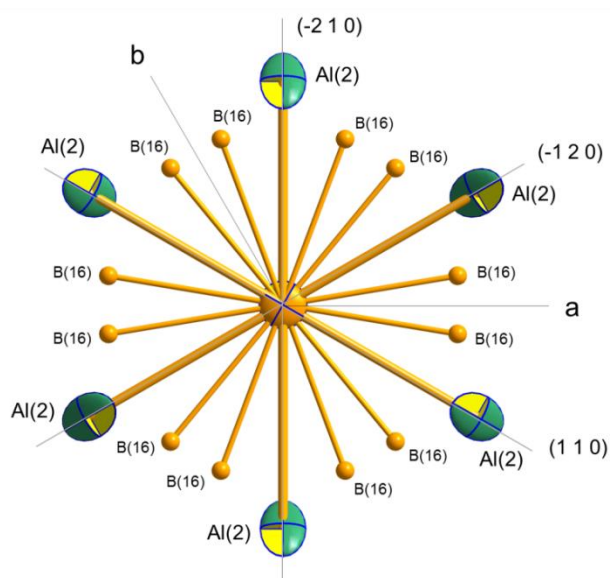


Figure 5.1.4-1 The atomic distribution near the B(15) atom (non-labeled atom in the center of the picture) shown along the c axis. Anisotropic displacement ellipsoids for Al(2) (D -site) and B(15) are shown with 50 % probability level. The mirror plane with Miller indices (1 1 0) and related to it (-1 2 0) and (-2 1 0) generated by the 3-fold rotation-inversion axis parallel to the c axis splits the position of B(16) over two sites.

The second peak $Q(2)$ of $3.5 \text{ e}/\text{\AA}^3$ was located at the D -site at the $18h$ (0.2071(5), 0.414(1), 0.1758(3)) position. The $Q(2)$ –B(15) distance appeared to be 2.393(9) Å which is close to Al–B distances in aluminum borides. For instance, in hexagonal $\text{Al}_{0.9}\text{B}_2$ they were found to be 2.3782(3) and 2.3784(3) Å [146] and in the tetragonal $\alpha\text{-AlB}_{12}$ the corresponding distances varied from 2.02(5) to 2.98(13) Å [148]. Therefore $Q(2)$ was assigned as partly occupied by the aluminum atom Al(2) with occupancy of 11.3(4) % (Figure 5.1.4-1). It is worth emphasizing that the Al(2) and the B(16) unlikely occupy the two positions simultaneously due to a very short distance of 0.93 Å between them. While the B(16)–B(13) interatomic distance of 1.60(2) Å is also too short for two B atoms occupying their positions at the same time, the Al(2)–B(13) distance of 1.98(1) Å could allow that for Al(2) and B(13). The occupancy of the B(13) atom was refined and appeared to be of 70.0(1) % which is close to the value obtained by Higashi *et al.* (68.2(7) %).

Overall composition of $\text{AlB}_{44.8(5)}$ is in a good agreement with 3(1) at. % Al obtained by EDX spectroscopy. The final least squares refinement gave $R(R_w)$ values of 3.78(10.21) % and revealed residual electron density peaks lower $0.5 \text{ e}/\text{\AA}^3$ to be located only between the B–B bonds or at the centers of some B–B–B triangle faces. The selected B–B and Al–B interatomic distances are represented in Table 5.1.4-3. The values are in a good agreement with those for $\beta\text{-B}$ [152] and AlB_{31} [126].

Dopants ordinarily either occupy only the D -site (like in $\text{CrB}_{\sim 41}$ [155], $\text{FeB}_{\sim 49}$ [16], and $\text{VB}_{\sim 65}$ [163]), or are displaced from it at $\sim 0.4 \text{ \AA}$ that results in splitting the position of the dopant atom (like in $\text{NiB}_{48.5}$ [164]). A situation when both the D -site and its disordered positions are present simultaneously has been reported for the structure of $\text{CuB}_{\sim 23}$ [165]. The atomic distribution we obtained around the D -site should be mentioned as quite unusual. The structures with a different atomic arrangements around the D -site are also presented by AlB_{31} [126], and $\text{SiB}_{30.17}\text{C}_{0.35}$ [127].

Higashi's *et al.* [126] refinement of the AlB_{31} crystal structure suggested a model of the atomic distribution near the D -site different from ours. According to [126], Al atoms occupy the D -site and two general positions nearby, (0.253(2), 0.449(2), 0.1679(5)) and (0.306(2), 0.484(1), 0.1666(6)), that results in general splitting over 5 positions. Using the model proposed by Higashi *et al.* [126], we reached $R_1(wR_2)$ -values, 3.65(9.96) %, slightly less than those we obtained with our model (3.78(10.21) %). The Al occupancies of the two general positions near D -site (according to Higashi's notation) are 7.6 ± 1.8 , 2.8(7) % and 2.4(5) %, respectively, that provides with the final chemical composition $\text{AlB}_{37.8(5)}$. The difference in the final R -values between the two models is rather small and no any significant advantages of one over the other could be deduced. Therefore we suppose that both models can be valid and it is hard to distinguish which one is the most appropriate. It is worth mentioning that Higashi *et al.* [126] mentioned a possible model identical to that one we found, but it wasn't discussed in detail.

Another possibility of the atomic arrangement near the D -site is described by Roger *et al.* [127] for the $\text{SiB}_{30.17}\text{C}_{0.35}$ crystal structure. Silicon atoms were proposed to occupy the D -site while carbon atoms to localize at a special position $18h$ (0.1583(8), 0, 0.5) in the mirror plane parallel to (1 0 0) to which the B(15) atom belongs. For this model being quite close to our solution, the $R(R_w)$ values were still higher 4.15(11.85) % than those for our model, and an additional peak of 0.6 e/\AA^3 shifted at 0.5 \AA from the B(16) atom revealed. Further assignment of the Q -peak as that of boron led to unstable refinement.

V. Results

Table 5.1.4-3 Selected interatomic distances (Å) (< 2.40 Å) for AlB_{44.8(5)}.

Al(1)	–B(5)	2.147(2)	B(4)	–B(4)	1.674(3)	B(11)	–B(14)	1.760(4)
	–B(7)	2.161(2)		–B(8)	1.729(2)		–B(10)	1.772(2)
	–B(1)	2.178(2)		–B(10)	1.833(2)		–B(12)	1.826(3)
				–B(11)	1.840(3)		–B(4)	1.840(3)
Al(2)	–B(13)	1.98(1)		–B(12)	1.848(2)		–B(11)	1.842(4)
	–B(12)	2.285(7)						
	–2B(13)	2.327(7)	B(5)	–B(7)	1.718(3)	B(12)	–B(14)	1.727(2)
	–B(3)	2.328(7)		–B(6)	1.737(3)		–B(3)	1.773(2)
	–B(15)	2.393(9)		–2B(6)	1.740(2)		–B(4)	1.848(2)
	–2B(3)	2.394(5)		–2B(5)	1.794(4)		–B(13)	1.860(3)
							–Al(2)	2.285(7)
B(1)	–B(2)	1.813(2)	B(6)	–B(8)	1.619(3)			
	–B(9)	1.819(3)		–B(5)	1.737(3)	B(13)	–B(15)	1.690(3)
	–B(2)	1.839(2)		–2B(5)	1.740(2)		–B(3)	1.782(3)
	–B(7)	1.863(2)		–B(6)	1.746(3)		–B(14)	1.794(5)
	–B(1)	1.924(3)					–B(16)	1.80(2)
	–2B(1)	1.935(4)	B(7)	–B(2)	1.783(2)		–B(12)	1.860(3)
	–Al(1)	2.178(2)		–B(9)	1.788(4)		–B(13)	1.897(6)
	–Al(2)	2.441(9)		–B(1)	1.863(2)			
						B(14)	–B(12)	1.727(3)
B(2)	–B(3)	1.712(2)	B(8)	–B(4)	1.729(2)		–B(11)	1.760(4)
	–B(7)	1.783(2)		–B(3)	1.781(3)		–B(13)	1.794(5)
	–B(1)	1.813(2)		–B(10)	1.834(3)			
	–B(2)	1.817(3)				B(15)	–B(13)	1.690(3)
	–B(9)	1.843(2)	B(9)	–B(10)	1.693(3)		–B(16)	1.89(2)
	–Al(2)	2.421(5)		–B(7)	1.788(4)			
				–B(1)	1.819(3)	B(16)	–B(13)	1.80(2)
B(3)	–B(2)	1.712(2)		–B(2)	1.843(2)		–B(16)	1.89(2)
	–B(12)	1.773(2)					–B(3)	2.05(2)
	–B(8)	1.781(3)	B(10)	–B(11)	1.772(2)			
	–B(13)	1.782(3)		–B(4)	1.833(2)			
	–B(4)	1.815(2)		–B(8)	1.834(3)			
	–B(3)	1.896(4)						
	–B(16)	2.05(2)						
	–Al(2)	2.328(7)						
	–2Al(2)	2.394(5)						

5.1.5. Conclusion

In summary, we have refined the crystal structure of aluminum doped β -rhombohedral boron. The structure is based on the three-dimensional framework made of B_{12} icosahedra with voids being occupied by the B_{28} –B– B_{28} units. Aluminum atoms partially fill certain types of voids (the A1- and D-sites). We have got two possible models of atomic distribution near the D-site as it was previously reported in literature for aluminum boride [126]. The similar atomic arrangement near the D-site has been revealed in a crystal structure of $SiB_{30.17}C_{0.35}$ [165]. Structural refinement of the two appropriate models results in two possible chemical compositions, $AlB_{44.8(5)}$ or $AlB_{37.8(5)}$, which fit well the chemical analysis data obtained by the EDX method using the scanning electron microscopy. These compositions get within the field of limited solubility of Al in β -B [31] in the Al-B phase diagram.

Supporting information available

Supplementary crystallographic data of $AlB_{44.8(5)}$ have been deposited in an Inorganic Crystal Structure Database [166], Fachinformationszentrum Karlsruhe (76344 Eggenstein-Leopoldshafen, Germany, fax: +49-7247-808-666) with ICSD reference no. 423891. The data can be obtained free of charge via http://www.fiz-karlsruhe.de/request_for_deposited_data.html.

5.2. Peierls distortion, magnetism, and high hardness of manganese tetraboride

H. Gou^{1,2}, A.A. Tsirlin³, E. Bykova^{1,2}, A.M. Abakumov³, G.V. Tendeloo³, A. Richter⁴, S.V. Ovsyannikov¹, A.V. Kurnosov¹, D.M. Trots¹, Z. Konôpková⁶, H.-P. Liermann⁶, L. Dubrovinsky¹, N. Dubrovinskaia²

¹*Bayerisches Geoinstitut, Universität Bayreuth, D-95440 Bayreuth, Germany*

²*Material Physics and Technology at Extreme Conditions, Laboratory of Crystallography, University of Bayreuth, D-95440 Bayreuth, Germany*

³*National Institute of Chemical Physics and Biophysics, Akadeemia tee 23, E-12618 Tallinn, Estonia*

⁴*Electron Microscopy for Materials Research (EMAT), University of Antwerp, Groenenborgerlaan 171, B-2020 Antwerp, Belgium*

⁵*Technische Hochschule Wildau, Bahnhofstrasse 1, D-15745 Wildau, Germany*

⁶*DESY Photon Science, Deutsches Elektronen Synchrotron, Notkestrasse 85, D-22607 Hamburg, Germany*

Phys. Rev. B **89**, 064108 (2014).

5.2.1. Abstract

We report crystal structure, electronic structure, and magnetism of manganese tetraboride MnB_4 synthesized under high-pressure high-temperature conditions. In contrast to superconducting FeB_4 and metallic CrB_4 , which are both orthorhombic, MnB_4 features a monoclinic crystal structure. Its lower symmetry originates from the Peierls distortion of Mn chains. This distortion nearly opens the gap at the Fermi level, but despite the strong dimerization and the proximity of MnB_4 to the insulating state, we find indications for the sizable paramagnetic effective moment of about $1.7 \mu_B/\text{f.u.}$, ferromagnetic spin correlations and, even more surprisingly, a prominent electronic contribution to the specific heat. However,

no magnetic order has been observed in standard thermodynamic measurements down to 2 K. Altogether, this renders MnB_4 a structurally simple but microscopically enigmatic material, and we argue that its properties may be influenced by electronic correlations.

5.2.2. Introduction

The “electron-deficient” character of boron and its chemical activity lead to the formation of numerous boron-rich compounds of various structural complexity [27,167,168]. A plethora of interesting physical and chemical properties of boron-based solids, such as mechanical strength, high hardness, superconductivity, catalytic activity and thermoelectricity, keeps them in focus of modern experimental and theoretic research [18,128,169,170].

The synthesis of diborides of 5d noble metals, OsB_2 and ReB_2 , was driven by expectations to obtain a new type of superhard materials [170–173] at ambient pressure. However, a careful analysis of the available data [174] and following investigations [175,176] did not confirm the proclaimed superhardness. Unexpected superhardness was found for iron tetraboride (FeB_4) synthesized at high pressures and temperatures [128], while other transition metal tetraborides (e.g. CrB_4 and WB_4) [9,177] are hard, but not superhard materials – their hardness is below 30 GPa in the asymptotic hardness region. Moreover, iron tetraboride was found to be superconducting [128], thus possessing a combination of useful properties, which are desirable for a variety of engineering applications. This particular example motivated us for a further exploration of transition metal tetraborides, in particular, MnB_4 . Its detailed structure investigation is still missing- the ICSD provides information about the monoclinic crystal structure of MnB_4 (space group $C2/m$), ICSD#15079, based on powder X-ray diffraction data of Andersson [24] and Andersson & Carlsson [25] obtained in late 1960s. So far MnB_4 has never been synthesized in a quantity sufficient for the investigation of its electronic and magnetic properties.

Here, we report the successful synthesis of single crystals of MnB_4 at high pressures and temperatures, solution and refinement of its crystal structure based on single-crystal X-ray diffraction, and results of investigations of the material’s compressibility, hardness, magnetic properties, and electronic structure.

5.2.3. Materials and methods

Starting materials and synthesis

Polycrystalline MnB_4 samples were synthesized at high-pressure and high-temperature conditions in a piston-cylinder apparatus. Boron (Chempur Inc., 99.99% purity) and manganese (Alfa Aesar, 99.9% purity) powders were mixed in a stoichiometric (4:1) ratio. The mixture was loaded into a double capsule consisting of *h*-BN (inner) and Pt (outer) parts and then compressed to 3 GPa and heat treated either at 1080 °C, 1350 °C, or 1500 °C. The duration of heating varied from 4 to 240 hours. The samples were abruptly quenched by switching off the furnace power.

Pressure calibration was performed prior to the synthesis. It is based on the quartz-coesite and kyanite-sillimanite transitions, as well as on the melting point of diopside. Measured pressure is considered to be accurate within less than $\pm 5\%$. Temperature was measured with a Pt-Pt10%Rh thermocouple. Temperature gradients are estimated to be less than 25 °C for the described experimental conditions.

Single-crystals of MnB_4 were synthesized at pressures of 10 and 12 GPa and temperature of 1600 °C (heating duration was 1 hour) in the Kawai-type multi-anvil apparatus [178] using 1000-ton (Hymag) and 1200-ton (Sumitomo) hydraulic presses and the 14/8 (octahedron edge length/cube truncation length) high-pressure assemblies. As starting materials we used a manganese rod (Goodfellow, 99.5% purity) and a boron powder (Chempur Inc., 99.99% purity) which were enclosed into a *h*-BN capsule. Pressure was calibrated based on the phase transitions of standard materials and temperature was determined using a W3Re/W25Re thermocouple.

Analytical techniques

The morphology and chemical composition of the synthesized samples of single crystals were studied by means of the scanning electron microscopy (SEM) (LEO-1530). Chemical purity of the samples was confirmed using wavelength dispersive X-ray (WDX) microprobe analysis (JEOL JXA-8200; focused beam; 12 keV and 15 nA or 15 keV and 12 nA). The LIFH and LDEB crystals were used to analyze Mn and B, respectively. Pure Mn and α -B or FeB were used as internal standards with ZAF correction.

Single-crystal X-ray diffraction

A black lustrous thin plate of MnB_4 with the size of $0.05 \times 0.04 \times 0.01 \text{ mm}^3$ was used for the crystal structure investigation by means of single-crystal X-ray diffraction. X-ray diffraction data were collected at ambient temperature using a four-circle Oxford Diffraction Xcalibur diffractometer ($\lambda = 0.7107 \text{ \AA}$) equipped with a Xcalibur Sapphire2 CCD detector. The intensities of reflections were measured by omega-scanning of narrow (0.5°) frames. The data collection and their further integration were performed with CrysAlisPro software [179]. Absorption corrections were applied empirically by the Scale3 Abspack program implemented in CrysAlisPro. The scaling and absorption correction was used due to the small size of the inspected crystal that makes difficult the precise face indexing. The structure was solved by the direct method and refined by the full matrix least-squares in the anisotropic approximation for all atoms using SHELXTL software [124]. The X-ray experimental details and crystallographic characteristics of MnB_4 are presented in Table 5.2.3-1. The DIAMOND software [162] was used to create molecular graphics.

The crystallographic data of MnB_4 and further details of the crystal structure investigation have been deposited in the Inorganic Crystal Structure Database [166] and may be obtained free of charge from Fachinformationszentrum Karlsruhe, 76344 Eggenstein-Leopoldshafen, Germany (fax: (+49)7247-808-666; e-mail: crysdata@fiz-karlsruhe.de, http://www.fiz-karlsruhe.de/request_for_deposited_data.html) on quoting the deposition number CSD-426691.

High-pressure powder X-ray diffraction

For *in situ* high-pressure X-ray diffraction studies we employed a piston-cylinder-type diamond anvil cell with a culet size of $350 \text{ }\mu\text{m}$ and a rhenium gasket. A small sample ($\sim 20 \text{ }\mu\text{m}$ in size) of a MnB_4 powder was loaded into a hole of $\sim 150 \text{ }\mu\text{m}$ in diameter drilled in the gasket pre-indented to $\sim 50 \text{ }\mu\text{m}$. Using a gas-loading apparatus at BGI [112], we loaded the pressure chamber with the sample along with a neon pressure-transmitting medium. The XRD experiments were carried out at the beamline P02.2 at PETRA III, DESY (Hamburg) [180]. The X-ray wavelength was $\lambda = 0.29135 \text{ \AA}$. Pressure was determined by the shift of the ruby luminescence line. The data were collected using a PerkinElmer XRD1621 detector and 2D X-ray images were integrated using the Fit2D program [181].

Table 5.2.3-1 Details on the X-ray diffraction data collection and structure refinement of MnB₄

Empirical formula	MnB ₄
Formula weight (g/mol)	98.18
Temperature (K)	296(2)
Wavelength (Å)	0.7107
Crystal system	Monoclinic
Space group	<i>P</i> 2 ₁ / <i>c</i>
<i>a</i> (Å)	5.4759(4)
<i>b</i> (Å)	5.3665(4)
<i>c</i> (Å)	5.5021(4)
β (°)	115.044(9)
<i>V</i> (Å³)	146.486(19)
<i>Z</i>	4
Calculated density (g/cm³)	4.452
Linear absorption coefficient (mm⁻¹)	8.319
<i>F</i>(000)	180
Crystal size (mm³)	0.05 x 0.04 x 0.01
Theta range for data collection (deg.)	4.11 to 34.57
Completeness to theta = 27.59°	100.0 %
Index ranges	-8 < <i>h</i> < 8, -8 < <i>k</i> < 7, -8 < <i>l</i> < 8
Reflections collected	2122
Independent reflections / <i>R</i>_{int}	593 / 0.0467
Max. and min. transmission	1.00000 and 0.78298
Refinement method	Full matrix least squares on <i>F</i> ²
Data / restraints / parameters	593 / 0 / 34
Goodness of fit on <i>F</i>²	1.043
Final <i>R</i> indices [<i>I</i> > 2σ(<i>I</i>)]	<i>R</i> ₁ = 0.0376, <i>wR</i> ₂ = 0.0731
<i>R</i> indices (all data)	<i>R</i> ₁ = 0.0652, <i>wR</i> ₂ = 0.0813
Largest diff. peak and hole (e / Å³)	0.728 and -0.911

Transmission electron microscopy

The sample for transmission electron microscopy (TEM) investigation was prepared by crushing the material in agate mortar under ethanol and depositing drops of suspension on a holey carbon grid. The electron diffraction (ED) patterns and high resolution TEM (HRTEM) images have been acquired using a FEI Tecnai G2 microscope operated at 200 kV. Theoretical HRTEM images were calculated using the JEMS software.

Hardness measurements

Vickers hardness (H_V) was measured using a microhardness tester (M-400-G2, LECO Corporation) under loads of 0.5 kgf (4.9 N), 1 kgf (9.8 N) and 1.5 kgf (14.7 N).

Nanoindentation (NI) measurements were performed using the electrostatic transducer of the UBI 1 Hysitron triboscope with a pristine diamond 90° cube corner tip. We made single (trapezoid) and multi-indentation measurements at 3 different locations on the sample with target loads 1.5/2.5/3.5/4.5/6 mN.

Thermodynamic measurements

The magnetic susceptibility was measured on small polycrystalline pieces of MnB_4 using the Quantum Design MPMS SQUID magnetometer. The data were collected at temperatures of 2–380 K in magnetic fields up to 5 T. The heat capacity was measured by a relaxation technique with the Quantum Design PPMS in the temperature range 1.8–200 K in fields of 0 and 5 T.

Electronic structure calculations

For electronic structure calculations, we used the full-potential local-orbital FPLO code and the standard Perdew-Wang local density approximation (LDA) for the exchange-correlation potential. The symmetry-irreducible part of the first Brillouin zone was sampled by a dense k mesh of 518 points. The convergence with respect to the k mesh was carefully checked.

5.2.4. Results

Crystal structure

The crystal structure of MnB_4 was initially established based on powder X-ray diffraction data as monoclinic [24,25] (space group $C2/m$). The reported unit cell parameters were $a = 5.5029(3)$, $b = 5.3669(3)$, $c = 2.9487(2)$ Å, $\beta = 122.710(5)^\circ$ and the structure was described as a 3-dimensional boron network with Mn atoms inside the voids [25]. Each Mn atom is surrounded by 12 boron atoms and the distorted MnB_{12} polyhedra pack in columns parallel to the c -direction (Figure 5.2.4-1a), so that the metal atoms form one-dimensional chains with the uniform Mn–Mn distances of $2.9487(2)$ Å. Every column of MnB_{12} polyhedra is shifted with respect to the four nearest ones for a half of the value of the c parameter. Andersson & Carlsson [25] described the structure of MnB_4 as highly similar to that of the orthorhombic CrB_4 (space group $Immm$) [134] with insignificant differences in the atomic arrangement.

Recent *ab initio* calculations [182] showed that the MB_4 ($M = \text{Cr, Mn, Fe, Tc, Ru}$) compounds are more stable if the structures have the symmetry described by the $Pnnm$ space group. Indeed, investigation of the synthesized CrB_4 powder [182] by means of the electron and X-ray diffraction confirmed the existence of the orthorhombic ($Pnnm$) CrB_4 phase, whose structure was refined by Knappschneider *et al.* [177] based on single crystal X-ray diffraction data. Our recent studies [128] showed that FeB_4 has the same crystal structure as CrB_4 . The unit cell contains three independent atoms: one $M(1)$ atom in the $(0, 0, 0)$ position associated with the center of inversion and two boron atoms, B(1) and B(2) in the $4g$ position. The major difference from the $Immm$ structure (used by Andersson & Lundstroem [134] to describe the CrB_4 structure) is a distortion of the 3-dimensional boron network (Figure

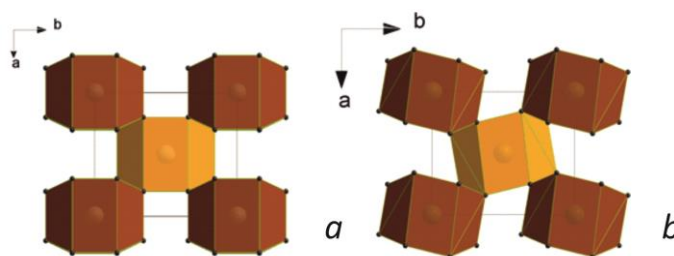


Figure 5.2.4-1 A comparison of the crystal structure of MnB_4 proposed by Andersson [24] (a), and that of FeB_4 (Ref. [128]) structure (b). In both cases MnB_{12} polyhedra pack in columns, each one is shifted on a $c/2$ distance along the c -direction with respect to its four nearest neighbors (light and dark polyhedra), however a distortion of the 3-dimensional boron network is different.

5.2.4-11b). Metal-metal distances in the *Pnnm* structures of CrB_4 and FeB_4 are 2.8659(1) and 2.9991(2) Å, respectively.

We could expect the orthorhombic *Pnnm* crystal structure in case of MnB_4 , but according to our findings, the β angle slightly differs from 90° . The distortion reduces the symmetry of the unit cell to monoclinic ($P2_1/n$) with $a = 4.6306(3)$, $b = 5.3657(4)$, $c = 2.9482(2)$ Å and $\beta = 90.307(6)^\circ$. Moreover in addition to the main reflections we have observed weak satellites at the $\frac{1}{2}[1\ 0\ 1]$. Using following transformation law $\mathbf{a}' = (\mathbf{a} + \mathbf{c})$, $\mathbf{b}' = -\mathbf{b}$, $\mathbf{c}' = (\mathbf{a} - \mathbf{c})$ it was possible to index all reflections in the monoclinic cell ($P2_1/c$) with $a = 5.4759(4)$, $b = 5.3665(4)$, $c = 5.5021(4)$ Å and $\beta = 115.044(9)^\circ$. The unit cell of the MnB_4 structure contains five independent atoms (Mn(1) and B(1–4) atoms, see Table 5.2.4-1). The average intensity of satellite reflections is approximately five times as weak as that of the main reflections that influences on anisotropic atomic displacement parameters (ADPs) for B(1) and B(4) whose ellipses become flattened. To provide them with a nearly spherical shape, we fixed ADPs of B(1) and B(3) as equal; the same was done for the B(2) and B(4) pair.

The structure obtained (Figure 5.2.4-2) can be described in terms of the parent *Pnnm* cell plus a symmetry breaking structural distortion. The analysis of symmetry modes performed with the program AMPLIMODES [183,184] have shown that the $P2_1/c$ distortion decomposes into two distortion modes of different symmetry corresponding to the irreducible representations (irreps) GM4+ and U1–.

Table 5.2.4-1 Atomic coordinates, positions and equivalent isotropic displacement parameters for MnB_4 .

Atom	Wyckoff site	<i>x</i>	<i>y</i>	<i>z</i>	$U_{\text{eq}}^a, \text{\AA}^2$
Mn(1)	4 <i>e</i>	0.26817(9)	0.0011(2)	0.273758	0.00465(15)
B(1)	4 <i>e</i>	0.3648(9)	0.1859(8)	0.6378(8)	0.0072(4) ^b
B(2)	4 <i>e</i>	0.6699(8)	0.1302(8)	0.3238(8)	0.0067(4) ^b
B(3)	4 <i>e</i>	0.8692(9)	0.1822(8)	0.1269(8)	0.0072(4) ^b
B(4)	4 <i>e</i>	0.1639(8)	0.1301(8)	0.8405(8)	0.0067(4) ^b

^a U_{eq} is defined as one third of the trace of the orthogonalized U^{ij} tensor.

^b ADPs for B(1) and B(3) and for B(2) and B(4) have been fixed to be equal to each other.

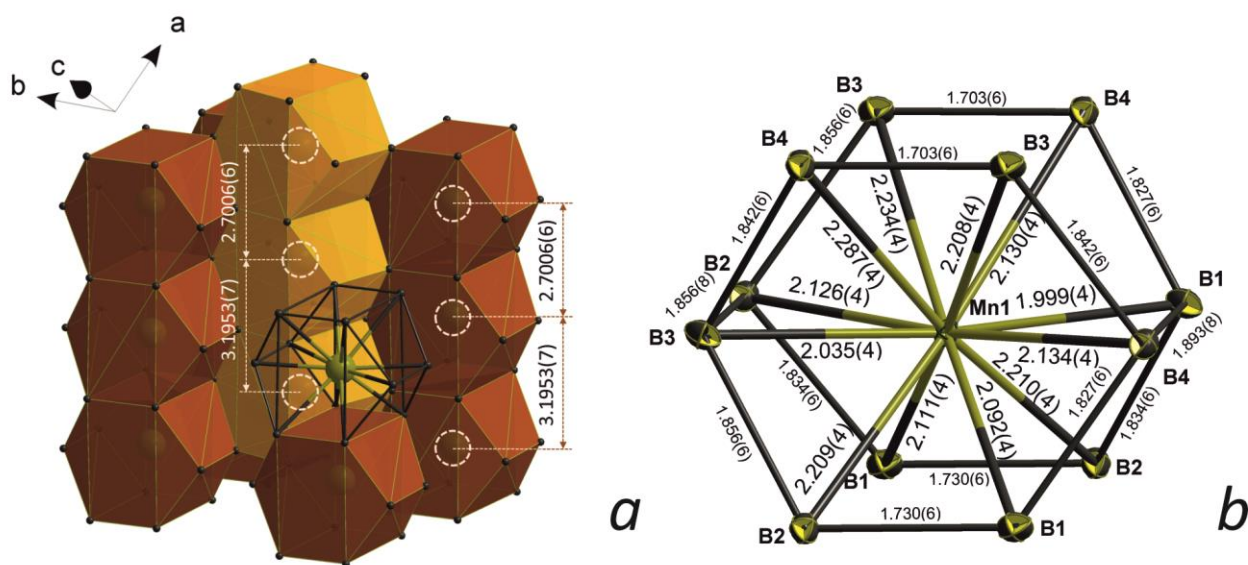


Figure 5.2.4-2 Structure of MnB_4 . MnB_{12} polyhedra pack in columns along $[1\ 0\ 1]$ direction with alternating Mn-Mn distances of 2.7006(6) and 3.1953(7) Å through the column (a). Interatomic distances (Å) in the MnB_{12} polyhedron (b).

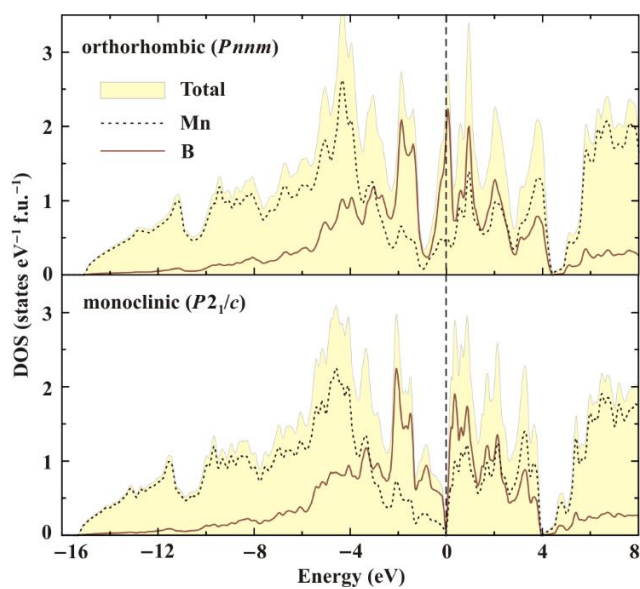


Figure 5.2.4-3 LDA DOS for MnB_4 in its fictitious FeB_4 -like (orthorhombic, top panel) and real (monoclinic, bottom panel) structures. The monoclinic distortion shifts the Fermi level away from the DOS maximum and nearly opens a gap.

The $U1^-$ irrep, associated with the k -vector $(1/2\ 0\ 1/2)$, occurs as a primary mode for this distortion. It involves the displacements of Mn atoms along $[1\ 0\ 1]$, thus resulting in two different Mn – Mn distances, namely 2.7004(6) and 3.1953(7) Å (Figure 5.2.4-2a). This effect can be understood as a Peierls distortion of the Mn chains. In Figure 5.2.4-3, we compare local density approximation (LDA) densities of states (DOS) calculated for the monoclinic $P2_1/c$ structure and for the idealized orthorhombic $Pnnm$ structure, which is constructed as an “average” of the experimental CrB_4 and FeB_4 structures (averaged lattice parameters and atomic positions). In the orthorhombic structure, the Fermi level of MnB_4 would match the peak in the DOS, thus destabilizing the system. This effect is mitigated by a conventional Peierls distortion that splits the Mn chains with uniform Mn–Mn distances of about 2.93 Å into dimerized Mn chains with alternating Mn–Mn distances of 2.7004(6) and 3.1953(7) Å (as revealed by single-crystal X-ray diffraction). This way, the Fermi level falls into a dip of the DOS, which is unusual for transition-metal tetraborides. Indeed, both CrB_4 and FeB_4 stay orthorhombic and feature a relatively high DOS at the Fermi level, but remain stable with respect to the Peierls distortion.

In the conference abstracts, Litterscheid *et al.* [185] reported recently about the growth of crystals of MnB_4 and its structure determination and refinement. However, neither synthesis was described, nor explicit structural information and details of the crystal structure investigation were given. The unit cell parameters were reported to be $a = 5.8982(2)$, $b = 5.3732(2)$, $c = 5.5112(2)$ Å and $\beta = 122.633(3)^\circ$. They correspond to the choice of the non-standard unit cell with the space group $P2_1/n$, while the authors [185] provided the $P2_1/c$ space group.

The results of the TEM analysis are in agreement with the single-crystal XRD. Figure 5.2.4-4 shows the ED patterns of MnB_4 . The patterns were indexed on a primitive monoclinic lattice with the cell parameters $a \approx 5.5$ Å, $b \approx 5.4$ Å, $c \approx 5.5$ Å, $\beta \approx 115^\circ$, in agreement with the crystal structure determined from X-ray diffraction data. The $[010]$ ED pattern (Figure 5.2.4-4d) demonstrates apparent orthorhombic symmetry which results from a superposition of two mirror twinned variants of the monoclinic structure, shown in Figure 5.2.4-4 (e and f). Taking

into account twinning, the reflection conditions can be determined as $h0l: l = 2n$ and $0k0: k = 2n$ (Figure 5.2.4-4a–d) that confirm the space group $P2_1/c$. The forbidden $0k0$, k - odd reflections on the $[001]$ and $[100]$ ED patterns are caused by multiple diffraction as confirmed by the absence of these forbidden reflections in the $[-101]$ ED pattern.

The $[010]$ HRTEM image in Figure 5.2.4-5 demonstrates that the MnB_4 structure is free of extended defects. At these particular imaging conditions, the bright dots in the image correspond to projections of the Mn columns. The simulated HRTEM image, calculated with the crystal structure refined from single crystal X-ray diffraction data, is in excellent agreement with the experimental one. Figure 5.2.4-6 demonstrates $[010]$ HRTEM image of two twinned domains of the monoclinic MnB_4 structure. In spite of the coherent twin, no well-defined twin boundary separating the two domains is visible.

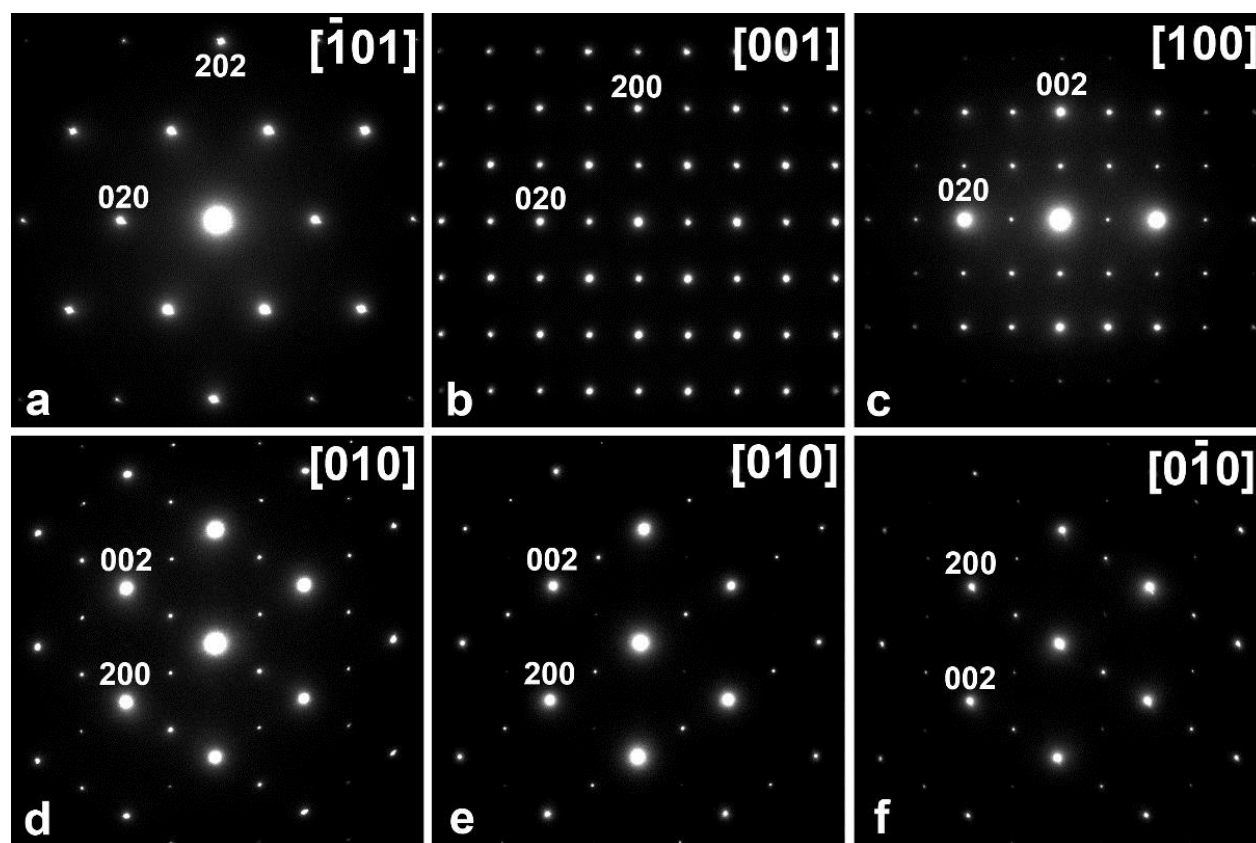


Figure 5.2.4-4 Electron diffraction patterns of MnB_4 . The $[010]$ ED pattern (d) is a superposition of two twinned variants (e) and (f).

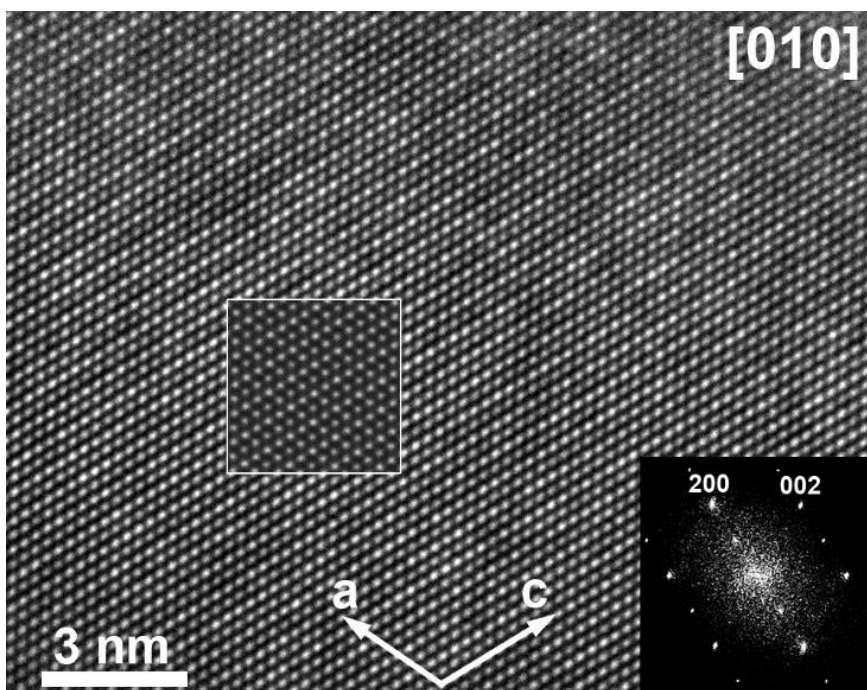


Figure 5.2.4-5 [010] HRTEM image of a single domain of MnB_4 and its Fourier transform. The insert shows a calculated HRTEM image (defocus $f = 7$ nm, thickness $t = 4.8$ nm).

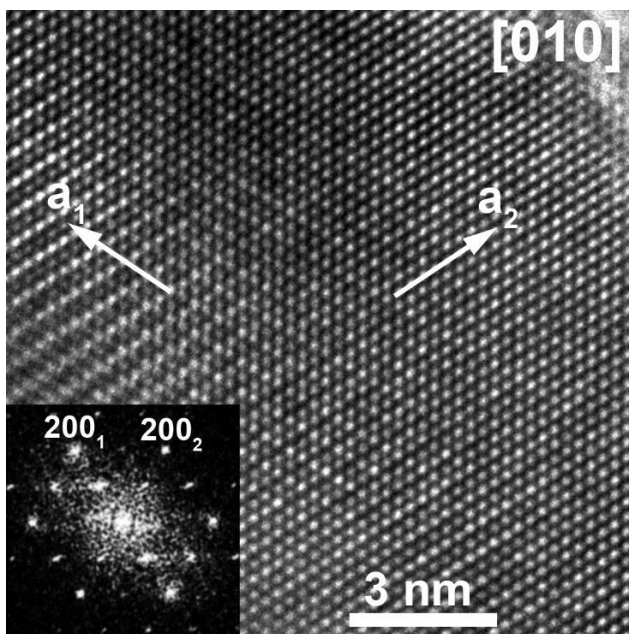


Figure 5.2.4-6 [010] HRTEM image of two twinned domains of the MnB_4 structure (at the left and right side of the image, respectively) and corresponding Fourier transform showing two mirror-related orientations of the a -axis of the domains. No well-defined twin boundary is visible.

Mechanical properties

Figure 5.2.4-2b shows interatomic distances in MnB_4 . The B–B distance of 1.703(6) Å is the shortest among MB_4 ($M = \text{Cr, Fe, Mn}$) compounds with similar crystal structures (see Table 5.2.4-2). According to Refs. [128,177], short B–B bonds are responsible for high hardness and low compressibility of CrB_4 and FeB_4 , therefore we could expect these properties in MnB_4 .

The variations of the volume and lattice parameters of MnB_4 with pressure up to 25 GPa are presented in Figure 5.2.4-7. The fit of the pressure-volume data with the third-order Birch-Murnaghan equation of state gave the bulk modulus of $K = 254(9)$ GPa and $K' = 4.4$ (Figure 5.2.4-7a). The value of the bulk modulus is very close to that reported for FeB_4 , 252(5) GPa [128]. Considerable anisotropy of the compressibility is also similar to that observed in FeB_4 [128]. Along the b direction (Figure 5.2.4-7b) the material is almost as incompressible as diamond [129] that can be linked to the mentioned above very short B–B bond (Figure 5.2.4-2b, Table 5.2.4-2) oriented along the b -axis.

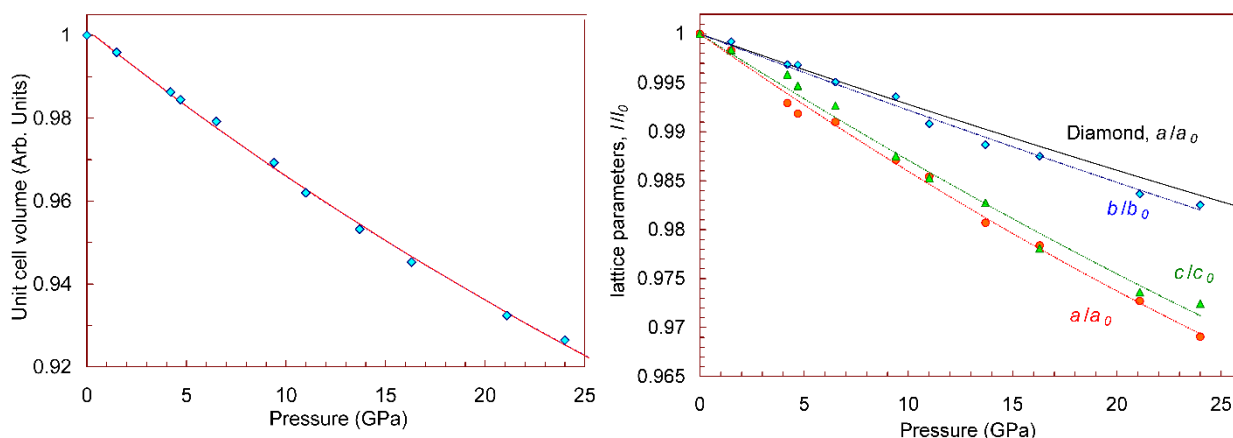


Figure 5.2.4-7 Compressibility of MnB_4 . (a) The pressure dependence of the unit cell volume based on powder synchrotron X-ray diffraction data. Solid line corresponds to the fit of the pressure-volume data with the third-order Birch-Murnaghan equation of state, which gave the bulk modulus $K = 254(9)$ GPa and $K' = 4.4$. (b) The relative changes of the unit cell parameters as a function of pressure. The stiffness of the MnB_4 structure along the b -direction is almost the same as that of diamond (continues black line according to [129]).

Table 5.2.4-2 Bond lengths in MB_4 ($M = \text{Mn, Cr, Fe}$) possessing similar structures.

Metal boride	$M\text{--}B$ distances, Å	$B\text{--}B$ distances, Å	Reference
MnB₄	1.999(4)–2.310(4)	1.703(6)– 1.893(8)	This work
CrB₄	2.053(4) 2.153(4) 2.178(3) 2.261(3)	1.743(6) 1.835(4) 1.868(6)	[131]
FeB₄	2.009(4) 2.109(4) 2.136(3) 2.266(3)	1.714(6) 1.8443(3) 1.894(6)	[128]

The Vickers hardness of the monoclinic MnB₄ was found to be 37.4 GPa at a load of 9.8 N and 34.6 GPa at 14.7 N what is larger than that of 5d transition metal borides, WB₄ (28.1 GPa [175] or 31.8 GPa [9] at 4.9 N), ReB₂ (18 GPa [176] at 9.8 N, 26.0–32.5 GPa [172] or 26.6 GPa [175] at 4.9 N), OsB₂ (19.6 GPa [171] or 16.8 GPa [175] at 4.9 N). Nanoindentation measurements resulted in the average hardness of 30.7 ± 2.3 GPa and the average indentation modulus of 415 ± 30 GPa. Thus MnB₄ is a fairly hard, but not superhard material. It is brittle, as indicated by the typical pop-ins and also cracks appearing sometimes after indentation and visible in the AFM images.

Magnetic properties and electronic structure

Magnetic susceptibility of MnB₄ reveals a weak ferromagnetic signal at low temperatures (Figure 5.2.4-8). Above 150–200 K, MnB₄ shows the paramagnetic Curie-Weiss behaviour with the effective magnetic moment of 1.6–1.7 μ_B and the ferromagnetic Weiss temperature of $\theta \sim 90$ K according to

$$\chi = C/(T - \theta). \quad (1)$$

In Figure 5.2.4-8 we show magnetic susceptibility data collected on two different samples which are both single-phase according to XRD and WDX. While the high-temperature regions match

quite well, the behaviour at low temperatures is remarkably different and shows a variable magnitude of the ferromagnetic signal. Magnetization isotherms measured at 2 K further show a small, but variable net moment (Figure 5.2.4-9). Therefore, we conclude that MnB₄ reveals ferromagnetic spin correlations evidenced by the positive θ value extracted from the robust high-temperature data. On the other hand, the low-temperature ferromagnetism of our samples (the net moment observed at low temperatures) appears to be extrinsic. Note also that no abrupt phase transition, such as ferromagnetic ordering, can be seen in the magnetization data.

Considering the LDA electronic structure of the stoichiometric monoclinic MnB₄ (Figure 5.2.4-3, bottom), one would expect a weak paramagnetic or even a diamagnetic behaviour of this compound, because the Fermi level falls into a dip in the DOS formed upon the Peierls distortion, hence the number of states at the Fermi level is extremely low, only $N(E_F) \sim 0.08$ eV⁻¹/f.u., compared to $N(E_F) \sim 1.0$ eV⁻¹/f.u. in FeB₄. Surprisingly, our low-temperature heat-capacity measurements revealed a large electronic contribution to the specific heat. In the 15–30 K temperature range, the heat capacity can be fitted to the conventional expression for metals:

$$C_p(T) = \gamma T + \beta T^3, \quad (2)$$

where the first and second terms stand for the electronic and lattice contributions, respectively (Figure 5.2.4-10). The fit yields $\gamma = 10.1$ mJ mol⁻¹ K⁻² and $\beta = 0.012$ mJ mol⁻¹ K⁻⁴. Below 15 K, an additional contribution to the specific heat is clearly seen in Figure 5.2.4-10. This contribution does not change in the applied field and may reflect non-magnetic impurity states leading to a series of Schottky anomalies. Its exact nature requires further investigation.

The β and γ parameters for MnB₄ are akin to those for FeB₄, where we previously reported $\gamma = 10.2$ mJ mol⁻¹ K⁻² and $\beta = 0.025$ mJ mol⁻¹ K⁻⁴ [128]. Compared to superhard FeB₄, the β value in MnB₄ is reduced by a factor of 2, which is well in line with our finding that MnB₄ is hard but not superhard. Its effective Debye temperature is $\theta_D \sim 540$ K, and the βT^3 behavior of the lattice specific heat persists up to at least 30 K.

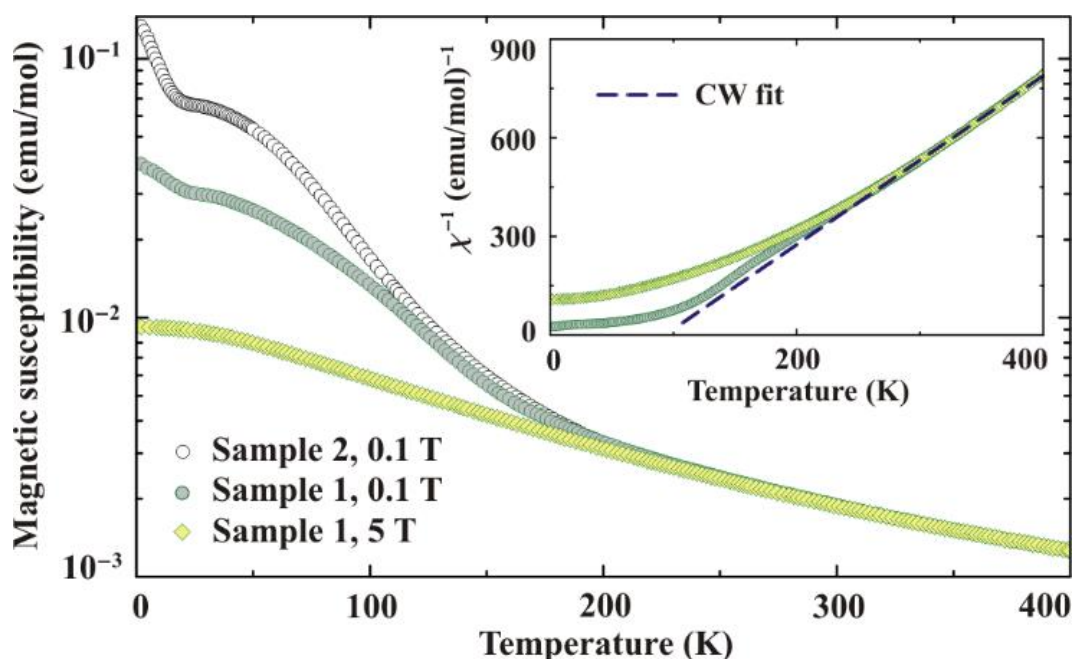


Figure 5.2.4-8 Magnetic susceptibility of MnB_4 measured on two different samples. At high temperatures, the susceptibility is nearly sample-independent and yields the Curie-Weiss (CW) parameters of $\mu_{\text{eff}} \sim 1.7 \mu_B$ and $\theta \sim 90 \text{ K}$ (see inset). At low temperatures, the susceptibility is strongly sample-dependent indicating a variable net moment, which is most likely extrinsic.

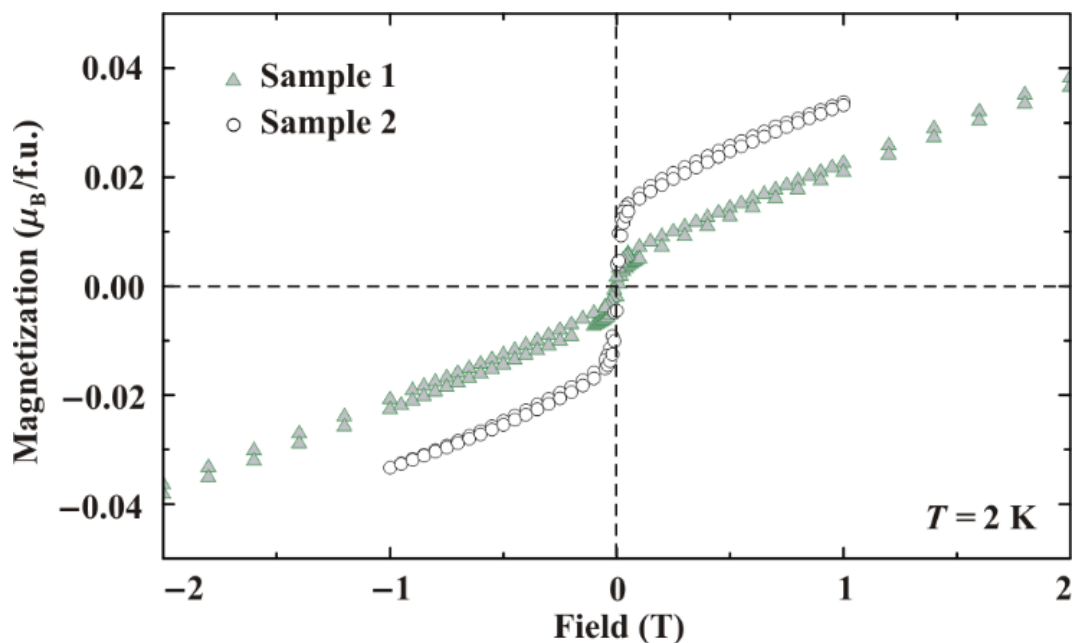


Figure 5.2.4-9 Magnetization curves of two MnB_4 samples measured at 2 K. Note the different net moments and the similar slope of the linear part.

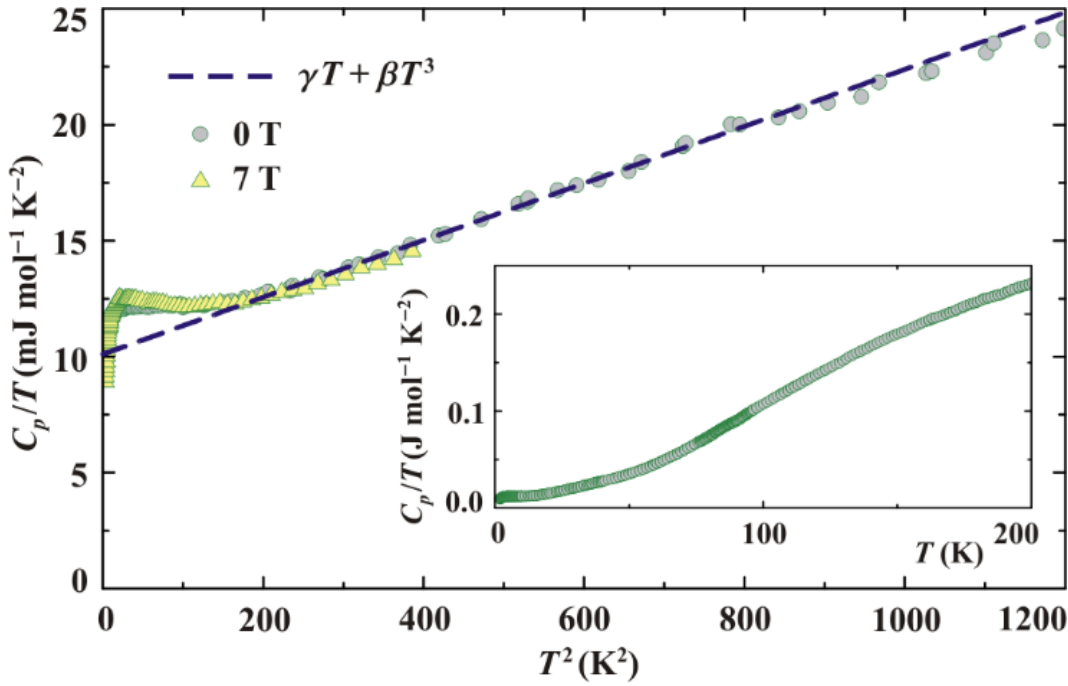


Figure 5.2.4-10 The specific heat of MnB_4 measured in the applied fields of 0 T (circles) and 7 T (triangles). The line shows the fit with Eq. (2). The inset displays the smooth temperature dependence of the specific heat in a broad temperature range up to 200 K.

Regarding the electronic contribution to the specific heat, the γ values of about $10 \text{ mJ mol}^{-1} \text{ K}^{-2}$ for MnB_4 and FeB_4 are remarkably similar. For a simple metal, they would imply a high density of states at the Fermi level, $N(E_F) \sim 4.3 \text{ states eV}^{-1} \text{ f.u.}^{-1}$, which is four times higher than the LDA estimate for FeB_4 ($\sim 1.0 \text{ states eV}^{-1} \text{ f.u.}^{-1}$, [18]) and 50 times higher than the LDA estimate for MnB_4 ($\sim 0.08 \text{ states eV}^{-1} \text{ f.u.}^{-1}$). Apparently, there is a strong renormalization of γ in transition-metal tetraborides, yet in MnB_4 this effect is particularly strong. Possible reasons behind it will be discussed below.

The high value of γ suggests that at least at low temperatures MnB_4 features a large number of charge carriers and should be metallic. While the small size of the available samples prevents us from resistivity measurements, we note that already the large γ value contradicts the simple scenario of a Peierls distortion that would drastically reduce the number of states at the Fermi level (Figure 5.2.4-3, bottom). Moreover, ferromagnetic spin correlations can not be understood on the basis of LDA results, because the Peierls dimerization typically leads to a

non-magnetic state. Indeed, spin-polarized LSDA calculations for MnB_4 converge to a non-magnetic solution, which contradicts the sizable effective moment and ferromagnetic spin correlations (positive θ value) observed in our magnetization measurements (Figure 5.2.4-8).

The discrepancies between the non-magnetic, nearly insulating LDA scenario and the experimental ferromagnetic metallic behaviour can be ascribed to several effects. First, tiny deviations from the ideal MnB_4 stoichiometry may push the Fermi level out of the dip and increase the number of states at the Fermi level. However, this effect is by far insufficient to reproduce our results. A tentative modelling of the non-stoichiometric MnB_4 within the virtual crystal approximation (VCA) that basically changes the charge on the Mn site and shifts the Fermi level toward lower or higher energies, fails to account for ferromagnetic spin correlations: the system remains non-magnetic even at the 10 % doping level, while the composition of our samples is established as stoichiometric MnB_4 with less than 1 % uncertainty. A more plausible explanation would be an increased tendency to electron localization on the Mn sites. This tendency can be reproduced by the LSDA+ U method that adds a mean-field Hubbard-like energy term and mimics the effect of the on-site Coulomb repulsion U . Although originally designed for insulators, the LSDA+ U method can be also applied to metallic systems and provides a rough guess on the behavior of correlated metals [186].

Here, we used LSDA+ U with the on-site Coulomb repulsion $U = 3$ eV and Hund's coupling $J = 0.5$ eV, which were taken about twice lower than standard estimates for strongly correlated insulating Mn oxides ($U = 5\text{--}6$ eV, $J = 1$ eV, [187,188]). This way, we are able to stabilize a ferromagnetic solution with a small moment of about $0.6 \mu_B$ on Mn atoms (Figure 5.2.4-11). This moment is still much lower than the high-temperature paramagnetic effective moment of about $1.7 \mu_B$. However, these two moments are not expected to match, because the LSDA+ U result pertains to the ordered moment at zero temperature, while the effective moment is the fluctuating moment at high temperatures. In fact, our calculated moment is in the same range as the ordered moment in Mn-based weak ferromagnets, such as MnSi: $\mu = 0.4 \mu_B$ [189]. Moreover, we find a sizable density of states at the Fermi level, $N(E_F) \sim 0.7 \text{ states eV}^{-1} \text{ f.u.}^{-1}$

(Figure 5.2.4-11) that now approaches $N(E_F) \sim 1.0$ states $\text{eV}^{-1} \text{f.u.}^{-1}$ for FeB_4 and better matches the experimental value of γ , although a large renormalization is still required.

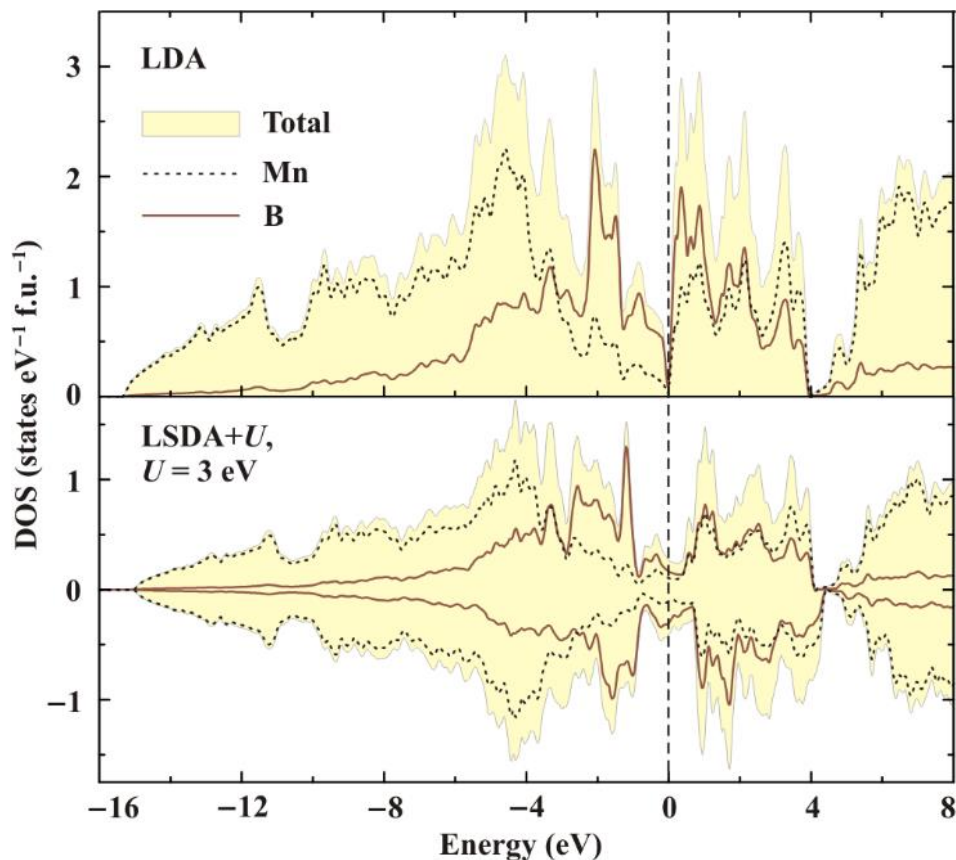


Figure 5.2.4-11 Electronic structure of monoclinic MnB_4 calculated within LDA (top panel) and LSDA+ U with $U = 3$ eV (bottom).

5.2.5. Discussion

MnB_4 has its distinct position in the family of transition-metal tetraborides. Both CrB_4 and FeB_4 are orthorhombic and, in general, well described by standard LDA that accurately predicted the orthorhombic crystal structure of FeB_4 and even the superconductivity of this compound [18,128]. In MnB_4 , the electron count is such that the Fermi level matches the maximum of the density of states. Then the orthorhombic structure becomes unstable and undergoes a monoclinic distortion. We ascribe this effect to a Peierls distortion, because in the monoclinic structure the Mn chains are dimerized, and the Fermi level falls into a dip in the density of states, which is strongly reminiscent of a band gap observed in other Peierls-distorted systems

[190,191]. Therefore, MnB_4 could even be similar to narrow-gap intermetallic compounds, such as FeGa_3 [192]. An important difference, though, is that in those compounds the band gap would typically open because of the strong hybridization (formation of separated bonding and anti-bonding states) between the transition-metal and *p*-element orbitals. In MnB_4 , the dip in the LDA DOS arises from the Mn–Mn interactions, while the mixing with the B states keeps the system metallic and provides a small yet non-zero number of states at the Fermi level.

Surprisingly, our experimental data are not consistent with this simple dimerization picture, because MnB_4 shows a large electronic contribution to the specific heat and a sizable high-temperature paramagnetic moment with clear signatures of ferromagnetic spin correlations. Phenomenologically, MnB_4 is similar to Mn-based ferromagnets, such as MnSi (compare, for example, the high-temperature paramagnetic moments of $\sim 1.7 \mu_B$ and $2.3 \mu_B$ [189], respectively), with the only exception that MnB_4 does not show any clear signatures of the long-range ferromagnetic order. We have shown that moderate electronic correlations may reconcile experimental observations with computational results and render MnB_4 ferromagnetic. However, the origin of these correlations is presently unclear, and the absence of the long-range magnetic ordering despite sizable ferromagnetic spin correlations remains an open problem as well.

5.2.6. Conclusion

The high-pressure high-temperature synthesis technique enabled us to synthesize high-quality single crystals of manganese tetraboride, MnB_4 . Single-crystal synchrotron X-ray diffraction data allowed the refinement of its crystal structure, which revealed dimerized Mn chains with alternating Mn–Mn distances, which were not identified in previous powder-XRD investigations of polycrystalline MnB_4 samples. We explained this phenomenon by Peierls distortion, which leads to reducing the symmetry of MnB_4 to monoclinic, compared to the orthorhombic symmetry of otherwise similar CrB_4 and FeB_4 structures. Mechanical property measurements revealed the high bulk modulus (254(9) GPa), strong anisotropy in compressibility (with the stiffness comparable to that of diamond, along the *b* crystallographic axis), and very high hardness (35–37 GPa) approaching that of superhard materials. Our experimental studies

provided previously unavailable data on magnetic properties of MnB_4 . The latter, complemented with our theoretical consideration of electronic properties of MnB_4 , allowed us to conclude that the relatively simple crystal structure with a well-defined and well-understood Peierls distortion hosts remarkably complex and even enigmatic low-temperature physics. Current efforts in the high-pressure synthesis should eventually result in the preparation of larger samples that would facilitate further studies on the electronic structure and magnetism of this interesting material.

5.2.7. Acknowledgments

H.G. gratefully acknowledges financial support of the Alexander von Humboldt Foundation. The work was supported by the German Research Foundation (DFG). N.D. thanks DFG for financial support through the Heisenberg Program and the DFG Project DU 954-8/1. A.T. was funded by the Mobilitas program of the ESF (grant no. MTT77). A.T. acknowledges fruitful discussions with Christoph Geibel and experimental support by Deepa Kasinathan. G.V.T. acknowledges the European Research Council, ERC grant No 246791 – COUNTATOMS. Portions of this research were carried out at the light source PETRA III at DESY, a member of the Helmholtz Association (HGF).

5.3. Novel non-magnetic hard boride Co_5B_{16} synthesized under high pressure

E. Bykova^{1,2}, A.A. Tsirlin³, H. Gou^{1,2}, L. Dubrovinsky¹, N. Dubrovinskaia²

¹*Bayerisches Geoinstitut, Universität Bayreuth, D-95440 Bayreuth, Germany*

²*Material Physics and Technology at Extreme Conditions, Laboratory of Crystallography, University of Bayreuth, D-95440 Bayreuth, Germany*

³*National Institute of Chemical Physics and Biophysics, Akadeemia tee 23, EE-12618 Tallinn, Estonia*

J. Alloys Compd. **608**, 69–72 (2014).

5.3.1. Abstract

A first cobalt boride with the Co:B ratio below 1:1, Co_5B_{16} , was synthesized under high-pressure high-temperature conditions. It has a unique orthorhombic structure (space group *Pmma*, $a = 19.1736(12)$, $b = 2.9329(1)$, and $c = 5.4886(2)$ Å, R_1 (all data) = 0.037). The material is hard, paramagnetic, with a weak temperature dependence of magnetic susceptibility.

5.3.2. Introduction

Transition-metal (TM) borides are interesting in both fundamental and applied aspects. Their high hardness related to the rigid boron network can be superimposed on interesting magnetic and electronic properties driven by the transition-metal ion. For example, FeB_4 is a non-magnetic iron boride that becomes superconducting below 2.9 K [18,128]. It is a unique material that combines superhardness and superconductivity [128]. However, it is metastable and can be prepared under high pressure only. In contrast, Fe-rich borides, such as Fe_2B and FeB , can be synthesized at ambient pressure. They are ferromagnets with remarkably high Curie temperatures (T_C) of 1015 K and 593 K, respectively [22]. On general grounds, one expects that the decrease in the Metal:B ratio will suppress the magnetism [193], while keeping the system metallic and giving rise to interesting low-temperature effects, such as superconductivity. Therefore, B-rich transition-metal borides remain tantalizing, but also difficult to synthesize.

Cobalt borides share many similarities with the Fe-B compounds. Co_2B and CoB are isostructural to Fe_2B and FeB , respectively, but they show a somewhat weaker magnetism. Co_2B becomes ferromagnetic below $T_c = 433$ K, whereas CoB is a paramagnetic metal [22]. Remarkably, no cobalt borides with the Co:B ratio below 1:1 have been reported. Here, report on high-pressure high-temperature synthesis, crystal structure, magnetic properties, and electronic structure of a novel hard boride Co_5B_{16} that fills this gap. This new compound reveals paramagnetic behavior related to a nearly complete occupation of the localized Co $3d$ states.

5.3.3. Material and methods

Starting materials and synthesis

Single-crystals of Co_5B_{16} were synthesized at pressure of 15 GPa and a temperature of 1873–1573 K (heating duration was 40 min) in the Kawai-type multi-anvil apparatus [178] using a 1000-ton (Hymag) hydraulic press. As starting materials we used a cobalt wire (Goodfellow, 99.5% purity) and a boron powder (Chempur Inc., 99.99% purity) which were enclosed into a h -BN capsule. The pressure was calibrated based on the phase transitions of standard materials and the temperature was determined using a W3Re/W25Re thermocouple.

Single crystal XRD

A black lustrous prismatic crystal of Co_5B_{16} with a size of $0.07 \times 0.05 \times 0.05$ mm³ was used for the crystal structure investigation by means of single-crystal X-ray diffraction. The diffraction data were collected at ambient temperature using a four-circle Oxford Diffraction Xcalibur diffractometer ($\lambda = 0.7107$ Å) equipped with an Xcalibur Sapphire2 CCD detector. The intensities of the reflections were measured by step scans in omega-scanning with a narrow step width of 0.5° . The data collection and their further integration were performed with the CrysAlisPro software [179]. Absorption corrections were applied empirically by the Scale3 Abspack program implemented in CrysAlisPro. The structure was solved by the direct method and refined by the full matrix least-squares in the anisotropic approximation for all atoms using SHELXTL software [124] implemented in the X-Seed program package [194]. The X-ray diffraction experimental details and crystallographic characteristics of Co_5B_{16} are presented in

Table 5.3.3-1 and Table 5.3.3-2. The DIAMOND software [162] was used to create molecular graphics.

The crystallographic data of Co₅B₁₆ and further details of the crystal structure investigation have been deposited in the Inorganic Crystal Structure Database [166] and may be obtained free of charge from Fachinformationszentrum Karlsruhe, 76344 Eggenstein-Leopoldshafen, Germany (fax: (+49)7247-808-666; e-mail: crysdata@fiz-karlsruhe.de, http://www.fiz-karlsruhe.de/request_for_deposited_data.html) on quoting the deposition number CSD-427205.

Hardness measurements

Vickers hardness (H_v) was measured using a microhardness tester (M-400-G2, LECO Corporation) under loads of 0.5 kgf (4.9 N), 1 kgf (9.8 N) and 1.5 kgf (14.7 N). The average value of hardness was found to be $H_v = 30.1 \pm 2$ GPa.

Magnetic properties

Magnetic susceptibility was measured with the MPMS SQUID magnetometer in the temperature range 2–380 K in magnetic fields up to 5 T. Heat capacity measurements were attempted with Quantum Design PPMS in zero field using relaxation technique, but no detectable signal could be obtained because of the diminutively small sample size.

Electronic structure calculations

Electronic structure of Co₅B₁₆ was calculated in the framework of density functional theory (DFT) using the FPLO code [195] and Perdew-Wang flavor of exchange-correlation potential (LDA) [196]. Reciprocal space was sampled with 135 k -points in the symmetry-irreducible part of the first Brillouin zone, and the convergence with respect to the number of k -points has been carefully checked.

Table 5.3.3-1 Experimental details and crystallographic characteristics for Co₅B₁₆.

Empirical formula	Co ₅ B ₁₆
Formula weight (g/mol)	467.61
Temperature (K)	296(2)
Wavelength (Å)	0.7107
Crystal system	Orthorhombic
Space group	<i>Pmma</i>
<i>a</i> (Å)	19.1736(12)
<i>b</i> (Å)	2.93290(10)
<i>c</i> (Å)	5.4886(2)
<i>V</i> (Å³)	308.65(2)
<i>Z</i>	2
Calculated density (g/cm³)	5.032
Linear absorption coefficient (mm⁻¹)	13.061
<i>F</i>(000)	430
Crystal size (mm³)	0.07 x 0.05 x 0.05
Theta range for data collection (deg.)	3.71 to 30.48
Completeness to theta = 25.00°	99.7 %
Index ranges	-20 < <i>h</i> < 27, -4 < <i>k</i> < 4, -7 < <i>l</i> < 7
Reflections collected	3345
Independent reflections / <i>R</i>_{int}	569 / 0.0532
Max. and min. transmission	0.5612 and 0.4617
Refinement method	Full matrix least squares on <i>F</i> ²
Data / restraints / parameters	569 / 0 / 67
Goodness of fit on <i>F</i>²	1.145
Final <i>R</i> indices [<i>I</i> > 2σ(<i>I</i>)]	<i>R</i> ₁ = 0.0282, <i>wR</i> ₂ = 0.0544
<i>R</i> indices (all data)	<i>R</i> ₁ = 0.0370, <i>wR</i> ₂ = 0.0569
Largest diff. peak and hole (e / Å³)	0.869 and -0.882

Table 5.3.3-2 Atomic coordinates, positions and equivalent isotropic displacement parameters for Co₅B₁₆.

Atom	Wyckoff site	<i>x</i>	<i>y</i>	<i>z</i>	$U_{eq}^a, \text{\AA}^2$
Co(1)	4 <i>i</i>	0.15330(3)	0	0.57345(11)	0.0048(2)
Co(2)	4 <i>j</i>	0.18369(3)	0.5	0.95008(12)	0.0046(2)
Co(3)	2 <i>a</i>	0	0	0	0.0045(2)
B(1)	2 <i>e</i>	0.25	0	0.7796(14)	0.0067(14)
B(2)	4 <i>i</i>	0.1614(3)	0	0.2119(9)	0.0044(9)
B(3)	4 <i>j</i>	0.0700(3)	0.5	0.5066(10)	0.0062(9)
B(4)	2 <i>f</i>	0.25	0.5	0.6068(14)	0.0073(14)
B(5)	4 <i>i</i>	0.678(3)	0	0.3065(10)	0.0061(10)
B(6)	4 <i>i</i>	0.1050(2)	0	0.9840(10)	0.0048(9)
B(7)	4 <i>j</i>	0.2026(3)	0.5	0.3273(10)	0.0055(9)
B(8)	4 <i>j</i>	0.0091(3)	0.5	0.2906(9)	0.0064(10)
B(9)	4 <i>j</i>	0.0772(3)	0.5	0.8208(10)	0.0056(10)

^a U_{eq} is defined as one third of the trace of the orthogonalized U^{ij} tensor.

Table 5.3.3-3 Co...B interatomic distances in CoB₁₂ and CoB₉ polyhedra (in Å).

Co(1)B ₁₂			Co(2)B ₉			Co(3)B ₁₂		
Co(1)–B(2)	1x	1.991(5)	Co(2)–B(2)	2x	2.097(4)	Co(3)–B(2)	2x	2.015(5)
Co(1)–B(1)	1x	2.172(4)	Co(2)–B(7)	1x	2.102(5)	Co(3)–B(7)	2x	2.126(5)
Co(1)–B(5)	1x	2.198(5)	Co(2)–B(6)	2x	2.112(3)	Co(3)–B(6)	4x	2.174(4)
Co(1)–B(3)	2x	2.199(4)	Co(2)–B(1)	2x	2.155(3)	Co(3)–B(1)	4x	2.304(4)
Co(1)–B(7)	2x	2.206(4)	Co(2)–B(9)	1x	2.162(5)			
Co(1)–B(4)	2x	2.3709(8)	Co(2)–B(4)	1x	2.273(7)			
Co(1)–B(6)	1x	2.436(5)						
Co(1)–B(9)	2x	2.475(4)						
<Co(1)–B>		2.275(5)	<Co(2)–B>		2.141(7)	<Co(3)–B>		2.183(5)

Table 5.3.3-4 Interatomic distances in metal borides with related structures.

Metal boride	<i>M–M</i> distances, Å	<i>M–B</i> distances, Å	<i>B–B</i> distances, Å	Reference
Co₅B₁₆	2.9329(1)	1.991(5)–2.475(4)	1.654(7)– 1.908(7)	This work
CrB₄	2.8681(5)	2.053(4)	1.743(6)	[13]
		2.153(4)	1.835(4)	
		2.178(3)	1.868(6)	
		2.261(3)		
FeB₄	2.9990(3)	2.009(4)	1.714(6)	[2]
		2.109(4)	1.8443(3)	
		2.136(3)	1.894(6)	
		2.266(3)		
MnB₄	2.7006(6), 3.1953(7)	1.999(4)–2.310(4)	1.703(6)–1.893(8)	[14]

5.3.4. Results and discussion

Crystal structure of Co₅B₁₆

Single-crystals of Co₅B₁₆ were synthesized at the pressure of 15 GPa and the temperature of 1873–1573 K. The structure of Co₅B₁₆ is orthorhombic (*Pmma* space group, Table 5.3.3-1, Table 5.3.3-2, Table 5.3.3-3, Table 5.3.3-4). Similar to structures of other boron-rich metal borides, it can be described based on a rigid network of boron atoms. In Co₅B₁₆ one can easily see honeycomb-like stripes (Figure 5.3.4-1) oriented along the *b*-axis and condensed into a complicated ramous structure. Such an arrangement of boron atoms gives rise to the straight, channel-like voids along the *b*-axis. Cobalt atoms occupy these voids creating infinite rows. Metal-metal distances in the rows are all equal, but they are larger than the sum of metallic radii of Co atoms (see Table 5.3.3-4). This is similar to the arrangement of metal atoms in other B-rich transition-metal borides, such as CrB₄ and FeB₄ [128,177], but different from that in MnB₄. Although MnB₄ has the structure closely related to that of CrB₄ and FeB₄, Mn–Mn distances in MnB₄ are not equal due to the Peierls distortion [130,197].

Despite some allusion to the tetraboride CrB₄ and FeB₄ structures, the Co polyhedra in Co₅B₁₆ are distinctly different. The Co atoms occupy three independent crystallographic sites, Co(1),

$\text{Co}(2)$ and $\text{Co}(3)$ (Table 5.3.3-2). The structure of Co_5B_{16} can be visualized in terms of packing of three kinds of Co-B polyhedra (Figure 5.3.4-1). An asymmetric part of the structure (Figure 5.3.4-1a) consists of three units: an irregular $\text{Co}(3)\text{B}_{12}$ polyhedron, its distorted counterpart $\text{Co}(1)\text{B}_{12}$, and a $\text{Co}(2)\text{B}_9$ polyhedron. Polyhedra of each kind ($\text{Co}(2)\text{B}_9$, $\text{Co}(1)\text{B}_{12}$ and $\text{Co}(3)\text{B}_{12}$) pack in columns by sharing common upper and bottom faces and create their own infinite columns parallel to the b -axis (Figure 5.3.4-1b). $\text{Co}(1)\text{B}_{12}$ polyhedra, as well as $\text{Co}(3)\text{B}_{12}$ ones, share the opposite parallelogram-shaped faces, which are parallel to the ac -plane. The Co atoms in these columns have the same y -coordinates. $\text{Co}(2)\text{B}_9$ polyhedra pack *via* common triangular faces and each polyhedron sticks to the neighboring $\text{Co}(1)\text{B}_{12}$ one through a side quadrilateral face (Figure 5.3.4-1b). As a result $\text{Co}(1)$ - and $\text{Co}(2)$ - atoms in neighboring columns are shifted on $b/2$ along the b -axis. A polyhedron topologically similar to $\text{Co}(2)\text{B}_9$ can be deduced from the $\text{Co}(3)\text{B}_{12}$ one by removing at once vertices of the two parallelogram-shaped faces of CoB_{12} and one vertex from the rectangular in the equatorial plain of the latter.

The Co–B distances in $\text{Co}(3)\text{B}_{12}$ vary from 2.015(5) to 2.304(4) Å and an average value is 2.183(5) Å (Table 5.3.3-3). $\text{Co}(1)\text{B}_{12}$ shares two of its side quadrilateral faces with the $\text{Co}(2)\text{B}_9$ polyhedra (see Figure 5.3.4-1). This leads to a distortion of the $\text{Co}(1)\text{B}_{12}$ geometry compared to

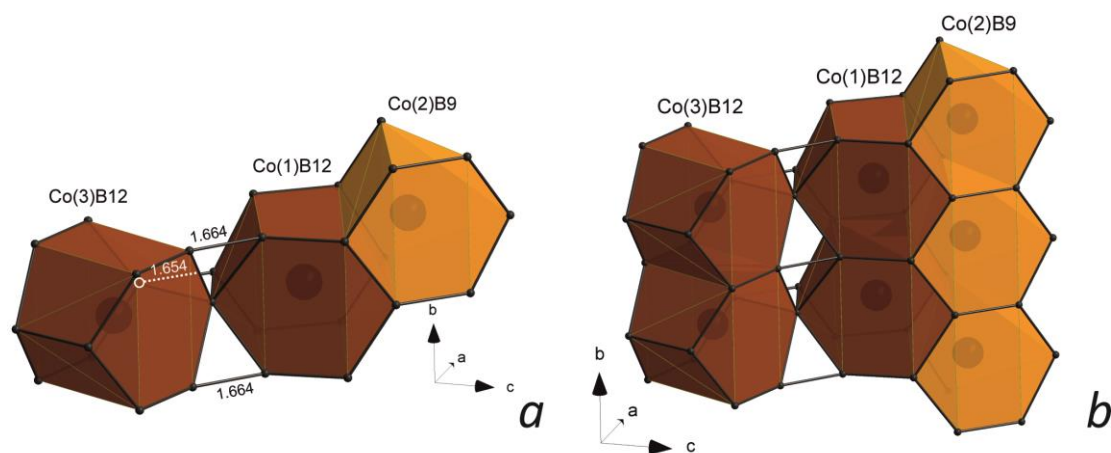


Figure 5.3.4-1 A polyhedral model of the structure of Co_5B_{16} . (a) An asymmetric part of the structure consisting of three units: an irregular $\text{Co}(3)\text{B}_{12}$ polyhedron, its distorted counterpart $\text{Co}(1)\text{B}_{12}$, and a $\text{Co}(2)\text{B}_9$ polyhedron. (b) Packing of the polyhedra in columns along the b -axis by sharing common faces. The y coordinates of Co atoms in light and dark polyhedra differ by $1/2$. B–B bonds are highlighted by bold lines, the shortest distances are labeled.

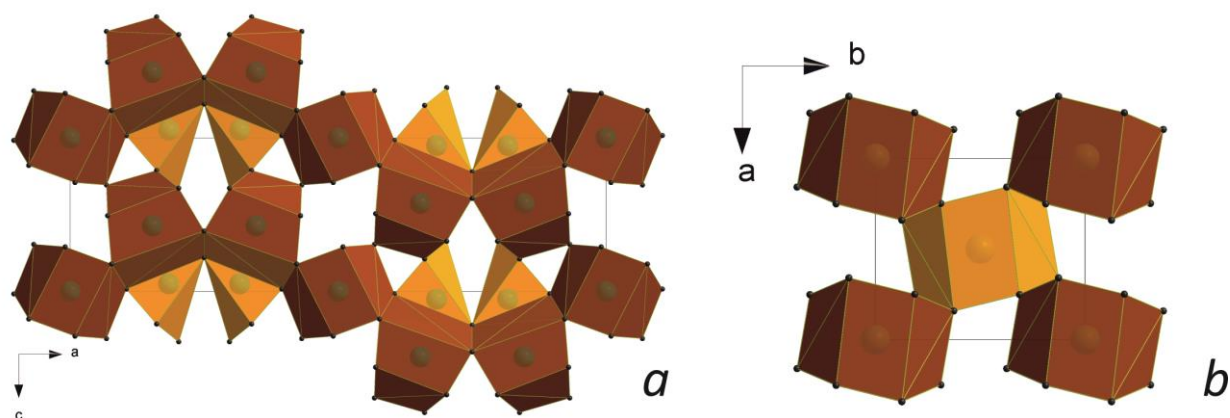


Figure 5.3.4-2 Comparison of the crystal structures of Co_5B_{16} and MB_4 ($M = \text{Cr, Fe, Mn}$) [128,130,177]. (a) Co_5B_{16} ; (b) MB_4 . In the both structures MB_{12} polyhedra pack in columns by sharing common parallelogram-shaped faces either along the b - (Co_5B_{16}) or c -axis (MB_4). Co_5B_{16} contains columns constructed of $\text{Co}(2)\text{B}_9$ polyhedra. Light and dark polyhedra differ in position along b - or c -axis, respectively.

that of $\text{Co}(3)\text{B}_{12}$: the Co-B distances' range is 1.991(5) to 2.475(4) Å and an average value increases to 2.275(5) Å. Due to the smaller coordination number of Co(2), the $\text{Co}(2)\text{B}_9$ polyhedron is the most compact with the average $\langle \text{Co}(2)\text{--B} \rangle$ distance of 2.141(7) Å.

Figure 5.3.4-2 provides a comparison of the structure of Co_5B_{16} with that of MB_4 tetraborides, where $M = \text{Cr, Fe, Mn}$ [128,130,177]. In tetraborides, there is only one kind of MB_{12} polyhedra packed in columns (Figure 5.3.4-2b), so that each column is shifted by $c/2$ along the c -axis with respect to its four nearest neighbors (shown in different colors, light and dark). In Co_5B_{16} , every column of $\text{Co}(3)\text{B}_{12}$ polyhedra has four neighboring $\text{Co}(1)\text{B}_{12}$ columns and shares common B(5) vertices with two of them, while the other two are attached by common edges, which form ...–B(6)–B(9)–B(6)–... zigzag chains (Figure 5.3.4-2a).

The B–B distances in the structure of Co_5B_{16} vary from 1.654(7) to 1.908(7) Å (Table 5.3.3-4). The shortest bond located at the ac plane is observed between B atoms of the neighboring $\text{Co}(3)\text{B}_{12}$ and $\text{Co}(1)\text{B}_{12}$ polyhedra. This is the smallest value of the B–B bond length among transition metal borides with related structures (Table 5.3.3-4). Dense atomic packing and short B–B contacts make Co_5B_{16} rather hard with the measured Vickers hardness $H_v = 30 \pm 2$ GPa, the value slightly higher than reported for CrB_4 [177], but lower than that of superhard FeB_4 [128].

Magnetic and electronic properties of Co₅B₁₆

Similar to FeB₄, the preparation of single-phase samples of Co₅B₁₆ is exceedingly difficult. The largest phase-pure sample available so far is about 0.4 mg and can be used for magnetization measurements only. Magnetic susceptibility shown in Figure 5.3.4-3 exhibits a weak temperature dependence and a more pronounced field dependence that is likely related to trace amounts of a ferromagnetic impurity. In higher magnetic fields, the impurity signal is suppressed, and a residual temperature-independent susceptibility of about $\chi_0 = 2 \times 10^{-4}$ emu/mol is observed (Figure 5.3.4-3). Therefore, Co₅B₁₆ behaves as a standard Pauli paramagnet. Small humps in the susceptibility below 100 K require further investigation. Our measurements in low magnetic fields did not show any signatures of superconductivity above 2 K.

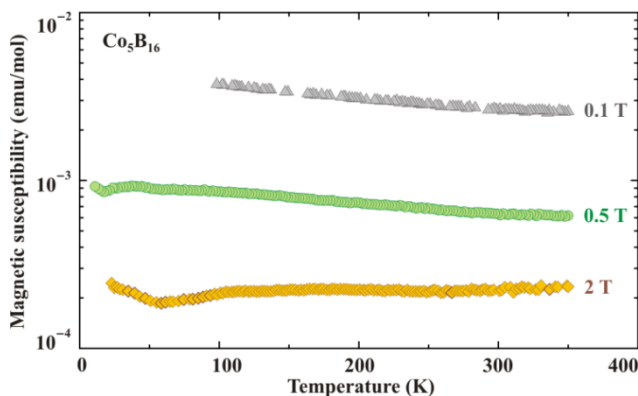


Figure 5.3.4-3 Magnetic susceptibility of Co₅B₁₆ measured in the applied fields of 0.1 T, 0.5 T, and 2 T. In the 0.1 T data, some of the data points were removed because of the low signal and strong noise.

Electronic structure of Co₅B₁₆ suggests metallic behavior (Figure 5.3.4-4), with a relatively high density of states at the Fermi level: $N(E_F) \sim 1 \text{ eV}^{-1}/\text{Co}$, similar to $1 \text{ eV}^{-1}/\text{Fe}$ in FeB₄ [18]. By correcting our experimental χ_0 for the core diamagnetism $\chi_{\text{dia}} \sim -2 \times 10^{-4} \text{ emu/mol}$ [198], we arrive at the Pauli contribution $\chi_{\text{Pauli}} = \chi_0 - \chi_{\text{dia}} \sim 4 \times 10^{-4} \text{ emu/mol}$ that is comparable, yet larger than the value of $1.6 \times 10^{-4} \text{ emu/mol}$ expected from our calculated $N(E_F)$. The states at the Fermi level are of mixed Co 3d and B 2p origin, but most of the Co 3d states are below the Fermi level and form a relatively narrow band complex between -3 eV and the Fermi level (Figure 5.3.4-4). These narrow bands should host more localized electrons that tend to become

magnetic. In Co_5B_{16} , the complete filling of these localized states excludes the magnetism. Indeed, spin-polarized calculations for Co_5B_{16} always converge to the non-magnetic solution.

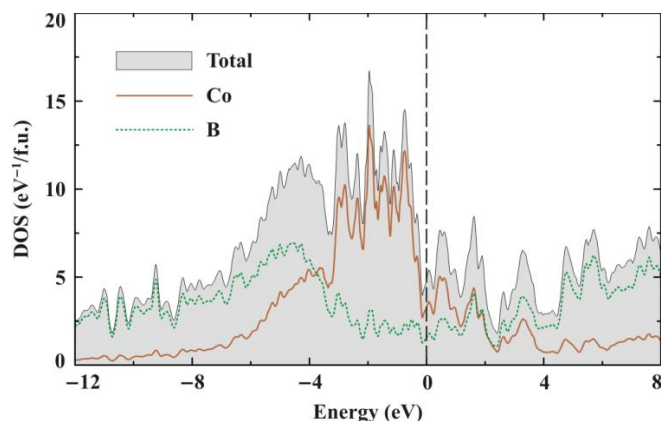


Figure 5.3.4-4 LDA density of states (DOS) for Co_5B_{16} . The total DOS is shown by shading. The solid and dotted lines denote the Co and B contributions, respectively. The Fermi level is at zero energy.

5.3.5. Conclusions

In conclusion, the novel boron-rich cobalt boride Co_5B_{16} synthesized at high-pressure and high-temperature conditions was found to be non-magnetic that is in line with the trend of the reduced magnetism upon the decrease in the TM:B ratio. Indeed, Co_3B ($T_C = 747$ K) [199] and Co_2B ($T_C = 433$ K) [22] are ferromagnetic, whereas CoB [22] and the Co_5B_{16} are non-magnetic metals. Early studies [200] argued that the behavior of TM-rich borides resembles that of pure transition metals, because boron atoms simply change electron concentration in the TM $3d$ bands. Apparently, this no longer holds for B-rich TM borides, where a large contribution of boron states is present at the Fermi level (see Figure 5.3.4-4), and Pauli-paramagnetic behavior is observed.

5.3.6. Acknowledgements

A.T. was supported by the Mobilitas grant MTT77 from the ESF. We thank Deepa Kasinathan and Valeriy Verchenko for technical assistance in magnetic susceptibility measurements. H.G. gratefully acknowledges financial support of the Alexander von Humboldt Foundation. The work was supported by the German Research Foundation (DFG). N.D. thanks the DFG for financial support through the Heisenberg Program and the DFG research grant (No. DU 954-8/1).

5.4. X-ray single-crystal and Raman study of knorringite, $\text{Mg}_3(\text{Cr}_{1.58}\text{Mg}_{0.21}\text{Si}_{0.21})\text{Si}_3\text{O}_{12}$, synthesized at 16 GPa and 1600 °C

E.A. Bykova¹, A.V. Bobrov², E.A. Sirotkina², L. Bindi^{3,4}, S.V. Ovsyannikov⁵, L.S. Dubrovinsky⁵, Yu.A. Litvin⁶

¹*Material Physics and Technology at Extreme Conditions, Laboratory of Crystallography, University of Bayreuth, 95440 Bayreuth, Germany*

²*Department of Petrology, Geological Faculty, Moscow State University, 119234 Leninskie Gory, Moscow, Russia*

³*Dipartimento di Scienze della Terra, Università di Firenze, Via La Pira 4, 50121 Florence, Italy*

⁴*C.N.R., Istituto di Geoscienze e Georisorse, Sezione di Firenze, Via La Pira 4, 50121 Florence, Italy*

⁵*Bayerisches Geoinstitut, University of Bayreuth, 95440 Bayreuth, Germany*

⁶*Institute of Experimental Mineralogy, 142432 Moscow District, Chernogolovka, Russia*

Phys. Chem. Miner. **41**, 267–272 (2013).

5.4.1. Abstract

The crystal structure of a knorringite-type compound, $\text{Mg}_3(\text{Cr}_{1.58}\text{Mg}_{0.21}\text{Si}_{0.21})\text{Si}_3\text{O}_{12}$, synthesized in a multi-anvil press at $P = 16$ GPa and $T = 1600$ °C, was refined from single-crystal X-ray diffraction data up to $R = 2.36$ % for 314 independent reflections. Garnet was found to be cubic, space group $Ia\bar{3}d$, with the unit cell parameters $a = 11.5718(1)$ Å, $V = 1549.54(2)$ Å³. The knorringite crystal studied contains 21 mol. % of majorite end-member. The structural characterization of knorringitic garnet is important because the study of its thermodynamic constants provides new constraints on thermobarometry of peridotitic garnet assemblages of the lowermost upper mantle. The Raman spectra of synthetic knorringite have been obtained for the first time.

5.4.2. Introduction

Garnet is an important constituent of the upper mantle rocks being stable over a wide range of pressures. Knorringite, $\text{Mg}_3\text{Cr}_2\text{Si}_3\text{O}_{12}$, is the chromium end-member and it is usually found either in rocks from the lowermost upper mantle or as inclusions in diamonds and constituents of ultramafic mantle xenoliths [32–34]. It was established that incorporation of knorringite in garnet does occur from 3 GPa (beyond the diamond depth facies), and the concentration of chromium achieves significant values (5–10 wt % Cr_2O_3 and more) in the pressure range of stability of most of natural diamonds (i.e. 4–7 GPa) [35], which is an indicative feature of diamondiferous dunite–harzburgite paragenesis of the lithospheric mantle.

Despite the importance of the knorringite component in garnets in the lowermost upper mantle, the stability and high-pressure phase relations of knorringite are still controversial. Its stability field has been investigated in several studies [36–41]. Ringwood [36] reported synthesis of knorringitic garnet in a quite wide pressure range (8–16 GPa) at temperatures of 1400–1500 °C. Irifune et al. [37] demonstrated the stability of knorringite at pressures >11.5 GPa at 1200 °C and at > 11.8 GPa at 1400 °C. By contrast, Turkin et al. [41] reported on the appearance of knorringite at significantly lower pressures of 8.0–9.5 GPa at 1200–1800 °C with a negative slope of phase boundary. Klemme [38] reported the synthesis of knorringite coexisting with eskolaite (Cr_2O_3) at 16 GPa and 1600 °C. Taran et al. [39] synthesized knorringite at 9–16 GPa and 1300–1600 °C. More recently it was demonstrated that knorringitic garnet synthesized in high-pressure experiments always contained admixture of majorite, which resulted in the appearance of eskolaite in run products [40,42].

The paucity of structural studies on Cr-rich garnets does not allow to fully understand the changes of thermodynamic and structural properties as a function of Cr incorporation in high-pressure garnets. There were some predictions based on the structure of natural garnets and empirical laws with account for cation radii [201], least-squares refinement of interatomic distances [202], and first-principles calculations based on density functional theory [203]. Space group $Ia\bar{3}d$ and lattice parameter of $a = 11.600(1)$ Å [36] and $a = 11.596(1)$ Å [37] have been reported from X-ray power diffraction studies. Recently the structure of a synthetic

knorringitic garnet with composition $\text{Mg}_3(\text{Cr}_{1.60}\text{Mg}_{0.20}\text{Si}_{0.20})\text{Si}_3\text{O}_{12}$ was refined by the Rietveld method using high-resolution synchrotron X-ray powder diffraction data [42].

Here we report new high-quality single-crystal diffraction and Raman spectroscopy data on knorringitic garnet with composition $\text{Mg}_3(\text{Cr}_{1.58}\text{Mg}_{0.21}\text{Si}_{0.21})\text{Si}_3\text{O}_{12}$, synthesized at 16 GPa and 1600 °C.

5.4.3. Experimental methods

Synthesis, EMPA, and Raman spectroscopy

Experiments at $P = 16$ GPa and $T = 1600$ °C were performed on a multi-anvil apparatus at the Bayerisches Geoinstitut (Bayeruth, Germany). The starting material ($\text{Mg}_3\text{Cr}_2\text{Si}_3\text{O}_{12}$) was a powdered mixture of chemically pure oxides (MgO , Cr_2O_3 , and SiO_2) homogenized at room temperature using ethanol and then dried in the stove at 100 °C. The details of experimental assembly and procedures were already described elsewhere [204]. A starting mixture was placed into a capsule of 3.5 mm in height and 2 mm in diameter made of a rhenium foil. High temperature was generated using a LaCrO_3 heater. The capsule was insulated from the heater by a MgO cylinder. The cell assembly with the sample was compressed between eight cubic tungsten carbide anvils with corners truncated to 5.0 mm edge lengths. The accuracy in determination of pressure and temperature was estimated to be ± 0.5 GPa and ± 50 °C, respectively. Typical heating times were about 4 h. A sample was rapidly quenched to ambient temperature by switching off a power supply with a quench rate of >200 °C.

Run products were subjected to visual examinations for homogeneity by using a binocular microscope. In order to obtain a preliminary phase composition of garnet, a piece of the sample was embedded into

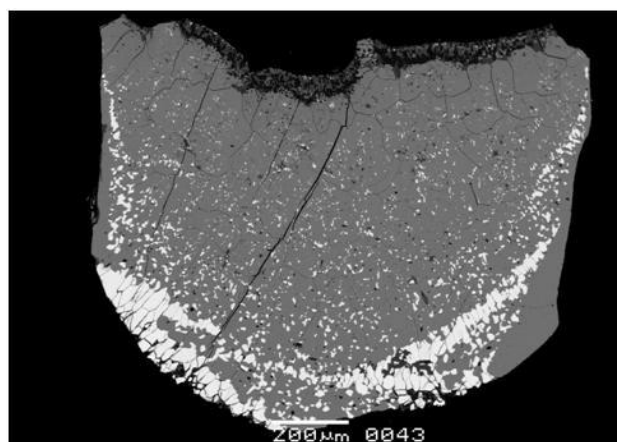


Figure 5.4.3-1 BSE image of an aggregate of euhedral knorringitic garnet crystals (gray) and small eskolaite (Cr_2O_3) grains (white) synthesized at $P = 16$ GPa and $T = 1600$ °C (Sample H3420).

epoxy and polished and then analyzed by using an energy-dispersive electron microprobe (Figure 5.4.3-1). The composition of the resulting products was studied in the Laboratory of Local Methods of Matter Study, Geological Faculty, Moscow State University, by using a Jeol JSM-6480LV electron microscope equipped with an energy-dispersive electron microprobe INCA Energy. Successively, Raman spectra were recorded from polished surfaces of single crystalline samples. The LabRam system (Horiba Scientific Inc.) with a He–Nd-laser (excitation wavelength 632 nm) was used for collection of the Raman spectra.

Data collection and crystal structure refinement

A transparent single crystal of knorringitic garnet was extracted from the experimental batch and mounted on an Oxford Diffraction Xcalibur diffractometer equipped with a Xcalibur Sapphire2 CCD detector using Mo radiation (Table 5.4.3-1). Data collection was carried out by measuring of intensities by omega-scanning of narrow (0.5°) frames. Data reduction was done with the CrysAlisPro program [157] and the absorption correction using ABSPACK scaling algorithm which is included in the CrysAlis RED software [158]. The full-matrix least-squares program SHELXL-97 [124] was used for the refinement of the structure. The occupancies of all the atoms were left free to vary. Cubic (Mg) and tetrahedral (Si) positions were found fully occupied and then their occupancy was fixed to lower the number of refined parameters. The refined electron number at the octahedral position, i.e. 21.7, was found to be in excellent agreement with the cation population obtained from the electron microprobe analysis (see below). The introduction of anisotropic temperature factors for all the atoms led to $R_1 = 2.03\%$ for 284 observed reflections [$F_o > 4\sigma(F_o)$] and $R_1 = 2.36\%$ for all 314 independent reflections. Neutral scattering curves for Cr, Mg, Si and O were taken from the *International Tables for X-ray Crystallography* [205]. Inspection of the difference Fourier map revealed that maximum positive and negative peaks were 0.59 and -0.37 e/Å³, respectively.

Experimental details and R indices are given in Table 5.4.3-2. Fractional atomic coordinates and anisotropic displacement parameters are shown in Table 5.4.3-2 and Table 5.4.3-3, respectively. Bond distances are given in Table 5.4.3-4.

Table 5.4.3-1 Crystal data and structure refinement for knorringite.

Empirical formula	Mg _{3.21} Cr _{1.58} Si _{3.21} O ₁₂
Formula weight (g/mol)	442.30
Temperature (K)	296(2)
Wavelength (Å)	0.7107
Crystal system	Cubic
Space group	<i>la-3d</i>
<i>a</i> (Å)	11.5718(1)
<i>V</i> (Å³)	1549.54(2)
<i>Z</i>	8
Calculated density (g/cm³)	3.792
Absorption correction	multi-scan (ABSPACK; [206])
Linear absorption coefficient (mm⁻¹)	3.089 mm ⁻¹
<i>F</i>(000)	1739
Crystal size (mm³)	0.10 × 0.08 × 0.08
Theta range for data collection (°)	4.31 to 35.98
Index ranges	-18 < <i>h</i> < 19, -18 < <i>k</i> < 19, -18 < <i>l</i> < 18
Reflections collected	9827
Observed reflections [<i>F</i>_o > 4σ(<i>F</i>_o)]	284
Independent reflections / <i>R</i>_{int}	314 / 0.0329
Completeness to theta = 25.00°	100.0 %
Max. and min. transmission	0.7902 and 0.7476
Refinement method	Full matrix least squares on <i>F</i> ²
Data / restraints / parameters	314 / 0 / 18
Goodness of fit on <i>F</i>²	1.313
Final <i>R</i> indices [<i>I</i> > 2σ(<i>I</i>)]	<i>R</i> ₁ = 0.0203, <i>wR</i> ₂ = 0.0626
<i>R</i> indices (all data)	<i>R</i> ₁ = 0.0236, <i>wR</i> ₂ = 0.0648
Largest diff. peak and hole (e / Å³)	0.586 and -0.366

Table 5.4.3-2 Atomic coordinates and equivalent isotropic displacement parameters for the selected crystal.

Atom	Wyck.	S.O.F.	x/a	y/b	z/c	U_{eq}^a (Å ²)
Cr1	16a	0.789	0	0	0	0.004(1)
Mg1	16a	0.105	0	0	0	0.004(1)
Si1	16a	0.105	0	0	0	0.004(1)
Mg2	24c		1/8	0	1/4	0.012(1)
Si2	24d		3/8	0	1/4	0.006(1)
O1	96h		0.03373(5)	0.05297(5)	0.65627(5)	0.009(1)

^a U_{eq} is defined as one third of the trace of the orthogonalized U_{ij} tensor.

Table 5.4.3-3 Anisotropic displacement parameters (Å²·10³) for the selected crystal

	U_{11}	U_{22}	U_{33}	U_{23}	U_{13}	U_{12}
Cr(1)	4(1)	4(1)	4(1)	0(1)	0(1)	0(1)
Mg(1)	4(1)	4(1)	4(1)	0(1)	0(1)	0(1)
Si(1)	4(1)	4(1)	4(1)	0(1)	0(1)	0(1)
Mg(2)	6(1)	15(1)	15(1)	5(1)	0	0
Si(2)	5(1)	6(1)	6(1)	0	0	0
O(1)	8(1)	11(1)	9(1)	1(1)	-1(1)	2(1)

Table 5.4.3-4 Bond lengths (Å) and angles (°) for the selected crystal.

Cr,Mg,Si(1)-O(1)	1.9489(6)	O(1)#1-Cr(1)-O(1)#2	92.46(3)
Cr,Mg,Si(1)-Mg(2)	3.2344	O(1)#12-Mg(2)-O(1)#13	68.29(3)
Mg(2)-O(1)#4	2.2194(6)	O(1)#4-Mg(2)-O(1)#15	93.413(18)
Mg(2)-O(1)#15	2.3414(6)	O(1)#13-Mg(2)-O(1)#15	72.43(3)
Mg(2)-Si(2)	2.8930	O(1)#14-Mg(2)-O(1)#15	71.62(2)
Si(2)-O(1)#19	1.6332(6)	O(1)#19-Si(2)-O(1)#13	114.72(2)
		O(1)#19-Si(2)-O(1)#20	99.42(4)

Symmetry transformations used to generate equivalent atoms:

#1 - y, -z+1/2, x, #2 z-1/2, -x, y, #4 -x, y, z-1/2, #12 x+1/4, -z+3/4, -y+1/4, #13 x+1/4, z-3/4, y+1/4,

#14 -x, -y, -z+1, #15 -z+3/4, y-1/4, -x+1/4, #19 -x+1/2, y, -z+1, #20 -x+1/2, -y+0, z-1

5.4.4. Results and discussion

The products of the HP-HT syntheses consisted of massive aggregate of pink garnet crystals with eskolaite in interstitials or rarely as inclusion in garnets (Figure 5.4.3-1). No zoning was observed in the experimental products. The composition of knorringitic garnet obtained by averaging of 15 microprobe analyses was as follows (wt %): SiO₂ 43.53 (21), MgO 29.27 (16), Cr₂O₃ 27.05 (12), total 99.85, which suggested a chemical formula as Mg_{3.00}(Cr_{1.58}Mg_{0.21}Si_{0.21})Si_{3.00}O₁₂ on basis of 12 oxygen atoms. As it follows from the formula, garnet exhibits higher Mg and Si and lower Cr concentrations with respect to pure knorringite Mg₃Cr₂Si₃O₁₂, thus indicating a 21 mol % of majorite end-member. Such a composition is thus nearly identical to that studied by Juhin et al. [42] by Rietveld refinement of high-resolution synchrotron X-ray powder diffraction data.

The refined cubic cell parameter ($a = 11.5718(1)$ Å) is smaller than the previous experimental values obtained for knorringitic garnets by X-ray powder diffraction: 11.600 Å [36], 11.596(1) Å [37], 11.5954(5) Å [39], and 11.5935(1) Å [42]. All of these garnets contain variable portions of majorite admixture. Our parameter is also inconsistent with the value (11.6040 Å) calculated by Ottonello et al. [202] for pure knorringite. However, incorporation of the majorite component in knorringitic garnet results in a decrease of the cell parameter.

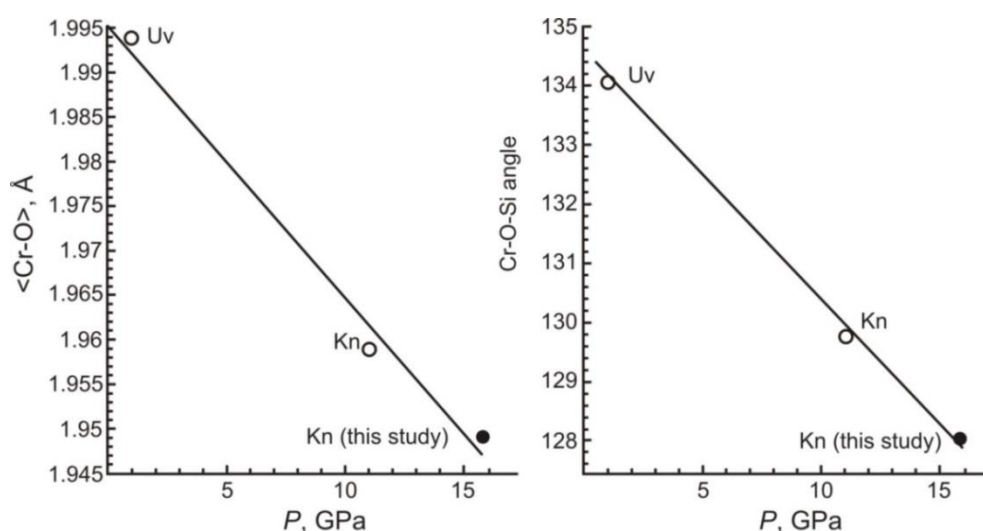


Figure 5.4.4-1 Dependencies of <Cr-O> distance (Å) and Cr-O-Si angle (°) on synthesis pressure (GPa) of Cr-bearing garnet end members. Uv, Ca₃Cr₂Si₃O₁₂ [207]; Kn, Mg₃Cr₂Si₃O₁₂ [42] and this study.

Although the close similarity between the crystal studied here and the powder analyzed by Juhin et al. [42], the Cr–O distance [1.9489(6) Å] obtained from the single-crystal structure refinement is smaller than the value [1.959(7) Å] from the Rietveld refinement. The octahedral bond distance obtained in our study is also smaller than those (1.958 and 1.960 Å) predicted by Novak and Gibbs [201] and Ottonello et al. [202], respectively, on the basis of a least-squares refinement procedure for natural samples. As it was already demonstrated by Juhin et al. [42], the Cr–O distance, as well as the Si–O–Cr angle in Cr-bearing garnets decrease with pressure. Such a dependence is confirmed by the data obtained in our work (Figure 5.4.4-1): the CrO_6 octahedron undergoes an increasing compression from uvarovite $\text{Ca}_3\text{Cr}_2\text{Si}_3\text{O}_{12}$ synthesized at ambient pressure [207] to knorringitic garnets synthesized at 11 [42] and 16 (this study) GPa.

The synthesized crystals were also examined by Raman spectroscopy. Figure 5.4.4-2 compares Raman spectra of the crystals studied in our work with those collected on pure majorite and uvarovite. A broad and weak peak near 600 cm^{-1} has been addressed to a Si–O–Si bending vibration involving both the SiO_4 tetrahedra and SiO_6 octahedra present in the structure of this high-pressure garnet [208]. The well-defined sharp modes between 800 and 1000 cm^{-1} are attributed to internal vibrations of the SiO_4 units, similar to those in normal garnets. A peak near 910 cm^{-1} is related to the ν stretching of the SiO_4 units. As our sample synthesized at 16 GPa belongs to the majorite–knorringite solid solution, Cr is responsible for a peak at $\sim 370\text{ cm}^{-1}$; the same mode is observed for pure uvarovite (Figure 5.4.4-2).

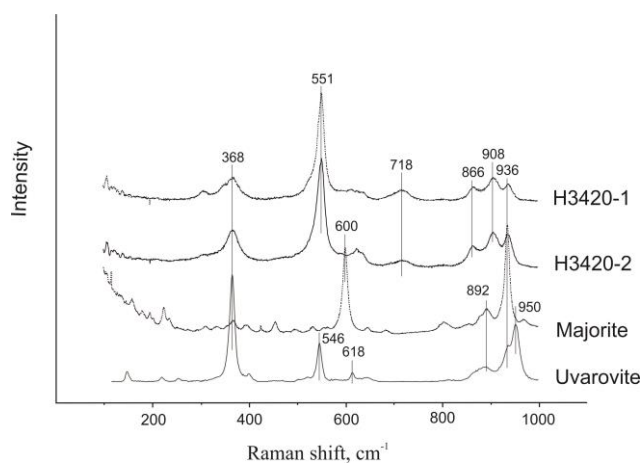


Figure 5.4.4-2 Raman spectra of knorringite (samples H3420-1 and H3420-2, this study) in comparison with majorite (<http://www.ens-lyon.fr/LST/Raman/spectres/majorite.pdf>) and uvarovite.

It is important to note that, similarly to previous studies, knorringitic garnet synthesized in our experiment contains admixture of majorite end-member. The latter is an important pressure indicator for garnets of mantle assemblages [209]. The concentration of aluminum and chromium in garnets decreases with pressure, whereas the amount of silicon in the octahedral site, as well as the concentration of divalent cations (Ca, Mg, Fe) and sodium, regularly increases [210], which results in the formation of garnet with the silicon content of >3 p.f.u. This is controlled by the beginning of dissolution of pyroxene components (mainly (Mg,Fe)SiO₃) in garnet already at 5 GPa [209]. The solubility of pyroxene in garnet increases with pressure achieving significant values at 10–15 GPa, which correspond to the lowermost upper mantle and transition zone. The relationship between majorite and knorringite at high pressure provides an evidence for similarity in their behavior, but, at the same time, this suggests a concurring reaction on pressure increase. Recently, the first experimental results were obtained for the knorringite–majorite (in chemical expression, MgO–SiO₂–Cr₂O₃) system in a wide range of PT-parameters [40]. In the light of the first single-crystal X-ray data on knorringite reported here, further careful investigations are needed to study the structural changes in the knorringite-majorite series.

5.4.5. Acknowledgments

The authors thank Sabrina Nazzareni for review and valuable comments. This study was supported by the Russian Foundation for Basic Research (project nos. 12-05-00426, 12-05-33044, and 14-05-31288) and by the Foundation of the President of the Russian Federation for Leading Scientific Schools (NSh-5877.2012.5).

5.5. Crystal chemistry of Fe³⁺-bearing (Mg, Fe)SiO₃ perovskite: a single-crystal X-ray diffraction study

R. Sinmyo¹, E. Bykova¹, C. McCammon¹, I. Kupenko^{1,2}, V. Potapkin^{1,2,3}, L. Dubrovinsky¹

¹Bayerisches Geoinstitut, Universitaet Bayreuth, D-95440 Bayreuth, Germany

²European Synchrotron Radiation Facility, BP 220, F-38043 Grenoble, France

³Jülich Centre for Neutron Science JCNS and Peter Grünberg Institut PGI, JARA-FIT, Forschungszentrum Jülich GmbH, D-52425 Jülich, Germany

Phys. Chem. Miner. **41**, 409–417 (2013).

5.5.1. Abstract

Magnesium silicate perovskite is the predominant phase in the Earth's lower mantle, and it is well known that incorporation of iron has a strong effect on its crystal structure and physical properties. To constrain the crystal chemistry of (Mg,Fe)SiO₃ perovskite more accurately, we synthesized single crystals of Mg_{0.946(17)}Fe_{0.056(12)}Si_{0.997(16)}O₃ perovskite at 26 GPa and 2073 K using a multianvil press and investigated its crystal structure, oxidation state and iron site occupancy using single-crystal X-ray diffraction and energy-domain Synchrotron Mössbauer Source spectroscopy. Single-crystal refinements indicate that all iron (Fe²⁺ and Fe³⁺) substitutes on the A-site only, where Fe³⁺/ΣFe ~ 20 % based on Mössbauer spectroscopy. Charge balance likely occurs through a small number of cation vacancies on either the A- or the B-site. The octahedral tilt angle (Φ) calculated for our sample from the refined atomic coordinates is 20.3°, which is 2° higher than the value calculated from the unit cell parameters ($a = 4.7877 \text{ Å}$, $b = 4.9480 \text{ Å}$, $c = 6.915 \text{ Å}$) which assumes undistorted octahedra. A compilation of all available single-crystal data (atomic coordinates) for (Mg,Fe)(Si,Al)O₃ perovskite from the literature shows a smooth increase of Φ with composition that is independent of the nature of cation substitution (e.g., Mg²⁺–Fe²⁺ or Mg²⁺Si⁴⁺–Fe³⁺Al³⁺ substitution mechanism), contrary to previous observations based on unit cell parameter calculations.

5.5.2. Introduction

It is widely accepted that MgSiO₃-dominant perovskite (referred to below as MgPv) is the most abundant phase in the Earth's lower mantle, and that this phase can accommodate a substantial amount of Fe, which is the third most abundant cation in the Earth's mantle. Many studies have attempted to understand details of the crystal structure of MgPv, because changes in this structure can have strong effects on its elastic and rheological properties as well as electrical/thermal conductivity [43–49]. MgPv has two cation sites, one that is a distorted 8- to 12-fold site (*A*-site, illustrated as a grey sphere in Figure 5.5.2-1) and another that is a 6-fold site (*B*-site, illustrated as BO₆ octahedra in Figure 5.5.2-1). The structural position (i.e., *A*- or *B*-site) and oxidation state (2+ or 3+) of a cation have a strong influence on whether or not iron spin transitions occur in MgPv under lower mantle pressure and temperature conditions [50–52]. For example, theoretical calculations predict that Fe³⁺ in the *B*-site of Al-free MgPv should undergo high-spin to low-spin crossover at 40–70 GPa, while Fe³⁺ in the *A*-site should be in the high-spin state at all mantle pressures [52]. The transition to the post-perovskite structure may also be linked to the nature of cation substitution in MgPv, since the transition can be related to the degree of octahedral tilting [53,54] which has been observed to depend on MgPv composition [44,46,55].

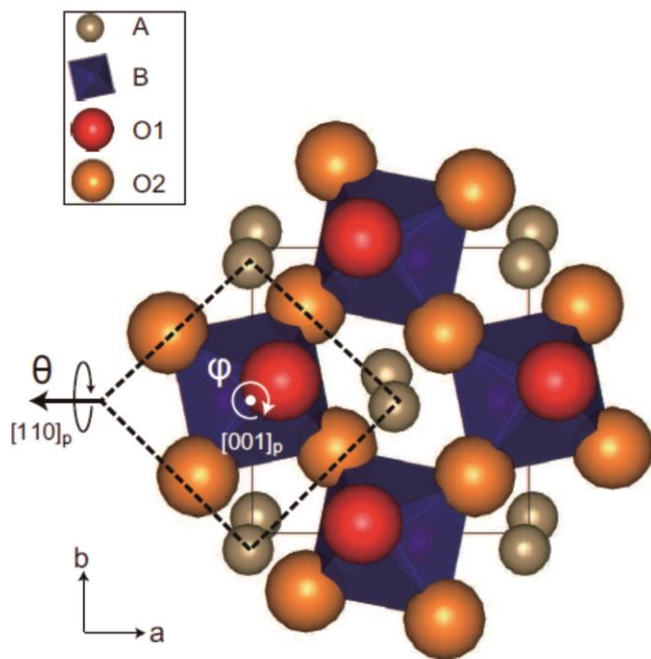


Figure 5.5.2-1 Schematic illustration of the crystal structure of *Pbnm* MgSiO₃ perovskite ($Z = 4$) viewed down the orthorhombic c axis, where the orthorhombic unit cell is indicated by solid lines. The pseudo-cubic unit cell ($Z = 1$) is shown as dashed lines, where the relation between the orthorhombic and cubic cell edges is a_p is $a \approx b \approx \sqrt{2} a_p$, $c \approx 2a_p$. Octahedral tilting, responsible for the orthorhombic distortion, can be viewed as a combination of tilting about the pseudo-cubic $[110]_p$ direction (angle θ) and the pseudo-cubic $[001]_p$ direction (angle φ), or described as a single tilt about the pseudo-cubic $[111]_p$ direction (angle Φ , not shown; [227]).

Fe^{2+} in MgPv has been shown to occupy the *A*-site using single-crystal X-ray diffraction and/or Mössbauer spectroscopy [56–60]. In contrast, the site preference of Fe^{3+} is not so unequivocal. Fe^{3+} in Al-free MgPv has been assigned to the *B*-site [58] or both the *A*- and *B*-sites [59] on the basis of Mössbauer spectroscopy. More recently, Hummer and Fei [61] suggested that Fe^{3+} substitutes on both the *A*- and *B*-sites in Al-free MgPv with 100 % $\text{Fe}^{3+}/\Sigma\text{Fe}$. Jephcoat et al. [62] reported that all iron (both Fe^{2+} and Fe^{3+}) occupied the *A*-site based on the results of Mössbauer spectroscopy and Rietveld refinement of powder X-ray diffraction data. Catalli et al. [50] reported that Fe^{3+} substitutes equally on both the *A*- and *B*-sites in Al-free MgPv with 100 % $\text{Fe}^{3+}/\Sigma\text{Fe}$ above 50 GPa based on a combination of time-domain synchrotron Mössbauer spectroscopy (also known as nuclear forward scattering), X-ray emission spectroscopy and powder X-ray diffraction measurements. The detailed crystal structure of, and site preference of Fe in, MgPv have been examined using single-crystal X-ray diffraction [56,60,63,64]; however the valence state of Fe was not determined in these studies. In order to characterize the effect of Fe substitution on the crystal structure of MgPv, it is important to determine both its valence state and site preference simultaneously. We therefore undertook an investigation of an Al-free, Fe-bearing MgPv sample using a combination of electron microprobe analysis, single-crystal X-ray diffraction and Mössbauer spectroscopy.

5.5.3. Experimental procedure

Synthesis

Fine grained MgO , SiO_2 and Fe_2O_3 (95 % enriched in ^{57}Fe) were ground together for 1 hour and then dehydrated at 1273 K in air before use. The starting material has a chemical composition of $\text{Mg}_{0.95}\text{Fe}^{3+}_{0.10}\text{Si}_{0.95}\text{O}_3$. Fe_2O_3 was used in order to maximize Fe^{3+} content. A Kawai-type multi-anvil press was used to generate the high pressure and temperature required for the synthesis [211]. The sample was loaded into a Re capsule and then packed into a MgO container. LaCrO_3 was used for the heater. The synthesis conditions were $P = 26$ GPa at $T = 2073$ K and a heating duration of 50 min.

Sample characterization

The recovered sample was examined using an electron microprobe (JEOL JXA-8200) and a field-emission-type scanning electron microscope (SEM) (Leo Gemini 1530). A typical SEM image of the sample is shown in Figure 5.5.3-1. The chemical composition of the sample was determined using electron microprobe analysis, where 46 points were analyzed under the operating conditions 15 kV and 15 nA (Table 5.5.3-1). Full results of the microprobe analysis are given in the supplementary material (Table S 5.5.8-1).

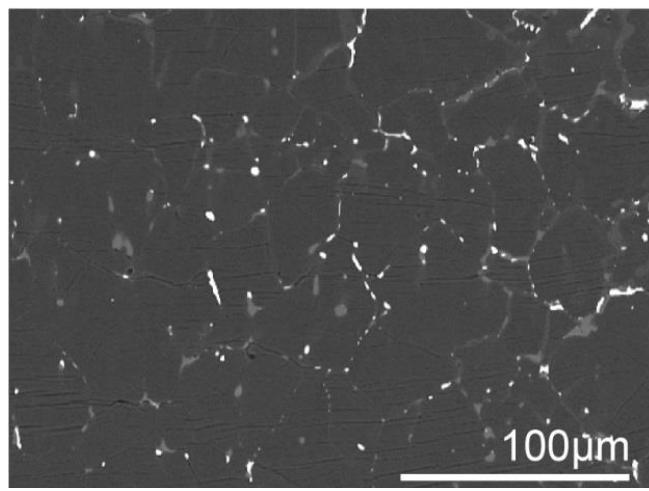


Figure 5.5.3-1 Back-scattered electron image of the investigated MgPv sample.

The sample was removed from the Re capsule and crushed into several pieces for powder X-ray diffraction (XRD) measurements using FR-D high-brilliance Rigaku diffractometer with Mo-K α radiation operated at 55 kV and 60 mA. After phase identification using powder XRD, the sample was carefully crushed further to obtain single crystals. Selected single crystals (about 50 μ m in diameter) were examined using an Oxford Diffraction Xcalibur diffractometer (Mo-K α radiation, $\lambda = 0.71073$ Å) with a CCD detector. Data treatment (integration, empirical absorption correction) was performed with CrysAlis RED software [158]. A total of 1115 reflections were collected covering the range $5.18^\circ < 2\theta < 31.26^\circ$. Symmetry equivalent reflections were merged ($R_{int} = 0.068$), resulting in 189 reflections with $I > 2\sigma(I)$ that were used for the structure refinement. The structure was refined in space group *Pbnm* with initial atom positions taken from the literature [63]. SHELXL software was used for full matrix least-squares refinement [124], and the site occupancy of iron was treated as a free parameter during the refinement. We used the scattering factor of neutral atoms in all refinements. The anisotropic displacement parameters were also refined.

Table 5.5.3-1 Chemical composition and cation distribution in MgPv.

		Microprobe ^a	XRD (Model 1) ^b	XRD (Model 2) ^b
Mg		0.946(17)	0.962(11)	0.939(7)
Fe ^{tot}		0.056(12)	0.038(11)	0.061(7)
Fe ²⁺		0.045(12)	-	-
Fe ³⁺		0.011(3)	-	-
Si		0.997(16)	0.964(13)	1
Total		1.998(26)	1.964(20)	2.000(10)
A-site	Mg ²⁺	0.946(17)	0.962(11)	0.939(7)
	Fe ²⁺	0.045(12)	0.038(11)	0.061(7)
	Fe ³⁺	0.008(3)		
B-site	Si ⁴⁺	0.997(16)	0.964(13)	1
	Fe ³⁺	0.003(3)	-	-

Values are in cations per formula unit (O = 3). Numbers in parentheses indicate the uncertainty of the final digit.

^aDetermined by electron microprobe + Mössbauer spectroscopy.

^bDetermined by single crystal XRD refinement (see text).

The Fe³⁺/ΣFe ratio was determined using Synchrotron Mössbauer Source (SMS) spectroscopy at the European Synchrotron Radiation Facility. The SMS methodology provides a beam with higher brilliance compared to conventional Mössbauer spectroscopy using a radioactive source, and the monochromatic synchrotron beam can be focused to around 10×10 μm² on the sample. A detailed description of the procedure is given in [212,213]. The Fe³⁺/ΣFe ratio of the MgPv sample was determined to be 0.20 ± 0.05.

5.5.4. Results

Electron microprobe analysis showed the MgPv sample to be chemically homogeneous with a composition of Mg_{0.946(17)}Fe_{0.056(12)}Si_{0.997(16)}O₃ (Table 5.5.3-1). This chemical formula can be also recast as Mg_{0.946(17)}Fe²⁺_{0.045(4)}Fe³⁺_{0.011(1)}Si_{0.997(16)}O₃ to incorporate the Fe³⁺ determined by Mössbauer spectroscopy. The typical grain size was ~50 μm at the central portion of the sample. While a trace amount of atomically heavier material was observed using SEM (Figure 5.5.3-1), powder XRD data showed only the presence of single-phase perovskite. The results of single-crystal X-ray diffraction measurements are summarized in Table 5.5.4-1 and Table 5.5.4-2.

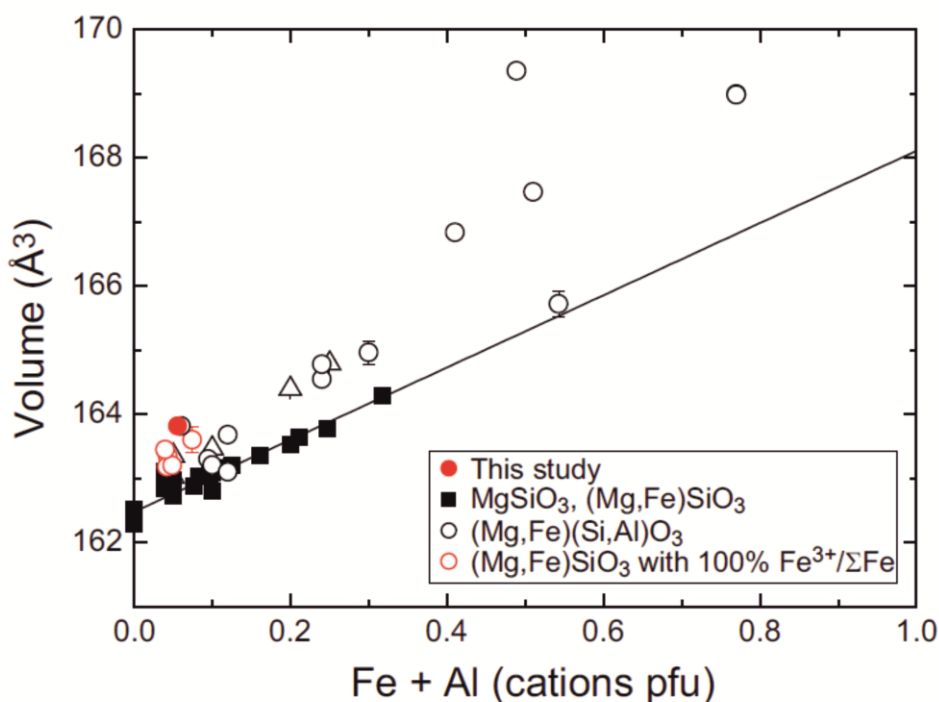


Figure 5.5.4-1 Unit cell volume of (Mg,Fe)(Si,Al)O₃ perovskite as a function of cation composition (Fe+Al) in cations per formula unit. Solid squares: MgSiO₃ and (Mg,Fe)SiO₃, black open circles: (Mg,Fe)(Si,Al)O₃, black open triangles: (Mg,Al)(Si,Al)O₃, red open circles: (Mg,Fe)SiO₃ with 100% Fe³⁺/ΣFe, red filled circle: this study. The data are taken from [44,46,49,51,55–57,60–62,64,214–223] and this study. The solid line is a linear fit to the data for (Mg,Fe)SiO₃ excluding the results of this study and Hummer and Fei [61], and the dashed line is a linear fit to the data for (Mg,Fe)(Si,Al)O₃.

The unit cell volume of our MgPv sample is higher than previously reported values for similar compositions (Figure 5.5.4-1), and is further discussed below. We refined the occupancy of the *B*-site for Si and Fe, and that of the *A*-site for Mg and Fe (Table 5.5.4-1 and Table 5.5.4-2). We found that placement of Fe on the *B*-site caused failure of the refinement for all investigated models. In the case where Fe was forced to occupy the *B*-site, the obtained *R*-value became unreasonably high in all models. Since Mg is known to occupy only the *A*-site, the *B*-site can be occupied by Si or a vacancy; hence, only Si occupancy on the *B*-site was refined. The chemical composition according to X-ray diffraction data refinement was determined to be Mg_{0.962(11)}Fe_{0.038(11)}Si_{0.964(13)}O₃ (Model 1). As an additional step, we alternatively refined the structure by fixing the site occupancy of Si in the *B*-site to 100 %. In this case the chemical

V. Results

Table 5.5.4-1 Unit cell parameters, refinement parameters, refined fractional occupancies, refined atomic coordinates and equivalent isotopic temperature factor of MgPv.

Cell parameters	Model 1	Model 2	Refinement	Model 1	Model 2
a (Å)	4.7877(18)	4.7877(18)	N . reflections (all)	273	273
b (Å)	4.9480(18)	4.9480(18)	N . reflections ($>2\sigma$)	189	189
c (Å)	6.915(3)	6.915(3)	R_1 (all)	0.0785	0.0793
V (Å ³)	163.82(10)	163.82(10)	R_1 ($>4\sigma$)	0.0445	0.0449
N . reflections	1115	1115	wR_2 (all)	0.0976	0.1001
Density (g/cm ³)	4.0751	4.1466	wR_2 ($>2\sigma$)	0.0879	0.0901
R_{int}	0.0681	0.0681	Goodness-of-fit	0.967	0.971
Mg, Fe (A-site)	Model 1	Model 2	Si (B-site)	Model 1	Model 2
x	0.5134(3)	0.5133(3)	x	0.5	0.5
y	0.5546(3)	0.5544(3)	y	0	0
z	0.2500	0.2500	z	0.5	0.5
U_{eq}	0.0111(6)	0.0116(6)	U_{eq}	0.0088(5)	0.0096(4)
x_{Mg}	0.962(11)	0.939(7)	x_{Si}	0.964(13)	1
x_{Fe}	0.038(11)	0.061(7)			
O ₁	Model 1	Model 2	O ₂	Model 1	Model 2
x	0.1021(8)	0.1022(8)	X	0.1958(5)	0.1959(5)
y	0.4645(8)	0.4645(8)	Y	0.2013(6)	0.2013(6)
z	0.2500	0.2500	Z	0.5523(4)	0.5523(4)
U_{eq}	0.0118(9)	0.0106(8)	U_{eq}	0.0133(8)	0.0120(7)

Model 1 = Mg_{0.962(11)}Fe_{0.038(11)}Si_{0.964(13)}O₃, Model 2 = Mg_{0.939(7)}Fe_{0.061(7)}SiO₃ (see text).

Table 5.5.4-2 Refined bond lengths of MgPv.

A–O (Å)	Model 1	Model 2	O–O (Å)	Model 1	Model 2	O–A–O (°)	O–A–O (°)
						Model 1	Model 2
A–O(1)	2.019(4)	2.018(4)	O(1)–O(2) (×2)	2.503(4)	2.503(4)	53.21(5)	53.23(5)
A–O(2) (×2)	2.058(3)	2.058(3)	O(1)–O(2) (×2)	2.503(4)	2.503(4)	66.62(7)	66.60(7)
A–O(1)	2.103(4)	2.103(4)	O(1)–O(2) (×2)	2.515(4)	2.515(4)	58.98(7)	58.97(7)
A–O(2) (×2)	2.295(3)	2.295(3)	O(1)–O(2) (×2)	2.515(4)	2.515(4)	69.61(11)	69.60(8)
A–O(2) (×2)	2.429(3)	2.429(3)	O(2)–O(2) (×2)	2.528(4)	2.528(4)	52.41(8)	52.42(8)
<A–O> 8	2.211(4)	2.211(4)	O(2)–O(2) (×2)	2.528(4)	2.528(4)	70.77(11)	70.76(11)
			O(2)–O(2) (×2)	2.547(4)	2.547(4)	54.34(10)	54.37(10)
A–O(1)	2.854(4)	2.854(4)	O(2)–O(2) (×2)	2.547(4)	2.547(4)	65.18(10)	65.17(10)
A–O(1)	2.971(4)	2.971(4)	O(1)–O(2) (×2)	2.577(4)	2.577(4)	58.29(8)	58.33(8)
A–O(2) (×2)	3.120(3)	3.120(3)	O(1)–O(2) (×2)	2.577(4)	2.577(4)	58.87(6)	58.86(6)
<A–O> 12	2.479(4)	2.479(4)	O(1)–O(2) (×2)	2.584(4)	2.584(4)	50.13(5)	50.14(5)
			O(1)–O(2) (×2)	2.584(4)	2.584(4)	70.35(6)	70.35(6)
B–O (Å)	Model 1	Model 2	O–O (Å)	Model 1	Model 2	O–B–O (°)	O–B–O (°)
						Model 1	Model 2
B–O(1) (×2)	1.787(3)	1.787(3)	O(1)–O(2) (×2)	2.503(4)	2.503(4)	88.35(9)	88.34(9)
B–O(1) (×2)	1.801(3)	1.801(3)	O(1)–O(2) (×2)	2.515(4)	2.515(4)	88.45(9)	88.45(9)
B–O(2) (×2)	1.805(1)	1.805(1)	O(2)–O(2) (×2)	2.528(4)	2.528(4)	89.57(12)	89.57(12)
<B–O>	1.798(3)	1.798(3)	O(2)–O(2) (×2)	2.547(4)	2.547(4)	90.43(12)	90.43(12)
			O(1)–O(2) (×2)	2.577(4)	2.577(4)	91.65(9)	91.66(9)
			O(1)–O(2) (×2)	2.584(4)	2.584(4)	91.56(9)	91.55(9)

Model 1 = Mg_{0.962(11)}Fe_{0.038(11)}Si_{0.964(13)}O₃, Model 2 = Mg_{0.939(7)}Fe_{0.061(7)}SiO₃ (see text)

composition was found to be $\text{Mg}_{0.939(7)}\text{Fe}_{0.061(7)}\text{SiO}_3$ (Model 2) with R -values increased slightly compared to the previous model (R_1 is 4.45 and 4.49 % for Models 1 and 2, respectively). If we incorporate the $\text{Fe}^{3+}/\Sigma\text{Fe}$ ratio obtained by Mössbauer spectroscopy, the chemical compositions obtained by XRD refinements can be expressed as $\text{Mg}_{0.962(11)}\text{Fe}^{2+}_{0.030(11)}\text{Fe}^{3+}_{0.008(11)}\text{Si}_{0.964(13)}\text{O}_3$ (Model 1) and $\text{Mg}_{0.939(7)}\text{Fe}^{2+}_{0.049(7)}\text{Fe}^{3+}_{0.012(7)}\text{SiO}_3$ (Model 2). Both models are in good agreement with the electron microprobe analysis. These two structural models are topologically indistinguishable, i.e., the coordinates, temperature factors, etc. are within the error of the two sets of data (Table 5.5.4-1 and Table 5.5.4-2). While the XRD method cannot distinguish unambiguously which of these slightly different models is more appropriate, the quality of the fits is sufficiently high to allow the unambiguous conclusion that all Fe occupies the A-site (Table 5.5.4-1).

5.5.5. Discussion

$\text{Fe}^{3+}/\Sigma\text{Fe}$ in MgPv

The MgPv sample was synthesized from a mixture of MgO, SiO_2 and Fe_2O_3 in order to maximize its Fe^{3+} content through a 100 % $\text{Fe}^{3+}/\Sigma\text{Fe}$ ratio of the starting material. Nevertheless, the $\text{Fe}^{3+}/\Sigma\text{Fe}$ ratio of the synthesized perovskite was much lower (~20 %), and moreover, no oxidized phases (such as magnetite or hematite) were observed by chemical analysis, XRD measurement or Mössbauer spectroscopy. Iron was most likely reduced during synthesis, since reduction of iron is not expected to occur during any of the procedures after sample recovery (e.g., mounting, polishing or analyzing). Reduction may have occurred due to the reaction of the sample with the surrounding Re capsule, for example through the following reaction:



While slightly higher, the $\text{Fe}^{3+}/\Sigma\text{Fe}$ ratio obtained in our work is still of similar magnitude to the Fe^{3+} contents of (Mg,Fe) SiO_3 perovskite obtained in previous experimental studies employing Re capsules [58,59]. In contrast, a recent study employing the same starting materials as the present work reported $\text{Fe}^{3+}/\Sigma\text{Fe}$ ratios of 100% [61] using Pt capsules (instead of Re) and with Fe_2O_3 placed outside the capsules to buffer oxygen fugacity. Since the Pt/ PtO_2 buffer is more

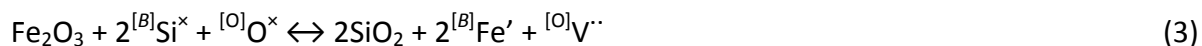
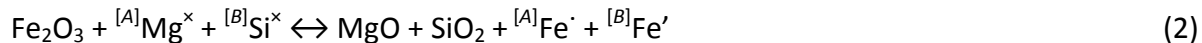
oxidizing than the Re/ReO₂ buffer, the difference in the Fe³⁺/ΣFe ratios of the resulting samples is plausible, particularly considering the presence of additional Fe₂O₃ in the Hummer and Fei experiments [61] used to maintain a high oxygen fugacity.

Fe³⁺ site occupancy

Results of our XRD refinements show the chemical composition to be either Mg_{0.962(11)}Fe²⁺_{0.030(11)}Fe³⁺_{0.008(11)}Si_{0.964(13)}O₃ or Mg_{0.939(7)}Fe²⁺_{0.049(7)}Fe³⁺_{0.012(7)}SiO₃, which is consistent with electron microprobe data (Table 5.5.3-1). The refined parameters show that all iron occupies the A-site (Table 5.5.4-1), indicating that both Fe²⁺ and Fe³⁺ substitute on the A-site. The site occupancy of Fe was refined as a free parameter, where we observed that the Fe occupancy of the B-site was below the detection limit (less than 0.002 atoms per formula unit). Jephcoat et al. [62] also reached a similar conclusion for MgPv samples with similar composition based on Rietveld refinements of powder XRD data. In contrast, McCammon [59] reported on the basis of Mössbauer measurements that Fe³⁺ substitutes on both the A- and the B-sites for a MgPv sample synthesized in a Re capsule. Likewise, Hummer and Fei [61] demonstrated using Mössbauer spectroscopy that Fe³⁺ substitutes on both sites for MgPv samples synthesized in Pt capsules. This difference in Fe³⁺ site preference for Al-free MgPv may be related to differences in oxygen fugacity, but it could also be related to other factors, such as the composition of the phase assemblage (e.g., whether samples are buffered by excess silica or excess oxide, such as MgO).

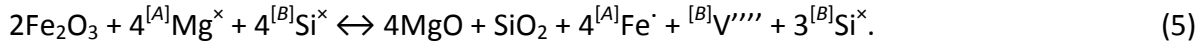
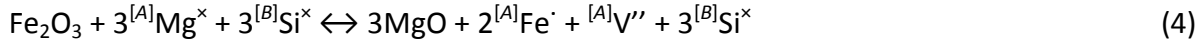
Substitution mechanism

Two previously proposed substitution mechanisms of Fe³⁺ in Al-free MgPv are:



where the superscripts [×], [·] and ['] indicate neutral, positive and negative charges, respectively [224], and V denotes a vacancy. The number of symbols in the superscript indicates the number of charges, for example, ^[O]V^{··} denotes a vacancy in the oxygen site, which has a charge of +2.

However neither of these substitution mechanisms is consistent with the result of this study, which indicates the substitution of Fe^{3+} only on the *A*-site. Instead, our results support the production of a cation vacancy on either the *A*- or *B*-site, such as:



Equation (4) places the cation vacancy on the *A*-site: $(\text{Mg}, \text{Fe}^{2+}, \text{Fe}^{3+})_{1-\delta}\text{SiO}_3$, while equation (5) places the vacancy on the *B*-site: $(\text{Mg}, \text{Fe}^{2+}, \text{Fe}^{3+})\text{Si}_{1-\delta}\text{O}_3$. Since the deviation of our MgPv sample from stoichiometry is smaller than the uncertainty of the electron microprobe analysis (Table 5.5.3-1), it is not possible to distinguish the mechanism of charge balance. In the case where Fe^{3+} substitutes equally on both sites in Al-free MgPv, no vacancies are required to balance charge. Hummer and Fei [61] observed this to be the case for one of their MgPv samples. For their other samples that contained excess Fe^{3+} on the *A*-site, they proposed that charge was balanced by vacancies on the *A*-site based on electrostatic energy considerations.

Unit cell volume and octahedral tilting

It has long been known that the unit cell volume of MgPv increases with substitution of both Fe and Al, where the effect of Al substitution is greater than that of Fe [44,46,49,55,214,216,219,225,226] and that the effect of Fe^{3+} substitution is greater than that of Fe^{2+} [50,61]. Hummer and Fei [61] attributed the latter observation to the larger difference between the ionic radii of Si^{4+} and Fe^{3+} for *B*-site substitution compared to the smaller difference between Mg^{2+} and Fe^{2+} for *A*-site substitution. We would therefore expect the volume of MgPv in the present study to follow the volume trend for Fe^{2+} , since substitution occurs only on the *A* site. Instead, however, the volume of our sample plots well above the trend for Fe^{2+} , and better fits the trend for Fe^{3+} (Figure 5.5.4-1). This observation can likely be attributed to the dependence of the *Pbnm* perovskite unit cell volume on not only the volume of octahedra, but also on the tilt angles between octahedra.

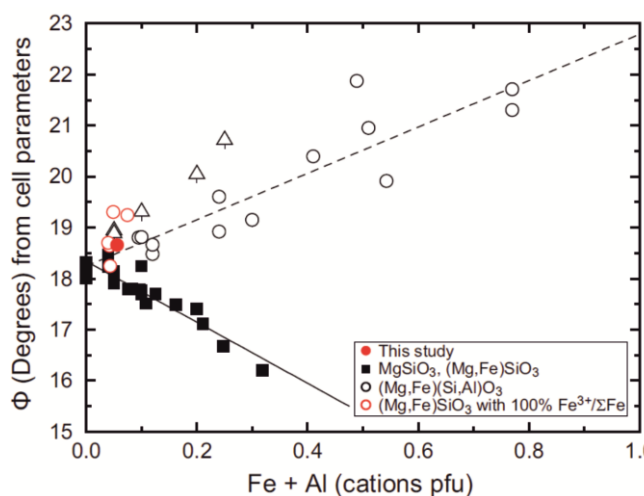


Figure 5.5.5-1 Variation of tilting angle Φ of (Mg,Fe)(Si,Al)O₃ perovskite with cation composition (Fe+Al) in cations per formula unit. Φ was calculated from the unit cell parameters of the data presented in Figure 5.5.4-1, where the symbols have the same meaning. The solid line is a linear fit to the data for (Mg,Fe)SiO₃ excluding the results of this study and Hummer and Fei [61], and the dashed line is a linear fit to the data for (Mg,Fe)(Si,Al)O₃.

The simplest method of estimating tilt angles between octahedra in *Pbnm* perovskites is from the unit cell parameters. Provided the octahedra remain regular, the tilt angle can be related to a single rotation about the [111] pseudo-cubic axis, designated as Φ , and given by

$$\Phi = \cos^{-1} (\sqrt{2} a^2/bc) \quad (6)$$

[227] (Figure 5.5.2-1). Since the two structural models are topologically identical (Table 5.5.4-1 and Table 5.5.4-2), the calculated tilt angles calculated on the basis of the two data sets will be the same. Many studies have examined the effect of Fe and Al substitution on the tilt angle based on the unit cell parameters, and have noted that Fe substitution reduces the tilt angle, while the addition of Al increases it [44,46,55,56,60,220,225]. We have plotted all available data in Figure 5.5.5-1, which is consistent with previous observations regarding the effect of Fe and Al to respectively decrease and increase the tilt angle. Further, the plot shows that the effect of Al substitution in the absence of Fe increases the tilt angle even more compared to the case when Fe is also present.

Tilt angles calculated from unit cell parameters are not always accurate, however, since octahedra are assumed to remain regular, and tilt angles are typically underestimated if octahedra become slightly distorted [228]. More realistic tilt angles can be calculated directly from the atomic coordinates, which for *Pbnm* perovskites are given as follows:

$$\tan \theta = 4 (u_{O1}^2 + v_{O1}^2)^{1/2}/c,$$

$$\tan \phi = 4 (u_{O2}^2 + v_{O2}^2)^{1/2} / (a^2 + b^2)^{1/2},$$

$$\cos \Phi = \cos \theta \cos \phi, \quad (7)$$

where

$$u_{O1} = a x_{O1},$$

$$v_{O1} = b (0.5 - y_{O1}),$$

$$u_{O2} = a (0.25 - x_{O2}),$$

$$v_{O2} = b (y_{O2} - 0.25), \quad (8)$$

a , b and c are the unit cell parameters, and x_{On} and y_{On} are the fractional atomic coordinates of the n th oxygen atom [229]. The variation of the tilt angle Φ based on the unit cell parameters from single crystal data show the same trends as the data based on powder X-ray diffraction (Figure 5.5.5-2a); however the tilt angles calculated from the atomic coordinates show a different behavior, namely that the variation of tilt angle with composition is independent of the nature of cation substitution in MgSiO_3 perovskite, such as the exact charge-compensation mechanism (Figure 5.5.5-2b).

Our results demonstrate that MgPv accommodates the substitution of Fe and Al in its crystal structure differently than previously thought. Figure 5.5.5-2b shows that the octahedral tilting angle is essentially the same for a given amount of Fe or Al substitution, independent of composition, which implies that individual octahedra must be more distorted with trivalent cation substitutions (Al or Fe^{3+}) compared to divalent cation substitutions (Fe^{2+}), even when octahedra are only occupied by Si. Such effects can influence the relative compressibility of octahedra, which in turn can affect the bulk compressibility. Oxidation of Fe^{2+} to Fe^{3+} in Fe-bearing MgPv, for example, would be predicted to change octahedral distortion without necessarily changing the octahedral tilting angle, but could affect MgPv elastic properties.

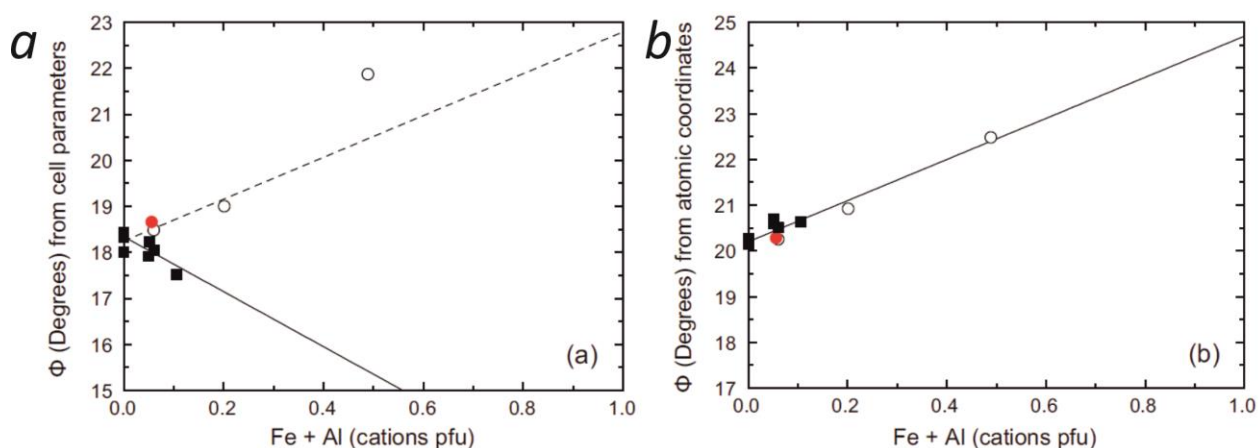


Figure 5.5.5-2 Variation of tilting angle Φ of (Mg,Fe)(Si,Al)O₃ perovskite with cation composition (Fe+Al) in cations per formula unit calculated from single-crystal or Rietveld refinement data based on (a) unit cell parameters, and (b) atomic coordinates. The symbols are the same as for Figure 5.5.4-1 and Figure 5.5.5-1 and the data are taken from [56,60,62–64,222,223] and this work. The solid and dashed lines in Figure 5.5.5-2a are taken directly from Figure 5.5.5-1, while the solid line in Figure 5.5.5-2b is a linear fit to all of the data.

5.5.6. Conclusions

The valence state and site distribution of iron in Al-free, Fe³⁺-bearing MgPv was investigated by a combination of single-crystal XRD refinement, electron microprobe analysis and Mössbauer spectroscopy. Results show that the chemical composition of synthesized perovskite is Mg_{0.946(17)}Fe²⁺_{0.045(4)}Fe³⁺_{0.011(1)}Si_{0.997(16)}O₃ and that both Fe²⁺ and Fe³⁺ occupy the A-site of the perovskite structure. Our data are consistent with the creation of cation vacancies on either the A-site: (Mg,Fe²⁺,Fe³⁺)_{1-δ}SiO₃ or the B-site: (Mg,Fe²⁺,Fe³⁺)Si_{1-δ}O₃ instead of Fe³⁺-Fe³⁺ coupled substitution or the creation of oxygen vacancies. Comparison of octahedral tilting angles calculated from the unit cell parameters with those obtained from atomic coordinates indicates that the effect of Fe substitution on the nature of B-site octahedra is clearly different between Fe³⁺ and Fe²⁺. This behavior suggests that the effect of Fe on physical/thermodynamic parameters of MgPv (e.g., bulk modulus, sound velocity and phase boundary between perovskite and post-perovskite) strongly depends on its valence state.

5.5.7. Acknowledgements

R.S. was supported by a Research Fellowship for Postdoctoral Researchers awarded by the Alexander von Humboldt Foundation. We thank the European Synchrotron Radiation Facility for provision of synchrotron radiation (ID18). We also thank Konstantin Glazyrin, Aleksandr I. Chumakov, Gennadii V. Smirnov, Rudolf Rüffer and Jean-Philippe Celse for additional technical assistance and Yoichi Nakajima for support during multianvil experiments. The project was partly financed by funds from the German Science Foundation (DFG) in their normal funding programme and Priority Programme SPP1236, the PROCOPE exchange programme and the German Federal Ministry for Education and Research (BMBF).

5.5.8. Supplementary material

Table S 5.5.8-1 Full results of microprobe analysis*.

#	Mg (wt%)	Fe	Si	#	Mg (wt%)	Fe	Si	#	Mg (wt%)	Fe	Si
1	42.53	5.58	51.89	17	42.92	5.07	52.01	32	41.97	6.05	51.98
2	42.82	5.71	51.47	18	42.65	5.50	51.85	33	42.08	5.71	52.22
3	42.28	5.63	52.09	19	42.74	5.21	52.06	34	43.06	5.17	51.77
4	42.85	5.39	51.77	20	42.47	5.68	51.85	35	42.64	5.29	52.07
5	42.44	5.63	51.93	21	42.25	5.70	52.04	36	42.72	5.10	52.18
6	42.36	6.02	51.62	22	42.63	5.50	51.87	37	42.44	5.15	52.41
7	42.62	6.06	51.32	23	41.80	6.19	52.01	38	42.81	5.72	51.46
8	41.16	6.18	52.66	24	42.31	5.76	51.94	39	41.49	6.59	51.92
9	42.66	5.95	51.39	25	42.28	6.05	51.67	40	42.19	5.47	52.34
10	41.96	7.11	50.93	26	41.91	6.34	51.75	41	42.27	6.61	51.13
11	42.44	5.74	51.82	27	42.23	5.89	51.88	42	42.04	5.95	52.00
12	43.21	5.37	51.42	28	43.13	4.87	52.00	43	42.61	5.27	52.13
13	42.71	6.19	51.10	29	42.64	5.24	52.11	44	42.73	5.98	51.29
14	42.85	5.18	51.97	30	43.56	5.39	51.06	45	42.22	6.41	51.37
15	42.91	5.41	51.68	31	42.87	5.65	51.49	46	42.62	6.61	50.77
16	42.74	6.15	51.10	31	42.87	5.65	51.49	31	42.87	5.65	51.49

* Oxygen was not quantified.

5.6. Discovery of a superhard iron tetraboride superconductor

H. Gou^{1,2}, N. Dubrovinskaia², E. Bykova^{1,2}, A.A. Tsirlin^{3,4}, D. Kasinathan³, W. Schnelle³, A. Richter⁵, M. Merlini⁶, M. Hanfland⁷, A.M. Abakumov⁸, D. Batuk⁸, G.V. Tendeloo⁸, Y. Nakajima¹, A.N. Kolmogorov⁹, L. Dubrovinsky¹

¹*Bayerisches Geoinstitut, Universität Bayreuth, D-95440 Bayreuth, Germany*

²*Laboratory of Crystallography, Material Physics and Technology at Extreme Conditions, University of Bayreuth, D-95440 Bayreuth, Germany*

³*Max Planck Institute for Chemical Physics of Solids, Nöthnitzer Straße 40, D-01187 Dresden, Germany*

⁴*National Institute of Chemical Physics and Biophysics, Akadeemia tee 23, 12618 Tallinn, Estonia*

⁵*Technische Hochschule Wildau, Bahnhofstraße 1, D-15745 Wildau, Germany*

⁶*Dipartimento di Scienze della Terra, Università degli Studi di Milano, Via Botticelli 23, 20133 Milano, Italy*

⁷*ESRF, Boîte Postale 220, 38043 Grenoble, France*

⁸*EMAT, University of Antwerp, Groenenborgerlaan 171, B-2020 Antwerp, Belgium*

⁹*Department of Physics, Applied Physics and Astronomy, Binghamton University, State University of New York, Vestal, New York 13850, USA*

Phys. Rev. Lett. **111**, 157002 (2013).

5.6.1. Abstract

Single crystals of novel orthorhombic (space group *Pnnm*) iron tetraboride FeB₄ were synthesized at pressures above 8 GPa and high temperatures. Magnetic susceptibility and heat capacity measurements demonstrate bulk superconductivity below 2.9 K. The putative isotope effect on the superconducting critical temperature and the analysis of specific heat data indicate that the superconductivity in FeB₄ is likely phonon mediated, which is rare for Fe-based superconductors. The discovered iron tetraboride is highly incompressible and has the

nanindentation hardness of 62(5) GPa; thus, it opens a new class of highly desirable materials combining advanced mechanical properties and superconductivity.

5.6.2. Manuscript

Modern computational materials design is gaining broad recognition as an effective means of reducing the number of experiments that can ultimately lead to materials discovery [19,230,231]: successful examples now include thermoelectrics, catalysts, electrode materials for Li-ion batteries, to name a few. Superconductors remain among the most challenging materials to develop [19,232–234]. So far theory successfully guided the experiment to a discovery only in a few cases related to thoroughly studied elemental materials, namely, silicon [235] and lithium [236] under pressure. The progress can be attributed to the improvement of density functional theory (DFT)-based methods [18,237], advances in compound prediction strategies [230,231], and the steady growth of computational resources. Nevertheless, the prediction of novel superconductors remains challenging [232]. First, only conventional (phonon-mediated) superconductors are understood well enough [232] to be described by theories with predictive power [233,238]. Calculation of the superconducting critical temperature, T_c , is possible but exceedingly demanding as a viable option in high-throughput screening for candidate materials. Second, the inverse correlation between the stability of a compound and its phonon-mediated superconducting T_c has been pointed out in a number of studies: a considerable density of states (DOS) at the Fermi level, beneficial for high T_c , is often an indication of structural instability [234]. One of the remarkable exceptions is the stoichiometric MgB_2 material [12] with naturally hole-doped σ bands and a T_c of 39 K.

The problem of thermodynamic instability can be mitigated under high pressure. When quenched to normal conditions, materials with a large DOS at the Fermi level may remain metastable and show superconductivity facilitated by this large DOS. Kolmogorov et al. [18] systematically examined the Fe-B system and showed that a previously unknown compound, FeB_4 , may exist under normal conditions in a previously unobserved orthorhombic crystal structure. The material was predicted to have naturally electron-doped bands and a large electron-phonon coupling [18], which can indicate that FeB_4 might be a *conventional* Fe-based

superconductor (rare cases are known, see [20,239,240]), as opposed to the recently discovered family of *unconventional* Fe-based superconductors [19,241]. Bialon et al. [21] suggested that the predicted FeB_4 phase could be synthesised under pressure. The wide and growing interest in Fe-based superconductors [19], simple chemical composition, and expected mild pressure-temperature conditions for synthesis [21] make iron tetraboride a good case for testing the computational predictive power and, thus, the degree of our theoretical comprehension of such a complex physical phenomenon as superconductivity. Here, we report synthesis of an iron boride with an unknown so far composition, the verification of theoretical predictions regarding the structure and superconductivity of this material, and the finding of its unexpectedly low compressibility and very high hardness.

The experimental Fe-B phase diagram [13] at ambient pressure shows only two compounds, tetragonal Fe_2B and orthorhombic FeB (Ref. [14]), although hexagonal FeB_2 (Ref. [15]) and rhombohedral $\text{FeB}_{\sim 49}$ (Ref. [16]) have also been reported in literature. Metastable cubic Fe_{23}B_6 and orthorhombic Fe_3B phases have also formed in a number of experiments [17,242,243].

We have undertaken a series of high pressure experiments (see the Supplemental Material for experimental details and technical procedures) aimed at the synthesis of the predicted boron-rich Fe-B phases (FeB_2 and FeB_4 [18]). Independent of pressure, a major component of the reacted mixture was stoichiometric FeB (Table S 5.6.4-1). At low pressures (3 GPa and below) and temperatures of 1323 K to 1973 K only known phases, orthorhombic FeB and rhombohedral $\text{FeB}_{\sim 49}$, were produced. Experiments at pressures of 8 GPa to 18 GPa and temperatures of 1523 K to 2023 K (Table S 5.6.4-1) led to the synthesis of previously unidentified orthorhombic FeB_4 , Fe_2B_7 , and tetragonal $\text{Fe}_{1+x}\text{B}_{50}$ ($x \approx 0.04$) phases. The compounds crystallize from the melt and by optimizing the sample geometry, heating duration, and temperature gradients along the capsules it was possible to increase the amount of boron-rich Fe-B phases. However, as seen in Figure 5.6.2-1a, all the products of the high-pressure synthesis, and particularly FeB_4 and Fe_2B_7 , are found in a tight mutual intergrowth, so that the procedure of phase separation is challenging.

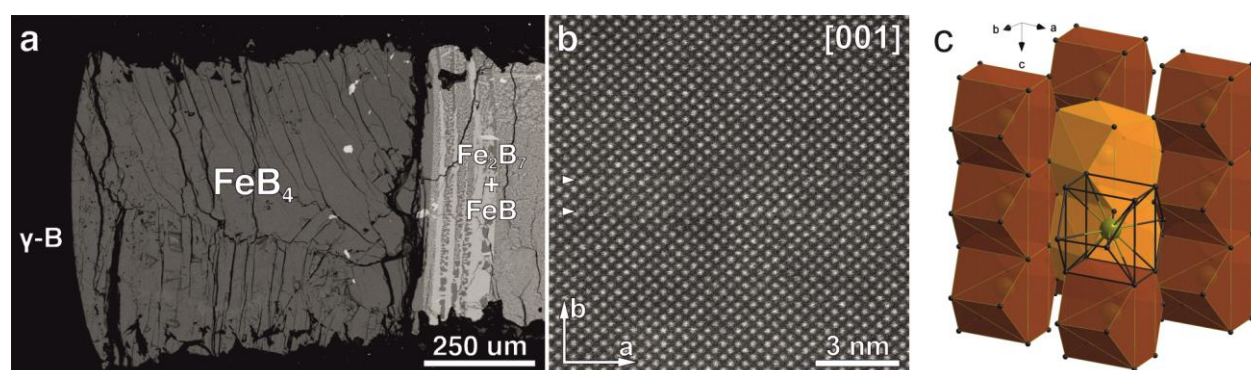


Figure 5.6.2-1 (a) The backscattered electron SEM image of the polished surface of a high-pressure sample. The central part of the image (dark gray field) represents FeB_4 produced by the reaction of Fe with B after melting. The adjacent area on the right appears brighter as it is composed of the phases with lower boron content, namely Fe_2B_7 and FeB . The surrounding black field is non-reacted boron which, however, underwent a pressure-induced phase transformation from $\beta\text{-B}$ to $\gamma\text{-B}$. Boron intrusions also fill the cracks in the FeB_4 phase. (b) The high resolution [001] HAADF-STEM image of FeB_4 (bright dots correspond to the Fe columns). Occasional planar defects (marked with arrowheads) are confined to the (010) plane and are visible as lines running parallel to the a -axis and consisting of pairs of the Fe columns with a shorter projected intercolumn distance in comparison with the FeB_4 matrix (see the Supplemental Material). (c) Crystal structure of FeB_4 presented as a packing of columns of FeB_{12} polyhedra along the c -direction; the columns are connected by common edges of the adjacent polyhedra, whose centers (Fe atoms) are displaced with respect to each other by $\frac{1}{2}$ along the body diagonal of the unit cell.

We have manually selected small pieces of FeB_4 and carefully characterized them with X-ray diffraction, wavelength dispersive X-ray (WDX) and energy dispersive X-ray (EDX) microprobe analysis (performed in SEM and TEM) (see the Supplemental Material) prior to further experiments. The largest pieces of phase-pure FeB_4 produced so far have dimensions on the order of $150 \times 150 \times 100 \mu\text{m}^3$. Maximal weight of phase-pure polycrystalline samples is of about 0.14 mg. We note, however, that standard characterization techniques are not sensitive enough to detect trace amounts of ferromagnetic impurities, such as metallic iron that is almost inevitably present in samples recovered after the high-pressure synthesis. These impurities are seen in magnetic susceptibility measurements (see the Supplemental Material), but do not affect any of our conclusions regarding the superconductivity and superhardness of FeB_4 .

The crystal structures of FeB_4 , Fe_2B_7 , and $\text{Fe}_{1+x}\text{B}_{50}$ have been solved from single crystal X-ray diffraction data (Table S 5.6.4-2). A detailed description of Fe_2B_7 and $\text{Fe}_{1+x}\text{B}_{50}$ is out of the scope of the present paper and will be published elsewhere.

According to the single crystal X-ray and electron diffraction (see the Supplemental Material), FeB_4 adopts an orthorhombic $Pnnm$ ($Z = 2$) crystal structure. The refined structure was confirmed by high angle annular dark field scanning transmission electron microscopy (HAADF-STEM) images along the $[100]$, $[010]$ and $[001]$ directions (Figure 5.6.2-1b, Figure S 5.6.4-10, Figure S 5.6.4-11). Additionally, planar defects confined to the (010) planes were occasionally observed in FeB_4 . These defects are not abundant in the material, as indicated by the absence of any related diffuse intensity on the electron diffraction patterns (Figure S 5.6.4-9).

A polyhedral model of the FeB_4 structure is shown in Figure 5.6.2-1c and Figure S 5.6.4-1. The structure is remarkably close to that theoretically predicted [18] (Table S 5.6.4-2), and found very recently also for CrB_4 [177,182].

Despite the very small size of the available phase-pure samples, we were able to confirm the prediction of superconductivity in FeB_4 . While resistivity measurements are presently unfeasible, magnetic susceptibility data collected on polycrystalline samples indicate superconductivity in FeB_4 . Magnetic susceptibility measurements under zero-field-cooling (ZFC) conditions reveal a strong diamagnetic response of FeB_4 samples below 3 K (Figure 5.6.2-2). Above 3 K, FeB_4 is weakly paramagnetic with a nearly temperature independent susceptibility above 70 K. Additionally, our samples showed a weak ferromagnetic signal of unknown origin below 30 K. This signal is certainly extrinsic, because its magnitude varies from sample to sample (see the Supplemental Material).

The strong diamagnetic response of FeB_4 is a clear footprint of superconductivity. The drop in the volume susceptibility (χ_v) is $4\pi(\Delta\chi_v) = -1.3$ that corresponds to the demagnetization factor of $N = 0.23$ according to $4\pi(\Delta\chi_v) = -1/(1 - N)$. This value of N is close to $N = 1/3$ expected for a spherical sample.

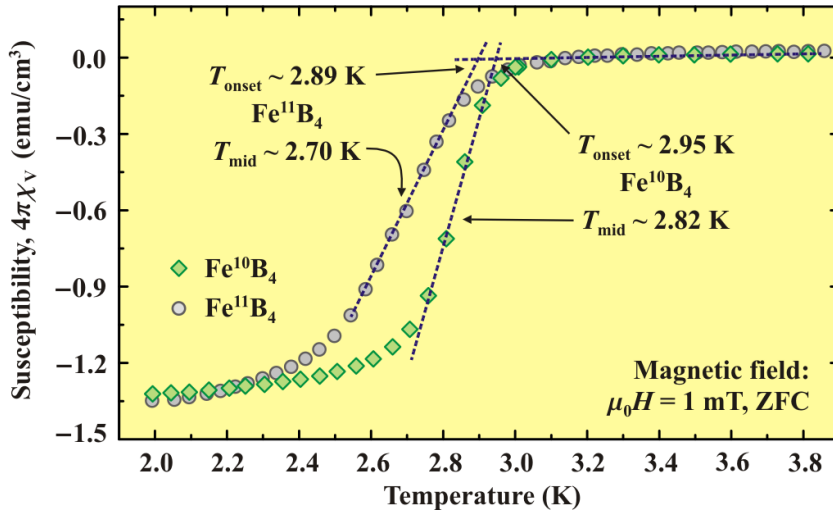


Figure 5.6.2-2 Magnetic susceptibility of FeB_4 measured in an applied field of 1 mT after zero-field cooling (ZFC). The susceptibility is normalized to the unit of volume (χ_v) and multiplied by 4π to facilitate the comparison with the expected value of $4\pi\chi_v = -1$ for the ideal superconductor with the demagnetization factor of $N = 0$. Two sets of data were collected on the samples enriched with ^{10}B and ^{11}B isotopes. Dashed lines denote the procedure for determining the onset temperature T_{onset} (see the Supplemental Material). The midpoints of the susceptibility drop (T_{mid}) are shown as well.

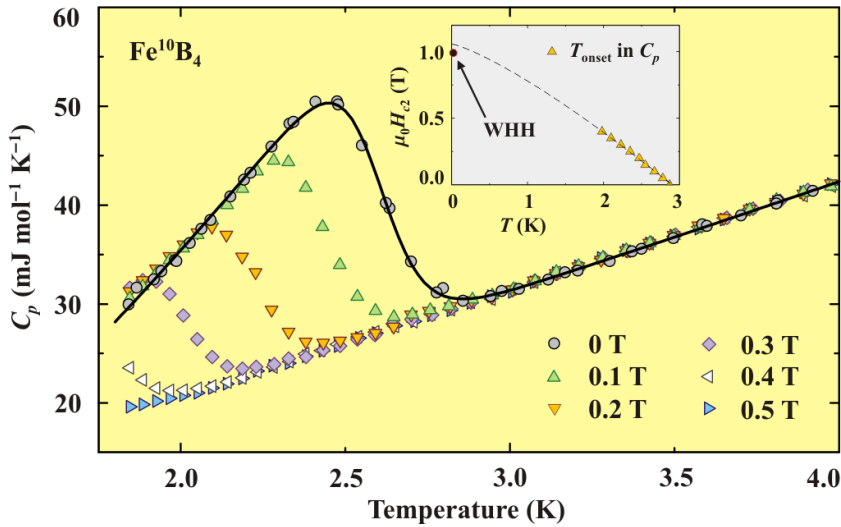


Figure 5.6.2-3 Specific heat (C_p) of FeB_4 measured on the ^{10}B -enriched sample. The jump in C_p indicates the bulk superconductivity with $T_{\text{onset}} \sim 2.9$ K in zero field. External magnetic field shifts the transition to lower temperatures. The critical field H_{c2} estimated from T_{onset} in different fields is plotted as an inset and approximated by the empirical formula $H_{c2}(T) = H_{c2}(0) (1 - (T/T_c)^n)$ shown by the dashed line. The WHH estimate of $\mu_0 H_{c2}(0) = 1.0$ T is shown as well. In the main figure, the solid line is the BCS fit including the Gaussian broadening [244] (see text for details).

The bulk nature of superconductivity is confirmed by heat capacity measurements showing a jump at the superconducting transition around 3 K (Figure 5.6.2-3). This jump is systematically shifted to lower temperatures in applied magnetic fields. Using the onset of superconductivity as a measure of T_c , we mapped the temperature dependence of the upper critical field H_{c2} . It increases upon cooling, with an initial slope of $dH_{c2}/dT = -0.5$ T/K at $T_c(0) \sim 2.9$ K. At lower temperatures, $H_{c2}(T)$ bends downwards. The critical field at zero temperature is extrapolated as $H_{c2}(0) = -0.693T_c(dH_{c2}/dT) \sim 1.0$ T according to the Werthamer-Helfand-Hohenberg formula [245]. Alternatively, $H_{c2}(0)$ can be determined from a fit with the empirical formula $H_{c2}(T) = H_{c2}(0) (1 - (T/T_c)^\alpha)$ yielding $\mu_0 H_{c2}(0) = 1.05$ T and $\alpha = 1.25$. Both estimates of $H_{c2}(0)$ are far below the Pauli-paramagnetic limit for weak electron-phonon coupling H_{c2} [Tesla] = $1.86T_c$ [Kelvin] ~ 5.4 T [246] and corroborate phonon-mediated superconductivity in FeB₄. In contrast, unconventional superconductors may have critical fields above the Pauli-paramagnetic limit.

To elucidate the nature of the observed superconducting transition, we compared the transition temperatures in the samples containing different boron isotopes (Figure 5.6.2-2). The sample enriched with the heavier B isotope shows a lower T_c (2.95 K and 2.89 K for T_{onset} or 2.82 K and 2.70 K for T_{mid} in the ¹⁰B and ¹¹B samples, respectively), as expected for a phonon-mediated superconductor. Indeed, our tentative estimate of the isotope effect (see the Supplemental Material) yields $\Delta T_c \sim 0.05$ K in good agreement with $\Delta T_c \sim 0.06\text{--}0.12$ K, as found experimentally. Specific heat data provide further evidence for phonon-mediated superconductivity. The specific heat of the normal state, as measured in the applied field of 1 T, follows $C_p = \gamma_n T + \beta T^3$ with $\gamma_n = 10.2(2)$ mJ mol⁻¹ K⁻² and $\beta = 0.025(1)$ mJ mol⁻¹ K⁻⁴ determined from the fit of C_p/T vs T^2 up to $T = 12$ K (Figure S 5.6.4-8). This β value yields the quite high Debye temperature $\theta_D \sim 730$ K indicating predominantly hard phonons, which are indeed expected for superhard FeB₄ (see below). The value of γ_n corresponds to $N(E_F) = 4.3$ states eV⁻¹ (f.u.)⁻¹ at the Fermi level and suggests a strong renormalization of the electronic DOS compared to the LDA result of $N(E_F) \sim 1$ state eV⁻¹ (f.u.)⁻¹ [18]. At zero field, the jump in C_p at the superconducting transition is $\Delta C_p \sim 35$ mJ/mol K yielding $\Delta C_p/\gamma_n T_c \sim 1.18$ in reasonable agreement with 1.43 expected for the BCS limit with weak electron-phonon

coupling. The proximity of ΔC_p to the BCS value is indicative of the conventional, phonon-mediated superconductivity in FeB₄. This finding is further corroborated by a fit of the zero-field $C_p(T)$ with the BCS expression by Mühlischlegel [244] yielding $\gamma_n = 8.8(1) \text{ mJ mol}^{-1} \text{ K}^{-2}$ in reasonable agreement with γ_n derived from the 1 T data.

Metal borides are known for their high hardness [27], so that characterisation of the elastic behavior of the newly synthesized boride and its stability under pressure is an important issue. No phase transitions were observed under compression of FeB₄ at ambient temperature in a diamond anvil cell up to about 40 GPa (see the Supplemental Material). Compressibility measurements on both compression and decompression revealed the relatively high bulk modulus, $K = 252(5) \text{ GPa}$ ($K' = 3.5(3)$, $V_0 = 72.79(4) \text{ Å}^3$) (Figure 5.6.2-4a), and a significant degree of anisotropy in the elastic behavior of FeB₄. The structure of FeB₄ is most compressible along the *a*-direction, while stiffest along the *b*-axis (Figure 5.6.2-4b). It may be related to the fact that the shortest (and thus least compressible) B–B contact (1.714(6) Å at ambient conditions) in this structure is almost parallel to the *b*-axis. The stiffness of the FeB₄ structure along the *b*-direction is the same as that of diamond [129] (Figure 5.6.2-4b) suggesting that the iron tetraboride may have remarkably advanced mechanical properties. Figure 5.6.2-4c,d presents the results, which are obtained by an average over several nanoindentation load-displacement charts on FeB₄ without the feature of a pop-in (see the Supplemental Material). The depth dependent indentation or reduced modulus E_r shows a clear plateau with $E_r = 633 \pm 30 \text{ GPa}$ (Figure 5.6.2-4c) that is far ahead compared to common ceramic materials like alumina [247] (~350 GPa) at room temperature. However, Young's moduli of diamond [248] (~1000 GPa) and cubic boron nitride [249] (~900 GPa) are still considerably larger. Nevertheless the nanoindentation hardness approaches an average value of $H = 62 \pm 5 \text{ GPa}$ (Figure 5.6.2-4d). Microhardness measurements were difficult to conduct because of the small size of the phase-pure samples of FeB₄. However, several successful tests (Figure S 5.6.4-2) with a load of 20 N gave values of the Vickers hardness ranging from 43 to 70 GPa, thus confirming that FeB₄ belongs to the group of superhard materials [132].

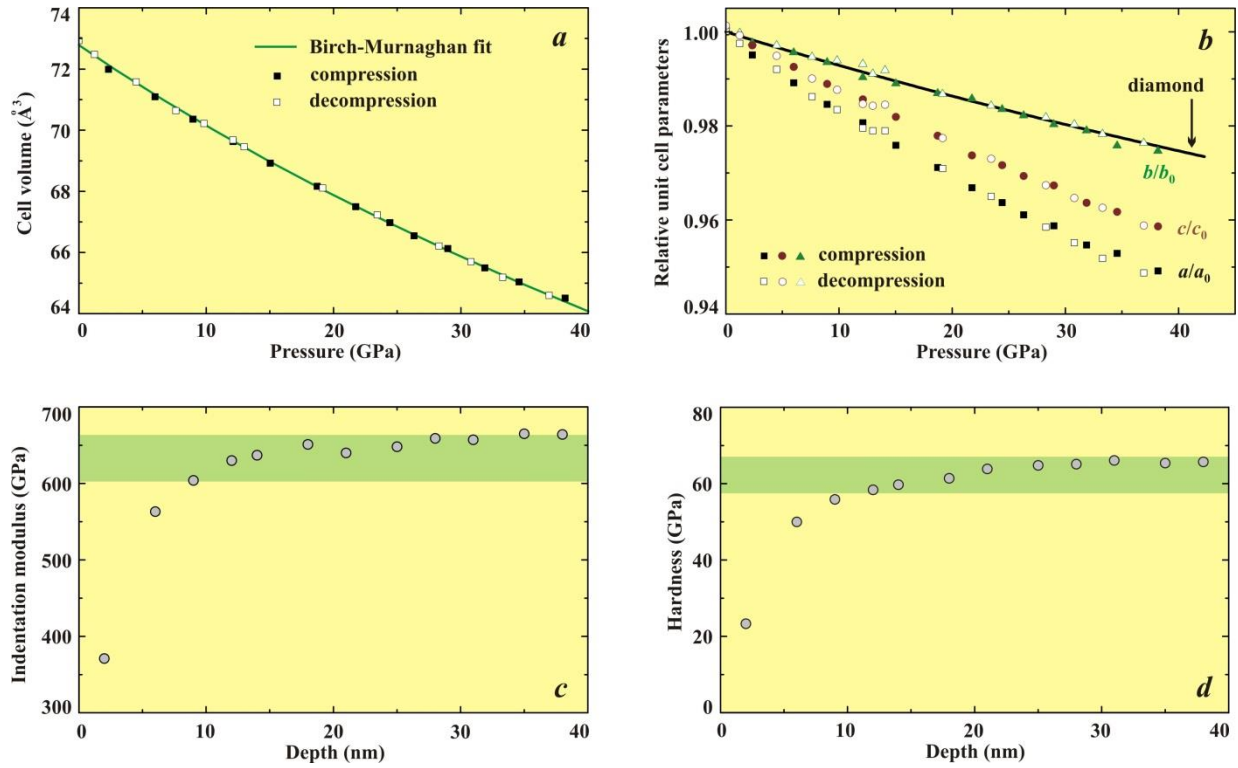


Figure 5.6.2-4 Compressibility of FeB₄ and the results of nanoindentation measurements. (a) The pressure dependence of the unit cell volume based on single crystal X-ray diffraction data. The fit of the pressure-volume data with the third-order Birch-Murnaghan equation of state (solid line) gave the bulk modulus $K = 252(5)$ GPa, $K' = 3.5(3)$, and $V_0 = 72.79(4)$ Å³/unit cell. (b) The relative changes of the unit cell parameters as a function of pressure. The stiffness of the FeB₄ structure along the b -direction is the same as that of diamond (continues line according to Ref. [129]). Filled symbols represent the data points obtained on compression and open ones – on decompression. The uncertainties are not shown since they are smaller than the size of symbols in the figure. (c) Depth dependent average values of indentation modulus. (d) Hardness of FeB₄. Load-displacement curves without pop-ins have been used for evaluation with tip compression correction.

In summary, we have prepared and characterized the novel superhard superconductor FeB₄. Our data not only support the predicted orthorhombic crystal structure [18], but also confirm the superconductivity of FeB₄ that was likewise predicted theoretically. We argue that the superconductivity of FeB₄ is mediated by phonons, which is highly unusual for an Fe-based materials [19,232]. In addition, the FeB₄ compound was found to be superhard, well exceeding the expectations about its potential mechanical properties [182]. This finding, bridging the gap between the superhardness and superconductivity community, may lead, for example, to a

possibility for designing new superconducting nanoelectromechanical systems and/or observation of new fundamental effects.

5.6.3. Acknowledgements

The work was supported by the German Research Foundation (DFG). N.D. thanks DFG for financial support through the Heisenberg Program and the DFG Project DU 954-8/1. H.G. gratefully acknowledges financial support of the Alexander von Humboldt Foundation. A.M.A., D.B. and G.V.T. acknowledge support from the ERC grant No 246791 “COUNTATOMS”. A.A.T. was partly supported by the MTT77 Mobilitas grant of the ESF.

5.6.4. Supplementary material

*Supplementary Tables***Table S 5.6.4-1** Summary of the high pressure synthesis experiments.

Experiments	Assembly	Starting materials	Experimental conditions			
			Pressure (GPa)	Temperature (K)	Heating time (min)	Products*
A517	PC	Fe _p + B	3	1573	120x60	FeB
A561	PC	Fe _p + B	3	1873	60	FeB
B631	PC	Fe _w + B	3	1973–1823	40	FeB + FeB ₄₉
B632	PC	Fe _w + B	2.5	1973–1523	40	FeB + FeB ₄₉
A532	PC	Fe _w + B	3	1973–1673	40	FeB + FeB ₄₉
S5269	10/5	Fe _p + B	15	1523	120	FeB ₄ + FeB
S5262	10/5	Fe _w + B	15	1973–1523	5	FeB ₄ + FeB
S5277	10/5	Fe _w + B	15	1973	30	FeB ₄ + FeB
S5294	10/5	Fe _w + B	15	1973–1473	30	FeB ₄ + Fe ₂ B ₇ + FeB
S5315	10/5	Fe _w + B	15	1973–1473	30	FeB ₄ + Fe ₂ B ₇ + FeB
S5330	10/5	Fe _w + B	15	1973–1673	30	FeB ₄ + Fe ₂ B ₇ + FeB
H3531	10/5	Fe _w + B	15	1973–1573	30	FeB ₄ + Fe ₂ B ₇ + FeB
S5537	10/5	Fe _w + B	15	1973–1473	30	FeB ₄ + Fe ₂ B ₇ + FeB
S5540	14/8	Fe _w + B	13	1973–1673	30	FeB + FeB ₄
S5546	18/11	Fe _w + B	13	1973	20	FeB ₄ + FeB
H3579	18/11	Fe _w + B	10	1973–1873	15	FeB ₄ + Fe ₂ B ₇ + FeB
H3565	18/11	Fe _w + B	12	1973–1673	30	FeB ₄ + FeB ₅₀ + FeB
Z834	25/15	Fe _w + B	13	1672	30	FeB ₄ + FeB
S5562	14/8	Fe _w + B	13	1973–1673	30	FeB ₄ + FeB
H3598	10/5	FeB _p + 2B	15	1493	60	FeB + Fe ₂ B ₇
S5584	10/5	FeB _p + 2B	15	1923	60	FeB ₄ + Fe ₂ B ₇ + FeB
H3600	10/5	Fe _w + B	15	2123	3	FeB ₄ + FeB
H3590	10/5	Fe _w + B	15	1873	10	FeB ₄ + FeB + Fe ₂ B ₇
S5598	14/8	Fe _w + B	12	1673	40	FeB ₄ + FeB ₅₀ + FeB + FeB ₂₂
S5610	10/5	FeB _p + 2B	15	1923	60	Fe ₂ B ₇ + FeB ₄ + FeB
S5624	14/8	Fe _w + B	12	1673	30	FeB ₄ + FeB + FeB ₅₀
S5549	18/11	Fe _w + B	12	1973	10	FeB + FeB ₄
S5641	14/8	FeB _p + 3B	13	1803	120	Mixture of FeB + FeB ₄
Z860	18/11	Fe _w + ¹¹ B	18	1773	60	FeB ₄ + FeB + FeB ₅₀

Notes:

Letters A and B in the numbers of experiments designate the experiments in piston-cylinder (PC) apparatus; Letters S, H, and Z in the numbers of experiments designate the experiments conducted in multi-anvil apparatus; B, Fe_p and FeB_p designate B, Fe and FeB powders; Fe_w designates an Fe wire; B denotes the isotope ¹⁰B; FeB_p + nB means a mixture of powders in a molar ratio 1 : n (n = 2, 3 and 4); If two values of temperature (1973–T) are given, it means that the sample was first heated to the target temperature (1973 K), kept at this temperature for 5–10 min, then cooled at a rate of 10 °C /min down to temperature T, and kept at this temperature during a time specified in the table as “heating time”. Finally the sample was temperature quenched by switching off power on the power supply.

*The γ-B was observed in products of all experiments with Fe_w + B as starting materials.

Table S 5.6.4-2 Experimental single crystal X-ray diffraction data for FeB₄ and the results of its structure solution compared to the structural data of FeB₄ theoretically predicted by Kolmogorov *et al.* [18].

Empirical formula	FeB ₄	FeB ₄ (Ref. [18])
Crystal system	Orthorhombic	Orthorhombic
Space group	<i>Pnnm</i>	<i>Pnnm</i>
<i>a</i> (Å)	4.5786(3)	4.521
<i>b</i> (Å)	5.2981(3)	5.284
<i>c</i> (Å)	2.9991(2)	3.006
<i>V</i> (Å³)	72.752(8)	71.810
<i>Z</i>	2	2
Atomic parameters		
(<i>x/a</i>, <i>y/b</i>, <i>z/c</i>, <i>U</i>_{eq} (Å²))		
Fe1, 2<i>a</i>	0, 0, 0, 0.00596(19)	0, 0, 0
B1, 4<i>g</i>	0.2487(9), 0.3123(7), 0, 0.0076(6)	0.2508, 0.3129, 0
B2, 4<i>g</i>	0.3411(8), 0.1263(7), ½, 0.0064(6)	0.3394, 0.1267, ½
Calculated density (g/cm³)	4.523	
Crystal size (mm³)	0.05 x 0.04 x 0.04	
Theta range for data collection (°)	5.89 to 36.13	
Completeness to theta = 25°, %	100	
Reflections collected	896	
Independent reflections / <i>R</i>_{int}	193 / 0.0345	
Data [<i>I</i> > 2σ(<i>I</i>)] / restraints / parameters	164 / 0 / 17	
Goodness of fit on <i>F</i>²	1.094	
Final <i>R</i> indices [<i>I</i> > 2σ(<i>I</i>)]	0.0279 / 0.0615	
<i>R</i>₁/<i>wR</i>₂		
<i>R</i> indices (all data)	0.0400 / 0.0666	
<i>R</i>₁/<i>wR</i>₂		
Largest diff. peak and hole (e / Å³)	0.924 and -1.090	

Table S 5.6.4-3 Bond lengths in the novel iron boride crystal structures and their comparison with those in previously known phases.

Iron boride	Fe–B distances, Å	B–B distances, Å	Reference
Fe ₃ B	2.139	3.123	predicted structure
	2.142		Ref. [17]
Fe ₂ B	2.1806(4)	2.1254(5)	Ref. [14]
FeB	2.159(8)	1.781(6)	Ref. [14]
	2.159(5)		
	2.172(5)		
	2.180(7)		
	2.195(8)		
FeB ₂	2.3223	1.758	Ref. [15]
	2.3224		
FeB ₄	2.009(4)	1.714(6)	This work
	2.109(4)	1.843(3)	
	2.136(3)	1.894(6)	
	2.266(3)		
FeB ₄	2.0007	1.7058	Predicted structure
	2.1019	1.8421	Ref. [18]
	2.1265	1.8800	
	2.2498		
FeB _{~49}	2.160(3) – 2.489(2) *	1.626(6) – 1.926(3) *	Ref. [16]
Fe _{1.04} B ₅₀	2.226(2)	1.669(4) – 2.008(3) *	This work
	2.5310(2)		
	2.550(2)		

* The structure contains a large number of non-equivalent atoms, therefore a list of distances is substituted by the ranges of their variation.

Supplementary Methods

Materials. For high pressure synthesis of iron borides polycrystalline β -boron (purity of 99.9995 at.%, grain size of $<1000\ \mu\text{m}$), purchased from *Chempur Inc.*, was used as a boron source material. As an iron source, either Fe (purity of 99.9 %, grain size of 6–9 μm), FeB (purity of 99 %) powders purchased from *Chempur Inc.*, or an iron wire (purity of 99.99+ %, 0.5 mm and 1 mm diameter), purchased from *Alfa Aesar*, were used. All experiments were conducted in a capsule made of *h*-BN.

High-pressure synthesis techniques. High pressure high temperature synthesis experiments were conducted using piston-cylinder and multi-anvil apparatus in a pressure range from 2.5 GPa to 20 GPa at temperatures between 1323 K and 1973 K according to the technique described elsewhere [250,251].

Synthesis experiments [250] in multianvil apparatuses were conducted using 1000-ton (Hymag) and 1200-ton (Sumitomo) hydraulic presses installed at the Bayerisches Geoinstitut (BGI). The Kawai-type multi-anvil system employs six tool-steel outer-anvils and eight tungsten carbide cubic inner-anvils to focus an applied load on an octahedral high-pressure chamber formed as a result of corner truncations on the inner-anvils. By varying the corner truncation size of the inner-anvils, various pressures on a sample can be attained. An octahedron made of magnesium oxide that matches the pressure chamber was used as a pressure medium. In our experiments 10/5 (the edge-length of an octahedron /anvil truncation edge-length, in millimetres), 14/8, 18/11, and 25/15 cell assemblies for pressures in the range of 10 GPa to 18 GPa were used. Duration of heating varied from 3 to 120 minutes. After the target pressure was reached, the sample was first heated to the target temperature, kept at this temperature for 5–10 min, then cooled at a rate of 10 °C/min down to temperature T , and kept at this temperature during a time specified in the Table S 5.6.4-1 as “heating time”. Finally the sample was temperature quenched by switching off power on the power supply. “Pressure in a chamber” vs “hydraulic oil pressure” in prior experiments was calibrated by observations of phase transitions in standard materials, and temperature was determined using a $\text{W}_3\text{Re}/\text{W}_{25}\text{Re}$ thermocouple. Pressure-temperature measurement uncertainties are estimated to be 0.5 GPa in pressure and 50 K in temperature. After experiments, a capsule was extracted from the

MgO octahedron, cut, and the material was either extracted, or polished for further investigations. Experiments at pressures of 2.5 GPa and 3 GPa were conducted using an end-loaded piston-cylinder type apparatus [156]. The sample material was loaded into 6 mm/13 mm (diameter/length) *h*-BN capsules which were placed into ½ inch talc-pyrex sample assemblies. These sample assemblies contained an internal, tapered, graphite resistance furnace to ensure minimal temperature gradients along the length of the capsule. Temperature gradients are estimated to be less than 25 °C for the experimental conditions used. Pressure was in prior calibrated against the quartz-coesite and kyanite-sillimanite transitions, as well as the melting point of diopside, and pressures are considered to be accurate to within less than $\pm 5\%$ of the stated value. Temperatures were measured with a Pt-Pt10%Rh Thermocouple and heating duration time varied between 40 min and 120 hours in various experiments. Pressure and temperature were continually monitored and maintained for the duration of the experimental runs. Experiments were quenched isobarically by turning off power to the heating circuit.

Analytical techniques. For the phase identification, selection of single crystals, and preliminary structural analysis, a high-brilliance Rigaku diffractometer (Mo- $K\alpha$ radiation) equipped with Osmic focusing X-ray optics and Bruker Apex CCD detector was used. The diffraction patterns were processed using Fit2D software.

The morphology and chemical composition of the synthesized samples of single crystals were studied by means of the scanning electron microscopy (SEM) (LEO-1530). Chemical purity of the samples was confirmed using wavelength dispersive X-ray (WDX) microprobe analysis (JEOL JXA-8200; focused beam; 20 keV, 20 nA).

Crystal structure solution. Crystal structure of FeB₄ at ambient conditions was obtained using four-circle Oxford Diffraction Xcalibur diffractometer ($\lambda = 0.7107 \text{ \AA}$) equipped with a Xcalibur Sapphire2 CCD detector under control of a CrysAlis CCD software [252]. Sample-to-detector distance, detector tilts, beam center position were calibrated using an YLID standard. Some experimental details are shown in Table S 5.6.4-2. The data treatment (integration, absorption corrections) was performed with CrysAlis RED software [206]. The structures were solved by the direct method and refined by full matrix least-squares using SHELXTL software [124].

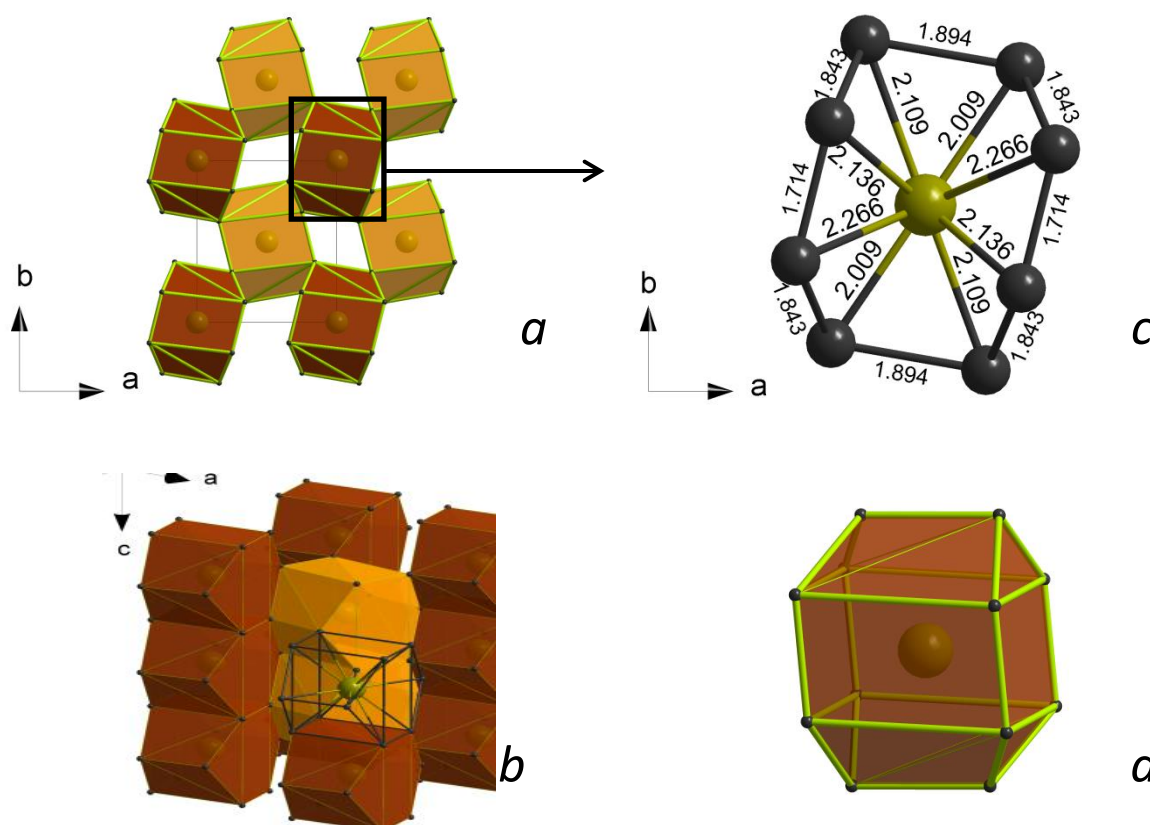


Figure S 5.6.4-1 Crystal structure of FeB₄. (a) The view along the *c*-direction; polyhedra with the same color have the same position in height in the *c*-direction; the structure consists of irregular FeB₁₂ polyhedra arranged in columns along the *c*-axis by sharing the parallelogram-shaped faces. (b) Packing of columns along the *c*-direction; the columns are connected by common edges of the adjacent polyhedra, whose centers (Fe atoms) are displaced with respect to each other by $\frac{1}{2}$ along the body diagonal of the unit cell. If viewed along the *c*-axis, the columns of polyhedra and empty channels alternate in a chessboard pattern. (c) Bond lengths in a FeB₁₂ polyhedron (only 8 B atoms, those lying in the same *ab* plane with Fe and above it, are shown). (d) A separate FeB₁₂ polyhedron. The 8 longer Fe–B bonds (2.136(3) Å and 2.266(3) Å) are related to the boron atoms forming parallelogram-shaped faces common for the two neighboring polyhedra. This is in agreement with the third Pauling rule which requires an increase of the cation-anion (Fe–B) distances in the face-sharing polyhedra to enlarge the separation of the corresponding cations (Fe–Fe). The Fe–B bonds located in the same *ab* plane (2.009(4), 2.109(4) Å) are the shortest among those known in iron borides [14,17] (Table S 5.6.4-3). The distances between boron atoms vary from 1.714(6) Å to 1.894(6) Å and are common for pure boron phases, but the closest B–B contact in the parallelogram-shaped face of the polyhedron is among the shortest B–B bonds known in borides [129].

Compressibility measurements. For measurements of the room temperature compressibility of FeB₄ we used a screw-driven piston cylinder-type BX90 diamond anvil cell [105] (DAC) with a pair of Boehler-Almax diamonds with culets of 0.25 mm in diameter. A single crystal of FeB₄ (of about 0.05 x 0.04 x 0.04 mm³ in size) was placed into a hole of 0.12 mm in diameter drilled in a pre-indented rhenium gasket. Ne was used as a pressure transmitting medium. The Ne gas was loaded at pressure of 1.2 kbar using a gas-loading system [112] which exploits mechanical closing of DACs. The pressure was determined by the ruby fluorescence method [253]. The single crystal synchrotron X-ray diffraction data were collected at ID09a beamline at ESRF ($\lambda = 0.41438$ Å). The reflection intensities were measured by phi-scanning of narrow (1°) frames from phi -40 to 40° with a MAR555 flat panel detector. The sample-to-detector distance, the detector tilt, and the beam center position were calibrated using a CeO₂ NIST standard from (CAS Number: 385781-69-1). The data were collected on compression from 2.3 to 38.2 GPa with steps of ~3 GPa that resulted in 13 pressure points. Afterwards we stepwise decreased pressure in the cell down to ambient conditions and collected data for 14 additional pressure points including that at 1 atm. The data treatment (integration, absorption corrections) was performed in both cases with CrysAlis RED software [206]. No special corrections for diamond absorption were implied. The structures were solved by the direct method and refined by full matrix least-squares using SHELXTL software [124].

Nanoindentation measurements. Nanoindentation (NI) measurements were performed using the electrostatic transducer of the UBI 1 Hysitron triboscope with a pristine diamond 90° cube corner tip. Calibration of the tip was performed by the standard curve-fitting method using fused quartz with its known reduced modulus as the reference to determine the actual area function A_c as a function of the contact depth h_c (Ref. [254]). Additionally, a commercial grid of ultra sharp conical silicon was used to get information about the indentation tip apex [255]. The blunt radius was determined as 112 nm. Indentation was achieved by single trapezoid load-time functions and by multi-indentation with repeated loading and unloading at the same location on the sample surface [256]. This type of data collection method does not suffer from lateral inhomogeneities of the sample. The measured data consisted of a load-displacement curve, which reflects the material response from the first indenter to sample contact down to

the maximum penetration. Thus, depth dependent mechanical properties are obtained. The maximum load was varied between 500 μN and 3000 μN resulting in penetration depths of less than 60 nm. All measurements were carried out at room temperature in air.

Microhardness measurements

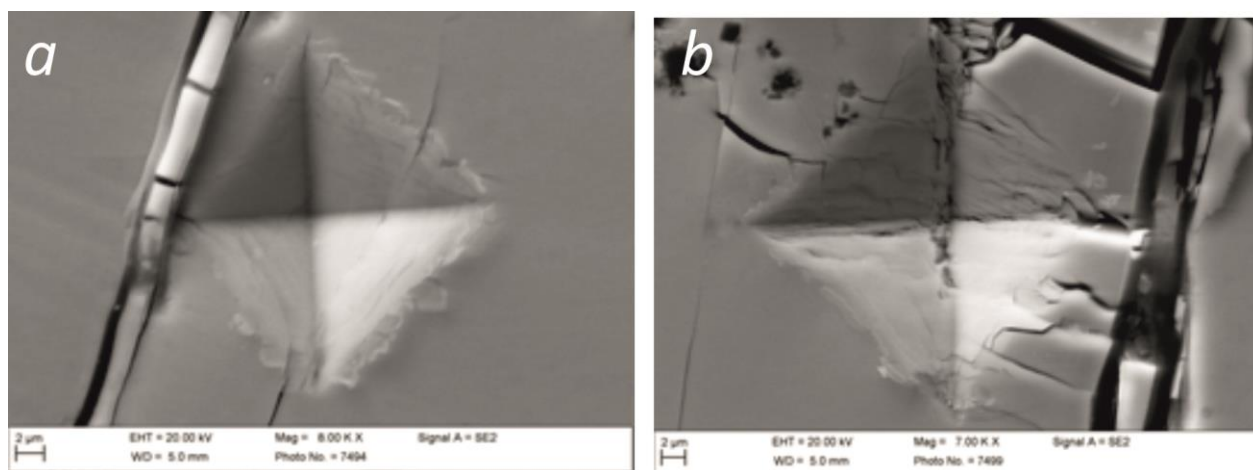


Figure S 5.6.4-2 Examples of the imprints obtained on the polished surface of FeB_4 during microhardness testing. Under the load of 20 N measured $H_v = 71.8$ GPa for the left imprint and $H_v = 43.5$ GPa for the right imprint. As seen, the material is brittle.

Magnetic susceptibility and heat capacity measurements. Magnetic susceptibility was measured on small (~ 0.14 mg) polycrystalline samples that were phase-pure according to XRD, WDX, and EDX. The measurements were performed with the Quantum Design MPMS SQUID magnetometer in the temperature range 2–300 K in applied magnetic fields up to 5 T. The samples were glued on paper using the standard GE varnish. The diamagnetic contribution of the paper and varnish assembly is negligibly small, as checked in an independent measurement run without the sample.

Several samples of FeB_4 consistently showed bulk superconductivity below $T_c \sim 2.9$ K. The bulk nature of the superconductivity is inferred from the strong diamagnetic response observed in low fields. At 2 K, the ZFC volume susceptibility (χ_v) reaches the value of $4\pi\chi_v = -1.6$ in the applied field of 1 mT (Figure S 5.6.4-4). The large susceptibility drop at the superconducting transition, $4\pi(\Delta\chi_v) = -1.3$, indicates the bulk nature of the superconductivity. The diamagnetic

response exceeds $4\pi(\Delta\chi_V) = -1$ because of the demagnetization effect. Unlike FeB_4 , both Fe_2B_7 and $\text{Fe}_{1+x}\text{B}_{50}$ ($x \approx 0.04$) do not show a superconducting transition.

Magnetic field is strongly detrimental for the superconductivity of FeB_4 . In fields of 1–10 mT (Figure S 5.6.4-4), the superconducting transition is gradually blurred and eventually disappears above 100 mT (Figure S 5.6.4-3). However, the diamagnetic response is lost already above 10 mT because in our samples of FeB_4 the low-temperature diamagnetism coexists with a weak ferromagnetic signal that emerges below 30 K. The low and variable values of the respective magnetic moment (Figure S 5.6.4-5) indicate the extrinsic nature of this ferromagnetic signal. While we are unaware of any existing iron boride with the ferromagnetic transition at 30 K, several predicted Fe–B compounds should be strongly ferromagnetic [18] and may be responsible for the observed ferromagnetic response of our sample. Ferromagnetic amorphous $\text{Fe}_{1-x}\text{B}_x$ alloys have also been reported [257,258]. Provided that their typical magnetic moment is above $1 \mu_B/\text{f.u.}$ (Ref. [257]), the moment of $0.01 \mu_B/\text{f.u.}$ implies less than 1 % of either amorphous or crystalline ferromagnetic impurity. This small amount of the foreign phase can not be detected by X-ray diffraction and other conventional characterization techniques, especially if this foreign phase is amorphous. Note, however, that our reference measurements on crystalline Fe_2B_7 and FeB_{50} samples did not show any signatures of the low-temperature ferromagnetism, as observed in FeB_4 .

Same comments apply to the magnetic susceptibility of the ^{11}B sample (Figure S 5.6.4-6). It shows the bulk superconductivity with $4\pi(\Delta\chi_V) = -1.3$ in an applied field of 1 mT. However, a larger contribution of the ferromagnetic impurity in this sample (Figure S 5.6.4-5) alters the absolute values of the magnetic susceptibility below 30 K. The variable net moment (about $0.01 \mu_B/\text{f.u.}$ and $0.02 \mu_B/\text{f.u.}$ for the ^{10}B and ^{11}B samples, respectively, see Figure S 5.6.4-5) further proves the extrinsic nature of this ferromagnetic contribution.

To explore the effect of isotope substitution on the superconductivity of FeB_4 , we introduced temperature-independent offsets of $+0.3 \text{ emu/cm}^3$ and $+0.8 \text{ emu/cm}^3$ for the ^{10}B and ^{11}B samples, respectively. This way we compensate for the different ferromagnetic contributions (see Figure S 5.6.4-5). The T_c can be determined as the crossing point of two lines. One line extrapolates

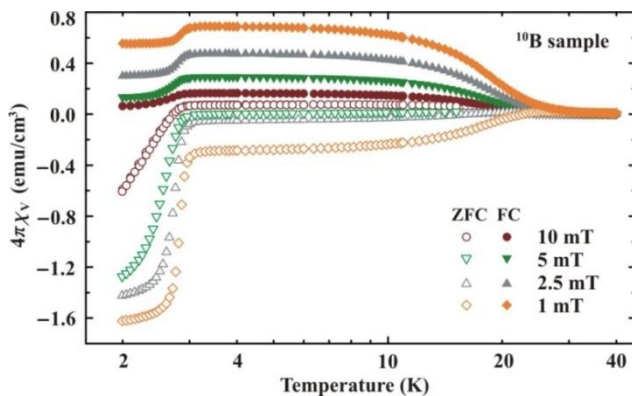


Figure S 5.6.4-4 Magnetic susceptibility of Fe^{10}B_4 measured in the applied fields of 1 mT, 2.5 mT, 5 mT, and 10 mT under field-cooling (FC) and zero-field-cooling (ZFC) conditions. Note the strong diamagnetic signal that appears below $T_c \sim 2.9$ K.

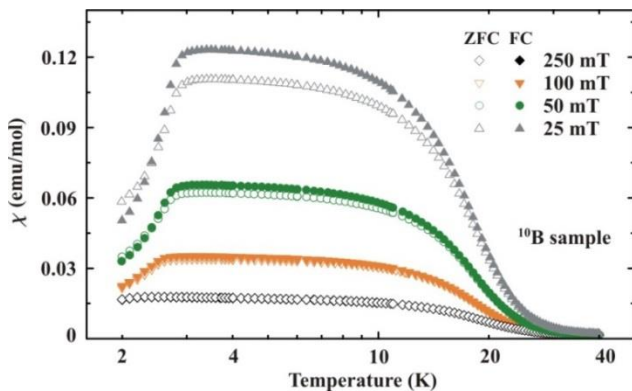


Figure S 5.6.4-3 Magnetic susceptibility of Fe^{10}B_4 measured in the applied fields of 25 mT, 50 mT, 100 mT, and 250 mT under field-cooling (FC) and zero-field-cooling (ZFC) conditions. Although the sample does not become diamagnetic at low temperatures, the sharp decrease in the susceptibility below $T_c \sim 2.9$ K indicates the onset of superconductivity.

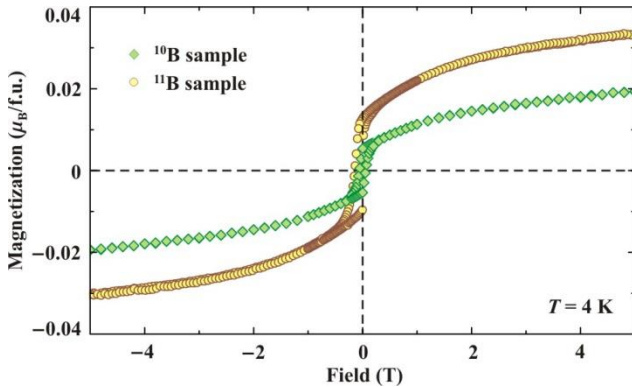


Figure S 5.6.4-5 Magnetization curves of FeB_4 (both ^{10}B and ^{11}B samples) measured at 4 K (above T_c). Note the variable remnant magnetization (magnetic moment) that points to an extrinsic nature of the ferromagnetic signal.

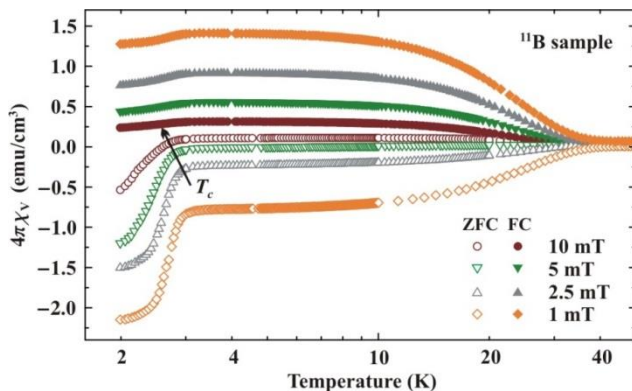


Figure S 5.6.4-6 Magnetic susceptibility of Fe^{11}B_4 measured in the applied fields of 1 mT, 2.5 mT, 5 mT, and 10 mT under field-cooling (FC) and zero-field-cooling (ZFC) conditions. The absolute values of the susceptibility are somewhat different from that in Figure S 5.6.4-1 (^{10}B sample), owing to the larger ferromagnetic signal (see Figure S 5.6.4-5). The arrow shows the suppression of T_c by the applied field.

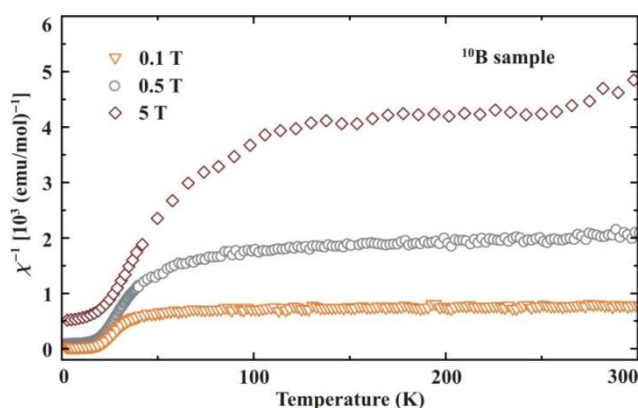


Figure S 5.6.4-7 Magnetic susceptibility of FeB_4 measured up to room temperature. Note that above 70 K the susceptibility is nearly temperature-independent. A weak ferromagnetic signal gives rise to a net moment of about $0.001 \mu_B/\text{f.u.}$ at room temperature, which is much smaller than the moment of $0.01\text{--}0.02 \mu_B/\text{f.u.}$ observed below 30 K. This residual ferromagnetic contribution is likely due to the metallic iron or another ferromagnet with a high T_C .

the susceptibility of the normal (non-superconducting) state above T_C . The second line marks the drop of the susceptibility right below T_C . We find $T_C \sim 2.95$ K and 2.89 K for the ^{10}B and ^{11}B samples, respectively. Judging by the smaller contribution of boron to the total electronic DOS at the Fermi level and to the total phonon DOS in the frequency range where the electron-phonon coupling picks up most of its total value [18], the isotope effect from boron substitution should be reduced by a factor of about 3. The rough theoretical estimate of -0.05 K ($\Delta T_C \approx 1/2T_C[\Delta M_B/M_B] \approx -0.15$ K divided further by 3) is then consistent with the -0.06 K value extracted from the experiment (for the calculation see, for instance, Hinks D.G & Jorgensen, J.D. The isotope effect and phonons in MgB_2 . *Physica C* 385, 98-104 (2003)).

The procedure described above determines the onset temperature T_{onset} , which is consistent with the specific heat data (see Figure 5.6.2-3 of the manuscript). Unfortunately, the standard way of determining T_{onset} from the deviation of the susceptibility from the straight line above T_C does not apply to our case, because the susceptibility above T_C is influenced by the ferromagnetic impurity. This can be seen from the data in Figure 5.6.2-2, where the susceptibility of the ^{10}B sample above 3.1 K is well approximated by the straight line, whereas that of the ^{11}B sample is somewhat curved, because this sample has a larger amount of the ferromagnetic impurity (Figure S 5.6.4-5). Therefore, the deviation of the susceptibility from the straight line may not be the correct onset temperature. While the line for the normal state entails certain ambiguity, the lower T_C of the ^{11}B sample is additionally confirmed by the midpoints of the susceptibility drop, $T_{\text{mid}} = 2.70$ K (^{11}B) and $T_{\text{mid}} = 2.82$ K (^{10}B), see Figure 5.6.2-2. The reduction in the T_C is accompanied by the broadening of the superconducting transition.

This broadening may reflect differences in the microstructure and crystallinity, which are inevitable in samples synthesized under high pressure and hinder the evaluation of the isotope effect.

Above 70 K, magnetic susceptibility of FeB_4 is nearly independent of temperature, as expected for a Pauli paramagnet (Figure S 5.6.4-7). A marginal ferromagnetic contribution is still present, as seen from the field dependence of the susceptibility and a very weak net moment of about $0.001 \mu_B/\text{f.u.}$ This residual ferromagnetic contribution, which is presumably of impurity origin (e.g., trace amounts of unreacted Fe), is much smaller than the ferromagnetic signal below 30 K. Assuming that the ferromagnetic contribution is inversely proportional to the applied field, we corrected the absolute values of the magnetic susceptibility and obtained $\chi_0 \sim 0.0002 \text{ emu/mol}$ for the intrinsic signal of FeB_4 at high temperatures.

Heat capacity measurements. Heat capacity was measured by relaxation technique using the Quantum Design PPMS in the temperature range of 1.8–20 K. Measurements in a broader temperature range are presently impossible owing to the very small size of available samples. Fortunately, trace amounts of ferromagnetic impurities do not affect the heat capacity data. Therefore, the data can be analyzed quantitatively, as described in the text of the article. Figure S 5.6.4-8 shows the fit of the normal-state heat capacity (applied field of 1 T) with $C_p = \gamma_n T + \beta T^3$. The upturn below 3 K is due to a Schottky anomaly related to nuclear degrees of freedom.

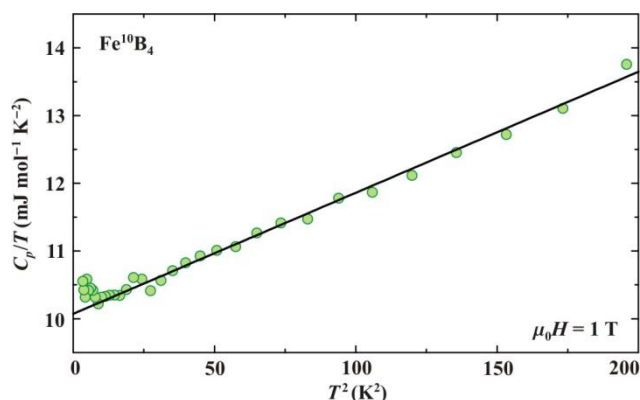


Figure S 5.6.4-8 Specific heat of the Fe^{10}B_4 sample measured in the applied field of 1 T and plotted as C_p/T vs. T^2 , together with the linear fit corresponding to $C_p = \gamma_n T + \beta T^3$.

Transmission electron microscopy study of FeB₄. The sample was characterized by means of electron diffraction (ED), high angle annular dark field scanning transmission electron microscopy (HAADF-STEM) and energy dispersive X-ray (EDX) analysis. The ED and EDX investigations have been carried out on a Phillips CM20 transmission electron microscope. The HAADF-STEM images have been acquired using a FEI Tecnai G2 microscope. Both instruments were operated at 200 kV.

The ED patterns of FeB₄ are shown in Figure S 5.6.4-9. They can be indexed on an orthorhombic lattice with cell parameters $a \approx 5.3 \text{ \AA}$, $b \approx 4.6 \text{ \AA}$, $c \approx 3.0 \text{ \AA}$. The $hk0$: $h + k = 2n$ and $h0l$: $h + l = 2n$ reflection conditions are observed in the $[100]$ and $[010]$ ED patterns, leading to the extinction symbol Pnn - and space groups $Pnn2$ or $Pnnm$. The reflection conditions $h00$: $h = 2n$, $0k0$: $k = 2n$, $00l$: $l = 2n$ are slightly violated in the $[001]$, $[101]$, $[110]$ and $[011]$ ED patterns because of multiple diffraction. The estimated cell parameters and the space group are consistent with the crystallographic data provided for the FeB₄ structure (Table S 5.6.4-2). The EDX spectra demonstrate that no side elements are present in the FeB₄ crystallites.

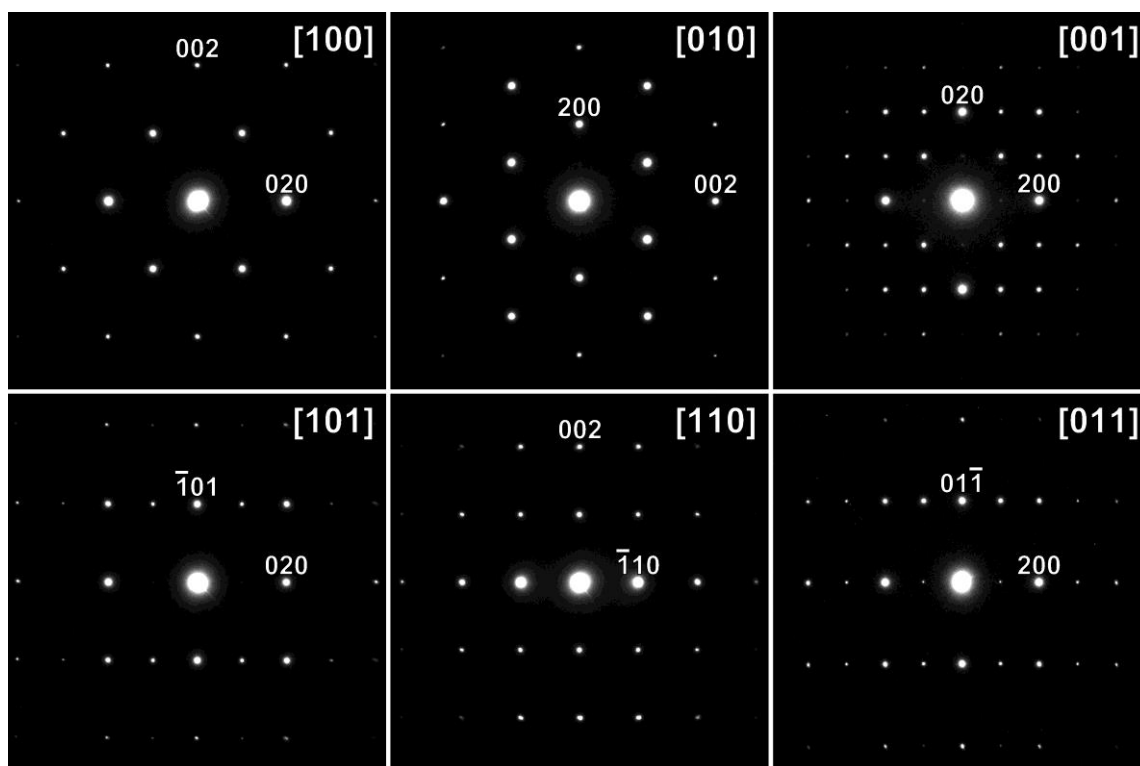


Figure S 5.6.4-9 ED patterns of FeB₄.

The HAADF-STEM images of FeB₄ acquired along the [001], [010] and [001] zone axes are shown in Figure S 5.6.4-10. In this microscopy technique, the intensity is proportional to Z^n , where Z is the average atomic number of the projected column ($1.6 < n < 1.9$). Therefore, the bright dots on the images are attributed to the Fe atomic columns ($Z_{\text{Fe}} = 26$); and the B ($Z_{\text{B}} = 5$) columns are indiscernible. The inserts in Figure S 5.6.4-10 show HAADF-STEM images simulated with the provided FeB₄ structure (Table S 5.6.4-2) using the QSTEM software [259]. They demonstrate a remarkably good correspondence with the experimental images. The sizes of the inserts shown on [100], [010] and [001] images are $7b \times 7c$, $7a \times 7c$ and $7a \times 7b$, respectively. In each case the images were calculated for the thickness of around 8 nm.

Planar defects have been observed in the structure. The fault planes are confined to the (010) crystal plane and appear on the [001] HAADF-STEM image (Figure S 5.6.4-11a) as lines running parallel to the a -axis and consisting of pairs of the Fe columns with shorter projected intercolumn distance in comparison with the matrix. A net of the projected Fe–Fe intercolumn separations within the basic structure and the defect plane are shown in Figure S 5.6.4-11a with lines. The normal intercolumn distances are shown in white, while the shortened ones are highlighted with green colour. The shortening of the projected Fe–Fe distances can be represented as resulting from a displacement of one structure fragment with respect to another one by a fraction of the [110] lattice vector. The fractional component of this vector has been estimated directly from the HAADF-STEM image by fitting the intensity profiles taken along the [110] direction with a set of Gaussian functions in a Fityk software [260]. The value of the displacement component along the [110] direction has been estimated as 0.10(2) [110]. Although the complete structure of the defects cannot be precisely revealed with the HAADF-STEM technique because of its low sensitivity to the B atoms, plausible speculation can be made taking into account tight intergrowth of the FeB₄ and Fe₂B₇ structures in the synthesized sample. The fault planes with shortened Fe–Fe separations can be considered as an insertion of the building elements of the Fe₂B₇ structure into the FeB₄ matrix. Such elements are enlarged 16-fold boron cages embracing double Fe columns as shown in Figure S 5.6.4-11b.

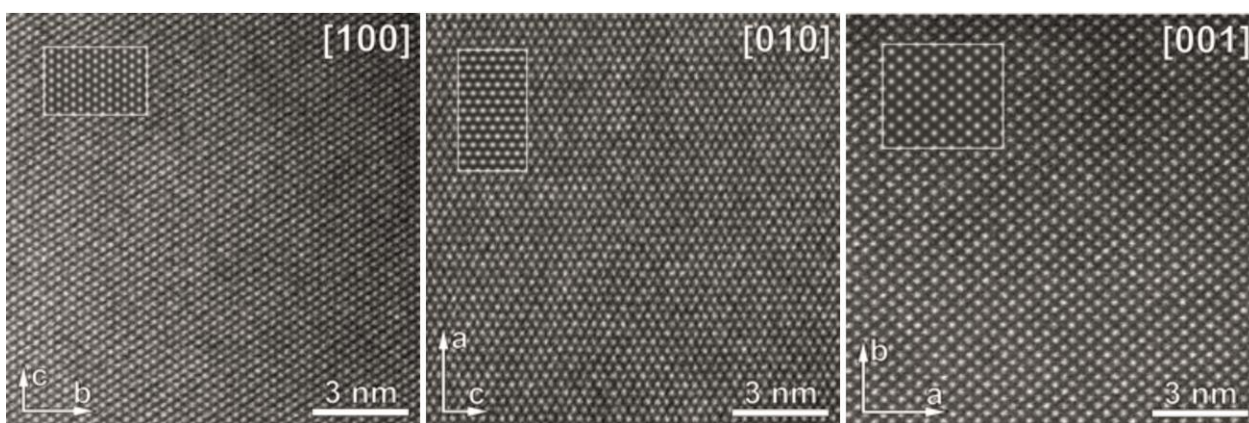


Figure S 5.6.4-10 HAADF-STEM images of FeB_4 . The inserts show simulated images.

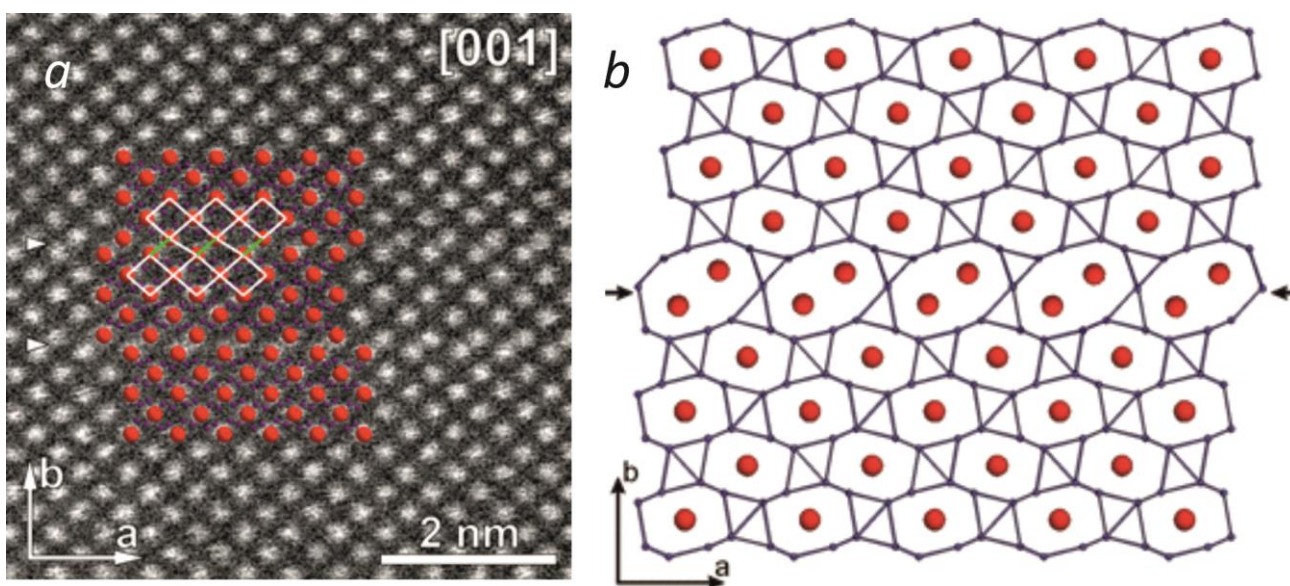


Figure S 5.6.4-11 Structure of FeB_4 . (a) HAADF-STEM image of the defect area in FeB_4 along with the structure projection (Fe columns are shown as red spheres). The white lines correspond to the normal projected Fe–Fe distances. The green ones are attributed to the shortened projected Fe–Fe distances at the defect plane. (a) Tentative defect model with insertion of the enlarged 16-fold boron cages with double Fe columns (marked with arrows).

5.7. Crystal structures and compressibility of novel iron borides Fe_2B_7 and Fe_xB_{50} synthesized at high pressure and high temperature

E. Bykova^{1,2}, H. Gou², M. Bykov², M. Hanfland³, N. Dubrovinskaia², L. Dubrovinsky¹

¹*Bavarian Research Institute of Experimental Geochemistry and Geophysics, University of Bayreuth, D-95440 Bayreuth, Germany*

²*Laboratory of Crystallography, University of Bayreuth, D-95440 Bayreuth, Germany*

³*European Synchrotron Radiation Facility, BP 220, Grenoble F-38043, France*

Prepared for submission in J. Solid State Chemistry

5.7.1. Abstract

We present here a detailed description of the crystal structures of novel iron borides, Fe_2B_7 and Fe_xB_{50} with various iron content ($x = 1.01(1), 1.04(1), 1.32(1)$), synthesized at high pressures and temperatures. As revealed by high-pressure single-crystal X-ray diffraction, the structure of Fe_2B_7 possesses short incompressible B-B bonds that results in high bulk modulus. Like similarly structured FeB_4 and MnB_4 , Fe_2B_7 is as stiff as diamond in one crystallographic direction, but its volume compressibility is even lower than that of FeB_4 and MnB_4 . Fe_xB_{50} adopts the structure of the tetragonal $\delta\text{-B}$, in which Fe atoms occupy an additional interstitial position. Fe_xB_{50} does not show anisotropy in elastic behavior.

5.7.2. Introduction

Metal borides are an important class of compounds having a number of remarkable properties like superconductivity (MgB_2 , FeB_4 [12,128]), low compressibility (OsB_2 , MnB_4 , FeB_4 , WB_4 [10,11,128,130]), and high hardness (tungsten borides, FeB_4 [9,128]). Therefore synthesis of novel metal borides and investigation of their properties have a great interest for material science and technology. Theoretical calculations can help in a search for the compounds with a combination of beneficial properties. Recently Komogorov *et al.* [18] predicted the existence of a superconducting iron tetraboride, FeB_4 . Later on Bialon *et al.* [261] calculated the formation conditions of tetraborides and suggested that the phases are stabilized by high pressure. We successfully synthesized FeB_4 using multianvil apparatuses and demonstrated its impressive

mechanical properties like high hardness of 62(5) GPa and very low compressibility with the bulk modulus of 252(5) GPa [128]. We propose that the low compressibility originates from short boron covalent bonds located along the *b* crystallographic axis that makes the structure of FeB₄ in corresponding direction as incompressible as diamond. Similar anisotropy in compressibility is found in MnB₄ structurally close to FeB₄. Recent high-pressure high-temperature (HPHT) synthesis of novel cobalt boride Co₅B₁₆ [133] suggests variety of structurally related borides with other transition metals. We mentioned [128] formation of other iron borides, Fe₂B₇ and Fe_{1.04(1)}B₅₀, along with FeB₄ upon HPHT synthesis of the latter. According to theoretical calculations [262] Fe₂B₇ is metastable up to 30 GPa. The authors [262] particularly emphasized that without *a priori* experimental knowledge *ab initio* prediction of the compound with such stoichiometry and a large unit cell “would have been no less than an act of clairvoyance”. In the current work we present a detailed description of the crystal structures of Fe₂B₇ and Fe_xB₅₀ and their behavior under compression to about 50 GPa. We observed that Fe_xB₅₀ is a boride with a structure based on δ -B (tetragonal B50) [263] where Fe atoms occupy a distinct interstitial crystallographic position in the structure. Interestingly, the occupancy of this position may vary in different crystals, as revealed by the crystal structure refinement. For the three crystals studied in the present work the occupancy of the iron structural position was found to be 50(1), 52(1) and 66(1) % that allowed us to assign to all of them a general chemical formula Fe_xB₅₀, where $x = 1.01(1), 1.04(1), 1.32(1)$. The results of compressibility studies, based on high-pressure single-crystal X-ray diffraction (XRD), are reported for Fe₂B₇, Fe_{1.01(1)}B₅₀ and Fe_{1.32(1)}B₅₀.

5.7.3. Materials and methods

Sample preparation

Single crystals of Fe₂B₇ and Fe_xB₅₀ were grown using a powder of β -boron (purity of 99.9995 *at.* %, grain size of <1000 microns, *Chempur Inc.*) and iron wire (purity of 99.99+ %, 0.5 mm and 1 mm diameter, *Alfa Aesar*) as starting materials.

High-pressure high-temperature synthesis of Fe₂B₇ was carried out in multianvil apparatus using a 1200-ton Sumitomo hydraulic press installed at the Bayerisches Geoinstitut (BGI,

Bayreuth, Germany). Starting materials placed in *h*-BN capsule and pressurized to 15 GPa were heated to 1700 °C and after 5–10 minutes cooled down to 1200 °C with a cooling rate of 10 °C/min. The sample was kept at 1200 °C for 30 minutes and then quenched by switching off the power supply.

Fe_xB₅₀ single crystals were grown in 1000-ton (Hymag) hydraulic press at the BGI in a similar manner. The synthesis was conducted at 12 GPa, after heating to 1700 °C for 5–10 minutes, the sample was cooled down to 1400 °C and kept for 30 minutes at this temperature, then quenched. See [128] for more details.

X-ray diffraction and data analysis

Single-crystal XRD of Fe₂B₇ and Fe_{1.04(1)}B₅₀ at ambient conditions was collected using four-circle Oxford Diffraction Xcalibur diffractometer (Mo-*K*α radiation) equipped with a Xcalibur Sapphire2 CCD detector under control of a CrysAlisPro software [264].

For high-pressure experiments in diamond anvil cells (DACs) we used a small platelet-shaped single crystal of Fe₂B₇ and two platelet crystals of Fe_xB₅₀ with an average size of 0.03 x 0.03 x 0.005 mm³. The crystals were pre-selected on a three-circle Bruker diffractometer equipped with a SMART APEX CCD detector and a high-brilliance Rigaku rotating anode (Rotor Flex FR-D, Mo-*K*α radiation) with Osmic focusing X-ray optics. Due to the small size of the samples it was not possible to obtain reliable XRD data using in-house diffractometer.

Selected crystals together with small ruby chips (for pressure estimation) were loaded into the BX90-type DACs [105]. Neon used as a pressure transmitting medium was loaded with a gas loading system installed at the BGI [112].

The single-crystal high pressure XRD experiments were conducted at ID09A beamline at the European Synchrotron Radiation Facility, Grenoble, France (MAR555 detector, $\lambda = 0.4144$ and 0.4141 Å, spot size ~ 10 μm in diameter). The sample-to-detector distance was calibrated using a LaB₆ powder. Nine and ten pressure points were collected for Fe_xB₅₀ and Fe₂B₇, respectively covering the pressure range up to 50 GPa. Below 10 GPa pressures were measured using the

ruby fluorescence [113] and above 10 GPa – the equation of state of Ne (<http://kantor.50webs.com/diffraction.htm>). XRD patterns were recorded during continuous rotation of DACs from -40 to +40 on omega, and data collection experiments were performed by narrow 1° scanning of the same omega range.

Integration of the reflection intensities was performed using CrysAlisPro software [264]. For ambient pressure experiments empirical absorption correction using spherical harmonics, implemented in SCALE3 ABSPACK scaling algorithm, was applied. The structures were solved by the direct method using the SHELXS software [124] implemented in X-Seed package [194]. Full matrix least squares refinement on F^2 was performed by means of SHELXL [124] and Jana2006 software package [125]. The crystallographic data of Fe₂B₇ and Fe_xB₅₀ ($x = 1.01(1)$ and $1.04(1)$, and $1.32(1)$) including high-pressure studies have been deposited in the Inorganic Crystal Structure Database [166]. The data may be obtained free of charge from Fachinformationszentrum Karlsruhe, 76344 Eggenstein-Leopoldshafen, Germany (fax: (+49) 7247-808-666; e-mail: crysdata@fiz-karlsruhe.de, http://www.fiz-karlsruhe.de/request_for_deposited_data.html) on quoting following deposition numbers: 426694 (Fe₂B₇ ambient conditions), 428924-428933 (compression of Fe₂B₇ from 3.4 to 41.1 GPa), 426695 (Fe_{1.04(1)}B₅₀ ambient conditions), 428915-428923 (compression of Fe_{1.01(1)}B₅₀ from 2.8 to 47.3 GPa), 428934-428942 (compression of Fe_{1.32(1)}B₅₀ from 2.8 to 47.6 GPa).

5.7.4. Results

Crystal structure of Fe₂B₇

The X-ray diffraction data obtained at ambient conditions for Fe₂B₇ and some experimental details are presented in Table 5.7.4-1. The unit cell of Fe₂B₇ is orthorhombic (*Pbam*, $a = 16.9699(15)$, $b = 10.6520(9)$, $c = 2.8938(3)$ Å). Similarly to other boron-rich metal borides, tetraborides MB_4 ($M = \text{Fe, Mn, Cr}$) and Co₅B₁₆ [128,130,133,134], the structure of Fe₂B₇ can be described based on a rigid covalent framework of boron atoms. Boron-boron distances in the network vary from 1.631(15) to 2.025(14) Å that corresponds well with those of MB_4 ($M = \text{Fe, Mn, Cr}$) and Co₅B₁₆ (see [133] for the values). Boron atoms do not form boron icosahedra typical for boron polymorphs, but instead the boron framework provides voids to be filled by

iron atoms, so that the structure can be characterized in terms of packing of iron coordination polyhedra of various kinds.

Table 5.7.4-1 X-ray diffraction data for $\text{Fe}_{1.04(1)}\text{B}_{50}$ and Fe_2B_7 measured at ambient conditions*.

Empirical formula	$\text{Fe}_{1.04(1)}\text{B}_{50}$	Fe_2B_7
Crystal system	Tetragonal	Orthorhombic
Space group	$P4_2/nnm$	$Pbam$
a (Å)	8.9866(4)	16.9699(15)
b (Å)	8.9866(4)	10.6520(9)
c (Å)	5.0620(4)	2.8938(3)
V (Å ³)	408.80(4)	523.09(8)
Z	1	8
Calculated density (g/cm ³)	2.431	4.758
Crystal size (mm ³)	0.11x0.10x0.04	0.07x0.07x0.05
Theta range for data collection (°)	3.21 to 33.66	2.26 to 30.50
Completeness to theta = 25°, %	99.5	100
Reflections collected	1607	2230
Independent reflections / R_{int}	424 / 0.0416	940 / 0.0655
Data [$I > 2\sigma(I)$] / restraints / parameters	358 / 0 / 36	604 / 0 / 67
Goodness of fit on F^2	1.208	0.978
Final R indices [$I > 2\sigma(I)$]	0.0496 / 0.1162	0.0529 / 0.1024
R_1/wR_2		
R indices (all data)	0.0623 / 0.1206	0.0736 / 0.0868
R_1/wR_2		
Largest diff. peak and hole (e / Å ³)	0.709 and -0.282	1.218 and -1.354
ISCD reference N	426695	426694

* X-ray data collected in-house on Oxford Diffraction Xcalibur diffractometer (Mo- $K\alpha$ radiation).

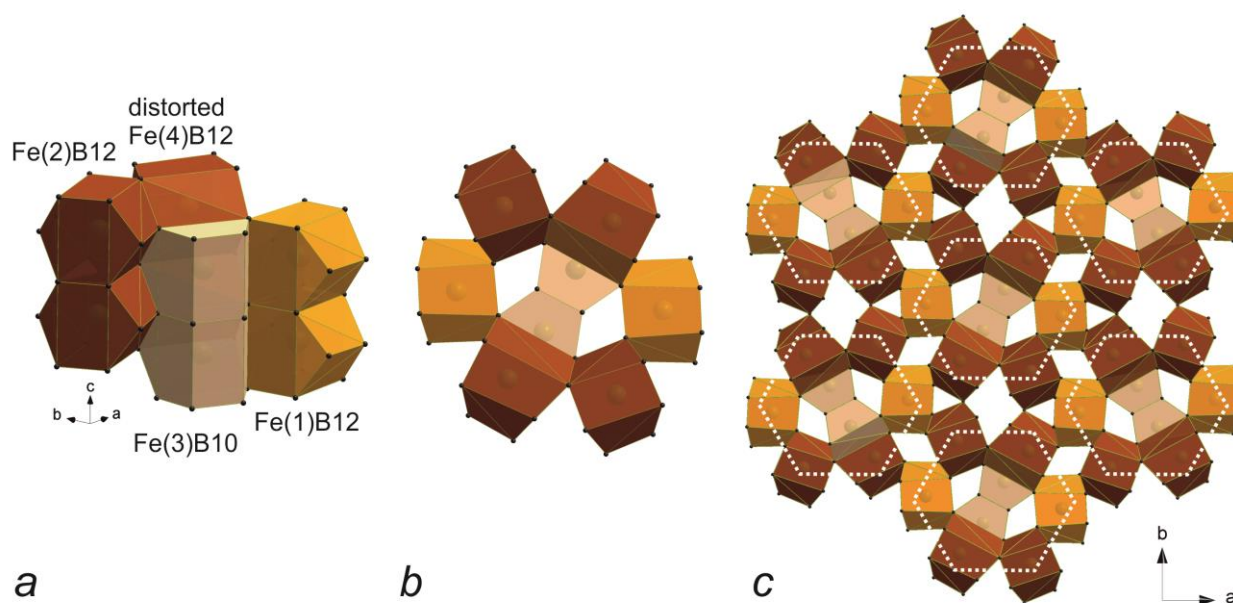


Figure 5.7.4-1 Crystal structure of Fe_2B_7 composed of Fe(3)B_{10} , Fe(1)B_{12} , Fe(2)B_{12} , Fe(4)B_{12} polyhedra. Polyhedra of each kind are packed in columns along the c -axis by sharing common top and bottom parallelogram faces (a). The z -coordinates of Fe atoms in light and dark polyhedra differ by $\frac{1}{2}$. Eight columns of polyhedra, two columns of each kind assembled together and provide a rod-like “hexagonal” fragment of the structure extended in the c -direction (b). The “rods” share common edges and vertices and create close packing.

Four crystallographically independent iron atoms in Fe_2B_7 are surrounded by 10 or 12 boron atoms, forming Fe(3)B_{10} , Fe(1)B_{12} , Fe(2)B_{12} , Fe(4)B_{12} polyhedra (Figure 5.7.4-1a). Fe(1)B_{12} and Fe(2)B_{12} polyhedra have an irregular shape, Fe-B bond lengths are weakly scattered: Fe(1)-B distances are in a range of 1.992(10)–2.287(8) Å, while Fe(2)-B distances vary from 1.972(10) to 2.285(8) Å. In Fe(1)B_{12} and Fe(2)B_{12} polyhedra Fe atom is surrounded by two B6 rings and as a result, four boron atoms form a parallelogram in the FeB_{12} -polyhedron’s equatorial plane, which is parallel to the ab -plane. Other four atoms are located above and the rest four – beneath the equatorial plane. Fe(4)B_{12} polyhedra have a distorted shape with larger variations in the interatomic distances, between 1.952(10) and 2.662(9) Å. The Fe(3)B_{10} polyhedron, compared to the FeB_{12} one, misses two vertices in the equatorial plane (Figure 5.7.4-1a). However, it does not affect the Fe–B distances, they vary in Fe(3)B_{10} from 2.076(7) to 2.278(8) Å.

Polyhedra of each kind are packed in columns along the c -axis by sharing common top and bottom parallelogram faces (Figure 5.7.4-1a, b) similarly to polyhedra packing in MB_4 ($M = \text{Fe}$,

Mn, Cr) and Co_5B_{16} . In Fe_2B_7 two columns of $\text{Fe}(3)\text{B}_{10}$ polyhedra are joined through common rectangular side faces. Additionally, the $\text{Fe}(3)\text{B}_{10}$ -column is connected to a column of $\text{Fe}(1)\text{B}_{12}$ polyhedra through sharing common triangular side faces. Iron atoms in $\text{Fe}(1)\text{B}_{10}$ and $\text{Fe}(3)\text{B}_{12}$ columns have same z -coordinates. The other two neighboring columns (formed by $\text{Fe}(2)\text{B}_{12}$ and $\text{Fe}(4)\text{B}_{12}$ polyhedra) (Figure 5.7.4-1a) are shifted by $c/2$ along the z -axis with respect to the $\text{Fe}(3)\text{B}_{10}$ one, so that the $\text{Fe}(2)\text{B}_{12}$ have common side edges with $\text{Fe}(3)\text{B}_{10}$, and $\text{Fe}(4)\text{B}_{12}$ are connected to $\text{Fe}(3)\text{B}_{10}$ through a rectangular side face. Eight columns of polyhedra, two columns of each kind (Fig. 1a), assembled together as shown in Figure 5.7.4-1b (the view along the c -axis) provide a rod-like “hexagonal” fragment of the structure extended in the c -direction. If the “rods”, connecting through common edges and vertices, are close packed in the ab -plane (Figure 5.7.4-1c), they form a three-dimensional structure of Fe_2B_7 .

Crystal structure of $\text{Fe}_{1.04(1)}\text{B}_{50}$, $\text{Fe}_{1.01(1)}\text{B}_{50}$ and $\text{Fe}_{1.32(1)}\text{B}_{50}$

As mentioned above, $\text{Fe}_{1.04(1)}\text{B}_{50}$ was a byproduct in experiments on HPHT synthesis of FeB_4 [128]. Single-crystal X-ray diffraction data for $\text{Fe}_{1.04(1)}\text{B}_{50}$ obtained at ambient conditions are provided in Table 5.7.4-1 along with the experimental details. The crystal structure of $\text{Fe}_{1.04(1)}\text{B}_{50}$ is shown on Figure 5.7.4-2. It is built on the basis of the structure of a tetragonal boron polymorph, $\delta\text{-B}$ [263]. In the structure of $\delta\text{-B}$ ($\text{B}_2\text{B}_{48} = \text{B}_2(\text{B}_{12})_4$) boron icosahedra form a 3-dimensional framework being arranged in the distorted cubic close (*fcc*) packing having 8 distorted tetrahedral cavities per a unit cell. Two of eight cavities are located in the $2a$ Wyckoff position, each one is surrounded by four B(3) atoms belonging to the corners of B12 icosahedra. In the crystal structure of $\delta\text{-B}$ this cavity is occupied by a boron atom forming covalent bonds with four corners of B12 icosahedra. Other two voids with the geometric centers in the $2b$ Wyckoff position are formed by 4 triangular faces B(3)–B(2)–B(2) of B12 icosahedra.

Similarly to $\delta\text{-B}$, in the structure of $\text{Fe}_{1.04(1)}\text{B}_{50}$ the first geometrically small cavity is occupied by boron B(5) atom covalently bonded to four corners of the icosahedra ($d_{\text{B}(5)\text{--B}(3)} = 1.720(2) \text{ \AA}$). The void of the second type is partially filled by Fe atoms, with Fe-B distances being of 2.2218(17) (Fe(1)–B(2)), 2.548(2) (Fe(1)–B(3)) and 2.52935(15) \AA (Fe(1)–B(5)). Other four

cavities in the structure with geometric centers in the $4c$ in $4d$ Wyckoff positions have the shorter distances from their centers to boron atoms belonging to icosahedra of ~ 1.882 and 1.956 \AA , respectively. The distances are too long for a B–B covalent bond; on the other hand the cavities are too small to be occupied by iron atoms and, therefore, they remain unfilled.

A similar atomic arrangement was found in $\text{B}_{48}\text{C}_2\text{V}_{1.29}$ and $\text{B}_{48}\text{C}_2\text{Ti}_{1.86}$ [265], where metal atoms fill the large cavity with a center in the $2b$ position, while carbon atoms occupy the $2a$ position and form covalent bonds with four boron atoms. We note that the occupation degree by a metal depends on its atomic radius. Small Ti atoms almost fully occupy the cavity (93%), whereas the amount of V and Fe does not exceed $\sim 65\%$

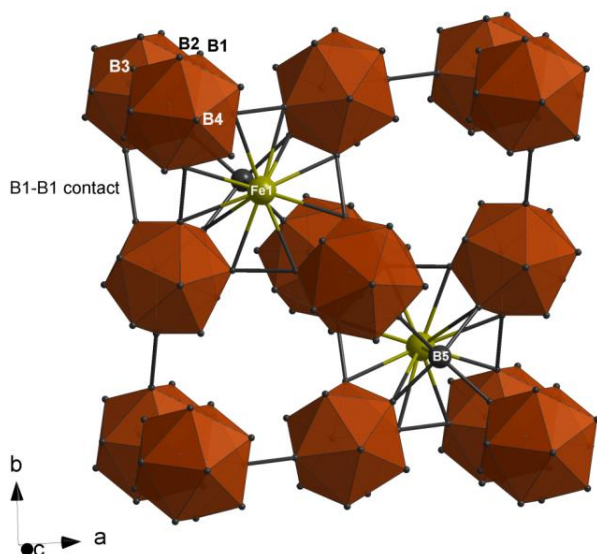


Figure 5.7.4-2 Crystal structure of Fe_xB_{50} ($x = 1.01(1), 1.04(1), 1.32(1)$) built on the basis of the structure of a tetragonal boron polymorph, δ -B. Boron icosahedra form a 3-dimensional framework being arranged in the distorted *fcc* packing having 8 distorted tetrahedral cavities per unit cell. Two of eight cavities are located in the $2a$ Wyckoff position and occupied by interstitial B(5) atoms forming short covalent bonds with four surrounding B(3) atoms belonging to the corners of B12 icosahedra. Two larger cavities with the geometric centers in the $2b$ Wyckoff position are partially filled by Fe(1) atoms. The B(1)...B(1) interatomic distances in $\text{Fe}_{1.32(1)}\text{B}_{50}$ are shorter than in $\text{Fe}_{1.01(1)}\text{B}_{50}$ that probably allows $\text{Fe}_{1.01(1)}\text{B}_{50}$ to contract more effectively during compression.

Compressibility of iron borides

Up to highest pressure reached (~41 GPa for Fe₂B₇ and ~48 GPa for Fe_xB₅₀) no phase transitions were detected (Figure 5.7.4-3). Therefore the whole volume-pressure data-sets were used to fit following parameters of Birch–Murnaghan equation of state (EOS): the zero-pressure unit cell volume (V_0), bulk modulus (K_0), and the first derivative K_0' (optional). Figure 5.7.4-3 shows the pressure dependence of the unit cell volume of Fe₂B₇ and Fe_xB₅₀ ($x = 1.01(1), 1.32(1)$) and corresponding fits of the Birch–Murnaghan EOSes. Table 5.7.4-2 contains the results of the fits in comparison with other borides and boron phases. The fit of the 3rd order Birch–Murnaghan EOS for Fe₂B₇ gave the following values: $K_0 = 268.9(1.7)$ GPa, $K_0' = 3.2(2)$, $V_0 = 523.10(8)$ Å³. The calculated value of V_0 is in a perfect agreement with that (523.09(8) Å³) obtained from single-crystal XRD at ambient conditions.

At ambient conditions no single-crystal XRD data for Fe_xB₅₀ ($x = 1.01(1), 1.32(1)$) were collected. Therefore accurate values of V_0 for these compounds were unknown. We used the unit cell volume of Fe_{1.04(1)}B₅₀ as an approximation for V_0 of Fe_{1.01(1)}B₅₀ and fit the volume-pressure data with the 3rd order Birch–Murnaghan EOS ($K_0 = 171.6(1.5)$ GPa, $K_0' = 4.1(2)$, $V_0 = 407.30(7)$ Å³). For Fe_{1.32(1)}B₅₀ such approximation is not valid anymore, therefore we refined the data with the 2nd order Birch–Murnaghan EOS ($K_0 = 186(9)$ GPa, $K_0' = 4$, $V_0 = 406.7(1.3)$ Å³). Note that Fe_{1.32(1)}B₅₀ with higher iron content has a slightly higher bulk modulus than Fe_{1.01(1)}B₅₀ (Figure 5.7.4-4).

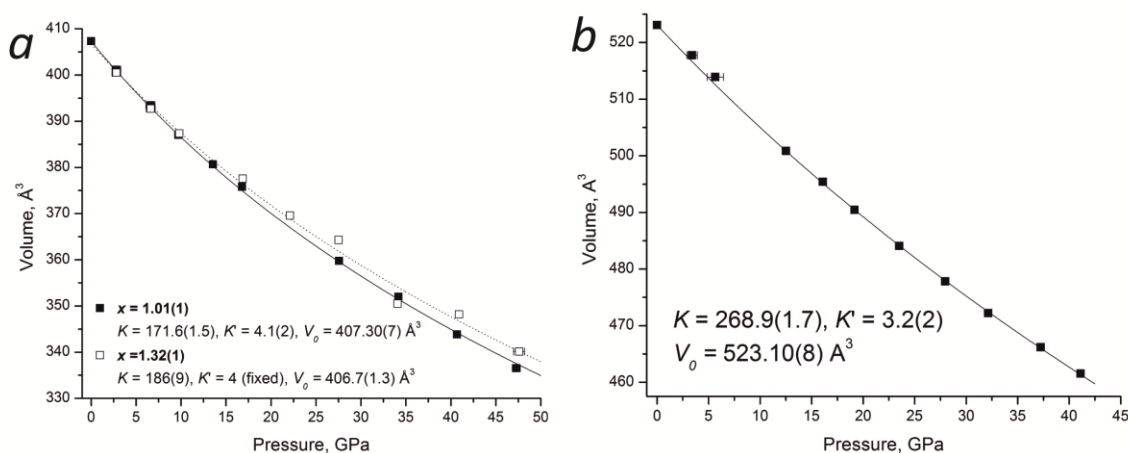


Figure 5.7.4-3 Volume compressibility of Fe_xB_{50} (*a*, filled squares – $\text{Fe}_{1.01(1)}\text{B}_{50}$, open squares – $\text{Fe}_{1.32(1)}\text{B}_{50}$), and Fe_2B_7 (*b*) based on high-pressure synchrotron single-crystal data. Solid and dashed lines correspond to the fit with the Birch–Murnaghan EOS. Fe_xB_{50} , having voids in the structure, contracts more effectively than Fe_2B_7 .

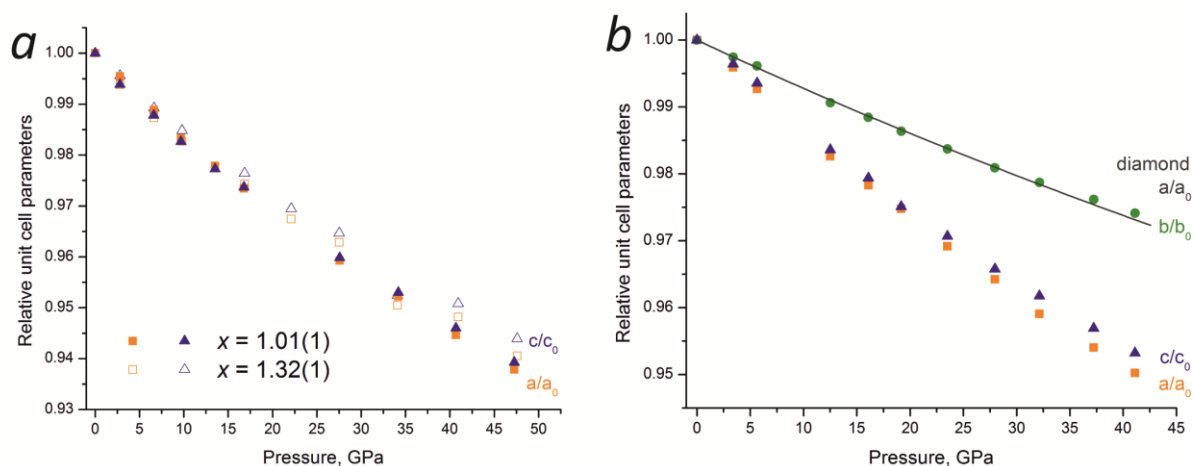


Figure 5.7.4-4 Axial compressibility of Fe_xB_{50} (*a*, filled symbols – $\text{Fe}_{1.01(1)}\text{B}_{50}$, open symbols – $\text{Fe}_{1.32(1)}\text{B}_{50}$) and Fe_2B_7 (*b*) based on high-pressure synchrotron single-crystal data. The unit cell parameters of Fe_xB_{50} change almost uniformly (*a*), while Fe_2B_7 along the b -axis is less compressible than in a and c -directions. Short B–B bonds oriented along the b -axis probably cause its high stiffness close to that of a diamond (solid line) [129].

Table 5.7.4-2 Bulk modulus (K_0) and its pressure derivative (K_0') for iron borides and boron phases.

Compound	K_0 , GPa	K_0'	Maximal pressure, GPa	Source	Reference
α -B	213(15)	4 (fixed)	5	Single-crystal XRD	[135]
α -B	207.1(12)	4.2(3)	100	Powder XRD	[136]
β -B	210(6)	2.23	97	Single-crystal XRD	[137]
β -B	201(9)	4.2(9)	31	Powder XRD	[138]
β -B	185(7)	-	10	Neutron powder diffraction	[135]
γ -B	227(3)	2.5(2)	40	Single-crystal XRD	[139]
γ -B	281(6)	2.8(9)	45-65	Single-crystal XRD	[139]
$\text{Fe}_{1.01(1)}\text{B}_{50}$	171.6(1.5)	4.1(2)	47.3	Single-crystal XRD	Current work
$\text{Fe}_{1.32(1)}\text{B}_{50}$	186(9)	4 (fixed)	47.6	Single-crystal XRD	Current work
FeB_4	252(5)	3.5(3)	38.2	Single-crystal XRD	[128]
MnB_4	258(5)	4 (fixed)	25	Powder XRD	[130]
WB_4	304(10) / 200(40)	4 (fixed) / 15.3(5.7)	25	Powder XRD	[175]
WB_4	339(3)	4 (fixed)	30	Powder XRD	[9]
WB_4	325(9)	5.1(6)	50.8	Powder XRD	[11]
Fe_2B_7	268.9(1.7)	3.2(2)	41.1	Single-crystal XRD	Current work

5.7.5. Discussion

The five crystalline boron polymorphs, α -, β -, γ -, δ -, ϵ - [27,263], are rather similarly composed. All their structures contain B12 icosahedra connected through covalent B–B bonds. Compressibility data were reported only for α -, β -, and γ -B [135–139], all polymorphs were found to contract almost uniformly in all directions.

Compressibility of Fe_xB_{50} gives a rough approximation for the one of δ -B phase so far unknown. The δ -B can be grown only as tiny $\sim 2\text{--}5\ \mu\text{m}$ thick needles [263] that in combination with low scattering power of boron atoms makes challenging high-pressure XRD studies. We can expect that a small amount of iron atoms in Fe_xB_{50} would have an insignificant influence on the rigidity of boron network. Indeed, Fe_xB_{50} phases have the bulk moduli even smaller than those of boron

polymorphs (171.6(1.5) GPa for Fe_{1.01(1)}B₅₀ and 186(9) GPa for Fe_{1.32(1)}B₅₀ *versus* 207–249 for α -B, 185–210 GPa for β -B and 227–281 GPa for γ -B). This is reasonable taking into account unoccupied voids in Fe_xB₅₀ that allow the structure to contract more effectively than α -, β -, and γ -B. Recent experimental high-pressure studies suggest B12 icosahedra sustain better on compression than intercluster bonds [137,139], while theoretical calculations give contradictory results [266,267]. Single-crystal XRD allowed us to follow changes of each individual interatomic distance in Fe_xB₅₀ ($x = 1.01(1), 1.32(1)$) up to ca. 48 GPa. There are 17 such interatomic contacts and therefore simple visualization of corresponding pressure dependencies is low-informative. We performed linear fits of these dependencies and plotted calculated lines' slopes against corresponding lengths of interatomic distances at the lowest pressure, 2.8 GPa (Figure 5.7.5-1a). The same analysis was done for Fe₂B₇ (Figure 5.7.5-1b, see below for detailed description) for which 55 interatomic distances were considered. There are distinct fields on the diagram of Fe_xB₅₀ related to intra- and intericosahedral bonds. Our data confirm previous experimental observations [137,139] that intraicosahedral bonds are stiffer than intericosahedral ones. Fe–B and intraicosahedral B–B bonds contract almost uniformly in all directions that maintain the c/a ratio constant at a pressure increase. The major difference appears for intericosahedral B(1)–B(1) bonds (Figure 5.7.5-1a). At 2.8 GPa $d_{B(1)-B(1)}(\text{Fe}_{1.32(1)}\text{B}_{50}) = 1.963(3) \text{ \AA}$ is shorter than $d_{B(1)-B(1)}(\text{Fe}_{1.01(1)}\text{B}_{50}) = 1.997(4) \text{ \AA}$ that probably allows Fe_{1.01(1)}B₅₀ to contract more effectively. As a result Fe_{1.32(1)}B₅₀ has slightly larger bulk modulus compared to Fe_{1.01(1)}B₅₀.

Contrary to icosahedra-based structures discussed above, boron-rich transition metal borides have a strong anisotropy upon contraction (Figure 5.7.4-4). In one direction, namely along the b -axis, they are extremely incompressible (like diamond), but in other crystallographic directions their compressibility is comparable with that along the a and b axes in γ -B and a and c axes in Fe_xB₅₀.

High axial incompressibility along the b -axis originates from short and incompressible B–B bonds aligned along the b -axis (Figure 5.7.5-1b): B(5)–B(10), B(3)–B(6) and B(2)–B(8) (1.647(13), 1.628(14) and 1.691(13) \AA , respectively). The shrinkage of the bonds at 40 GPa is just ~ 1.5 –2.2 %, while other B–B bonds shrink much more effectively, they shorten by 2.9 to 6.0 %.

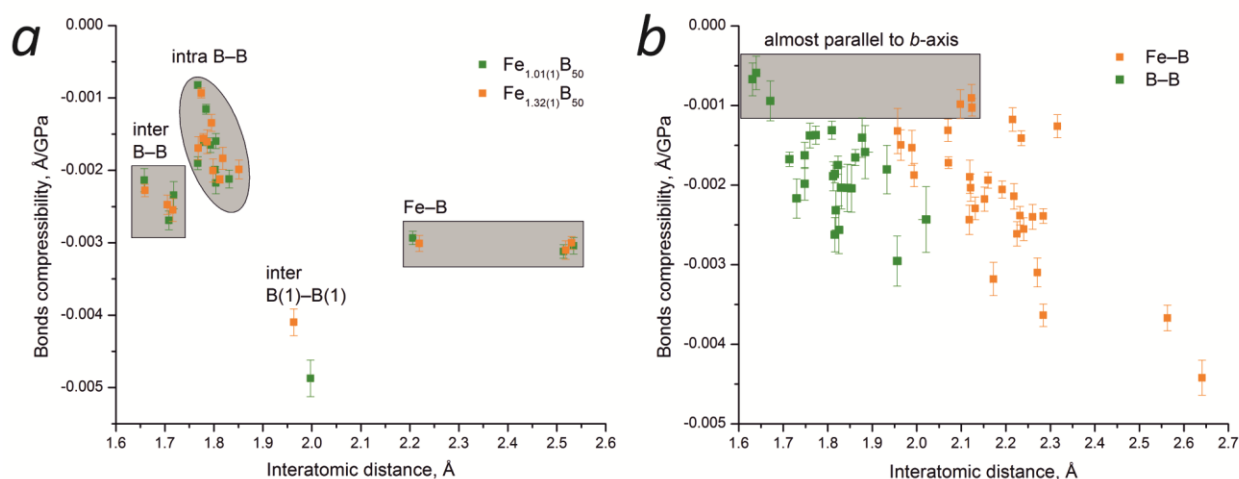


Figure 5.7.5-1 Relative change of interatomic distances ('Bonds compressibility' for short) for Fe_xB_{50} (*a*, green symbols – $\text{Fe}_{1.01(1)}\text{B}_{50}$, orange symbols – $\text{Fe}_{1.32(1)}\text{B}_{50}$) and Fe_2B_7 (*b*, green symbols – B-B, orange symbols – Fe-B) plotted against their lengths at the lowest pressure of 2.8 GPa (see text for detailed description). Interatomic distances in $\text{Fe}_{1.01(1)}\text{B}_{50}$ and $\text{Fe}_{1.32(1)}\text{B}_{50}$ demonstrate similar behavior under compression, only B(1)...B(1) contact was found to change differently. Intraicosahedral B-B bonds (ellipse) are harder to compress than intericosahedral ones. In Fe_2B_7 (*b*) the least compressible contacts (highlighted with grey rectangle) are oriented along the 'diamond-like-stiff' *b*-axis.

On the other hand, there is no such a tendency for Fe–B bonds that is likely a consequence of contraction of the boron network. The least compressible Fe–B bonds similarly shorten by 1.7–1.9 % and vary from 2.09 to 2.15 Å, while the shortest Fe–B bond (below 2 Å) contracts almost twice as effective (by 3.0 to 3.8%). The least contracting bonds are located on the *ab*-plane, while the B–B bonds contributing to the axial stiffness are almost strictly directed along the *b*-axis. Fe–B bonds generally follow this trend, however, they have a larger component along the *a*-axis. In comparison with FeB_4 and MnB_4 , Fe_2B_7 demonstrates the highest bulk modulus (see Table 5.7.4-2).

5.7.6. Conclusions

Our study of Fe_2B_7 and Fe_xB_{50} demonstrates how differences in crystal structure influence the high-pressure behavior of boron carbides. Fe_xB_{50} is composed of B12 icosahedra connected through boron and iron atoms. Such a network contracts easier upon compression due to the presence of large voids. Contrary, Fe_2B_7 has no pronounced voids in its structure and, similarly

to MnB_4 and FeB_4 , it is low compressible. Moreover the bulk modulus of Fe_2B_7 has the highest value in comparison with tetraborides and boron phases. We connect this remarkable mechanical property of Fe_2B_7 with short incompressible boron-boron contacts being one of the shortest among known boron phases and borides.

5.7.7. Acknowledgments

The work was supported by the German Research Foundation (DFG). N.D. thanks DFG for financial support through the Heisenberg Program and the DFG Project DU 954-8/1. H.G. gratefully acknowledges financial support of the Alexander von Humboldt Foundation.

5.8. Pressure-induced hydrogen bond symmetrization in iron oxyhydroxide

Weiming M. Xu¹, Eran Greenberg¹, Gregory Kh. Rozenberg¹, Moshe P. Pasternak¹,

Elena Bykova², Tiziana Boffa-Ballaran², Leonid Dubrovinsky²,

Vitali Prakapenka³, Michael Hanfland⁴,

Olga Yu. Vekilova⁵, Sergey I. Simak⁵, Igor A. Abrikosov⁵

¹*School of Physics and Astronomy, Tel Aviv University, 69978, Tel Aviv, Israel*

²*Bayerisches Geoinstitut, University of Bayreuth, Bayreuth, Germany*

³*Consortium for Advanced Radiation Sources, University of Chicago, 9700 South Cass Avenue, Argonne, IL 60439*

⁴*European Synchrotron Radiation Facility (ESRF), 6 rue Jules Horowitz, BP 220, F-38043 Grenoble Cedex, France*

⁵*Department of Physics, Chemistry and Biology (IFM), Linköping University, SE-581 83 Linköping, Sweden*

Phys. Rev. Lett. **111**, 175501 (2013).

5.8.1. Abstract

Under high pressures the hydrogen bonds were predicted to transform from a highly asymmetric soft O–H···O to a symmetric rigid configuration in which the proton lies midway between the two oxygen atoms. Despite four decades of research on hydroxyl containing compounds, pressure induced hydrogen bond symmetrization remains elusive. Following single-crystal X-ray diffraction, Mössbauer and Raman spectroscopy measurements supported by *ab initio* calculations, we report the H-bonds symmetrization in iron oxyhydroxide, FeOOH, resulting from the Fe³⁺ high-to-low spin crossover at above 45 GPa.

5.8.2. Manuscript

The hydrogen bond in oxyhydroxides and hydroxides is an attractive interaction between a hydrogen atom from a hydroxyl (O–H) group and a near neighbor oxygen atom or a group of atoms [65]. In contrast to other interacting atoms, H-bonds undergo large variations of their energetic and geometrical parameters under pressure [66–69]. At ambient pressure the O–H···O configuration is highly asymmetric. For example, in goethite, α -FeOOH, a common mineral in soils, sediments, and ore deposits, the angle formed by the (O–H) and the adjacent O is $161(3)^\circ$, the O–H length is $0.88(4)$ Å, and H···O is $1.90(4)$ Å [70]. As observed by Holzapfel [66] even moderate compression reduces the H···O distances, barely affecting the hydroxyl bond length, which leads to the strengthening of the hydrogen bond at high pressure [69]. Benoit *et al.* [67] and Lin *et al.* [68] predicted that higher compression will also lead to linearization of the O–H···O bond and eventually the formation of a *symmetric* O–H–O hydrogen species of equal O–H distances.

Symmetrization of hydrogen bonds is expected to have a significant effect on crystal structure and the behavior of materials [69]. Suggestions that the phenomena may occur under compression were reported for a number of compounds, namely, the hydrogen halides [71], δ -AlOOH(D), $\text{MgSi}_2\text{O}_4(\text{OH})_2$, δ -Al(OH)₃, CrOOH(D), GaOOH, InOOH, and formic acid [72–76], but only in H₂O ice-X, at pressures approaching 100 GPa, the elusive symmetrization has been unambiguously demonstrated [77–80].

Studies of hydrogen bond properties at pressures exceeding 20 GPa are difficult. The reason is that the ordinary direct and indirect structural methods such as powder X-ray diffraction (XRD), and vibration spectroscopy, Raman or Infra-Red (IR), are unable to locate the position of hydrogen [73–79]. Neutron diffraction, the perfect method for this purpose, is currently limited to pressures of <20 GPa [75]. Yet the combination of single crystal XRD and vibrational spectroscopy, as demonstrated in the example of ice-X [80], may be adequate to resolve the geometry of the hydrogen bond as a function of pressure. Recent developments of single crystal XRD in diamond anvil cells (DACs) enable the refinement of atomic positions in complex crystal structures into the 100 GPa range [102]. This creates a unique opportunity to trace the

geometry of the hydrogen bond by its effect on the shape of atomic groups or polyhedrons forming crystal structure. For example, the structure of α -FeOOH (space group $Pnma$) [70] at ambient conditions consists of highly distorted FeO₆ octahedra (Figure 5.8.2-1) with three short (1.933(3), 1.962(2) Å) and three long (2.107(3) Å) Fe–O bonds. The longer Fe–O bonds designated as Fe–O1 correspond to the covalently bound oxygen of the hydroxyl, while the other oxygen O2 ligands are weakly bound to H of the nearest neighbor hydroxyl. Thus, the octahedral moiety can be described as Fe(O \cdots H)₃(O–H)₃. If under compression the hydrogen bonds symmetrize, namely, all O–H bond lengths become equal, this should lead to a reduction in the distortion of the FeO₆ octahedra easily measurable by single crystal XRD. Thus, a detection of this abrupt reduction of the FeO₆ octahedral asymmetry becomes the primary goal of this study.

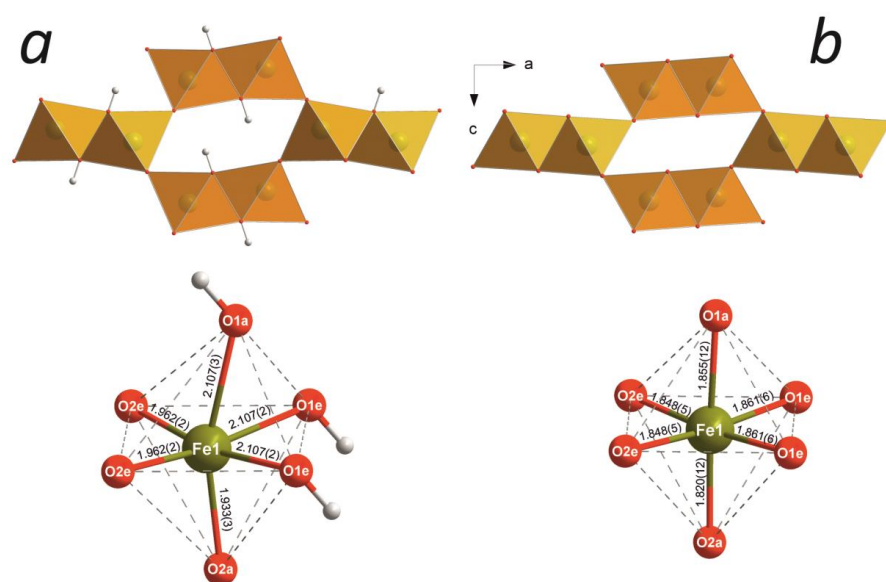


Figure 5.8.2-1 Crystal structure of α -FeOOH along b direction as well as FeO₆H₃ octahedra at ambient pressure (a) and at 47.6(2) GPa (b). α -FeOOH crystallizes in an orthorhombic structure (space group $Pnma$) and can be described in terms of a slightly distorted hexagonally close packed arrangement of O anions with Fe cations occupying two-thirds of the octahedral sites. The FeO₆ octahedra are linked together by sharing edges and vertices to form infinite 2x1 channels parallel to the b axis with H atoms inside the channels. There are two independent oxygen sites: O1, at ambient conditions covalently bound to hydrogen (O–H bond), and O2, characterized by a weak H \cdots O bond; in the selected octahedron one can distinguish O1_a and O2_a atoms in the axial position and two O1_e and two O2_e atoms in the equatorial position. The octahedral Fe(O–H)₃(O \cdots H)₃ moiety is highly distorted at ambient pressure (a): the Fe–O1 bonds are significantly longer than those of Fe–O2, and becomes regular above the transition pressure (b).

High pressure structural studies of goethite up to ~ 29 GPa have been performed by several groups [81,82]. Nagai *et al.* [81] carried out powder XRD studies to 24 GPa and derived a bulk modulus $K_0 = 111(2)$ GPa and its pressure derivative $K' = 4$. Studies to 29 GPa by Gleason *et al.* [82] deduced values of K_0 and K' of 140(4) GPa and 4.6(4), respectively. The behavior of goethite under pressure has been studied theoretically by Otte *et al.* [268] using density-functional theory (DFT) which has predicted a pressure-induced high-spin to low-spin (HS–LS) transition at ~ 8 GPa concurrent with a structural transition to the ϵ -FeOOH polymorph. But taking into account electronic correlation effects at the DFT+U level, the spin crossover in the ϵ phase has been shown to take place at ~ 56 GPa. At the same time, a possibility of the HS–LS transition in the α -phase has not been discussed in this work. Based on the spin-polarized *ab initio* calculations within the DFT+U method Tunega [83] concluded that antiferromagnetic high-spin (HS) state should be stable up to 80 GPa. Because of this, the structural parameters were investigated for the α -FeOOH polymorph in the HS state only. On the other hand conventional spin-polarized calculations using the generalized-gradient approximation (GGA) suggest a HS–LS transition at ~ 55 GPa, and, moreover, DFT+U total energies indicated a possibility of the LS state stabilization at high pressure. In view of the controversies in the structural/electronic properties of the above mentioned studies, diverse experimental structural and electronic methods have been employed in the present work: single crystal and powder XRD, Mössbauer effect at variable (P, T), Raman spectroscopy, and resistance $R(P, T)$ studies. The experiment has been supported by state-of-the-art theoretical calculations. This methodology combination ultimately sheds new light on exciting pressure-induced structural and electronic properties in this transition-metal oxyhydroxide.

Upon compression to 44 GPa, the lattice parameters and unit cell volume of FeOOH gradually decrease (Figure 5.8.2-2, Figure S 5.8.3-1). A close examination of the dependence of the normalized stress versus Eulerian strain, $P_N(f_E)$ (Figure S 5.8.3-5), and $V(P)$ shows that at $P > 16$ GPa the elastic properties change. The best fitting for $V(P)$ could be obtained assuming two different equations of state (EOS) for the 0–16 and the 16–44 GPa pressure ranges (Figure 5.8.2-2). These changes at ~ 16 GPa are even more obvious from the analysis of interatomic distances. Up to 16 GPa the O1...O2 distances, involved in the hydrogen bond and located across channels formed by octahedra (Figure 5.8.2-1), decrease much more rapidly than

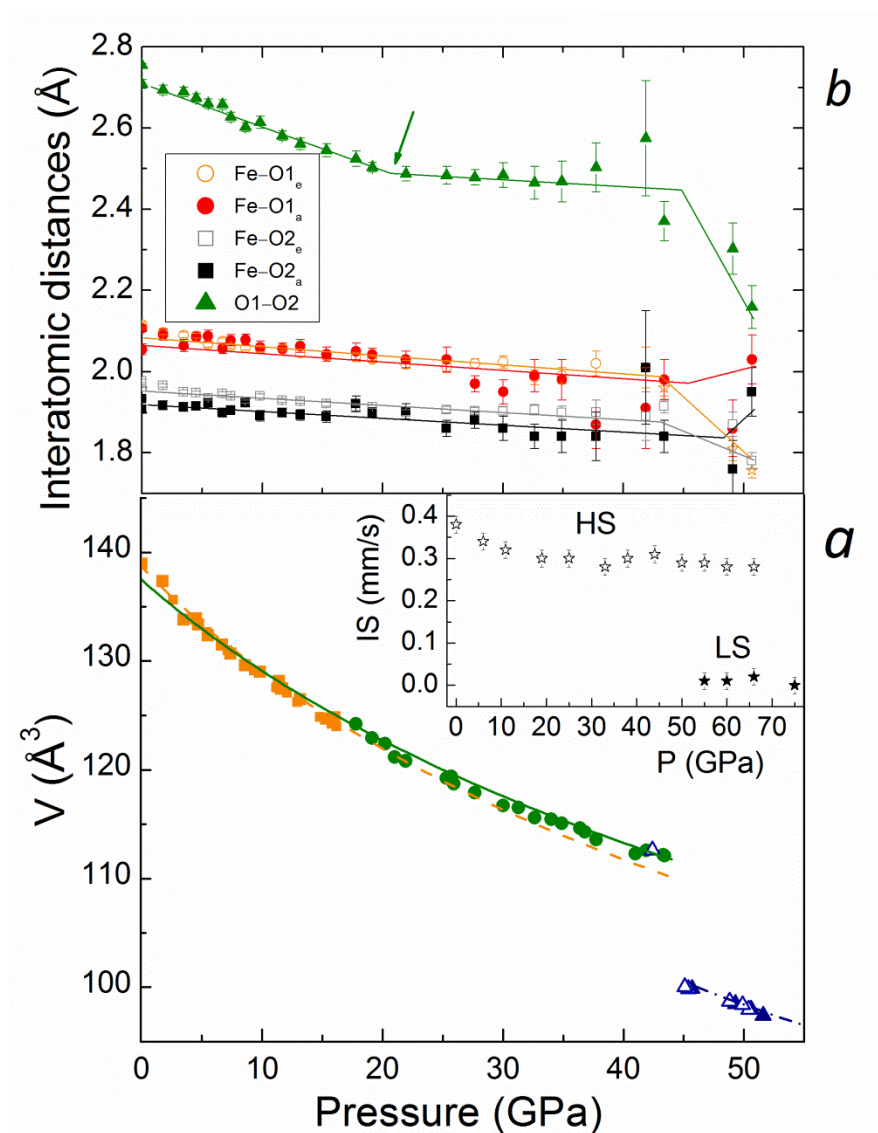


Figure 5.8.2-2 Dependence on pressure of unit cell volume (a) and interatomic distances (b) as revealed by *in situ* X-ray diffraction. The data (a) are divided into three intervals (below 16 GPa – orange square symbols, between 16 and 44 GPa – green circles, and above 44 GPa – solid triangles upon compression and open upon decompression), and fitted by 2nd order Birch-Murnaghan equations of state (curves, dashed orange with parameters $K_0 = 120(3)$ GPa, $V_0 = 138.4(3)$ \AA^3 /unit cell, solid green with parameters $K_0 = 140(5)$ GPa, $V_0 = 137.2(6)$ (2) \AA^3 /unit cell, and dash-dot blue $K_{44} = 224(13)$ GPa, $V_{44} = 100.5(1)$ \AA^3 /unit cell; $K' = 4$). The solid curves (b) serve only as guides to the eyes. The arrow marks a change in pressure dependency of the O1–O2 distances at ~20 GPa. The O–O and Fe–O distances drastically change above 45 GPa. The inset (a) shows the pressure dependence of the isomer shift obtained from Mössbauer spectroscopy. Above 50 GPa an onset of the low spin state is observed characterized by an abrupt drop in the IS value, signaling the sharp decrease of the average $\langle \text{Fe–O} \rangle$ distances.

the Fe–O distances (Figure 5.8.2-2, Figure S 5.8.3-1). This indicates that up to 16 GPa, similar to isostructural α -AlOOH [140], bulk compression takes place through contraction of the channels, involving shortening of the hydrogen bonds, rather than slimming down of the FeO_6 octahedra [82]. At ~ 16 GPa the compressibility of the $\text{O1-H}\cdots\text{O2}$ bond decreases sharply and becomes comparable to the compressibility of the Fe–O bonds (Figure 5.8.2-2). It is noteworthy, that up to 44 GPa the difference in compressibility of Fe–O1 and Fe–O2 bonds (~ 0.0035 Å/GPa for Fe–O1 and ~ 0.0017 Å/GPa for Fe–O2) affects the shape of the octahedral $\text{Fe}(\text{O}\cdots\text{H})_3(\text{O-H})_3$ moiety. The octahedral distortion can be characterized by the deviation Δ of the $\text{O1}_a\text{--Fe--O2}_a$ angle from 180° and by the ratio of the average iron-oxygen distances $\langle\text{Fe--O2}\rangle/\langle\text{Fe--O1}\rangle$. Figure 5.8.2-3 shows that under compression FeO_6 octahedra demonstrate a clear trend to symmetrization, which is nevertheless far from complete at ~ 44 GPa.

At ~ 45 GPa an isostructural phase transition takes place manifested by a drastic reduction of the molar volume (by $\sim 11\%$), and vanishing of the Raman modes (Figure 5.8.2-2, Figure S 5.8.3-1, Figure S 5.8.3-2). Within the experimental errors the transition is reversible upon decompression with no obvious signs of hysteresis (Figure 5.8.2-2). The discontinuous volume drop with no change in symmetry group is usually characteristic of an electronic transition. To further elucidate the origin of the volume contraction ^{57}Fe Mössbauer spectroscopy studies were carried out in the 0–75 GPa range and in the 6–300 K temperature range.

The Mössbauer spectrum (MS) at ambient pressure can be well fitted with a single sextet component, with a hyperfine field (H_{hf}) of 50.2 T, typical of a six-coordinated $\text{Fe}^{3+}\text{--O}$ species in the high-spin configuration ($S = 5/2$) [269]. Up to ~ 50 GPa the antiferromagnetic low-temperature spectra barely change. The isomer shift (IS), which is negatively proportional to the s -density (ρ_s) at the Fe nucleus, decreases monotonically with pressure increase (Figure 5.8.2-2, inset). Above 50 GPa a new magnetic component appears (Figure 5.8.2-4) and eventually becomes dominant at higher pressure. This component is characterized by smaller values of IS, H_{hf} (7.2 T), Neel temperature (T_N) and larger quadrupole splitting (QS), all typical of a Fe^{3+} low-spin state ($S = 1/2$, $^2T_{2g}$). At 75 GPa the only remaining component is this high pressure component (Figure 5.8.2-4).

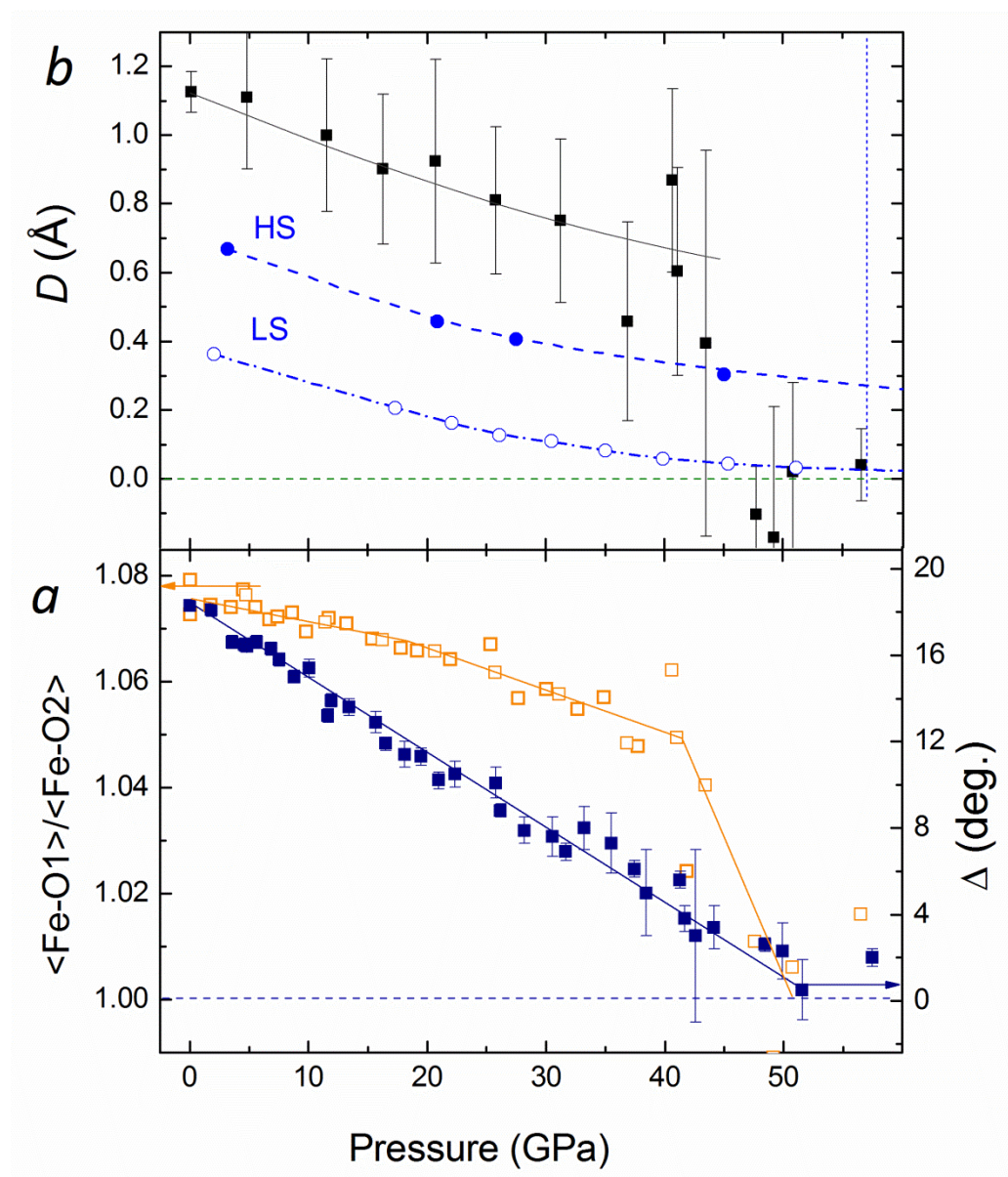


Figure 5.8.2-3 Distortion of FeO6 octahedra (a) and asymmetry of hydrogen bond (b) in FeOOH as a function of pressure. In goethite, distortion of the octahedra (a) can be characterized by the deviation Δ from 180° of the O1a-Fe-O2a angle (open squares) or by the ratio of average iron-oxygen distances $\langle \text{Fe-O2} \rangle / \langle \text{Fe-O1} \rangle$ (solid squares) (see Figure 5.8.2-1 for atoms assignment). The asymmetry of the hydrogen bond D (b) is characterized by the difference in length between O1-H and O2...H. The individual O1-H and O2...H bonds lengths calculated either (black squares) based on experimentally determined atomic positions of iron and oxygen atoms and the valence bond rule (see Supplementary information) or *ab initio* calculation for models with iron in high spin (solid circles) and low spin (open circles) states. The curves serve as guides to the eyes. Note that according to *ab initio* calculations in the HS state the symmetrization of the H-bonds should be observed only at pressures above 100 GPa, but in the LS state it happens at ~ 50 GPa.

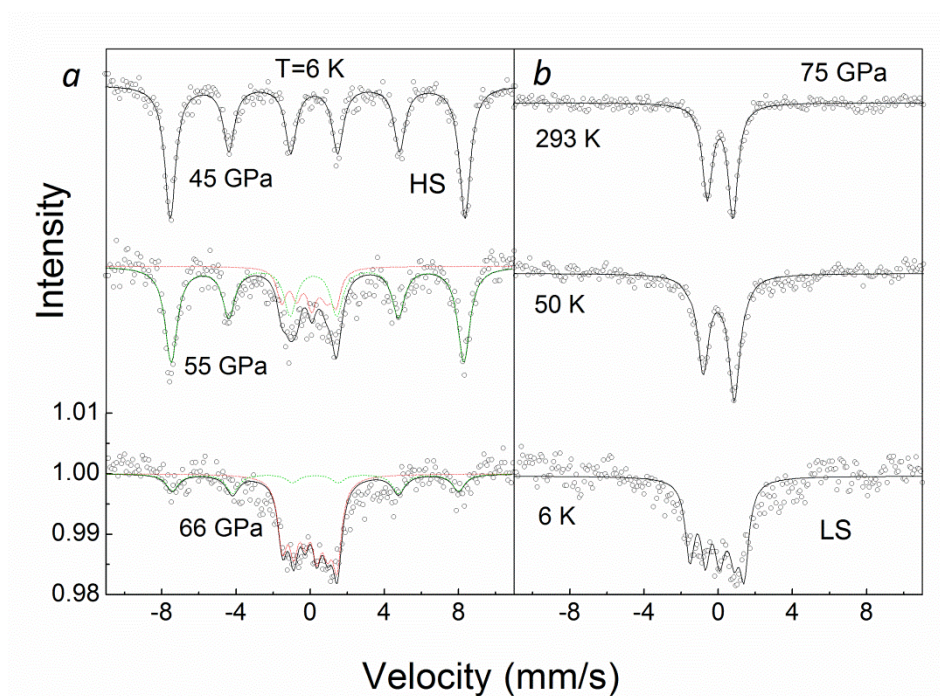


Figure 5.8.2-4 Mössbauer spectra of FeOOH as function of pressure at 6 K (a) and at different temperatures at 75 GPa (b). At 45 GPa the spectrum (a) can still be well fitted with a single sextet. At 55 GPa appears a new component (red dotted line), which is characterized by the significantly reduced H_{hf} of ~ 7.2 T. This component becomes the only remaining component at 75 GPa. The quadrupole splitting (QS) value barely changes upon cooling at 75 GPa (b) and remains ~ 2.5 mm/s. At 50 K a slight broadening of the doublet takes place, followed by the onset of a magnetic splitting clearly observed at 6 K. This means a considerable drop of Neel temperature (T_N) as compared to T_N above 300 K of the low-pressure phase. Thus, the high pressure phase is characterized by the significantly reduced isomer shift and hyperfine field, lower T_N , and enlarged QS values as compared to the low pressure phase: all these changes are features of the low-spin state of Fe^{3+} .

Additional evidence of the strong electronic transformation taking place around 45 GPa is the sharp decrease of the $R(P, 300 \text{ K})$ by 5-orders of magnitude (Figure S 5.8.3-3). From the T -dependence (see inset) no metallization takes place up to the highest P . Thus we can conclude that around 45 GPa a corroborating electronic and isostructural transformation takes place; namely, a HS–LS transition leading to a significant reduction of the Fe^{3+} ionic radius and the corresponding large drop in volume.

While the quality of the single crystal deteriorates upon the transition, we found the X-ray data still sufficient for accurate determination of the positions of iron and oxygen atoms in the high

pressure phase (Table S 5.8.3-1). This phase is characterized by significantly shorter O1...O2 distances, the same as measured in ice-X at 145 GPa where symmetrization of the hydrogen bond has been observed [80] (Figure 5.8.2-2). Furthermore, the distortion of $\text{Fe}(\text{O}\cdots\text{H})_3(\text{O}-\text{H})_3$ moiety is strikingly reduced (Figure 5.8.2-1, Figure 5.8.2-3) with the $\text{O1}_a-\text{Fe}-\text{O2}_a$ angle approaching 180° and nearly equal $\langle\text{Fe}-\text{O2}\rangle$ and $\langle\text{Fe}-\text{O1}\rangle$ bond lengths. The exact position of the hydrogen atom cannot be directly determined from XRD data, but the interatomic distance of the hydroxyl and the $\text{O}\cdots\text{H}$ species can be derived using the *valence bond* rule and the experimentally measured atomic positions of iron and oxygen atoms (for details see Supplementary information and references therein). As can be seen at $P \geq 50$ GPa (Figure 5.8.2-3a) the difference D between the interatomic distances of $(\text{O1}-\text{H})$ and $(\text{H}\cdots\text{O2})$ vanishes. Thus, we conclude, that the single crystal XRD data provide strong evidence for a symmetric hydrogen bond in the high-pressure FeOOH phase. This H-bonds symmetrization is induced by the spin crossover, which converts the largely asymmetric polyhedra of $\text{Fe}_{\text{HS}}^{3+}(\text{O}-\text{H})_3(\text{O}\cdots\text{H})_3$ into an axially symmetric $\text{Fe}_{\text{LS}}^{3+}(\text{O}-\text{H})_6$ orthorhombic octahedra, accompanied by a $\sim 11\%$ volume collapse.

It is worth mentioning that solely a reduction of the Fe^{3+} ionic radius, due to the transition to the LS state, is not sufficient to fully explain the obtained result. In diasporite ($\alpha\text{-AlOOH}$), an isostructural oxyhydroxide with much smaller molar volume than $\alpha\text{-FeOOH}$ and smaller Al^{3+} ionic radius even compared with the low-spin Fe^{3+} , no hydrogen bond symmetrization has been observed to 50 GPa and it has been theoretically predicted to take place only at ~ 110 GPa [83,140,269]. Importantly, the observed drastic volume change in $\alpha\text{-FeOOH}$ at the spin transition is a consequence not only of the $\text{Fe}^{3+}-\text{O}$ bond length reduction, but also of the change of the O1...O2 distances which are reduced by $\sim 10\%$. The latter reflects, obviously, a drastic redistribution of the electron density in the $\text{Fe}(\text{O}\cdots\text{H})_3(\text{O}-\text{H})_3$ moiety following the spin transition.

To further substantiate our findings we employed *ab initio* calculations in order to investigate the stability and structural properties of HS and LS Fe^{3+} states in $\alpha\text{-FeOOH}$ with (Figure S 5.8.3-4). The anti-ferromagnetic (*afm*) HS state with a local magnetic moment $\mu(\text{Fe}^{3+}) = 4.2 \mu_B$

was found to have the lowest total energy, namely, the most stable configuration in the 0–57 GPa range (Figure S 5.8.3-4). Above 57 GPa (insert Figure S 5.8.3-4) the stable configuration becomes the LS phase with $\mu = 1.1 \mu_B$, in excellent agreement with the present experimental results. The theoretical analysis even implies (Figure 5.8.2-3b) that the spin crossover results in nearly symmetric hydrogen bonds. Thus the two phenomena – electronic transition in Fe^{3+} and modification of the hydrogen bond, resulting in the dissociation of the hydroxyl, are closely interlinked.

Our experimental studies combined with the *ab initio* calculations suggest that hydrogen bond symmetrization may occur in other inorganic oxy-hydroxide transition metal (TM) species at relatively low pressures in cases of pressure-induced electronic processes, such as spin crossover or pressure-induced oxidation of the TM ion which eventually leads to substantial volume reduction and change of electronic state. Such an effect may be common for crystalline materials and minerals containing water and transition metals, particularly for components of Earth and planetary mantles. Indeed, water is expected to be carried into Earth's interiors by ferric iron bearing oxides and silicates [270] and, induced by spin transition in iron, at conditions of the middle lower mantle, changes in hydrogen bonding may significantly affect water balance and dynamics.

5.8.3. Supporting Materials

Supplementary table

Table S 5.8.3-1 Interatomic distances evolution with pressure increase, based on synchrotron single crystal XRD data. Hydrogen positions have been calculated by bond valence analysis except at ambient pressure, where it was determined from a residual electron density map.

P, GPa	Interatomic distances, Å					
	Fe–O1 _e	Fe–O1 _a	Fe–O2 _e	Fe–O2 _a	O1...O2	H1...O2
0.0001	2.107(2)	2.107(3)	1.962(2)	1.933(3)	2.755(4)	1.954(6)
4.7(1)	2.085(5)	2.083(11)	1.946(4)	1.917(10)	2.661(10)	1.89(11)
11.4(1)	2.070(7)	2.051(15)	1.929(5)	1.921(13)	2.563(13)	1.78(11)
16.2(1)	2.065(8)	2.001(16)	1.933(5)	1.875(14)	2.565(14)	1.73(11)
20.6(2)	2.03(1)	2.05(2)	1.908(7)	1.917(19)	2.465(17)	1.69(15)
25.7(2)	2.029(8)	1.991(17)	1.915(5)	1.867(14)	2.486(15)	1.65(11)
31.1(2)	2.003(9)	1.989(19)	1.899(6)	1.870(16)	2.429(17)	1.59(12)
36.8(2)	2.004(11)	1.92(2)	1.922(8)	1.81(2)	2.50(3)	1.48(14)
40.6(2)	1.998(8)	1.964(16)	1.891(7)	1.829(16)	2.428(17)	1.65(13)
41.0(2)	1.969(13)	2.00(3)2	1.898(9)	1.86(2)	2.36(3)	1.48(15)
43.4(2)	1.96(2)	1.98(5)	1.915(17)	1.84(4)	2.37(5)	1.4(3)
47.6(2)	1.861(5)	1.855(12)	1.848(5)	1.82(12)	2.334(11)	1.12(7)
49.1(2)	1.81(3)	1.84(7)	1.88(3)	1.76(7)	2.30(7)	1.07(19)
50.7(2)	1.757(19)	2.03(6)	1.78(2)	1.95(6)	2.16(6)	1.09(13)
56.5(2)	1.845(9)	1.862(19)	1.835(7)	1.74(17)	2.322(17)	1.18(5)

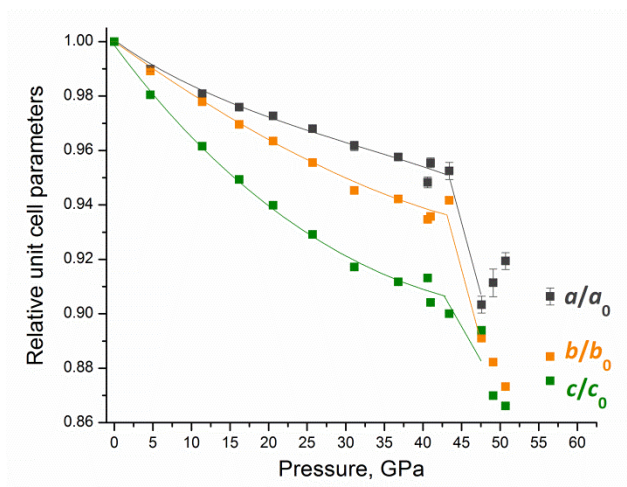
Supplementary figures

Figure S 5.8.3-1 Variations of lattice parameters as a function of pressure based on single-crystal synchrotron XRD data.

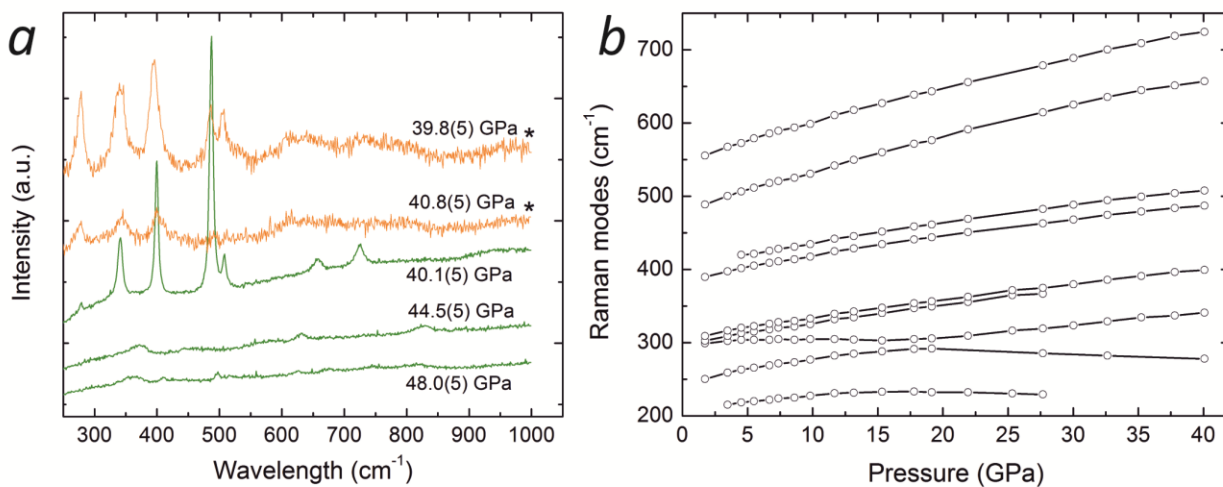


Figure S 5.8.3-2 Examples of Raman spectra (a) and the positions of Raman bands (b) of FeOOH as a function of pressure. Raman spectra demonstrate a drastic decrease in intensity of the Raman modes in the transition region, $P > 44$ GPa. Graphs marked by an asterisk denote spectra obtained upon decompression (a). Note the change of the behaviour of the Raman modes at the range 200–300 cm^{-1} between 15 and 20 GPa, at the same pressures at which changes in compressibility was revealed.

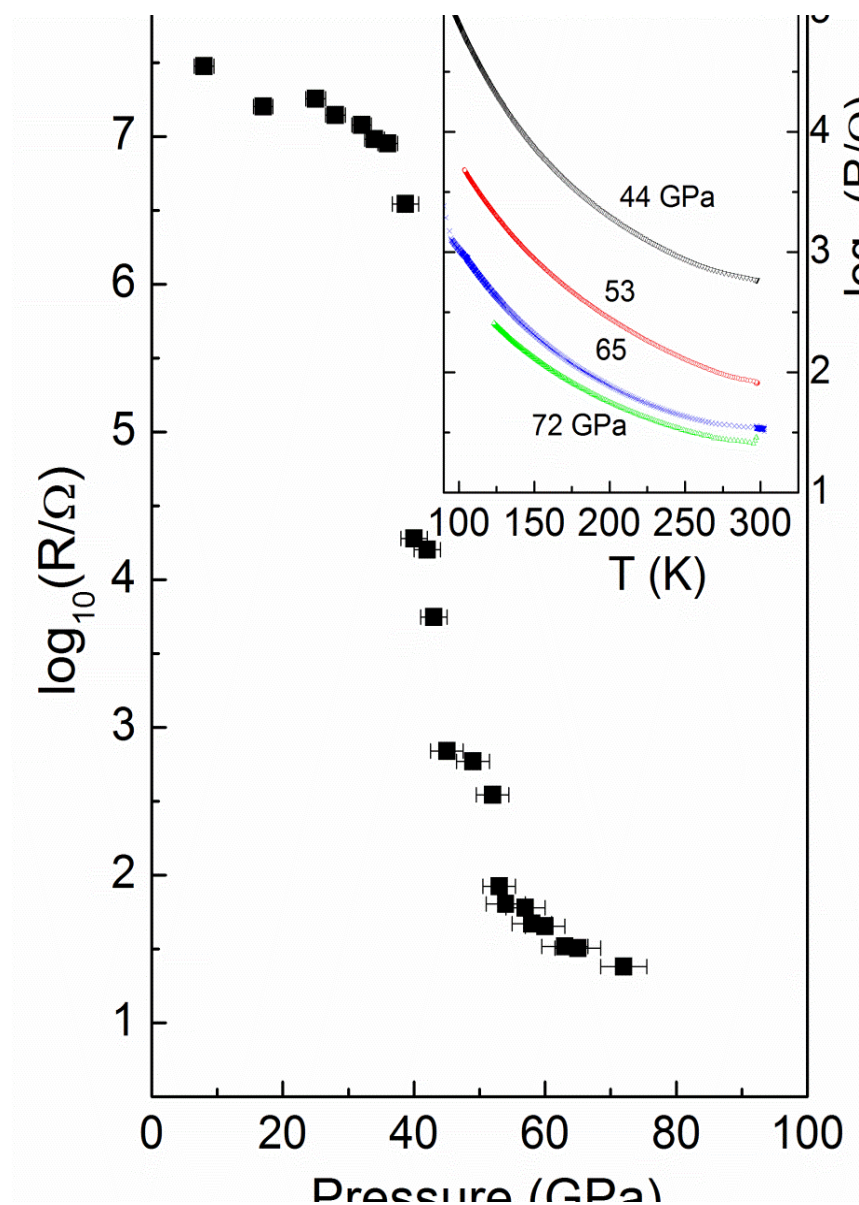


Figure S 5.8.3-3 The variation of the resistance of FeOOH with pressure at room temperature. The inset shows the temperature dependence of the resistance at selected pressures. A sharp decrease in the resistance of five orders of magnitude is observed between 40 and 50 GPa. However, the sign of the resistance derivative dR/dT still shows a gapped state with the gap value decreasing from 51 to 32 meV at the 44–72 GPa range.

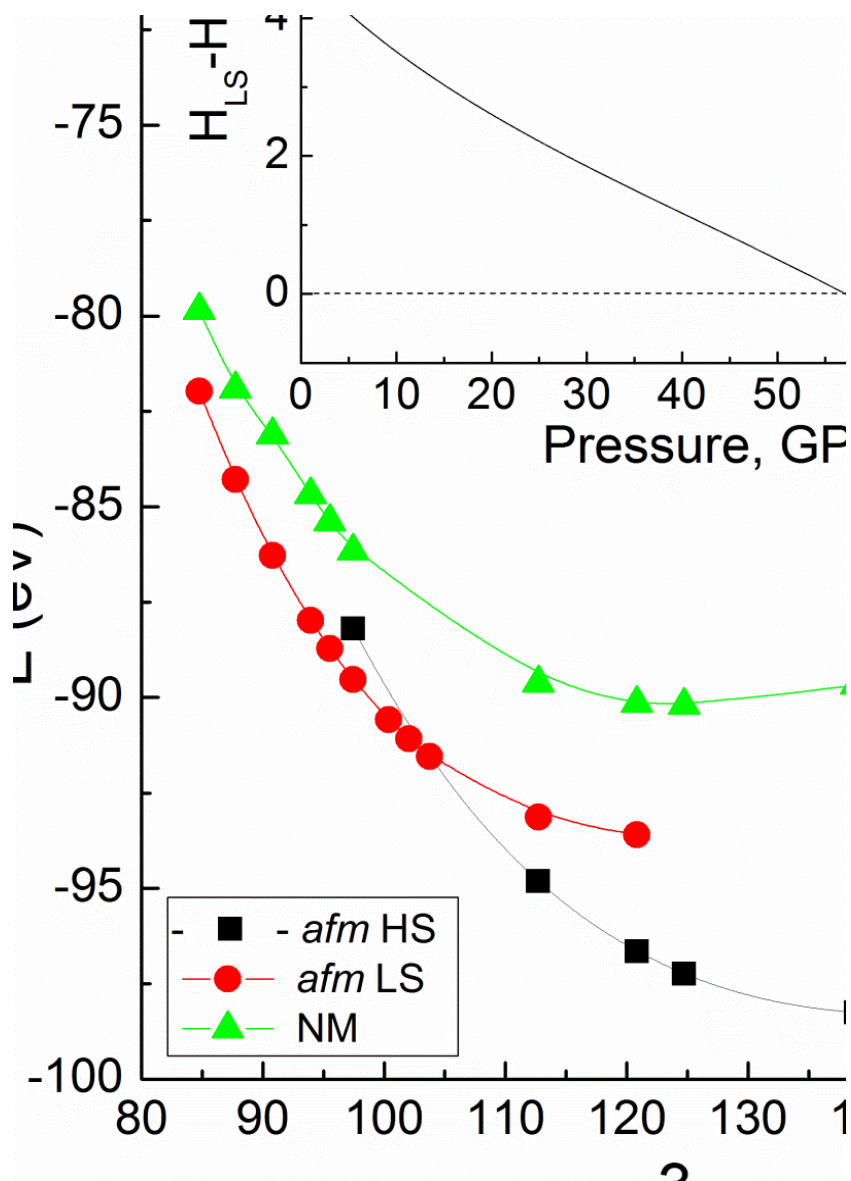


Figure S 5.8.3-4 Dependence of the total energy as function of unit cell volume of orthorhombic FeOOH. The *afm* HS solution (black symbols) with local magnetic moment $4.2\mu_B$ on iron was found to have the lowest total energy and therefore it is the most stable from 0 to ~ 57 GPa. At ~ 57 GPa (see insert) it transforms to the *afm* LS phase (red symbols) with iron having the local magnetic moment of $1.1\mu_B$. The non-magnetic (*nm*) configuration of FeOOH (green symbols). is higher in energy than the *afm* phases in the whole range of considered volumes. The ferromagnetic solution was also considered in the calculations, but was found to be higher in energy than the *afm* one. The energy and the volume are given per unit cell. Our results agree well with calculations reported in Ref. [268]. But the inset showing the difference between enthalpies of the anti-ferromagnetic (*afm*) LS and HS states as a function of pressure, clearly demonstrate that the isostructural phase transition might take place, in agreement with experiment.

Supplementary methods

Two samples were used throughout the experiments. The single crystal experiments were performed with a natural sample of goethite provided by W. Schmaal (LMU, München, Germany). Synchrotron powder XRD, Mössbauer spectroscopy and electrical transport experiments were performed with the polycrystalline sample enriched by ^{57}Fe synthesized at LANL, USA. The polycrystalline FeOOH was prepared from the precipitate of $\text{Fe}^{57}(\text{NO}_3)_3 \cdot 9\text{H}_2\text{O}$ and KOH solutions. Pressure was generated using cells with diamond anvils with culet sizes of 250–300 μm , and rhenium gaskets. In a combination with Boehler-Almax diamond anvils they provide a high opening angle of 80° (4θ) necessary for single-crystals XRD studies. Mössbauer spectroscopy measurements were performed using liquid N_2 pressure transmitting media, whereas XRD spectra were collected using He or Ne loaded at pressures of ~ 1.3 kbar. Pressure was measured using the ruby R_1 -line fluorescence spectroscopy [113] and an Au pressure marker for the powder XRD measurements.

Mössbauer spectra (MS) were recorded up to 75 GPa in the 5–300 K temperature range and MS parameters were extracted using least-squares methods similar to Ref. [271].

Four-probe DC electrical resistance measurements as a function of pressure and temperature were carried out using a methodology similar to Ref [271].

Powder XRD measurements were carried out at room temperature in angle-dispersive mode with a wavelength of 0.3344 Å at the 13-IDD beamline at APS, Argonne. Diffraction images were collected using a MAR CCD detector. The image data were integrated using the FIT2D program (<http://www.esrf.eu/computing/scientific/FIT2D/>) and the resulting diffraction patterns were analyzed with the GSAS (<https://subversion.xray.aps.anl.gov/trac/EXPGUI/wiki>) program.

Single crystal XRD measurements were carried out both with ‘in-house’ and synchrotron facilities at ambient temperature. In-house experiments were performed using a four-circle Oxford Diffraction Xcalibur diffractometer ($\lambda = 0.7107$ Å) equipped with an Xcalibur Sapphire2 CCD detector under control of CrysAlis CCD software. Sample-to-detector distance, detector tilts, and the beam center position were calibrated using an YLID standard. For each pressure

point a series of narrow (0.5°) omega scans with certain positions of the detector ($2\theta = \pm 20, \pm 40^\circ$) were collected. In addition we collected such series of omega scans for the cell rotated along imaginary chi-axis on $30, 60$ and 90° ; altogether 884 frames for each pressure point with an exposure time of ~ 40 s. In order to stabilize the pressure after each compression steps the DAC was kept for ~ 24 hours before data collection. The mean pressure change during data collection was ~ 0.2 GPa.

Single crystal synchrotron X-ray diffraction experiments have been performed at the ID09A beam line at ESRF ($\lambda = 0.41491 \text{ \AA}$) following the procedure described previously [102]. The structures were solved by the direct method and refined by full matrix least-squares using SHELXTL software (<http://shelx.uni-ac.gwdg.de/SHELX/register.php>). The total number of refined parameters varied from 10 to 13 and includes atomic coordinates of Fe, O1 and O2, thermal isotropic displacement parameters for O1 and O2, anisotropic displacement parameters for Fe, scale factor and weight scheme. Below 40 GPa the discrepancy index R_1 values were in the range of 2–11 % for in-house datasets, and of 2–5 % for data obtained at ESRF. Above 40 GPa the R_1 values increased up to 25 % and 11 %, respectively. Despite degradation in the quality of the crystal above 40 GPa, the atomic positions could still be refined.

Raman spectra were collected in several runs parallel to collecting X-ray powder and single-crystal data covering the pressure range up to 50 GPa. Spectra were acquired using a LabRam (Horiba Scientific Inc.) system with a 632.8 nm Ne-He laser excitation line. The spectra were collected in two ranges, 200–1000 and 2800–3800 cm^{-1} .

Ab initio spin-polarized calculations were carried out in the framework of the DFT [272] with GGA for the exchange-correlation potential and energy. The effect of strong correlations was included via the GGA+ U approach [273–276]. The choice of the GGA+ U parameters $U = 5$ eV and $J = 1$ eV for the d -orbitals of Fe was made in accordance with [268]. Simulations were done using the Projector Augmented Wave (PAW) method [277,278] as implemented in the VASP code [279–282]. The calculations were performed with the 16 atom unit cell with the $8 \times 8 \times 8$ k -point grid for the integration over the Brillouin zone. The plane-wave energy cut-off was set

to 550 eV. The α -phase of FeOOH was constructed based on the experimental data including hydrogen positions determined at low pressures. The shape of the unit cell and all the atomic positions were fully relaxed. Calculations were done at 0 K for pressures up to ~ 120 GPa. The anti-ferromagnetic, ferromagnetic and non-magnetic structures were studied. Two initial magnetic states, with the spin magnetic moment $\sim 4\mu_B$ (HS solution) and $\sim 1\mu_B$ (LS solution), were considered.

Supplementary discussion

Change of the elastic properties around 16 GPa. The $V(P)$ data up to 44 GPa could be fitted with a 3rd-order Birch-Murnaghan equation of state [283] with the following parameters: $K_0 = 112(8)$ GPa and $V_0 = 138.7(5)$ Å³ where K_0 and V_0 are the bulk modulus and the unit cell volume at ambient conditions, respectively. The obtained pressure derivative value is rather high: $K'_0 = 5.4(5)$. An additional measure of the consistency of the data provided by the normalized pressure P_N versus Eulerian strain f_E plot shows a significant increase from ~ 100 to 135 GPa when f_E increases to 0.08. Meanwhile, splitting into two ranges, 0–16 GPa and 16–44 GPa, improves the quality of the EOS fit resulting in bulk modulus $K_0 = 120(3)$ GPa and $V_0 = 138.4(3)$ Å³, and $K_{16} = 197(5)$ GPa and $V_{16} = 124.8(2)$ Å³ [284] (Figure 5.8.2-2), respectively, $K'_0 = 4$ is fixed. In that case, in contrast to the fit for the entire pressure range 0–44 GPa, P_N does not show an appreciable change as a function of the Eulerian strain (Figure S 5.8.3-5).

A similar change of the elastic properties was previously detected at pressures up to 15 GPa in δ -AlOOH(D) [73], CrOOH(D), GaOOH, InOOH [285] and was explained by the symmetrization of the hydrogen bonds. However, we did not find any indications of the symmetrization of the hydrogen bonds in FeOOH around 16 GPa. Thus, the obtained O1...O2 distances (d_{OO}) are still ~ 2.5 Å (Figure 5.8.2-2, Table S 5.8.3-1), a value typical for ice VII with so called high barrier H bonds with the bimodal proton distribution. This value is much larger compared to $d_{OO} \sim 2.3$ Å typical for low barrier H bonds in which the potential remains double wellled but the proton distribution is unimodal due to zero-point motion [67,68]. But only at even shorter separations, within the stability range of ice X, the potential becomes single wellled, which means a complete symmetrization of the hydrogen bond. Similar to the present results, neutron

diffraction studies of δ -AlOOH(D) [72] revealed a large value of $d_{00} \sim 2.45$ Å at the range of the compressibility change. It is noteworthy, that at ~ 16 GPa the observed significant distortion of FeO_6 octahedra and significant difference in the O1–H and H \cdots O2 distances (Figure 5.8.2-3) also disprove the suggestion of symmetrization of the hydrogen bonds.

Experimental $\text{IR}(P)$ studies of Williams et al. [286] attribute this change in the elastic properties to the linearization of O1–H \cdots O2 bond taking place at ~ 15 GPa: namely, the linearization could be inferred from the convergence of the soft bending modes above 13 GPa. A similar trend to the linearization of O1–H \cdots O2 bond was observed also in neutron diffraction studies of δ -AlOOH [72]. Thus, we suggest that changes in the elastic properties of α -FeOOH at ~ 16 GPa, as well as similar effect(s) reported in δ -AlOOH [73], CrOOH(D), GaOOH, InOOH [285], are associated with changes in the geometry and properties of hydrogen bonds but not related to their symmetrization.

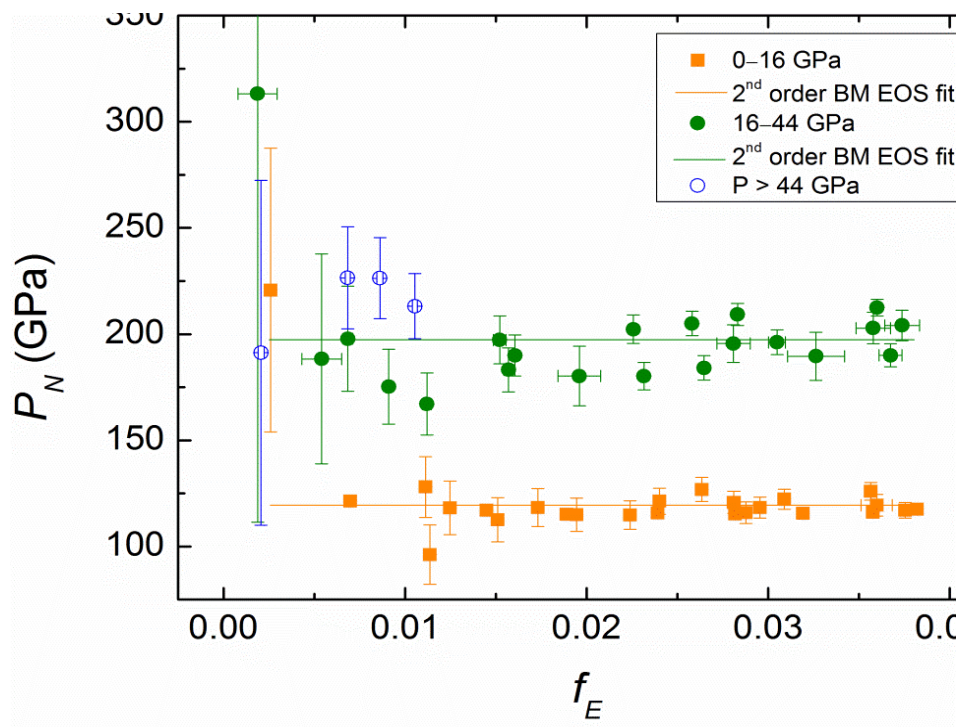


Figure S 5.8.3-5 Normalized pressure P_N as a function of Eulerian strain f_E calculated for the discussed regions. Straight lines: solid orange (below 16 GPa), and dash green (16–44 GPa) show the dependences fitting with assumption that $K_0' = 4$.

Estimation of hydrogen positions using bond-valence analysis. While localization of hydrogen atoms from X-ray diffraction data collected at high pressure in DACs is problematic, the bond valence method [287,288] can provide a good description of the geometry of hydrogen bonding if the positions of all non-hydrogen atoms are known. According to Pauling's 2nd law a sum of bond valences reaching on an ion should yield the absolute value of its charge. A bond valence S_{ij} for a bond between the i^{th} and j^{th} atoms could be expressed with the following formula [287,288]:

$$S_{ij} = \exp\left(\frac{R_0 - R_{ij}}{B}\right),$$

where R_{ij} is the interatomic distance between the i^{th} and j^{th} atoms, R_0 , B – empirical values refined using observed crystal structures to satisfy valence sums around central atoms. Bond-valence parameters R_0 and B are dependent on atoms which form a bond and their values are tabulated for ambient conditions [288]. While interatomic distances R_{ij} are established from refined structural data for each pressure point, the valence parameters change under compression; therefore one should refine them as a function of pressure. The following expression has been used to calculate R_0 for Fe^{3+} cations (value of B^{Fe} was fixed to a typical one of 0.37 Å as recommended in Ref. [287]):

$$R_0^{\text{Fe}} = B^{\text{Fe}} \cdot \ln \left(\frac{3}{2 \exp\left(-\frac{R_{\text{Fe-O1e}}}{B^{\text{Fe}}}\right) + \exp\left(-\frac{R_{\text{Fe-O1a}}}{B^{\text{Fe}}}\right) + 2 \exp\left(-\frac{R_{\text{Fe-O2e}}}{B^{\text{Fe}}}\right) + \exp\left(-\frac{R_{\text{Fe-O2a}}}{B^{\text{Fe}}}\right)} \right).$$

Note that $R_0^{\text{Fe}}(P)$ dependences of goethite practically coincide with those of hematite, $\alpha\text{-Fe}_2\text{O}_3$, containing only Fe–O bonds (structural data are taken from [289]).

According to Ref. [288], the weak H...O2 bond is responsible for forming the H-bond and determination of H position should be done using its valence (S_h). S_h is equal to a charge deficiency for oxygen atom O2 given by the difference between O2 charge and its valence sum without the contribution of hydrogen:

$$S_h = 2 - 2 \exp\left(\frac{R_0^{Fe} - R_{Fe-O2e}}{B^{Fe}}\right) + \exp\left(\frac{R_0^{Fe} - R_{Fe-O2a}}{B^{Fe}}\right).$$

The H...O2 distances were estimated using the experimental dependence between H–O bond valence and bond-length calculated from accurately determined H-bonds [288]. The O1–H distances were determined as the difference between O1...O2 and H...O2 distances, since their numerical estimation is difficult due to insensitivity of the bond to its valence and resulting in large uncertainties.

5.9. Novel high pressure monoclinic Fe₂O₃ polymorph revealed by single-crystal synchrotron X-ray diffraction studies

E. Bykova^{1,2}, M. Bykov², V. Prakapenka³, Z. Konôpková⁴, H.-P. Liermann⁴, N. Dubrovinskaia², L. Dubrovinsky¹

¹*Bavarian Research Institute of Experimental Geochemistry and Geophysics, University of Bayreuth, Bayreuth, Germany*

²*Laboratory of Crystallography, University of Bayreuth, Bayreuth, Germany*

³*Center for Advanced Radiation Sources, University of Chicago, IL 60437, USA*

⁴*Photon Science, DESY, Hamburg, Germany*

High Press. Res. **33**, 534–545 (2013).

5.9.1. Abstract

A novel high-pressure polymorph of iron sesquioxide, *m*-Fe₂O₃, has been identified by means of single crystal synchrotron X-ray diffraction. Upon compression of a single crystal of hematite, α -Fe₂O₃, in a diamond anvil cell, the transition occurs at pressure of about 54 GPa and results in ~10 % volume reduction. The crystal structure of the new phase was solved by the direct method (monoclinic space group $P2_1/n$, $a = 4.588(3)$, $b = 4.945(2)$, $c = 6.679(7)$ Å and $\beta = 91.31(9)^\circ$) and refined to $R_1 \sim 11\%$. It belongs to the cryolite double-perovskite structure type and consists of corner-linked FeO₆ octahedra and FeO₆ trigonal prisms filling the free space between the octahedra. Upon compression up to ~71 GPa at ambient temperature no further phase transition were observed. Laser heating to $\sim 2100 \pm 100$ K promotes a transition to *Cmcm* CaIrO₃-type (post-perovskite, PPv) phase. The PPv-Fe₂O₃ crystal structure was refined by means of single crystal X-ray diffraction at ~65 GPa. On decompression the PPv-Fe₂O₃ phase fully transforms back to hematite at pressures between ~25 and 15 GPa.

5.9.2. Introduction

High pressure behavior of iron sesquioxide, Fe₂O₃, has been a long-standing subject of research due to its importance for mineral physics as a proxy for modeling materials behavior in deep Earth's interiors. From the solid state physics point of view the compound is interesting since at pressures between 40 and 60 GPa it undergoes a series of transformations manifesting in structural changes (transition to an orthorhombic phase with a large volume discontinuity (~10 %) [94,98]), a drop of the resistivity [95,290], a spin crossover of Fe³⁺ [96], and a disappearance of the ordered magnetic state [95]. The crystal structure of the Fe₂O₃-orthorhombic phase, which might shed light on the physics of the observed pressure-induced phenomena, has remained controversial for a long time. Perovskite [94,291] and Rh₂O₃-II structural types [95,97,98] were proposed based on Mössbauer spectroscopy and powder X-ray diffraction (XRD) data. Recent single crystal XRD studies demonstrated that compression of hematite to 40 GPa and laser heating to 2300 K results in formation of the Rh₂O₃-II-type phase with a rather small volume change (~1.3 %) [102]. The crystal structure of the phase(s) observed on compression above 50 GPa at ambient temperature [95,97,98] is still under question since only powder XRD data were available so far and Mössbauer and Raman spectroscopy studies cannot provide definitive structural information.

A reconstructive phase transition was reported to occur during laser heating of Fe₂O₃ compressed above 70 GPa [88,99,100]. Powder X-ray diffraction pattern was indexed in the CaIrO₃ structure type; however crystallographic data provided was based only on a Rietveld refinement of the powder pattern. The CaIrO₃ structural type has been assigned to the high pressure modification of (Mg,Al)(Si,Fe)O₃ perovskite, known as post-perovskite; the transition perovskite – post-perovskite is thought to be responsible for many anomalies of the D" layer, the lowest part of the Earth's mantle [292].

An ambiguity in the crystal structure of Fe₂O₃ in the 40–60 GPa pressure region and the absence of precise crystallographic data for the post-perovskite Fe₂O₃ phase encouraged us to perform a series of high-pressure and high-temperature XRD experiments on single crystals that provides a more accurate unit cell parameters a structure model and refinement.

Within, we report high pressure behavior of hematite up to 50 GPa based on a single crystals study and compare our results with previously available data. We found a structural transition to a novel monoclinic phase, $m\text{-Fe}_2\text{O}_3$, space group $P2_1/n$, and analyzed its relations with Rh_2O_3 -II and perovskite type structures. Upon laser heating at about 70 GPa the monoclinic phase transforms to post-perovskite ($\text{PPv-Fe}_2\text{O}_3$, space group $Cmcm$). The structure of the latter was preserved upon decompression down to at least ~ 25 GPa.

5.9.3. Experimental

Samples preparation

In this study we used the same hematite single crystals which were described in the work by Schouwink *et al.* [289]. High-quality single crystals with an average size of $0.03 \times 0.03 \times 0.005 \text{ mm}^3$ were pre-selected on a 3-circle Bruker diffractometer equipped with a SMART APEX CCD detector and a high-brilliance Rigaku rotating anode (Rotor Flex FR-D, Mo- $K\alpha$ radiation) with Osmic focusing X-ray optics.

High-pressure experiments

All high-pressure experiments have been performed using the diamond anvil cell (DAC) technique. Pressure was generated by means of 4-screw-driven BX90 type DACs [105] equipped with Boehler-Almax [293] or spherical diamond [294] anvils (250 μm culet sizes). Rhenium gaskets were pre-indented to about 30 μm thickness and drilled with a 120 μm hole and placed between two diamonds to form a pressure chamber. The pressure chamber with the sample and a small ruby chip was loaded with Ne at ~ 1.5 kbar using the gas-loading system installed in Bayerisches Geoinstitut by means of mechanical closing of the DACs [112]. Pressure was determined using the ruby R_1 fluorescence line as a pressure marker and by measuring a position of the (111) X-ray diffraction line of Ne (<http://kantors50webs.com/diffraction.htm>).

Upon compression of hematite up to 54 GPa at ambient temperature X-ray diffraction measurements were carried out in an angle-dispersive mode ($\lambda = 0.3344 \text{ \AA}$, the beam size $4 \times 8 \mu\text{m}^2$) at the 13-IDD beamline at the Advanced Photon Source (APS), the Argonne National Laboratory. X-ray diffraction wide images (from -35 to $+35^\circ$ on omega) were collected with a

MAR CCD detector at three different positions to increase a coverage of the reciprocal space. The sample was compressed from 12 to 40 GPa with a 5 to 7 GPa step and afterwards the pressure steps were decreased to ~2 GPa. For several pressure points a complete data collection was performed by narrow 1° omega-scanning in a range from -35 to +35°.

Another set of experiments has been performed at the Extreme Conditions Beamline (P02.2) at PETRA III, Hamburg, Germany ($\lambda = 0.28978 \text{ \AA}$, beam size $2.3(\text{H}) \times 1.4(\text{V}) \mu\text{m}^2$). Diffraction images were collected using a Perkin Elmer flat panel detector by 1° omega-scanning from -40 to +40°. The first experiment with Fe₂O₃ was used to collect single crystal XRD data from 48 to 71 GPa with a 5 to 7 GPa step. The second one, compressed to 68 GPa, was heated for about 5 min with a NIR laser at $2100 \pm 100 \text{ K}$ and quenched afterwards. Then the sample was decompressed to 15 GPa with 5 to 10 GPa steps. At every step XRD wide images were obtained (from -35 to +35° of omega), and for several pressure points a complete data collection was performed as described above.

The data treatment (integration and absorption corrections) collected at the ECB was performed with the CrysAlis RED [206] software. The collection of intensities from wide-scan images collected at GSECARS the refinement of the unit cell parameters was done using GSE ADA software [295]. The structures were solved by the direct method and refined by full matrix least-squares using the SHELXS and SHELXL software [124], respectively, implemented in the X-Seed program package [194]. The results of the crystal structure refinement for *m*-Fe₂O₃ and PPv-Fe₂O₃ phases at 54.3(2) and 64.6(2) GPa, respectively, and ambient temperature are summarized in Table 5.9.4-1.

5.9.4. Results and discussion

Compression of hematite, α -Fe₂O₃

Figure 5.9.4-1a presents the pressure dependence of the normalized unit cell volume, V/Z , (V is the unit cell volume, Z is the number of formula units per a unit cell) for hematite and high-pressure modifications of Fe₂O₃. The room temperature P – V data for hematite obtained in the present work agree well with those reported by Schouwink *et al* [289], who compressed a single crystal up to 25 GPa (solid line in Figure 5.9.4-1a corresponds to the equation of state from [289]).

Table 5.9.4-1 Crystallographic data for $P2_1/n$ (54.3(2) GPa) and $Cmcm$ (64.6(2) GPa) phases of Fe_2O_3 at room temperature.

	$P2_1/n$	$Cmcm$
a (Å)	4.588(3)	2.665(3)
b (Å)	4.945(2)	8.609(5)
c (Å)	6.679(7)	6.379(6)
β (°)	91.31(9)	90
V (Å ³)	151.5(2)	146.4(2)
Z	4	4
$F(000)$	304	304
Facility	ID-13D GSECARS, APS	P02.2 ECB, Petra III
Wavelength (Å)	0.33440	0.28978
Theta range for data collection (°)	2.51 to 10.81	2.33 to 10.31
Completeness to $d = 0.8$ Å (%)	54.6	79.0
Index ranges	$-4 < h < 4,$ $-5 < k < 5,$ $-5 < l < 6$	$-2 < h < 2,$ $-10 < k < 9,$ $-6 < l < 7$
Reflections collected	218	160
Independent reflections / R_{int}	124 / 0.0553	79 / 0.0638
Refinement method	Full matrix least squares on F^2	
Data / restraints / parameters	124 / 0 / 19	79 / 0 / 9
Goodness of fit on F^2	1.363	1.225
Final R indices [$I > 2\sigma(I)$]	$R_1 = 0.1111$, $wR_2 = 0.3068$	$R_1 = 0.0970$, $wR_2 = 0.2256$
R indices (all data)	$R_1 = 0.1195$, $wR_2 = 0.3241$	$R_1 = 0.1017$, $wR_2 = 0.2427$
Largest diff. peak and hole (e/Å ³)	1.746 and -1.813	3.645 and -4.298
Atomic coordinates and equivalent isotropic displacement parameters (Å²).		
	$P2_1/n$	$Cmcm$
Fe1	2a (0, 0, 0, 0.027(3))	Fe1 4a (0, 0, 0, 0.0070(19))
Fe2	2b (0, 0, 0.5, 0.030(3))	Fe2 4c (0, 0.2467(3), 0.25, 0.0059(19))
Fe3	4e (0.5282(11), 0.0828(11), 0.7505(8), 0.030(3))	O1 4c (0.5, 0.4102(17), 0.25, 0.010(4))
O1	4e (0.338(5), 0.185(3), 0.072(4), 0.023(5))	O2 8f (0.5, 0.1443(13), 0.060(2), 0.010(3))
O2	4e (0.325(6), 0.181(3), 0.430(4), 0.036(6))	
O3	4e (0.852(6), 0.063(3), 0.262(5), 0.030(6))	

Table 5.9.4-2 Interatomic distances (Å) in a double perovskite $P2_1/n$ (at 54.3(2) GPa) and post-perovskite $Cmcm$ (at 64.6(2) GPa) phases of Fe₂O₃ at ambient temperature.

$P2_1/n$		$Cmcm$	
Octahedron 1		Octahedron	
Fe1—O2	1.82(2)x2	Fe1—O1	1.772(6)x2
Fe1—O1	1.85(2)x2	Fe1—O2	1.861(8)x4
Fe1—O3	1.92(3)x2	Bicapped trigonal prism	
Octahedron 2		Fe2—O1	1.938(11)x2
Fe2—O3	1.74(4)x2	Fe2—O2	2.007(9)x4
Fe2—O1	1.796(15)x2	Fe2—O2	2.189(13)x2
Fe2—O2	1.81(2)x2		
Bicapped trigonal prism			
Fe3—O1	1.87(3)		
Fe3—O3	1.89(3)		
Fe3—O2	1.910(19)		
Fe3—O3	1.931(19)		
Fe3—O2	2.14(3)		
Fe3—O1	2.196(16)		
Fe3—O2	2.37(3)		
Fe3—O1	2.39(3)		

Combining Schouwink's *et al.* [289] data and our new results on compression of a single crystal of hematite to over 52 GPa, we have refined the 3rd order Birch-Murnaghan equation of state [296] keeping the value of $V_0 = 301.88(18) \text{ Å}^3$ constant. Obtained $K = 201(4) \text{ GPa}$ and $K' = 4.3(2)$ are fairly close to the previously reported values ($K = 199(8) \text{ GPa}$, $K' = 5.3(9)$ [289]). The compressibility data reported for hematite powder samples [97,98] disagree with these of Schouwink's *et al.* [289] and our new results. Latter may contributed to the non-hydrostatic stresses propagating though powder specimens. However, the variation of the ratio of the lattice parameters c/a with pressure (Figure 5.9.4-1b) is similar for all the datasets; the c/a ratio decreases with pressure [88,97,98,101,102,289,297]. The same trend was observed in corundum-like V₂O₃ and Ti₂O₃ undergoing a pressure-induced insulator-to-metal transition [298], while corundum itself (Al₂O₃) displays a constant c/a ratio during compression, thus remaining an insulator [299].

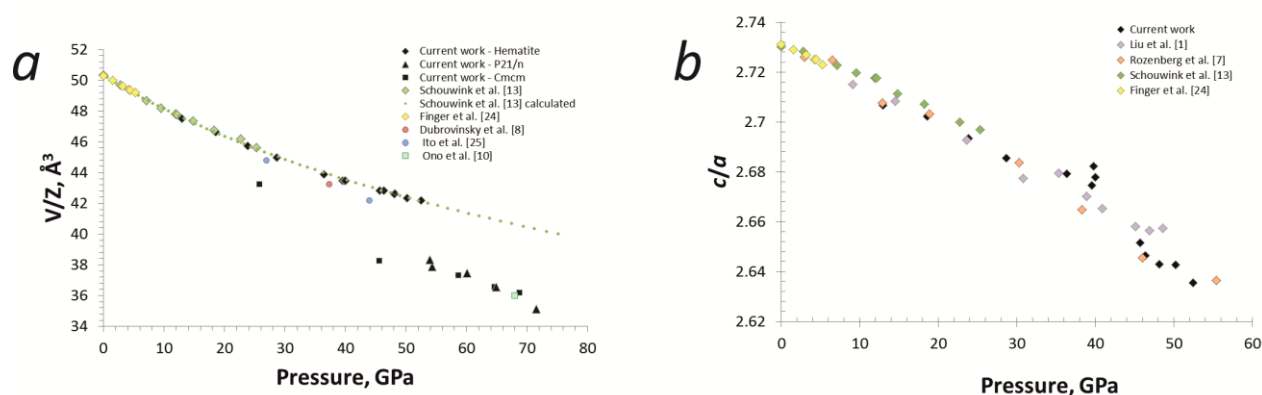


Figure 5.9.4-1 Volume compressibilities for Fe_2O_3 polymorphs (a) and the c/a ratio of hematite as a function of pressure (b). All black symbols designate XRD experiments performed in the current work, colored symbols are for literature data [88,101,102,289,297]. The green dots correspond to the equation of state of hematite from [289]. Symbol's type indicates the crystal structure observed: \diamond - $R\text{-}3c$ (hematite); \circ - $Pbna$ (Rh_2O_3 -II structural type); \triangle - $P2_1/n$ (double perovskite cryolite structural type); \square - $Cmcm$ (post-perovskite structural type). Uncertainties in V/Z values are within the symbol size.

Phase transformation upon compression at ambient temperature

Upon compression, at 54.3(2) GPa we observed the appearance of new reflections (Figure 5.9.4-2a, b) that indicated a phase transformation. The transition pressure could be determined very accurately, since the transformation was repeated within 0.3(2) GPa during two experiments at different XRD facilities. The data set obtained in the experiment conducted at the APS facility at pressure of ~ 54 GPa, immediately after the phase transition, enabled us to solve the structure of the new phase which we called $m\text{-Fe}_2\text{O}_3$. We found a monoclinic unit cell (space group $P2_1/n$) with $a = 4.588(3)$, $b = 4.945(2)$, $c = 6.679(7)$ \AA and $\beta = 91.31(9)^\circ$ (see Table 5.9.4-1 for structural details).

The unit cell parameters of $m\text{-Fe}_2\text{O}_3$ are very close to those of the orthorhombic phase previously reported on compression of hematite at ambient temperature [94,97,98,100] in powder XRD experiments. The splitting of the reflections, reducing the symmetry to monoclinic, might have not been noticed earlier due to the broadening of the reflections accompanying the compression under non-hydrostatic conditions.

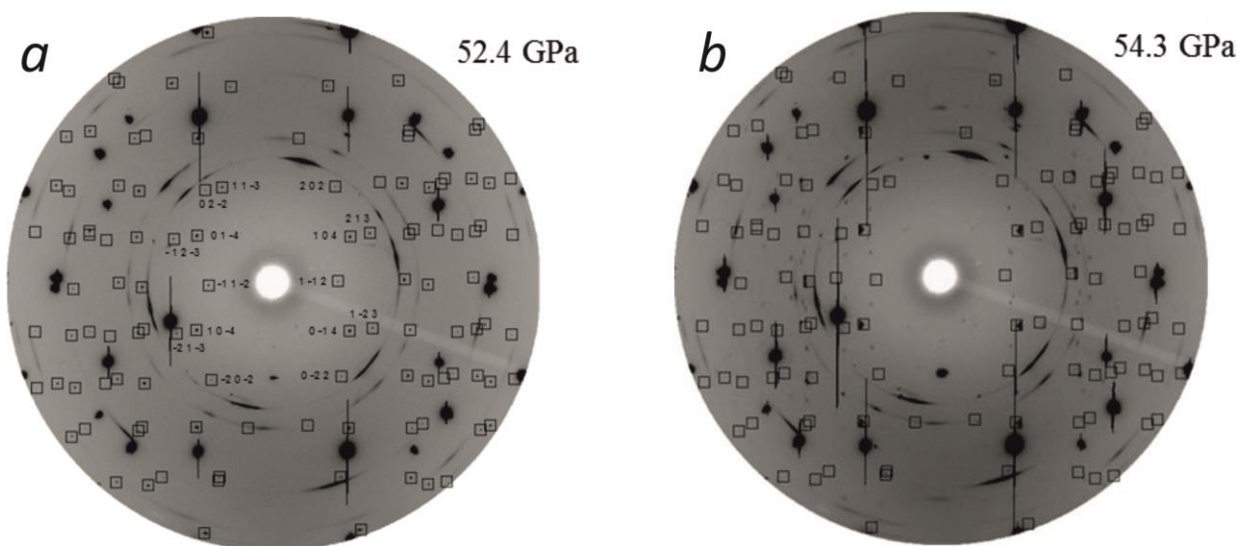


Figure 5.9.4-2 Rotation images of Fe₂O₃ at 52.4 GPa (a) and at 54.3 GPa (b). Squares show predicted positions of the Fe₂O₃ reflections based on the unit cell parameters. At 54.3 GPa the peaks split and in addition the new peaks appear that suggests a formation of a new phase. Inspection of the reciprocal space suggests 2 twin domains rotated by 120°.

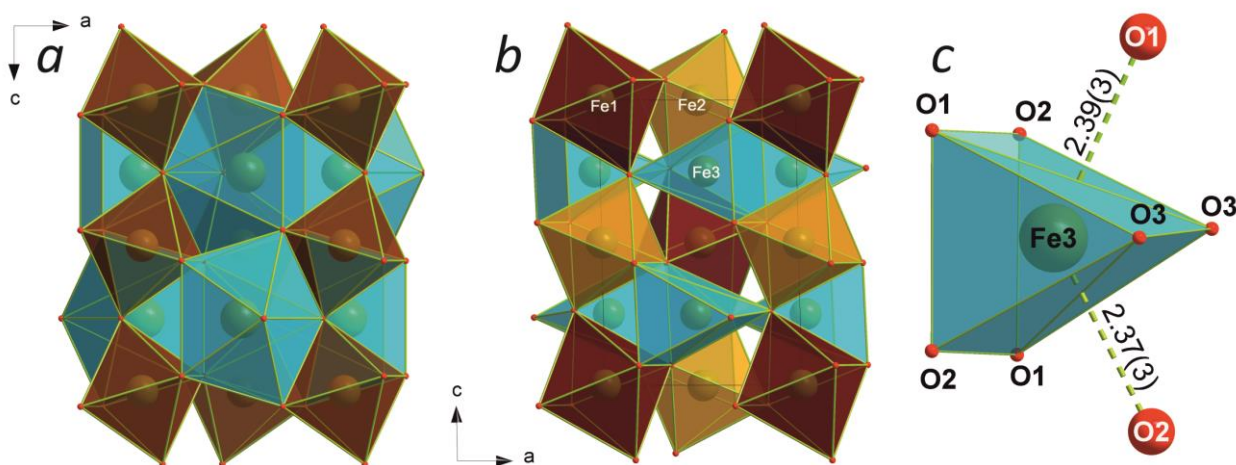


Figure 5.9.4-3 Relations between orthorhombic GdFeO₃-type perovskite (a) and double perovskite cryolite-type (b) structures. The perovskite structure contains a 3 dimensional network of corner-shared FeO₆ octahedra (B-position) and additional Fe atoms located in bicapped trigonal prismatic voids (A-position). In the double perovskite structure B-position is occupied by two alternating atomic species (Fe1 and Fe2 designated by darker and lighter colors). Fe3 atom possessing two significantly larger Fe3—O distances could be considered as having trigonal-prismatic coordination with two additional Fe—O bonds (c).

The crystal structure of $m\text{-Fe}_2\text{O}_3$ can be described as the so-called double perovskite structure with a general formula $A_2B'B''\text{O}_6$ [228]. Figure 5.9.4-3 illustrates relations between the monoclinic cryolite-type (space group $P2_1/n$) and orthorhombic GdFeO_3 -type (space group $Pbnm$) perovskite structures. Both are constructed of a 3-dimensional network of tilted corner-shared BO_6 octahedra (B site in the orthorhombic perovskite and crystallographically non-equivalent B' and B'' sites in the monoclinic double perovskite) with additional A -atoms located inside bicapped trigonal prismatic voids (A -site). In monoclinic cryolite-type double perovskites B' and B'' atoms have distinctly different atomic radii either due to an occupation with different atomic species (ex. $\text{Ca}_2\text{FeMoO}_6$, Ca_2MnWO_6 [300,301]) or with cations of alternating charges (ex. $\text{Ba}_2\text{Bi}^{3+}\text{Bi}^{5+}\text{O}_6$ [302]). In the case of Fe_2O_3 all metal sites are occupied by Fe but interatomic distances differ (see Table 5.9.4-2); Fe3—O (A site) distances are considerably larger than Fe1—O and especially Fe2—O are stretched (B' and B'' sites); a possible explanation for this phenomenon is described below. The A -void demonstrates a significant scatter of Fe—O distances, two of them (2.37(3) and 2.39(3) Å) are much larger in comparison to the remaining six distances (1.87(3)—2.196(16) Å). The six oxygen atoms form a trigonal prism around the Fe atom. If the two longer Fe—O contacts are included into the coordination polyhedron of Fe in the A -position, the polyhedron acquires a shape of a bicapped trigonal prism (Figure 5.9.4-3).

The monoclinic cryolite-type structure can be described in terms of the parent orthorhombic perovskite structure plus a symmetry breaking structural distortion corresponding to the irreducible representation Γ_3^+ [303]. In the GdFeO_3 perovskite Fe1 and Fe2 atoms, as well as O1 and O2 atoms, are equivalent and related by a mirror plane perpendicular to the c -axis (in $Pbnm$ setting), while Fe3 and O3 atoms are located on the mirror plane. The distortion moves the O3 atom from the mirror plane towards to Fe2 position which breaks mirror plane symmetry and results in two non-equivalent positions for both Fe and O atoms.

A reason for formation of Fe_2O_3 with the monoclinic double perovskite cryolite-type structure may be an alternation of the electronic (low-spin, LS, and high-spin, HS) state of the iron atoms. The Fe^{3+} ion in the low-spin state possesses a smaller atomic radius compared to that in the high-spin state, so that systematically shorter Fe2—O distances (1.74(4)—1.81(2) Å) compared

to the Fe1—O ones (1.82(2)—1.92(3) Å) may indicate the spin crossover (the HS-to-LS transition) in Fe³⁺ at the Fe2 position associated with the atom shift responsible for the monoclinic distortion in the structure of Fe₂O₃. The drastic volume reduction at ca. 54 GPa also supports this assumption. Structural transitions associated with the spin crossover in Fe³⁺ under pressure (in the same pressure region of about 50 GPa) are known for CaFe₂O₄ [304], FeOOH [305] and FeBO₃ (private communication with E. Greenberg). The Fe2—O distances in *m*-Fe₂O₃ are well consistent with the possible LS state of Fe2 if compared with the corresponding literature data (Figure 5.9.4-4). However, the Fe1—O distances are rather short for HS Fe1 state, therefore the question about the spin state of iron in different structural positions in *m*-Fe₂O₃ cannot be presently answered unambiguously and requires further Mössbauer spectroscopy studies. Note that larger interatomic Fe—O distances 1.820(11)—2.146(19) Å reported for the Rh₂O₃-II-type Fe₂O₃ phase [102] supported the HS state for Fe in this phase synthesized upon laser heating at about 40 GPa [102] (Figure 5.9.4-4).

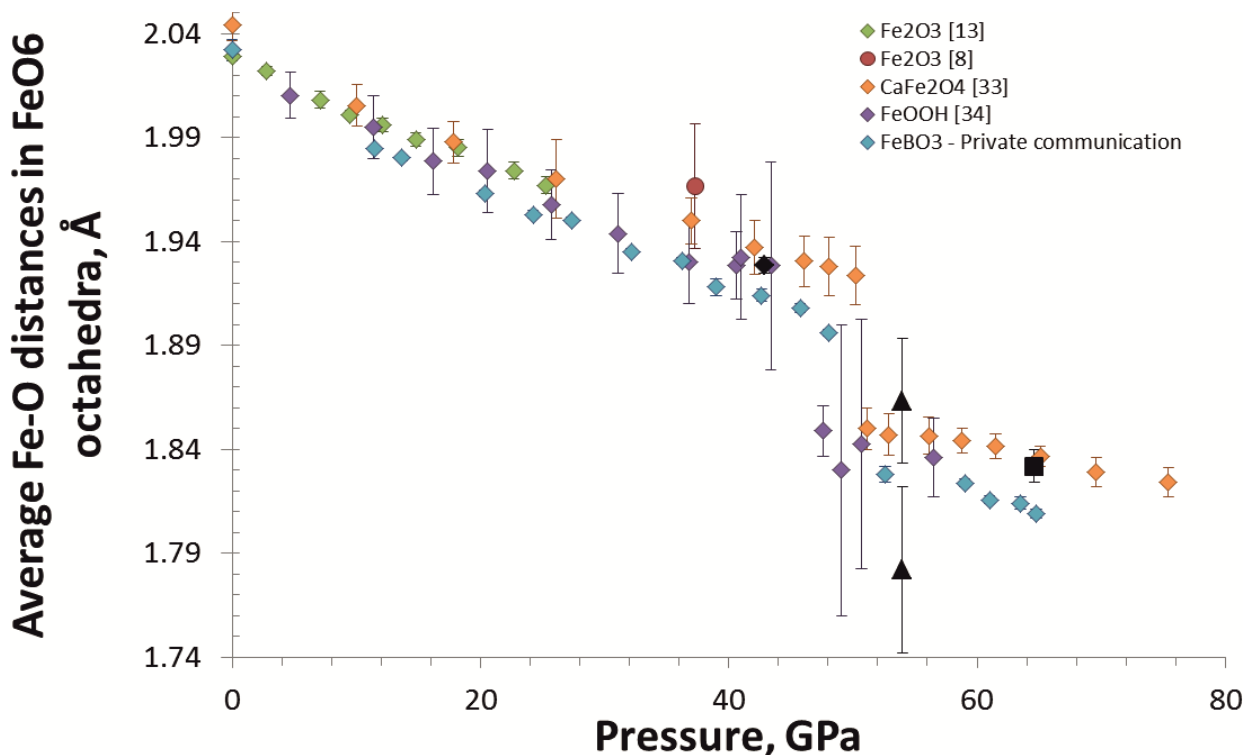


Figure 5.9.4-4 Average Fe-O distances in FeO₆ octahedra. All black symbols with the error-bars designate XRD results of the current work, colored symbols are for literature data [102,289,304,305]. Symbols type indicates on a crystal structure observed: \diamond - *R*-3*c* (hematite); \circ - *Pbn̄a* (Rh₂O₃-II structural type); \triangle - *P*2₁/*n̄*; \square - *Cmcm* (post-perovskite structural type).

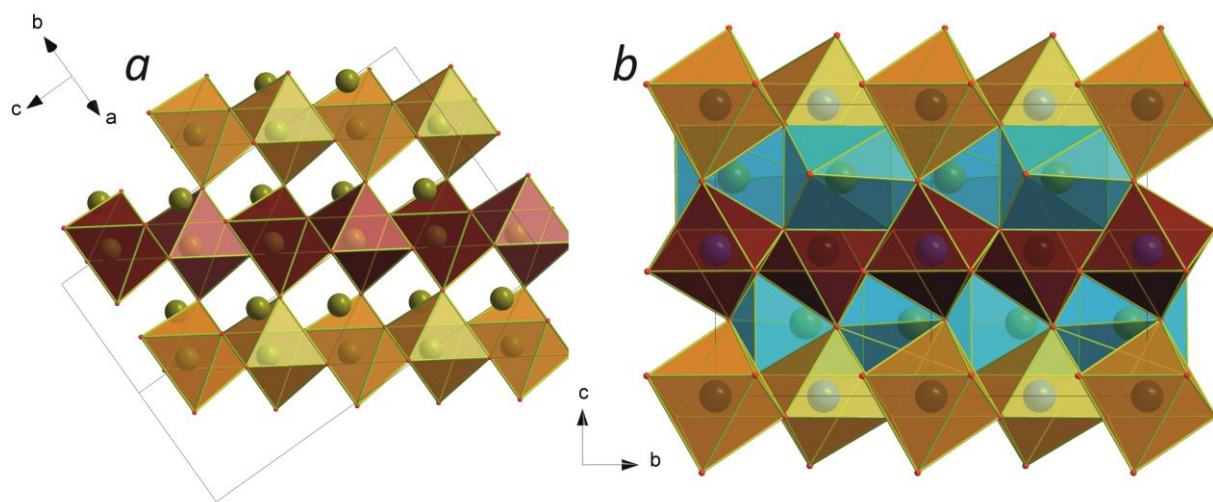


Figure 5.9.4-5 Similarity of building blocks in corundum-type (*a*) and double perovskite (*b*) structures. In the double perovskite structure *B*-position is occupied by Fe1 and Fe2 atoms (FeO₆ octahedra are designated by darker and lighter colors). The same fragments are marked at the corundum structure.

Hematite and *m*-Fe₂O₃ structures are not connected by the group-subgroup relations. However, they consist of the common building blocks shown in Figure 5.9.4-5. Hematite (corundum-type) structure can be considered as a set of layers of corner-shared FeO₆ octahedra stacked along the $[1\bar{1}2]$ direction with additional Fe atoms located in the octahedral voids. The layers are shifted with respect of each other in the $(1\bar{1}2)$ plane and connected via shared vertices of octahedra. In the *m*-Fe₂O₃ structure two layers are related with the mirror plane symmetry and, as a result, the void changes from octahedral to bicapped prismatic one. The distortion from the corundum to Rh₂O₃-II-type structure has a rather different mechanism and, according to [306], requires altering a position of 1/6 of oxygen atoms. Both structures are considered as a combination of pairs of MO₆ octahedra with common faces [306], but in the corundum structure such pairs share three common edges and in Rh₂O₃-II-type structure only two. The transformation of the corundum-type hematite structure to *m*-Fe₂O₃ destroys pairs of the FeO₆ octahedra and preserves only the corner-shared network.

Phase transformation of m -Fe₂O₃ into PPv-Fe₂O₃ upon laser heating above 70 GPa

Formation of a new phase during laser heating above 2500 K of Fe₂O₃ compressed to 70 GPa was first observed by Ono *et al.* [88,99] by means of powder XRD in the DAC and the phase was assigned an orthorhombic cell (the *Cmcm* space group), the CaIrO₃ structural type (PPv-Fe₂O₃). More recent studies were concentrated mostly on magnetic and electronic properties of the HP phase [306]; however no accurate data for atomic coordinates were reported so far. We observed a formation of PPv-Fe₂O₃ upon laser heating of *m*-Fe₂O₃ at 2100 ± 100 K compressed to ~ 68 GPa. Laser heating resulted in a formation of variety of closely-oriented single crystals (Figure 5.9.4-6). Nevertheless the peaks remained sharp and well resolved; therefore the data integration using small masks provided appropriate results for data collected at 65 GPa. Upon decompression the number of domains decreased and at 25 GPa only two distinct domains mutually rotated by $\sim 5^\circ$ along the *b* axis remained.

Crystal structure of the PPv-Fe₂O₃ phase displays two independent positions for the iron atoms, namely Fe1 with the octahedral coordination and Fe2 with the bicapped trigonal prismatic (Table 5.9.4-2). Octahedra connect via common edges in rutile-like layers stacked along the *b* direction.

The octahedral layers are interconnected by the face-shared bicapped trigonal prisms (Figure 5.9.4-7). The Fe2—O interatomic distances in the prisms of 1.938(11)—2.189(13) Å in PPv-Fe₂O₃ are longer than those in *m*-Fe₂O₃ suggesting the HS state of iron, while the distances in octahedra (three of 1.772(7) and three of 1.862(8) Å) are considerably smaller and suggest the LS state of the Fe³⁺ ions in the Fe1 position. Synchrotron nuclear forward scattering study and *ab initio* calculations performed by Shim *et al.* [100] suggested the HS state for Fe in the prism position in PPv-Fe₂O₃ while the spin assignment of iron in octahedra remained uncertain [100].

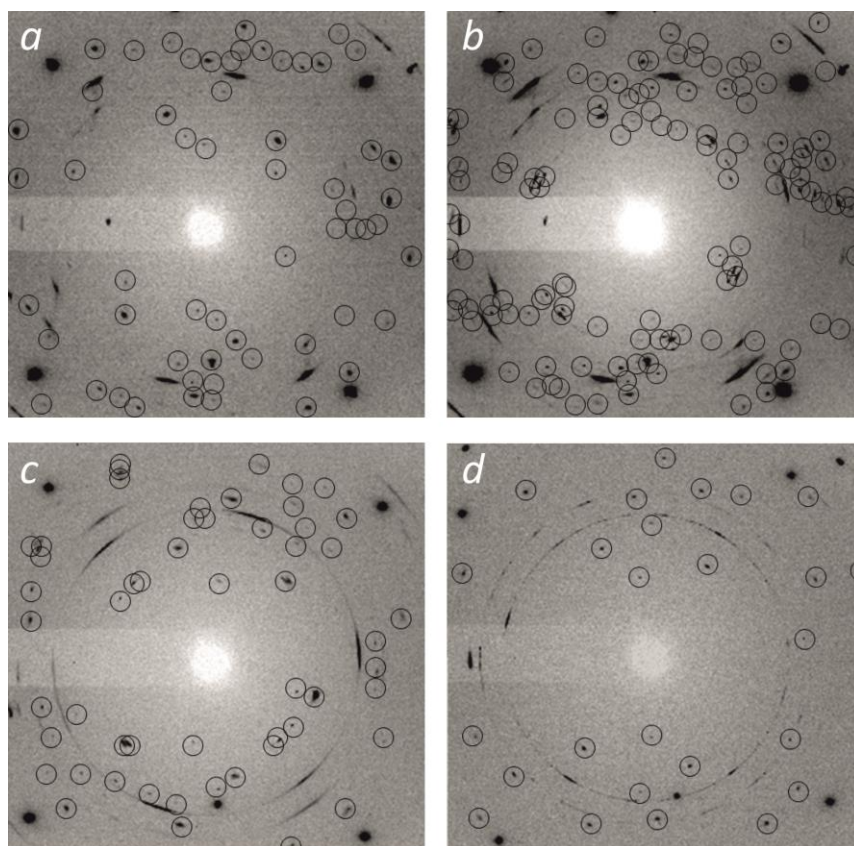


Figure 5.9.4-6 Central part of rotation images of Fe_2O_3 at 68.3 GPa ($P2_1/n$ phase) at ambient temperature (a) and at 68.8 GPa after laser annealing which induces the formation of the closely oriented crystals (b). During decompression intensity of the peaks belonging to the $Cmcm$ phase decreases (c) and they completely disappear to 15 GPa that indicates complete transformation back to the multi-domain hematite phase (d). Circles designate corresponding phases; diamond peaks and diffraction lines attributed to neon are not marked.

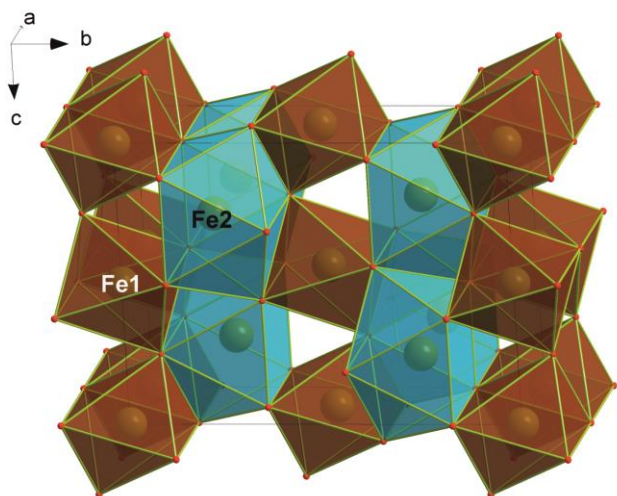


Figure 5.9.4-7 Crystal structure of the PPv- Fe_2O_3 ($Cmcm$) phase which possess two independent iron atoms, namely Fe1 with the octahedral coordination and Fe2 with the bicapped trigonal prismatic one.

Compressional behavior of high-pressure polymorphs of Fe_2O_3

Among metal sesquioxides, M_2O_3 , corundum, Al_2O_3 , and bixbyite, $(\text{Mn,Fe})_2\text{O}_3$, structural types are known to be common at ambient conditions. Corundum structure is composed of a hexagonal closest packing of oxygen atoms with 2/3 of the octahedral voids being occupied by a metal atom. Each MO_6 polyhedron shares 3 edges with neighboring polyhedra forming honeycomb-like layers and, in addition one face with the polyhedron from the neighboring layer. Cubic bixbyite can be described as the CaF_2 -type structure with 1/4 of oxygen being removed creating a network of MO_6 octahedra connected only through edges.

Compression of compounds induces a formation of phases with higher degree of the packing density. For the M_2O_3 family the coordination number of the cation can remain and the increase of the density is achieved through a strong distortion of the octahedra like in Rh_2O_3 -II [306]. Much more effective volume reduction in sesquioxides could be achieved through the increase of the metal coordination number. For example, so-called A-RES and B-RES structural types, with 7-coordinated metal atoms appear during compression of Eu^{3+} -doped Y_2O_3 [307]. High-pressure and high-temperature treatment of B-RES-type phases of Sc_2O_3 and Y_2O_3 results in formation of the Gd_2S_3 -type structure with 7+8-fold coordination polyhedra [308,309]. At ~ 15 GPa and upon heating to ~ 1200 K Ti_2O_3 transforms into the Th_2S_3 -type phase with the metal coordination number varying from 6 to 8 [310,311]. So far, the transition to perovskite and post-perovskite structural types having 8-coordinated metal atoms in bicapped trigonal prisms has been reported only for Mn_2O_3 [312].

In our experiments the orthorhombic Fe_2O_3 (Rh_2O_3 -II-type) phase was not observed during compression up to 73 GPa at ambient temperature; a transformation to the monoclinic ($P2_1/n$) phase was detected at 54 GPa instead. The transition to the Rh_2O_3 -II-type phase [102] is accompanied with an abrupt volume decrease but it is relatively small (~ 1.3 %) to be attributed to the HS-to-LS transition suggested previously [96]. Contrary, a significant difference in molar volumes of $m\text{-Fe}_2\text{O}_3$ and hematite (~ 10.2 %) points toward the spin crossover upon transition accompanied with a structural change. The volume discontinuity in Fe_2O_3 of about 10 % at 50 GPa has been reported in [94,98], but the high-pressure phase was indexed in the

orthorhombic unit cell. Although both Rh_2O_3 -II-type and $m\text{-Fe}_2\text{O}_3$ phases were observed at close P,T -conditions, it seems that the former appears only upon heating even at moderate pressures (~ 32 GPa and 800 K according to [101]), while the latter forms during compression above 54 GPa at ambient temperature (as observed in our single crystal X-ray diffraction experiments).

The laser heating at 68 GPa results in a transition to the orthorhombic ($Cmcm$) $\text{PPv-Fe}_2\text{O}_3$ phase. Studies of this phase performed on decompression for the first time unambiguously show that $\text{PPv-Fe}_2\text{O}_3$ can be preserved down to pressures of 25 GPa; any traces of the post-perovskite phase disappear upon pressure release to 15 GPa (Figure 5.9.4-6c and d).

The quality of the P — V data obtained in the current study on compression of $m\text{-Fe}_2\text{O}_3$ and on decompression of $\text{PPv-Fe}_2\text{O}_3$ appeared insufficient for accurate determination of the EOSs of these phases because of the multi-domain nature of samples and weak peaks intensities. However, available data suggest that the molar volumes of $m\text{-Fe}_2\text{O}_3$ and $\text{PPv-Fe}_2\text{O}_3$ are quite similar (Figure 5.9.4-1). We would like to note that the molar volume difference between perovskite and post-perovskite phases for a number of compounds (namely, NaNiF_3 , NaZnF_3 , MgSiO_3 , MgGeO_3 , MnGeO_3 , CaSnO_3 , CaRuO_3 , CaRhO_3 , CaIrO_3) is just about 1.5 % [313].

5.9.5. Conclusions

In the present work we describe in detail the structural changes that occur during the compression of single crystals of $\alpha\text{-Fe}_2\text{O}_3$ and its transition to a double-perovskite-type phase with the monoclinic unit cell (space group $P2_1/n$) at about 54 GPa. The transition associated with a drastic volume reduction of 10.2 % unlike to the previously reported phase transition to the Rh_2O_3 -II-type phase, which resulted in only a ~ 1.3 % volume change [102]. The analysis of the interatomic Fe—O distances in $m\text{-Fe}_2\text{O}_3$ suggests the HS-LS crossover in iron atoms located at least in one of the two octahedral positions. Based on available single crystal X-ray diffraction data we suggest that the iron sesquioxide undergoes a reconstructive transition to the Rh_2O_3 -II-type phase only upon heating at pressures below 50 GPa, while at room temperature it transforms to the $m\text{-Fe}_2\text{O}_3$ phase at 54 GPa. Laser heating at 70 GPa provokes a transition to the post-perovskite ($Cmcm$) structure.

5.9.6. Acknowledgments

The work was supported by the German Research Foundation (DFG). N.D. thanks DFG for financial support through the Heisenberg Program and the DFG Project DU 954-8/1. Use of the Advanced Photon Source (APS), Argonne National Laboratory, was supported by the U. S. Department of Energy, Office of Science, Office of Basic Energy Sciences, under Contract No. DE-AC02-06CH11357. GeoSoilEnviroCARS (Sector 13) of APS, where part of synchrotron diffraction experiments were performed, is supported by the National Science Foundation-Earth Sciences (EAR 1128799) and Department of Energy- Geosciences (DE-FG02-94ER14466).

5.10. Fate of banded iron formations subducted into the lower mantle

E. Bykova^{1,2}, L. Dubrovinsky¹, N. Dubrovinskaia², M. Bykov², C. McCammon¹, S.V. Ovsyannikov¹, H.-P. Liermann³, I. Kopenko^{1,4}, A.I. Chumakov⁴, R. Rüffer⁴, M. Hanfland⁴, V. Prakapenka⁵

¹*Bavarian Research Institute of Experimental Geochemistry and Geophysics, University of Bayreuth, D-95440 Bayreuth, Germany*

²*Laboratory of Crystallography, University of Bayreuth, D-95440 Bayreuth, Germany*

³*Photon Sciences, Deutsches Elektronen-Synchrotron, D-22603 Hamburg, Germany*

⁴*European Synchrotron Radiation Facility, BP 220, Grenoble F-38043, France*

⁵*Center for Advanced Radiation Sources, University of Chicago, IL 60437 Argonne, USA*

Submitted in Nat. Geoscientific.

5.10.1. Abstract

Banded Iron Formations (BIFs) and ironstones are sedimentary rocks occurring on all continents with thicknesses up to several hundred meters and length up to hundreds of kilometers. The main iron-bearing minerals in BIFs are hematite, α -Fe₂O₃, and magnetite, Fe₃O₄, constituting up to 85 wt.% of BIFs [84]. Deposited in the world's oceans, BIFs as part of the ocean floor are recycled into the Earth's interior by subduction [85,86] to depths extending possibly to the core-mantle boundary (CMB) region [85]. The behavior of iron oxides at these extreme pressure- temperature conditions can influence geochemical processes in the deep Earth. Here we report a systematic investigation of the behavior of iron oxides (Fe₃O₄ and Fe₂O₃) at pressures over 100 GPa and temperatures above 2500 K employing single crystal X-ray diffraction (XRD) [103,121] and synchrotron Mössbauer source (SMS) spectroscopy [212]. We discovered a number of previously unknown iron oxide phases that form successively upon pressure and temperature increase, and also that Fe₂O₃ releases oxygen at pressures above 60 GPa and temperatures of 2000 K through a decomposition that forms an unusual Fe₅O₇ phase. Thus, BIFs subducted into the lower mantle may provide a source of an oxygen-rich fluid in the deep Earth's interior leading to significant heterogeneity in oxygen fugacity in different parts of the mantle.

5.10.2. Manuscript

Banded Iron Formations and ironstones formed starting from the late Precambrian (between 2.8 and 1.8 billion years ago) until the Pliocene [84]. Typical BIFs consist of distinctly separated alternating iron-rich (magnetite and hematite) and amorphous silica-rich layers. Together with downwelling lithosphere BIFs are expected to penetrate deep into the mantle [85,86]. Available experimental data [85,87,88] suggest that iron oxides melt above the geotherm in the entire mantle and thus remain solid in slabs that are colder than the surrounding mantle. Solid state chemical reactions are controlled by diffusion whose rate is very low. Even if subduction is slow at 1 cm/year and the time for a slab to reach a depth of about 2000 km is ~200 Ma, this geological time is sufficient to influence only a few tens of meters of rocks beneath the BIF's surface. Thus the fate of iron oxides, a major component of subducted BIFs, depends on the pressures and temperatures (P – T) to which they are exposed.

Previously based on powder XRD experiments in externally heated (up to about 1200 K) diamond anvil cells (DACs), magnetite (Fe_3O_4) was shown to transform into a CaTi_2O_4 -structured phase [89] at pressures above ~25 GPa. Theoretical calculations suggest [314] this phase to be stable at least up to 120 GPa. Our single-crystal synchrotron XRD study of magnetite at ambient temperature confirmed the phase transition between 29 and 31 GPa and the CaTi_2O_4 -type structure (space group $Bbmm$, No. #63) of the high-pressure $HP\text{-Fe}_3\text{O}_4$ phase (Figure ED 5.10.5-1). Laser heating of $HP\text{-Fe}_3\text{O}_4$ at 2350(100) K and pressures up to 50 GPa does not result in any chemical or structural modifications (Table ED 5.10.5-1). Evidence for the existence of the $HP\text{-Fe}_3\text{O}_4$ phase at even higher P,T conditions was found in our independent experiments on siderite (FeCO_3). By studying products of its decomposition after treatment at 70(1) GPa and 2400(100) K, we identified reflections in the XRD pattern that belong to $HP\text{-Fe}_3\text{O}_4$. Thus, our experimental results show that $HP\text{-Fe}_3\text{O}_4$ may exist to depths of at least 2000 km.

Due to its significance in condensed matter and mineral physics, the high-pressure behavior of hematite, $\alpha\text{-Fe}_2\text{O}_3$ (Figure 5.10.2-1a), has been investigated even more intensively than that of Fe_3O_4 . Particular attention has been focused on elucidating the nature of phase transition(s) and

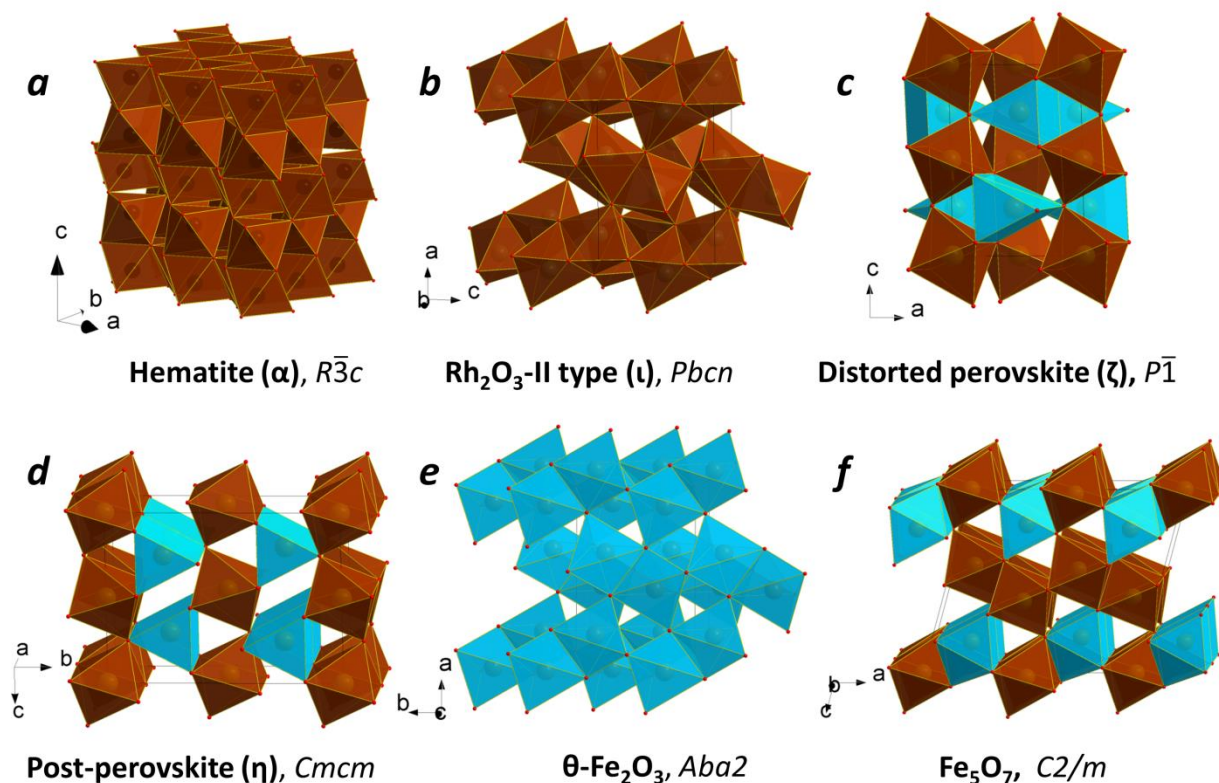


Figure 5.10.2-1 Crystal structures of hematite, HP polymorphs of Fe_2O_3 and a new compound, Fe_5O_7 , studied in the present work. Building blocks are octahedra (brown) and trigonal prisms (blue). The prisms in Fe_5O_7 and $\eta\text{-Fe}_2\text{O}_3$ have additional apices (one and two, respectively). Hematite (*a*) consists of FeO_6 octahedra connected in a corundum-like motif, namely each octahedron connects with 3 neighbors via edges in honeycomb layers, and layers are interconnected through common triangular faces of octahedra. The $\iota\text{-Fe}_2\text{O}_3$ structure (*b*) is built of only FeO_6 octahedra but each 2 octahedra are connected through a common triangular face; such units pack in a herringbone pattern and layers pack with a shift along the *c*-direction having common edges. In distorted perovskite $\zeta\text{-Fe}_2\text{O}_3$ (*c*) octahedra connect through common vertices and prisms share only common edges. $\theta\text{-Fe}_2\text{O}_3$ (*e*) adopts the packing motif from $\iota\text{-Fe}_2\text{O}_3$ but instead of octahedra it consists of FeO_6 prisms. Post-perovskite (*d*) and Fe_5O_7 (*f*) are members of a homological series $n\text{FeO} \cdot m\text{Fe}_2\text{O}_3$ (see Figure ED 5.10.5-3), where prisms are connected through common triangular faces, while octahedra connect only via shared edges.

the structure of the high-pressure phase of hematite observed above ~ 50 GPa [94–103]. For this phase two structures have been proposed by different groups: Rh_2O_3 -II-type (space group $Pbcn$, No. #60) and GdFeO_3 -perovskite-type (space group $Pbnm$, No. #62) structures [94,97]. While Mössbauer spectroscopic and resistivity measurements clearly demonstrate the importance of electronic changes in Fe^{3+} and seem to support the Rh_2O_3 -II-type structure [95], powder diffraction data collected by various groups over several decades did not allow an unambiguous assignment of the structural type (see Refs. 11, 12, 14, 15 and references therein). Only recent single-crystal high- P,T diffraction data [103] were able to solve this challenge: they demonstrated that the Rh_2O_3 -II-type phase of Fe_2O_3 (which we further call ι - Fe_2O_3 , Figure 5.10.2-1b) forms upon laser heating at pressures above ~ 40 GPa, whereas compression of hematite at ambient temperature to over ~ 50 GPa results in the formation of a phase with distorted GdFeO_3 -perovskite-type, dPv ζ - Fe_2O_3 , structure (Figure 5.10.2-1c). Experiments in laser-heated DACs revealed the formation of a CaIrO_3 -type phase (“post-perovskite”, PPv η - Fe_2O_3 , Figure 5.10.2-1d) at pressures above ~ 60 GPa [88,99,100,103]. However, the behavior of this phase under compression is not well studied. The phase diagram of Fe_2O_3 at megabar pressure range is incomplete and the data are often conflicting [88,99–101]. Therefore, in order to study the behavior of ferric iron (Fe^{3+}) in subducting BIFs, we applied the complementary methods of single crystal XRD in laser-heated DACs and SMS spectroscopy (see Methods).

In agreement with previous studies [94,95,97,98,103], our cold compression experiments of hematite single crystals to 54(1) GPa results in a transition to the ζ - Fe_2O_3 phase manifested by a ~ 8.4 % volume discontinuity (Figure ED 5.10.5-2). Although earlier [103] we indexed the diffraction pattern of ζ - Fe_2O_3 in a monoclinic unit cell, the new extended data-set acquired in the present work showed that the structure is in fact triclinic (see Supplementary Information for details), similar to Mn_2O_3 [312]. An insufficient number of independent reflections prevented structural refinement of ζ - Fe_2O_3 in triclinic symmetry, so we used a monoclinic model [103] to qualitatively constrain the atomic arrangement in ζ - Fe_2O_3 . Upon further pressure increase from 54(1) to 67(1) GPa, a reduction in the splitting of reflections was observed, indicating an increase in symmetry. The structure of ζ - Fe_2O_3 thus becomes closer to

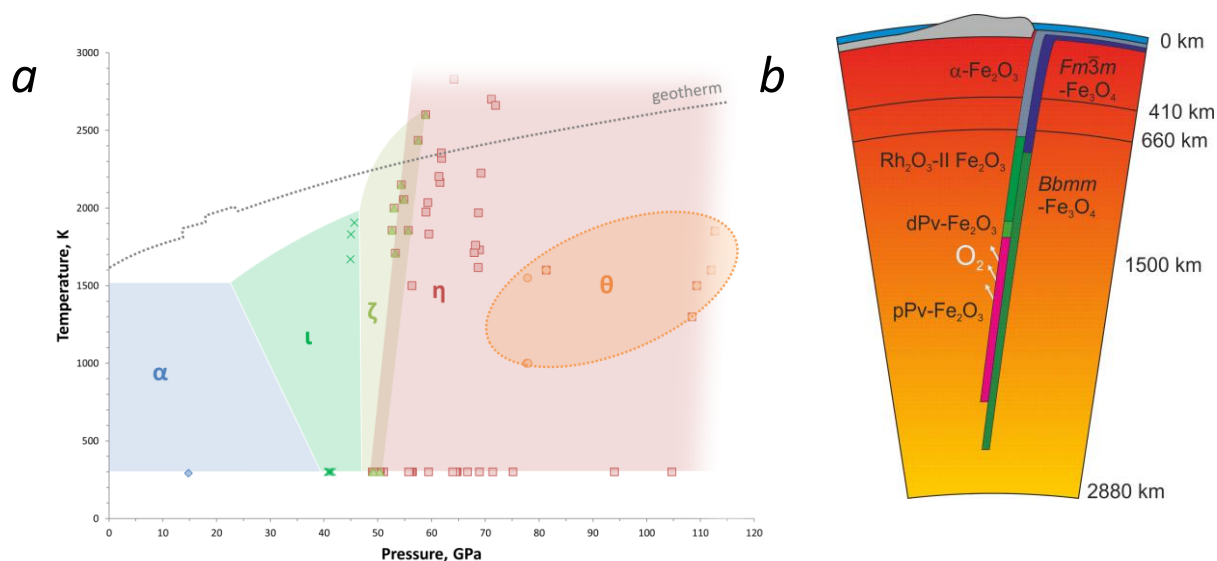


Figure 5.10.2-2 Transformational phase diagram of Fe₂O₃ and its implications for subducted BIFs. Left figure (a) shows the apparent fields of stability of the Fe₂O₃ high-pressure phases established in this study. The right figure (b) demonstrates the possible consequence of phase transitions of Fe₂O₃ and Fe₃O₄ in a BIF subducted to the lower mantle. Legend (a): ◇ - *R-3c* hematite (α -Fe₂O₃), △ - *P-1* distorted perovskite (ζ -Fe₂O₃), ○ - *Aba2* (θ -Fe₂O₃), □ - *Cmcm* post-perovskite (η -Fe₂O₃), × - Rh₂O₃-II type phase (ρ -Fe₂O₃). Symbols represent experiments involving laser heating. The boundary between hematite α -Fe₂O₃ and ρ -Fe₂O₃ is defined according to [101]. The geotherm is defined according to [315,316].

that of GdFeO₃-type-perovskite (Supplementary Information, Figure ED 5.10.5-3). At 67(1) GPa a small drop in the unit cell volume (~1.7 %) manifests the next transformation to the θ -Fe₂O₃ phase (Figure 5.10.2-1e) with orthorhombic symmetry (space group *Aba2*, No. #41, $a = 4.608(7)$, $b = 4.730(4)$, $c = 6.682(18)$ Å (Table ED 5.10.5-2). On compression at ambient temperature θ -Fe₂O₃ can be observed to at least 100 GPa (Figure ED 5.10.5-2). The transformational P - T diagram for Fe₂O₃ is given in Figure 5.10.2-2.

During *in situ* laser heating of θ -Fe₂O₃ between ~1000 and 1550(50) K at 78(2) GPa, no evidence of a phase transformation was observed. The absence may be either evidence that θ -Fe₂O₃ is stable at these conditions, or an indication that higher temperatures are required to overcome kinetic barriers for further structural transitions. Indeed, heating at 1600(50) K results in the formation of post-perovskite PPv type η -Fe₂O₃ coexisting with θ -Fe₂O₃. Both phases (θ -Fe₂O₃

and $\eta\text{-Fe}_2\text{O}_3$) were observed *in situ* simultaneously upon heating to 1850(50) K at pressures up to 113(1) GPa. However, temperature-quenched products contained only $\eta\text{-Fe}_2\text{O}_3$ (Figure 5.10.2-2). Once synthesized, $\eta\text{-Fe}_2\text{O}_3$ may be preserved at ambient temperature down to at least 26 GPa. At lower pressures it transforms back to hematite (see Figure 5.10.2-1 & 2 for structures and phase relations). Moderate heating to ~ 2000 K at pressures of about 50 GPa provokes a transition to the dPv $\zeta\text{-Fe}_2\text{O}_3$ phase. Decompression of $\zeta\text{-Fe}_2\text{O}_3$ or $\eta\text{-Fe}_2\text{O}_3$ to 41(1) GPa with heating at 1800(100) K results in growth of $\text{Rh}_2\text{O}_3\text{-II}$ type $\iota\text{-Fe}_2\text{O}_3$ (Figure ED 5.10.5-2, Table ED 5.10.5-2). Interestingly, $\iota\text{-Fe}_2\text{O}_3$ was synthesized earlier [101,102] from hematite, thus bracketing the possible P - T stability field of the phase (Figure 5.10.2-2).

The sequence of phase transitions in Fe_2O_3 in the megabar pressure range and temperatures up to about 2500 K (Figure 5.10.2-2) can be neatly rationalized through the variation of molar volumes of the phases observed as a function of pressure (Figure ED 5.10.5-2), complemented by the corresponding SMS spectroscopy data (Figure 5.10.2-3, see Supplementary information for detailed description of magnetic and electronic transformations in Fe_2O_3).

The behavior of $\eta\text{-Fe}_2\text{O}_3$ under heating is rather remarkable. Firstly, we noted that its unit cell volume increases by up to 1 % upon laser heating to about 2000 K at ~ 56 GPa and 64 GPa. (Figure ED 5.10.5-4). Secondly, after heating for a few seconds to 2700-3000 K and 71 GPa we observed the immediate appearance of new sharp spots in the diffraction pattern. The peaks were indexed in the $C2/m$ space group and the structure solution using direct methods identified the phase as a novel mixed-valence iron oxide Fe_5O_7 ($\text{FeO}\cdot 2\text{Fe}_2\text{O}_3$). The phase is preserved on decompression down to at least 41(1) GPa. Thus, we explain our observations as a continuous loss of oxygen by $\eta\text{-Fe}_2\text{O}_3$ upon heating at moderate temperatures and pressures above ~ 60 GPa, according to the reaction $\eta\text{-Fe}_2\text{O}_3 \rightarrow \eta\text{-Fe}_2\text{O}_{3-\delta} + 0.5\delta\text{O}_2$. Note that a similar process is well known for perovskites [317] and other oxides [318]. The reaction is accompanied by a partial reduction of Fe^{3+} to larger-sized Fe^{2+} that consequently increases the unit cell volume. Upon heating at sufficiently high temperature (above ~ 2700 K), the oxygen deficiency in $\eta\text{-Fe}_2\text{O}_3$ reaches a critical limit and provokes a reconstructive phase transition resulting in the formation of the mixed-valence iron oxide Fe_5O_7 : $5\eta\text{-Fe}_2\text{O}_3 \rightarrow 2\text{Fe}_5\text{O}_7 + 0.5\text{O}_2$. We did not find

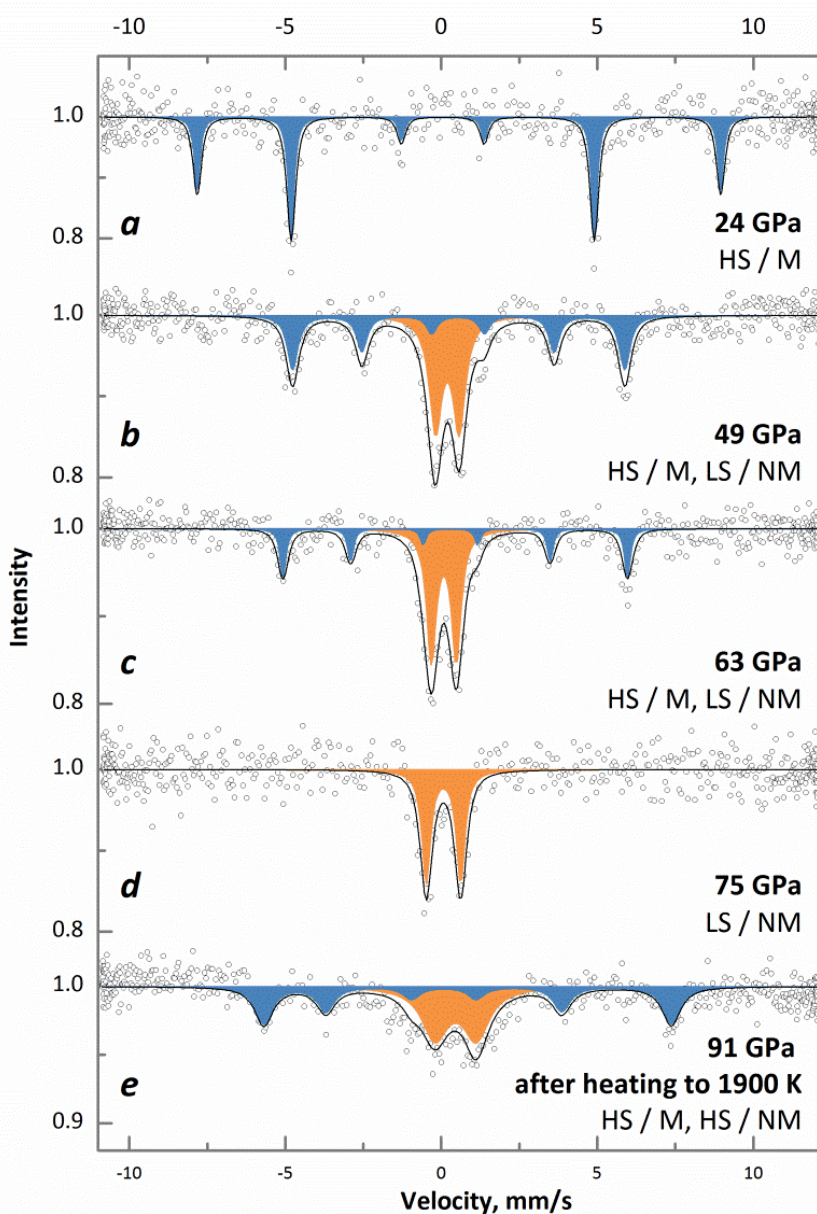


Figure 5.10.2-3 Evolution of synchrotron Mössbauer source spectra of Fe_2O_3 . Spectra collected during compression (*a* – *d*) and after heating (*e*). In hematite (*a*) iron atoms have a high-spin (HS) state (at ~ 24 GPa $\text{CS} = 0.306(4)$ mm/s), and spectra are split due to magnetic ordering (M). After the first transition at 49 GPa (*b*) a new non-magnetic (NM) component appears with centre shift (CS) of $0.074(5)$ mm/s corresponding to a low-spin (LS) state. During further compression a fraction of the magnetic component decreases (*c*) and it disappears completely after the second transition to the $\theta\text{-Fe}_2\text{O}_3$ phase (*d*) that has only one non-magnetic position of LS iron atoms in the crystal structure. After heating above $1600(50)$ K (*e*) a transformation to $\eta\text{-Fe}_2\text{O}_3$ occurs. The crystal structure has 2 HS-iron positions (both CS are ~ 0.45 mm/s), where one position is magnetically ordered and the other is non-magnetic.

any sign of involvement of the carbon from diamond anvils in the chemical reactions. Indeed this was not expected, because at the HPHT conditions of our experiments carbon and oxygen do not react [319].

Similarities in the crystal structures of η -Fe₂O₃, Fe₅O₇, *HP*-Fe₃O₄, and the recently discovered Fe₄O₅ [141] (Figure ED 5.10.5-1) demonstrate [142] that iron oxide phases form a homological series $n\text{FeO} \cdot m\text{Fe}_2\text{O}_3$ (with wüstite, FeO and η -Fe₂O₃ as the end-members), so that potentially other mixed-valence iron oxides may be found under pressure temperature conditions of the lower mantle.

Our results demonstrate clearly the complex experience of iron oxide subjected to the high pressures and temperatures of the Earth's interior. Upon subduction of BIFs into the lower mantle, hematite undergoes numerous phase transformations. At pressures above ~60 GPa the HP phase η -Fe₂O₃ starts to decompose, producing oxygen. Based on estimates of the amount of BIFs subducted into the Earth's mantle and that BIFs may consist of approximately 50 % Fe₂O₃ by volume, the amount of oxygen produced by the formation of Fe₅O₇ can be as high as 8 masses of oxygen in the modern atmosphere. Even if iron-rich part of BIFs contained 25 % of Fe₃O₄ by volume that fully reacted with oxygen (or Fe₂O₃) to form Fe₅O₇, the remaining amount of released oxygen would correspond to two masses of oxygen in the modern atmosphere, a geochemically significant quantity. Extrapolation of available data [320] indicates that oxygen is in a liquid state at geotherm temperatures. Since the oxygen fugacity of the lower mantle is considered to be constrained by equilibrium with metallic iron, an oxygen-rich fluid could locally oxidize surrounding material (particularly Fe²⁺ in ferropericlasite as well as bridgmanite, and metallic iron in a (Fe,Ni)-metal phase [321]). On the other hand, a low oxygen chemical activity at high pressure [319,322,323] could prevent the immediate reaction of oxygen in the lower mantle or even in the transition zone, and instead allow an oxygen-rich fluid to pass to the upper mantle, thus shifting Fe²⁺/Fe³⁺ equilibria in silicate minerals and greatly raising the oxygen fugacity in this region. In any case, our study suggests the presence of an oxygen-rich fluid in the deep Earth's interior that can significantly affect geochemical processes by changing oxidation states and mobilizing trace elements.

5.10.3. Methods

Sample preparation

Single crystals of $^{57}\text{Fe}_2\text{O}_3$ and $^{57}\text{Fe}_3\text{O}_4$ were grown in a 1200-tonne Sumitomo press at Bayerisches Geoinstitut (Bayreuth, Germany). Hematite was synthesized at 7 GPa and 800 °C from an equal mixture of conventional powder of hematite of 99.998 % purity and 96.64 %-enriched pure $^{57}\text{Fe}_2\text{O}_3$, while magnetite synthesis was performed at 9.5 GPa and 1100 °C. Synthesis of non-enriched hematite single crystals was described in [289].

Single crystals with an average size of $0.03 \times 0.03 \times 0.005 \text{ mm}^3$ were pre-selected on a three-circle Bruker diffractometer equipped with a SMART APEX CCD detector and a high-brilliance Rigaku rotating anode (Rotor Flex FR-D, Mo-K α radiation) with Osmic focusing X-ray optics.

Selected crystals together with small ruby chips (for pressure estimation) were loaded in BX90-type DACs [105]. Neon was used as a pressure transmitting medium loaded at Bayerisches Geoinstitut.

X-ray diffraction

The single-crystal XRD experiments were conducted on the ID09A beamline at the European Synchrotron Radiation Facility (ESRF), Grenoble, France (MAR555 detector, $\lambda = 0.4126\text{--}0.4130 \text{ \AA}$); on the 13-IDD beamline at the Advanced Photon Source (APS), Chicago, USA (MAR165 CCD detector, $\lambda = 0.3344 \text{ \AA}$); and on the Extreme Conditions Beamline P02.2 at PETRA III, Hamburg, Germany (Perkin Elmer XRD1621 flat panel detector, $\lambda = 0.2898\text{--}0.2902 \text{ \AA}$). The X-ray spot size depended on the beamline settings and varied from 4 to 30 μm , where typically a smaller beam was used for laser heating experiments. A portable double-sided laser heating [121] system was used for experiments on ID09A to collect *in situ* single-crystal XRD. Pressures were calculated from the positions of the XRD lines of Ne (<http://kantors50webs.com/diffraction.htm>). XRD images were collected during continuous rotation of DACs typically from -40 to $+40^\circ$ on omega; while data collection experiments were performed by narrow $0.5\text{--}1^\circ$ scanning of the same omega range.

Data analysis

Integration of the reflection intensities and absorption corrections were performed using CrysAlisPro software [264]. The structures were solved by the direct method and refined in the isotropic approximation by full matrix least-squares using the SHELXS and SHELXL software [124], respectively.

Synchrotron Mössbauer source spectroscopy

Energy-domain Mössbauer measurements were carried out at the Nuclear Resonance beamline ID18 at ESRF (see [212] for more details).

5.10.4. Acknowledgements

We thank L. Ismailova for the synthesis of $^{57}\text{Fe}_3\text{O}_4$, K. Glazyrin for synthesis of non-enriched Fe_2O_3 and V. Cerantola for synthesis of FeCO_3 and for assistance with HPHT experiments at ESRF and APS. N.D. thanks the Deutsche Forschungsgemeinschaft (DFG) for financial support through the Heisenberg Program and DFG Project DU 954-8/1, and the Federal Ministry of Education and Research (Germany) for the BMBF grant 5K13WC3 (Verbundprojekt O5K2013, Teilprojekt 2, PT-DESY).

5.10.5. Extended data

Building blocks:

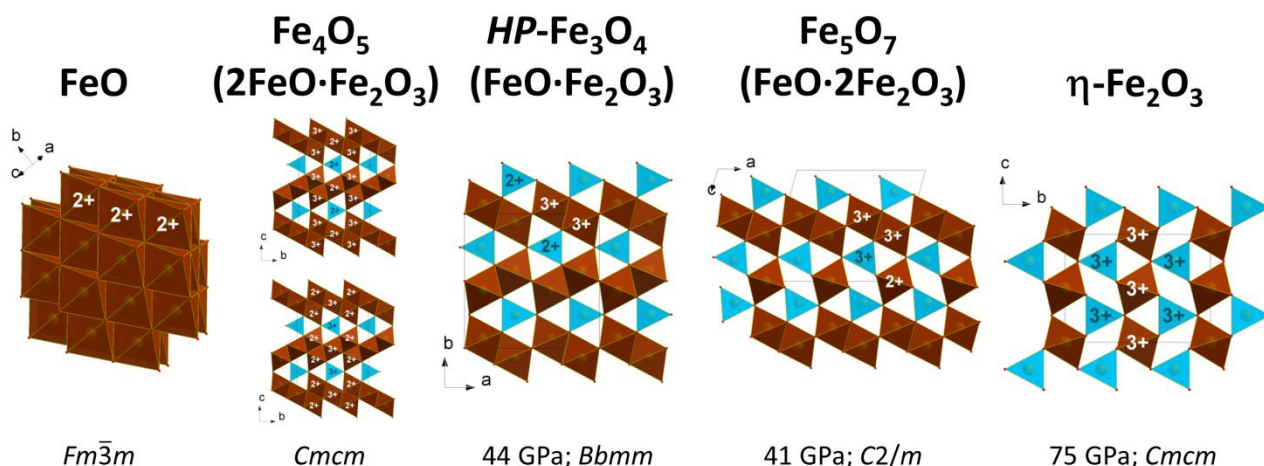
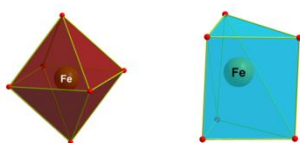


Figure ED 5.10.5-1 Homological series of iron oxides described by the common formula $nFeO \cdot mFe_2O_3$. The structures may be described as constructed from two building blocks, FeO_6 octahedra and trigonal prisms (prisms could be two-capped but they are not shown for simplicity). Prisms connect to each other through triangular faces, while octahedra share only edges. Increasing Fe^{2+} content favors octahedral packing over mixed octahedral and prismatic packing; however no preference of coordination type (octahedral or prismatic) for Fe^{2+} or Fe^{3+} is observed. The PPv $\eta-Fe_2O_3$ and Fe_5O_7 quasi-two-dimensional structures are constructed of parallel columns of triangular face-shared prisms and edge-shared octahedra. Increasing Fe^{2+} content in Fe_5O_7 favors octahedral packing over mixed octahedral and prismatic packing. This requires denser packing of FeO_6 octahedra and as a result columns of octahedra condense in slabs by sharing common edges. In particular, $\eta-Fe_2O_3$ has ordinary columns of prisms and octahedra with a chequerboard-like arrangement, Fe_5O_7 has ordinary and doubled columns of octahedra, and the high-pressure polymorph of Fe_3O_4 ($HP-Fe_3O_4$) possesses only doubled columns. In the sequence from $\eta-Fe_2O_3$ to FeO the packing of octahedra becomes denser, which is reflected in an increase of connectivity between octahedra through common edges. The end-member of the homological series wüstite (FeO) consists of octahedra with a maximum (12) number of edge-shared neighbors. “2+” and “3+” represent the charges of iron ions.

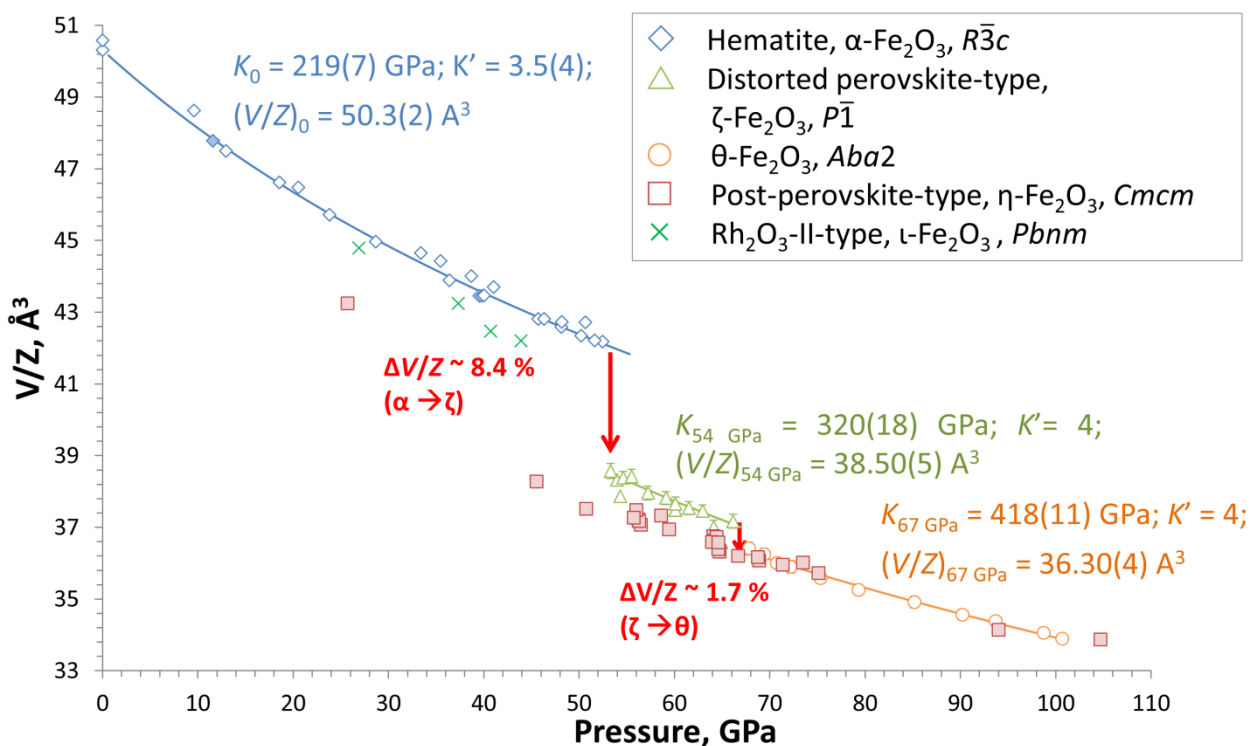


Figure ED 5.10.5-2 P - V plot for Fe₂O₃ summarized from current experimental results, where unit cell volumes are normalized to the amount of structural units Z . Open symbols represent ambient-temperature experiments and solid symbols indicate samples subjected to laser heating. The volume relaxation of η -Fe₂O₃ under decompression shows apparent discontinuities after annealing at ~ 56 GPa and 64 GPa due to possible decomposition (see Figure ED 5.10.5-4 for details). The volume of the high-temperature polymorph ι -Fe₂O₃ is lower than the volume of hematite at the identical pressure conditions.

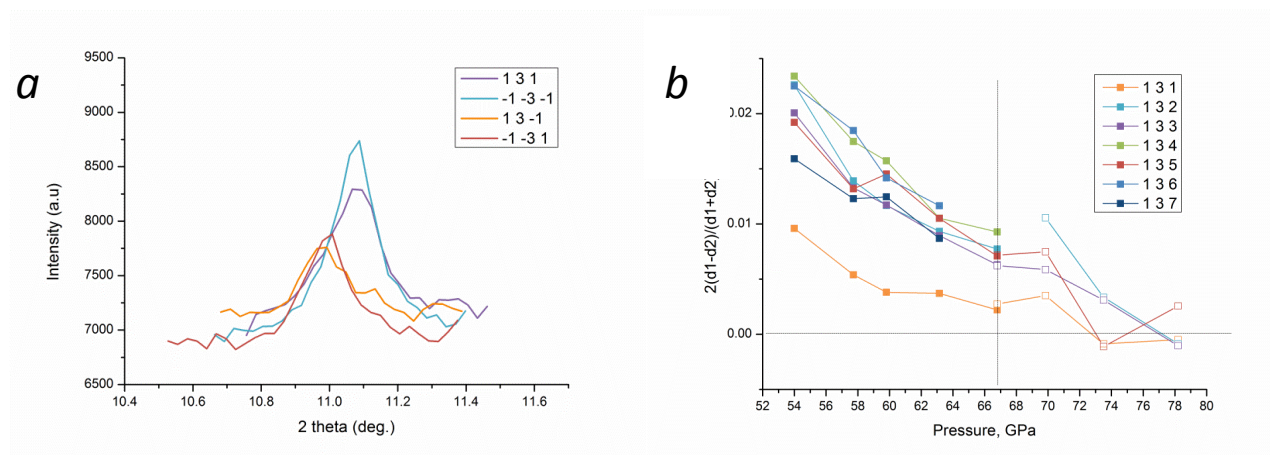


Figure ED 5.10.5-3 Verification of ζ -Fe₂O₃ crystal system (see Supplementary information for details) using one dimensional profiles of reflection 131 and its symmetrical equivalents in the hypothetical orthorhombic space group (a) reconstructed from the wide image recorded at 60.0(7) GPa. While d -spacings for Friedel mates (131 and -1-3-1 / -1-31 and 13-1) show a perfect match, the first pair has smaller d -spacings (corresponding to $2\theta = 10.98^\circ$) than the second one ($2\theta = 11.08^\circ$). The cumulative picture for reflections 13/ l ($l = 1...7$) shows how the difference in d -spacings (normalized to correspondent sums) decreases under compression to half its value before the phase transition to θ -Fe₂O₃ at 67 GPa (vertical dotted line) (b).

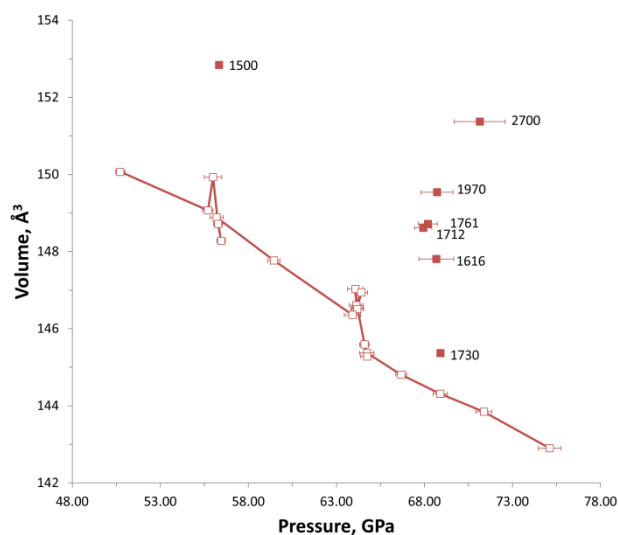


Figure ED 5.10.5-4 Unit cell volume of η -Fe₂O₃ under decompression and laser annealing (the figure reads from right to left). Numbers refer to the heating temperature with an average deviation of 100 K. Heating at ~ 56 GPa and 64 GPa provokes a unit cell volume increase of up to 1 % that is likely associated with the loss of oxygen by η -Fe₂O₃ and partial reduction of Fe³⁺ to Fe²⁺.

Table ED 5.10.5-1 Details of crystals structure refinement of *HP*-Fe₃O₄ and Fe₅O₇.

Crystallographic data	<i>HP</i> -Fe ₃ O ₄	Fe ₅ O ₇
XRD measurement conditions	44.3(5) GPa, after annealing at 2350(100) K	40.7(3) GPa, after annealing at 1800(100) K
Crystal system	Orthorhombic	Monoclinic
Space group	<i>Bbmm</i>	<i>C2/m</i>
<i>a</i> (Å)	9.309(3)	9.208(7)
<i>b</i> (Å)	9.282(2)	2.7327(10)
<i>c</i> (Å)	2.6944(9)	8.270(5)
β (°)	90	105.50(8)
<i>V</i> (Å ³)	232.80(11)	200.5(2)
<i>Z</i>	4	2
<i>F</i> (000)	440	372
Theta range for data collection (°)	3.56 to 11.05	2.77 to 10.78
Completeness to <i>d</i> = 0.8 Å, %	83.7	39.6
Index ranges	-10 < <i>h</i> < 10, -11 < <i>k</i> < 10, -3 < <i>l</i> < 3	-8 < <i>h</i> < 9, -2 < <i>k</i> < 2, -8 < <i>l</i> < 9
Reflections collected	517	106
Independent reflections / <i>R</i> _{int}	123 / 0.0544	72 / 0.0385
Refinement method	Full matrix least squares on <i>F</i> ²	
Data / restraints / parameters	123 / 0 / 17	72 / 0 / 18
Goodness of fit on <i>F</i> ²	1.257	1.053
Final <i>R</i> indices [<i>I</i> > 2σ(<i>I</i>)], <i>R</i> ₁ / <i>wR</i> ₂	0.0686 / 0.1656	0.0642 / 0.1552
<i>R</i> indices (all data), <i>R</i> ₁ / <i>wR</i> ₂	0.0691 / 0.1656	0.0677 / 0.1594
Largest diff. peak / hole (<i>e</i> / Å ³)	2.258 / -1.634	1.139 / -1.009

Table ED 5.10.5-2 Details of crystals structure refinement of high-pressure Fe₂O₃ phases.

Crystallographic data	θ -Fe ₂ O ₃	η -Fe ₂ O ₃	η -Fe ₂ O ₃	ι -Fe ₂ O ₃
P, T conditions of XRD experiment	73.8(7) GPa	63.9(5) GPa, after annealing at 2200(100) K	75.1(7) GPa after annealing at 1850(100) K	40.7(3) GPa, after annealing at 1800(100) K
Crystal system	Orthorhombic	Orthorhombic	Orthorhombic	Orthorhombic
Space group	<i>Aba2</i>	<i>Cmcm</i>	<i>Cmcm</i>	<i>Pbcn</i>
<i>a</i> (Å)	6.524(9)	2.640(6)	2.6393(7)	7.062(10)
<i>b</i> (Å)	4.702(3)	8.639(9)	8.5177(15)	4.8108(13)
<i>c</i> (Å)	4.603(7)	6.414(14)	6.358(2)	5.0019(8)
<i>V</i> (Å³)	141.2(3)	146.3(5)	142.93(7)	169.9(2)
<i>Z</i>	4	4	4	4
<i>F</i>(000)	304	304	304	304
Theta range for data collection (°)	6.95 to 26.72	2.67 to 11.10	3.76 to 10.96	3.08 to 10.82
Completeness to <i>d</i> = 0.8 Å, %	50.7	69.7	62.2	48.0
Index ranges	-7 < <i>h</i> < 4, -5 < <i>k</i> < 5, -4 < <i>l</i> < 5	-2 < <i>h</i> < 2, -9 < <i>k</i> < 9, -6 < <i>l</i> < 5	-2 < <i>h</i> < 2, -9 < <i>k</i> < 9, -5 < <i>l</i> < 5	-2 < <i>h</i> < 4, -5 < <i>k</i> < 5, -5 < <i>l</i> < 5
Reflections collected	54	93	81	206
Independent reflections / <i>R</i>_{int}	45 / 0.0329	53 / 0.0637	46 / 0.0372	61 / 0.1003
Refinement method	Full matrix least squares on <i>F</i> ²			
Data / restraints / parameters	45 / 1 / 12	53 / 0 / 9	46 / 0 / 9	61 / 0 / 16
Goodness of fit on <i>F</i>²	1.235	1.214	1.174	1.247
Final <i>R</i> indices [<i>I</i> > 2σ(<i>I</i>)]	0.0940 / 0.1664	0.0652 / 0.1632	0.0864 / 0.2107	0.0756 / 0.1952
<i>R</i>₁ / <i>wR</i>₂				
<i>R</i> indices (all data)	0.1055 / 0.1732	0.0909 / 0.1804	0.0913 / 0.2139	0.0848 / 0.1996
<i>R</i>₁ / <i>wR</i>₂				
Largest diff. peak / hole (<i>e</i> / Å³)	1.419 / -1.794	1.865 / -1.412	1.743 / -2.443	1.291 / -1.098

Table ED 5.10.5-3 Glossary of Fe₂O₃ phases.

Name	Structural type	Unit cell parameters	Conditions	Reference or No in ICSD*
α-Fe₂O₃ hematite	Corundum	<i>R</i> -3 <i>c</i> , <i>a</i> = 5.0354(17), <i>c</i> = 13.7477(48) Å	Ambient	Current work
β-Fe₂O₃	Bixbyite	<i>Ia</i> 3, <i>a</i> = 9.393(2) Å	Ambient	108905
γ-Fe₂O₃ maghemite	Inverse spinel structure with ~17 % of iron vacancies in octahedral positions	Possible space groups (<i>Fd</i> -3 <i>m</i> , <i>P</i> ₄ ₃ 32, <i>P</i> ₄ ₁ 2 ₁ 2) depend on ordering of vacancies	Ambient	87121
δ-FeO_{(3-x)/2}(OH)_x, <i>x</i> = 0...3 (former δ-Fe₂O₃)	Hexagonal close-packed oxygen-hydroxyl lattice with ~80% of Fe ³⁺ occupying octahedral sites and the remainder in tetrahedral sites	<i>Cubic</i> , <i>a</i> = 8.386 Å	Ambient	[324]
ε-Fe₂O₃	AlFeO ₃	<i>Pna</i> 2 ₁ , <i>a</i> = 5.1019(3), <i>b</i> = 8.7807(6), <i>c</i> = 9.4661(5) Å	Ambient	161785
ζ-Fe₂O₃	distorted perovskite GdFeO ₃	<i>P</i> -1, <i>a</i> = 4.576(7), <i>b</i> = 4.948(2), <i>c</i> = 6.81(2) Å α = 90.39(9), β = 89.8(3), γ = 90.03(7) °	53.4(5) GPa, 300 K	Current study
η-Fe₂O₃	CaIrO ₃ (post-perovskite)	<i>Cmcm</i> , <i>a</i> = 2.6393(7), <i>b</i> = 8.5177(15), <i>c</i> = 6.358(2) Å	75.1(7) GPa, after laser annealing at	[103], Current study

V. Results

Name	Structural type	Unit cell parameters	Conditions	Reference or No in ICSD*
			1850(100) K	
θ -Fe ₂ O ₃	Crystal structure can be deduced from Rh ₂ O ₃ -II-type if octahedral coordination of Fe atoms is switched to trigonal-prismatic coordination	<i>Aba2</i> , $a = 6.524(9)$, $b = 4.702(3)$, $c = 4.603(7)$ Å	73.8(7) GPa, 300 K	Current study
ι -Fe ₂ O ₃	Rh ₂ O ₃ -II-type	<i>Pbcn</i> , $a = 7.062(10)$, $b = 4.8108(13)$, $c = 5.0019(8)$ Å	40.7(3) GPa, after laser annealing at 1800(100) K	[102], Current study

* ICSD – Inorganic Crystal Structure Database, Fachinformationszentrum Karlsruhe, 76344 Eggenstein-Leopoldshafen, Germany (fax: (+49)7247-808-666; e-mail: crysdata@fiz-karlsruhe.de)

5.10.6. Supplementary text

Verification of ζ -Fe₂O₃ crystal system

Following our previous study [103] we verified the symmetry of the unit cell by inspecting d -spacings of those reflections that should have been equivalent in orthorhombic symmetry but differed in lower symmetries. It should be noted that previous powder diffraction studies were not able to resolve such differences due to the strong broadening of closely overlapping reflections. In single crystal XRD the overlapping problem is solved since the reflections are located at different places on the frames and their d -spacings could be measured separately.

The absence of orthorhombic symmetry can be clearly demonstrated by considering sets of candidate reflections $13l$ ($l = 1, 2, \dots, 7$) with the following equivalents: $13l$, $-1-3l$, $13-l$ and $-1-3-l$. Figure ED 5.10.5-3a shows that the $-1-31$ and $13-1$ reflections have larger d -spacings than the 131 and $-1-3-1$ ones. There is a perfect match in d -spacings between Friedel mates (131 and $-1-3-1$ / $-1-31$ and $13-1$) indicating negligible effects of strain created by the DAC.

A verification of the monoclinic unit cell using a similar approach was hindered due to the lack in of equivalent reflections for the particular symmetry defined by the specific orientation of the crystal in the DAC. Therefore we refined the unit cell based on the available reflections without symmetry constraints, i.e., a triclinic cell. As a result the alpha and beta angles show systematic scatter from 90° of about 0.4° while gamma varies by much less, $\sim 0.1^\circ$. The overall scatter, representing the distortion from the orthorhombic perovskite type is demonstrated on Figure ED 5.10.5-1b, where it is expressed as the difference between d -spacings of the close reflections normalized to their sum.

Magnetic and electronic transformations in Fe₂O₃

The bulk modulus of hematite, 219(7) GPa, is in a good agreement with previous studies [289] and at 67 GPa it reaches $\sim 392(10)$ GPa, whereas the bulk modulus of ζ -Fe₂O₃ at 54 GPa is remarkably low, 320(18) GPa. Such a significant (of about 18 %) drop of bulk modulus, associated with the large reduction of molar volume (~ 8.4 %), is very unusual and is likely caused by changes in the electronic state of Fe³⁺. The Mössbauer spectrum of ζ -Fe₂O₃ collected

immediately after the transition at ~50 GPa shows (Figure 5.10.2-3b) two components – a magnetic sextet having centre shift (CS 0.424(7) mm/s) corresponding to the high-spin (HS) state of Fe^{3+} , and a doublet (CS 0.074(5) mm/s) with hyperfine parameters characteristic for low-spin- Fe^{3+} (LS) in an octahedral oxygen environment [305]. The relative abundance of the components is ~1 : 1, as expected for the perovskite-type structure of $\zeta\text{-Fe}_2\text{O}_3$ with HS- Fe^{3+} located in large bipolar prisms and LS- Fe^{3+} in smaller octahedra (Figure 5.10.2-1c). Upon further compression of $\zeta\text{-Fe}_2\text{O}_3$ the amount of HS- Fe^{3+} decreases (Figure 5.10.2-3c), which explains the anomalously high compressibility of this phase.

Transformation to $\theta\text{-Fe}_2\text{O}_3$ is associated with a small decrease of molar volume (1.7 %) and with an anticipated increase of bulk modulus (418(11) GPa of $\theta\text{-Fe}_2\text{O}_3$ at 67 GPa versus 371(20) GPa of $\zeta\text{-Fe}_2\text{O}_3$ at 70 GPa) (Figure ED 5.10.5-2). The Mössbauer spectrum of $\theta\text{-Fe}_2\text{O}_3$ (Figure 5.10.2-3d) shows that all Fe^{3+} is in the LS state and there is only one type of iron atom in the crystal structure in accordance with the single crystal XRD data (Figure 5.10.2-1e).

Heating of $\theta\text{-Fe}_2\text{O}_3$ above 1600 K at pressures above 70 GPa resulted in partial or complete transformation into CaIrO_3 -PPv-type $\eta\text{-Fe}_2\text{O}_3$ (Figure 5.10.2-2). The Mössbauer spectrum of pure $\eta\text{-Fe}_2\text{O}_3$ at 91(2) GPa (Figure 5.10.2-3e) contains two components (a magnetically ordered sextet and a paramagnetic doublet) with equal abundances and almost equal center shifts (~0.45 mm/s) corresponding to HS- Fe^{3+} . Within the accuracy of our XRD data the molar volumes of $\theta\text{-Fe}_2\text{O}_3$ and as-synthesized $\eta\text{-Fe}_2\text{O}_3$ are not distinguishable (Figure ED 5.10.5-2), suggesting that the atomic packing density increase in the CaIrO_3 -PPv-type $\eta\text{-Fe}_2\text{O}_3$ structure compensates the difference in ionic radii of HS and LS Fe^{3+} ions in the $\zeta\text{-Fe}_2\text{O}_3$ structure. Note that Shim *et al.* [100] also reported magnetic ordering in $\eta\text{-Fe}_2\text{O}_3$ based on nuclear forward scattering (NFS) measurements. One of the magnetic sites described by the authors [100] has hyperfine parameters close to those that we observed; however the second non-magnetic component in the NFS spectra was not identified in [100].

VI. Bibliography

1. Dubrovinsky, L., Dubrovinskaia, N., Prakapenka, V. B. & Abakumov, A. M. Implementation of micro-ball nanodiamond anvils for high-pressure studies above 6 Mbar. *Nat. Commun.* **3**, 1163 (2012).
2. Tange, Y., Irifune, T. & Funakoshi, K. Pressure generation to 80 GPa using multianvil apparatus with sintered diamond anvils. *High Pressure Res.* **28**, 245–254 (2008).
3. McMillan, P. F. New materials from high-pressure experiments. *Nat. Mater.* **1**, 19–25 (2002).
4. Vepřek, S. Nanostructured superhard materials. In *Handbook of ceramic hard materials* (ed. Riedel, R.) 104–139 (Wiley-VCH Verlag GmbH, 2000).
5. Kurakevych, O. O. & Solozhenko, V. L. Experimental study and critical review of structural, thermodynamic and mechanical properties of superhard refractory boron suboxide B₆O. *J. Superhard Mater.* **33**, 421–428 (2011).
6. Rizzo, H. F., Simmons, W. C. & Bielstein, H. O. The existence and formation of the solid B₆O. *J. Electrochem. Soc.* **109**, 1079–1082 (1962).
7. He, D., Zhao, Y., Daemen, L., Qian, J., Shen, T. D. & Zerda, T. W. Boron suboxide: As hard as cubic boron nitride. *Appl. Phys. Lett.* **81**, 643 (2002).
8. Domnich, V., Reynaud, S., Haber, R. A. & Chhowalla, M. Boron carbide: structure, properties, and stability under stress. *J. Am. Ceram. Soc.* **94**, 3605–3628 (2011).
9. Mohammadi, R., Lech, A. T., Xie, M., Weaver, B. E., Yeung, M. T., Tolbert, S. H. & Kaner, R. B. Tungsten tetraboride, an inexpensive superhard material. *Proc. Natl. Acad. Sci. USA* **108**, 10958–10962 (2011).
10. Cumberland, R. W., Weinberger, M. B., Gilman, J. J., Clark, S. M., Tolbert, S. H. & Kaner, R. B. Osmium diboride, an ultra-incompressible, hard material. *ChemInform* **36**, 7264–7265 (2005).
11. Liu, C., Peng, F., Tan, N., Liu, J., Li, F., Qin, J., Wang, J., Wang, Q. & He, D. Low-compressibility of tungsten tetraboride: a high pressure X-ray diffraction study. *High Pressure Res.* **31**, 275–282 (2011).
12. Nagamatsu, J., Nakagawa, N., Muranaka, T., Zenitani, Y. & Akimitsu, J. Superconductivity at 39 K in magnesium diboride. *Nature* **410**, 63–64 (2001).
13. Okamoto, H. B-Fe (Boron-Iron). *J. Phase Equilibria Diffus.* **25**, 297–298 (2004).

14. Kapfenberger, C., Albert, B., Pöttgen, R. & Huppertz, H. Structure refinements of iron borides Fe₂B and FeB. *Z. Kristallogr.* **221**, 477–481 (2006).
15. Voroshnin, L. G., Lyakhovich, L. S., Panich, G. G. & Protasevich, G. F. The structure of Fe-B alloys. *Met. Sci. Heat Treat.* **12**, 732–735 (1970).
16. Callmer, B. & Lundström, T. A single-crystal diffractometry investigation of iron in β -rhombohedral boron. *J. Solid State Chem.* **17**, 165–170 (1976).
17. Yao, B., Su, W. H., Li, F. S., Ding, B. Z. & Hu, Z. Q. Phase transition from Fe₃B to Fe₂B under high pressure. *J. Mater. Sci. Lett.* **16**, 1991–1993 (1997).
18. Kolmogorov, A. N., Shah, S., Margine, E. R., Bialon, a. F., Hammerschmidt, T. & Drautz, R. New superconducting and semiconducting Fe-B compounds predicted with an ab initio evolutionary search. *Phys. Rev. Lett.* **105**, 217003 (2010).
19. Mazin, I. I. Superconductivity gets an iron boost. *Nature* **464**, 183–186 (2010).
20. Mazin, I. I., Papaconstantopoulos, D. A. & Mehl, M. J. Superconductivity in compressed iron: Role of spin fluctuations. *Phys. Rev. B* **65**, 100511 (2002).
21. Bialon, A. F., Hammerschmidt, T., Drautz, R., Shah, S., Margine, R. & Kolmogorov, A. N. Possible routes for synthesis of new boron-rich Fe-B and Fe_{1-x}Cr_xB₄ compounds. *Appl. Phys. Lett.* **98**, 81901 (2011).
22. Cadeville, M. C. & Meyer, A. J. P. Points de Curie et moments des borures ferromagnetiques du groupe du fer de type M₂B, MB, (M₁, M₂)₂B et (M₁, M₂)B. *Cr. Hebd. Acad. Sci.* **255**, 3390–3391 (1962).
23. Sun, W., Du, Y., Liu, S., Huang, B. & Jiang, C. Thermodynamic assessment of the Mn-B system. *J. Phase Equilibria Diffus.* **31**, 357–364 (2010).
24. Andersson, S., Jacobsen, G. G., Seip, H. M., Lindblad, C.-G., Lindberg, A. A., Jansen, G., Lamm, B. & Samuelsson, B. A Note on the Crystal Structure of MnB₄. *Acta Chem. Scand.* **23**, 687–688 (1969).
25. Andersson, S. & Carlsson, J.-O. The Crystal Structure of MnB₄. *Acta Chem. Scand.* **24**, 1791–1799 (1970).
26. Parakhonskiy, G., Dubrovinskaia, N., Bykova, E., Wirth, R. & Dubrovinsky, L. Experimental pressure-temperature phase diagram of boron: resolving the long-standing enigma. *Sci. Rep.* **1**, 96 (2011).

27. Albert, B. & Hillebrecht, H. Boron: elementary challenge for experimenters and theoreticians. *Angew. Chem. Int. Ed. Engl.* **48**, 8640–68 (2009).
28. Slack, G. A., Hejna, C. I., Garbaskas, M. & Kasper, J. S. X-ray Study of Transition-metal Dopants In β -boron. *J. Solid State Chem.* **76**, 64–86 (1988).
29. Hebbache, M. & Živković, D. Investigation of Hard Boron Rich Solids: Osmium Diboride and β -Rhombohedral Boron. In *Boron Rich Solids* (eds. Orlovskaya, N. & Lugovy, M.) 115–130 (Springer Netherlands, 2011).
30. Werheit, H., Schmechel, R., Kueffel, V. & Lundstrom, T. On the electronic properties of β -rhombohedral boron interstitially doped with 3d transition metal atoms. *J. Alloys Compd.* **262**, 372–380 (1997).
31. Duschaneck, H. & Rogl, P. The Al-B (aluminum-boron) system. *J. Phase Equilibria* **15**, 543–552 (1994).
32. Taylor, L. A. & Anand, M. Diamonds: time capsules from the Siberian Mantle. *Chem. Erde-Geochem.* **64**, 1–74 (2004).
33. Sobolev, N. V. *Deep-seated inclusions in kimberlites and the problem of the composition of the upper mantle*. 279 p. (American Geophysical Union, 1977).
34. Meyer, H. O. A. Inclusions in diamond. In *Mantle Xenoliths* (ed. Nixon, P. H.) 501–523 (Wiley, 1987).
35. Malinovskii, I. Y., Doroshev, A. M. & Ran, E. N. The stability of chromium-bearing garnets pyrope–knorringite series. In *Experimental studies on the mineralogy (1974-1976)* 110–115 (Institute of Geology and Geophysics of the Siberian Branch of AS USSR, 1975).
36. Ringwood, A. E. Synthesis of pyrope-knorringite solid solution series. *Earth Planet. Sci. Lett.* **36**, 443–448 (1977).
37. Irifune, T., Ohtani, E. & Kumazawa, M. Stability field of knorringite $\text{Mg}_3\text{Cr}_2\text{Si}_3\text{O}_{12}$ at high pressure and its implication to the occurrence of Cr-rich pyrope in the upper mantle. *Phys. Earth Planet. Inter.* **27**, 263–272 (1982).
38. Klemme, S. The influence of Cr on the garnet-spinel transition in the Earth's mantle: experiments in the system $\text{MgO-Cr}_2\text{O}_3\text{-SiO}_2$ and thermodynamic modelling. *Lithos* **77**, 639–646 (2004).
39. Taran, M. N., Langer, K., Abs-Wurmbach, I., Frost, D. J. & Platonov, A. N. Local relaxation around $[\text{6}]\text{Cr}^{3+}$ in synthetic pyrope-knorringite garnets, $[\text{8}]\text{Mg}_3[\text{6}](\text{Al}_{1-x}\text{Cr}_x^{3+})_2[\text{4}]\text{Si}_3\text{O}_{12}$, from electronic absorption spectra. *Phys. Chem. Miner.* **31**, 650–657 (2004).

40. Zou, Y. & Irifune, T. Phase relations in $\text{Mg}_3\text{Cr}_2\text{Si}_3\text{O}_{12}$ and formation of majoritic knorringite garnet at high pressure and high temperature. *J. Mineral. Petrol. Sci.* **107**, 197–205 (2012).
41. Turkin, A. I., Doroshev, A. M. & Malinovskii, I. Y. A study of the phase composition of garnet-bearing assemblages in the system $\text{MgO}-\text{Al}_2\text{O}_3-\text{Cr}_2\text{O}_3-\text{SiO}_2$ at high temperatures and pressures. In *Silicate systems at high pressures* 5–24 (Institute of Geology and Geophysics, 1983).
42. Juhin, A., Morin, G., Elkaim, E., Frost, D. J., Fialin, M., Juillot, F. & Calas, G. Structure refinement of a synthetic knorringite, $\text{Mg}_3(\text{Cr}_{0.8}\text{Mg}_{0.1}\text{Si}_{0.1})_2(\text{SiO}_4)_3$. *Am. Mineral.* **95**, 59–63 (2009).
43. Xu, Y. The effect of alumina on the electrical conductivity of silicate perovskite. *Science* **282**, 922–924 (1998).
44. Andrault, D., Bolfan-Casanova, N. & Guignot, N. Equation of state of lower mantle (Al,Fe)- MgSiO_3 perovskite. *Earth Planet. Sci. Lett.* **193**, 501–508 (2001).
45. Andrault, D., Bolfan-Casanova, N., Bouhifd, M. A., Guignot, N. & Kawamoto, T. The role of Al-defects on the equation of state of Al-(Mg,Fe) SiO_3 perovskite. *Earth Planet. Sci. Lett.* **263**, 167–179 (2007).
46. Walter, M. J., Kubo, A., Yoshino, T., Brodholt, J., Koga, K. T. & Ohishi, Y. Phase relations and equation-of-state of aluminous Mg-silicate perovskite and implications for Earth's lower mantle. *Earth Planet. Sci. Lett.* **222**, 501–516 (2004).
47. Holzapfel, C., Rubie, D. C., Frost, D. J. & Langenhorst, F. Fe-Mg interdiffusion in (Mg,Fe) SiO_3 perovskite and lower mantle reequilibration. *Science* **309**, 1707–1710 (2005).
48. Ohta, K., Onoda, S., Hirose, K., Sinmyo, R., Shimizu, K., Sata, N., Ohishi, Y. & Yasuhara, A. The electrical conductivity of post-perovskite in Earth's D'' layer. *Science* **320**, 89–91 (2008).
49. Saikia, A., Ballaran, T. B. & Frost, D. J. The effect of Fe and Al substitution on the compressibility of MgSiO_3 -perovskite determined through single-crystal X-ray diffraction. *Phys. Earth Planet. Inter.* **173**, 153–161 (2009).
50. Catalli, K., Shim, S.-H., Prakapenka, V. B., Zhao, J., Sturhahn, W., Chow, P., Xiao, Y., Liu, H., Cynn, H. & Evans, W. J. Spin state of ferric iron in MgSiO_3 perovskite and its effect on elastic properties. *Earth Planet. Sci. Lett.* **289**, 68–75 (2010).

51. Catalli, K., Shim, S.-H., Dera, P., Prakapenka, V. B., Zhao, J., Sturhahn, W., Chow, P., Xiao, Y., Cynn, H. & Evans, W. J. Effects of the Fe^{3+} spin transition on the properties of aluminous perovskite—New insights for lower-mantle seismic heterogeneities. *Earth Planet. Sci. Lett.* **310**, 293–302 (2011).
52. Hsu, H., Blaha, P., Cococcioni, M. & Wentzcovitch, R. M. Spin-state crossover and hyperfine interactions of ferric iron in MgSiO_3 perovskite. *Phys. Rev. Lett.* **106**, 118501 (2011).
53. Martin, C. D. & Parise, J. B. Structure constraints and instability leading to the post-perovskite phase transition of MgSiO_3 . *Earth Planet. Sci. Lett.* **265**, 630–640 (2008).
54. Tateno, S., Hirose, K., Sata, N. & Ohishi, Y. Structural distortion of CaSnO_3 perovskite under pressure and the quenchable post-perovskite phase as a low-pressure analogue to MgSiO_3 . *Phys. Earth Planet. Inter.* **181**, 54–59 (2010).
55. Nishio-Hamane, D., Seto, Y., Fujino, K. & Nagai, T. Effect of FeAlO_3 incorporation into MgSiO_3 on the bulk modulus of perovskite. *Phys. Earth Planet. Inter.* **166**, 219–225 (2008).
56. Kudoh, Y., Prewitt, C. T., Finger, L. W., Darovskikh, A. & Ito, E. Effect of iron on the crystal structure of $(\text{Mg,Fe})\text{SiO}_3$ perovskite. *Geophys. Res. Lett.* **17**, 1481–1484 (1990).
57. McCammon, C. A., Rubie, D. C., Ross, C. R., Seifert, F. & O'Neill, H. S. C. Mossbauer-spectra of $^{57}\text{Fe}_{0.05}\text{Mg}_{0.95}\text{SiO}_3$ Perovskite at 80 K and 298 K. *Am. Mineral.* **77**, 894–897 (1992).
58. Fei, Y., Virgo, D., Mysen, B. O., Wang, Y. & Mao, H. K. Temperature-dependent Electron Delocalization In $(\text{Mg,Fe})\text{SiO}_3$ Perovskite. *Am. Mineral.* **79**, 826–837 (1994).
59. McCammon, C. A. The crystal chemistry of ferric iron in $\text{Fe}_{0.05}\text{Mg}_{0.95}\text{SiO}_3$ perovskite as determined by Mossbauer spectroscopy in the temperature range 80–293 K. *Phys. Chem. Miner.* **25**, 292–300 (1998).
60. Vanpeteghem, C. B., Angel, R. J., Ross, N. L., Jacobsen, S. D., Dobson, D. P., Litasov, K. D. & Ohtani, E. Al, Fe substitution in the MgSiO_3 perovskite structure: A single-crystal X-ray diffraction study. *Phys. Earth Planet. Inter.* **155**, 96–103 (2006).
61. Hummer, D. R. & Fei, Y. Synthesis and crystal chemistry of Fe^{3+} -bearing $(\text{Mg,Fe}^{3+})(\text{Si,Fe}^{3+})\text{O}_3$ perovskite. *Am. Mineral.* **97**, 1915–1921 (2012).
62. Jephcoat, A. P., Hriljac, J. A., McCammon, C. A., O'Neill, H. S. C., Rubie, D. C. & Finger, L. W. High-resolution synchrotron X-ray powder diffraction and Rietveld structure refinement of two $(\text{Mg}_{0.95}\text{Fe}_{0.05})\text{SiO}_3$ perovskite samples synthesized under different oxygen fugacity conditions. *Am. Mineral.* **84**, 214–220 (1999).

63. Horiuchi, H., Ito, E. & Weidner, D. J. Perovskite-type MgSiO_3 - single-crystal X-ray-diffraction study. *Am. Mineral.* **72**, 357–360 (1987).
64. Dobson, D. P. & Jacobsen, S. D. The flux growth of magnesium silicate perovskite single crystals. *Am. Mineral.* **89**, 807–811 (2004).
65. Arunan, E., Desiraju, G. R., Klein, R. A., Sadlej, J., Scheiner, S., Alkorta, I., Clary, D. C., Crabtree, R. H., Dannenberg, J. J., Hobza, P., Kjaergaard, H. G., Legon, A. C., Mennucci, B. & Nesbitt, D. J. Definition of the hydrogen bond (IUPAC Recommendations 2011). *Pure Appl. Chem.* **83**, 1637–1641 (2011).
66. Holzapfel, W. B. On the symmetry of the hydrogen bonds in ice VII. *J. Chem. Phys.* **56**, 712–716 (1972).
67. Benoit, M., Marx, D. & Parrinello, M. Tunnelling and zero-point motion in high-pressure ice. *Nature* **392**, 258–261 (1998).
68. Lin, L., Morrone, J. a. & Car, R. Correlated Tunneling in Hydrogen Bonds. *J. Stat. Phys.* **145**, 365–384 (2011).
69. Gilli, G. & Gilli, P. *The nature of the hydrogen bond*. 304 p. (Oxford University Press, 2009).
70. Yang, H., Lu, R., Downs, R. T. & Costin, G. Goethite, $\alpha\text{-FeO(OH)}$, from single-crystal data. *Acta Crystallogr. E* **62**, i250–i252 (2006).
71. Aoki, K., Katoh, E., Yamawaki, H., Sakashita, M. & Fujihisa, H. Hydrogen-bond symmetrization and molecular dissociation in hydrogen halides. *Phys. B* **265**, 83–86 (1999).
72. Sano-Furukawa, A., Komatsu, K., Vanpeteghem, C. B. & Ohtani, E. Neutron diffraction study of $\delta\text{-AlOOH}$ at high pressure and its implication for symmetrization of the hydrogen bond. *Am. Mineral.* **93**, 1558–1567 (2008).
73. Sano-Furukawa, A., Kagi, H., Nagai, T., Nakano, S., Fukura, S., Ushijima, D., Iizuka, R., Ohtani, E. & Yagi, T. Change in compressibility of $\delta\text{-AlOOH}$ and $\delta\text{-AlOOD}$ at high pressure: A study of isotope effect and hydrogen-bond symmetrization. *Am. Mineral.* **94**, 1255–1261 (2009).
74. Hushur, A., Manghnani, M. H., Smyth, J. R., Williams, Q., Hellebrand, E., Lonappan, D., Ye, Y., Dera, P. & Frost, D. J. Hydrogen bond symmetrization and equation of state of phase D. *J. Geophys. Res.* **116**, B06203 (2011).

75. Matsui, M., Komatsu, K., Ikeda, E., Sano-Furukawa, A., Gotou, H. & Yagi, T. The crystal structure of δ -Al(OH)₃: Neutron diffraction measurements and ab initio calculations. *Am. Mineral.* **96**, 854–859 (2011).
76. Goncharov, A. F., Manaa, M. R., Zaug, J. M., Gee, R. H., Fried, L. E. & Montgomery, W. B. Polymerization of formic acid under high pressure. *Phys. Rev. Lett.* **94**, 65505 (2005).
77. Pruzan, P. Pressure effects on the hydrogen bond in ice up to 80 GPa. *J. Mol. Struct.* **322**, 279–286 (1994).
78. Goncharov, A. F., Struzhkin, V. V, Somayazulu, M. S., Hemley, R. J. & Mao, H. K. Compression of ice to 210 gigapascals: Infrared evidence for a symmetric hydrogen-bonded phase. *Science* **273**, 218–220 (1996).
79. Aoki, K., Yamawaki, H., Sakashita, M. & Fujihisa, H. Infrared absorption study of the hydrogen-bond symmetrization in ice to 110 GPa. *Phys. Rev. B* **54**, 15673–15677 (1996).
80. Loubeyre, P., LeToullec, R., Wolanin, E., Hanfland, M., Hausermann, D. & Husermann, D. Modulated phases and proton centring in ice observed by X-ray diffraction up to 170 GPa. *Nature* **397**, 503–506 (1999).
81. Nagai, T., Kagi, H. & Yamanaka, T. Variation of hydrogen bonded O center dot center dot center dot O distances in goethite at high pressure. *Am. Mineral.* **88**, 1423–1427 (2003).
82. Gleason, A. E. E., Jeanloz, R. & Kunz, M. Pressure-temperature stability studies of FeOOH using X-ray diffraction. *Am. Mineral.* **93**, 1882–1885 (2008).
83. Tunega, D. Theoretical study of properties of goethite (alpha-FeOOH) at ambient and high-pressure conditions. *J. Phys. Chem. C* **116**, 6703–6713 (2012).
84. Castro, L. O. Genesis of banded iron-formations. *Econ. Geol.* **89**, 1384–1397 (1994).
85. Dobson, D. P. & Brodholt, J. P. Subducted banded iron formations as a source of ultralow-velocity zones at the core-mantle boundary. *Nature* **434**, 371–374 (2005).
86. Polat, A., Hofmann, A. W. & Rosing, M. T. Boninite-like volcanic rocks in the 3.7–3.8 Ga Isua greenstone belt, West Greenland: geochemical evidence for intra-oceanic subduction zone processes in the early Earth. *Chem. Geol.* **184**, 231–254 (2002).
87. Ozawa, H., Hirose, K., Tateno, S., Sata, N. & Ohishi, Y. Phase transition boundary between B1 and B8 structures of FeO up to 210 GPa. *Phys. Earth Planet. Inter.* **179**, 157–163 (2010).

88. Ono, S. & Ohishi, Y. In situ X-ray observation of phase transformation in Fe_2O_3 at high pressures and high temperatures. *J. Phys. Chem. Solids* **66**, 1714–1720 (2005).
89. Dubrovinsky, L. S., Dubrovinskaia, N. A., McCammon, C., Rozenberg, G. K., Ahuja, R., Osorio-Guillen, J. M., Dmitriev, V., Weber, H.-P., Bihan, T. Le & Johansson, B. The structure of the metallic high-pressure Fe_3O_4 polymorph: experimental and theoretical study. *J. Phys. Condens. Matter* **15**, 7697–7706 (2003).
90. Pasternak, M., Nasu, S., Wada, K. & Endo, S. High-pressure phase of magnetite. *Phys. Rev. B* **50**, 6446–6449 (1994).
91. Mao, H.-K., Takahashi, T., Bassett, W. A., Kinsland, G. L. & Merrill, L. Isothermal compression of magnetite to 320 kbar and pressure-induced phase transformation. *J. Geophys. Res.* **79**, 1165–1170 (1974).
92. Fei, Y., Frost, D. J., Mao, H.-K., Prewitt, C. T. & Haeusermann, D. In situ structure determination of the high-pressure phase of Fe_3O_4 . *Am. Mineral.* **84**, 203–206 (1999).
93. Haavik, C., Stølen, S. & Fjellvåg, H. Equation of state of magnetite and its high-pressure modification: Thermodynamics of the Fe-O system at high pressure. *Am. Mineral.* **85**, 514–523 (2000).
94. Olsen, J. S., Cousins, C. S. G., Gerward, L., Jhans, H. & Sheldon, B. J. A study of the crystal structure of Fe_2O_3 in the pressure range up to 65 GPa using synchrotron radiation. *Phys. Scr.* **43**, 327–330 (1991).
95. Pasternak, M., Rozenberg, G., Machavariani, G., Naaman, O., Taylor, R. & Jeanloz, R. Breakdown of the Mott-Hubbard state in Fe_2O_3 : A first-order insulator-metal transition with collapse of magnetism at 50 GPa. *Phys. Rev. Lett.* **82**, 4663–4666 (1999).
96. Badro, J., Fiquet, G., Struzhkin, V., Somayazulu, M., Mao, H., Shen, G. & Le Bihan, T. Nature of the high-pressure transition in Fe_2O_3 hematite. *Phys. Rev. Lett.* **89**, 205504 (2002).
97. Rozenberg, G., Dubrovinsky, L., Pasternak, M., Naaman, O., Le Bihan, T. & Ahuja, R. High-pressure structural studies of hematite Fe_2O_3 . *Phys. Rev. B* **65**, 064112 (2002).
98. Liu, H., Caldwell, W. A., Benedetti, L. R., Panero, W. & Jeanloz, R. Static compression of $\alpha\text{-Fe}_2\text{O}_3$: linear incompressibility of lattice parameters and high-pressure transformations. *Phys. Chem. Miner.* **30**, 582–588 (2003).
99. Ono, S., Kikegawa, T. & Ohishi, Y. High-pressure phase transition of hematite, Fe_2O_3 . *J. Phys. Chem. Solids* **65**, 1527–1530 (2004).

100. Shim, S.-H., Bengtson, A., Morgan, D., Sturhahn, W., Catalli, K., Zhao, J., Lerche, M. & Prakapenka, V. Electronic and magnetic structures of the postperovskite-type Fe_2O_3 and implications for planetary magnetic records and deep interiors. *Proc. Natl. Acad. Sci. USA* **106**, 5508–12 (2009).
101. Ito, E., Fukui, H., Katsura, T., Yamazaki, D., Yoshino, T., Aizawa, Y., Kubo, A., Yokoshi, S., Kawabe, K., Zhai, S., Shatzkiy, A., Okube, M., Nozawa, A. & Funakoshi, K.-I. Determination of high-pressure phase equilibria of Fe_2O_3 using the Kawai-type apparatus equipped with sintered diamond anvils. *Am. Mineral.* **94**, 205–209 (2009).
102. Dubrovinsky, L., Boffa-Ballaran, T., Glazyrin, K., Kurnosov, A., Frost, D., Merlini, M., Hanfland, M., Prakapenka, V. B., Schouwink, P., Pippinger, T. & Dubrovinskaia, N. Single-crystal X-ray diffraction at megabar pressures and temperatures of thousands of degrees. *High Pressure Res.* **30**, 620–633 (2010).
103. Bykova, E., Bykov, M., Prakapenka, V., Konôpková, Z., Liermann, H.-P., Dubrovinskaia, N. & Dubrovinsky, L. Novel high pressure monoclinic Fe_2O_3 polymorph revealed by single-crystal synchrotron X-ray diffraction studies. *High Pressure Res.* **33**, 534–545 (2013).
104. Merrill, L. & Bassett, W. A. Miniature diamond anvil pressure cell for single crystal x-ray diffraction studies. *Rev. Sci. Instrum.* **45**, 290 (1974).
105. Kantor, I., Prakapenka, V., Kantor, A., Dera, P., Kurnosov, A., Sinogeikin, S., Dubrovinskaia, N. & Dubrovinsky, L. BX90: a new diamond anvil cell design for X-ray diffraction and optical measurements. *Rev. Sci. Instrum.* **83**, 125102 (2012).
106. Mao, H. K. & Bell, P. M. Design and varieties of the megabar cell. *Carnegie I. Wash.* **77**, 904–908 (1978).
107. Letoullec, R., Pinceaux, J. P. & Loubeyre, P. The membrane diamond anvil cell: A new device for generating continuous pressure and temperature variations. *High Pressure Res.* **1**, 77–90 (1988).
108. Miletich, R., Allan, D. R. & Kuhs, W. F. High-pressure single-crystal techniques. In *High-temperature and high-pressure crystal chemistry* (eds. Hazen, R. M. & Downs, R. T.) 445 – 520 (The Mineralogical Society of America, 2001).
109. Pippinger, T., Miletich, R. & Burchard, M. Multipurpose high-pressure high-temperature diamond-anvil cell with a novel high-precision guiding system and a dual-mode pressurization device. *Rev. Sci. Instrum.* **82**, 095108 (2011).
110. Boehler, R. & De Hantsetters, K. New anvil designs in diamond-cells. *High Pressure Res.* **24**, 391–396 (2004).

111. Prescher, C., Dubrovinsky, L., Bykova, E., Kuppenko, I., Glazyrin, K., Anastasia, K., Miyajima, N., McCammon, C., Mookherjee, M., Prakapenka, V., Cerantola, V., Nakajima, Y., Dubrovinskaia, N., Rüffer, R., Chumakov, A. & Hanfland, M. Carbon in the Earth's core accounts for its high Poisson's ratio. *Submitt. to Nat. Geosie.* (2014).
112. Kurnosov, A., Kantor, I., Boffa-Ballaran, T., Lindhardt, S., Dubrovinsky, L., Kuznetsov, A. & Zehnder, B. H. A novel gas-loading system for mechanically closing of various types of diamond anvil cells. *Rev. Sci. Instrum.* **79**, 045110 (2008).
113. Mao, H. K., Xu, J. & Bell, P. M. Calibration of the ruby pressure gauge to 800 kbar under quasi-hydrostatic conditions. *J. Geophys. Res.* **91**, 4673–4676 (1986).
114. Chijioke, A. D., Nellis, W. J., Soldatov, a. & Silvera, I. F. The ruby pressure standard to 150 GPa. *J. Appl. Phys.* **98**, 114905 (2005).
115. Hess, N. J. & Schiferl, D. Pressure and temperature dependence of laser-induced fluorescence of Sm:YAG to 100 kbar and 700 °C and an empirical model. *J. Appl. Phys.* **68**, 1953–1961 (1990).
116. Dorfman, S. M., Prakapenka, V. B., Meng, Y. & Duffy, T. S. Intercomparison of pressure standards (Au, Pt, Mo, MgO, NaCl and Ne) to 2.5 Mbar. *J. Geophys. Res.* **117**, B08210 (2012).
117. Fei, Y., Ricolleau, A., Frank, M., Mibe, K., Shen, G. & Prakapenka, V. Toward an internally consistent pressure scale. *Proc. Natl. Acad. Sci. USA* **104**, 9182–9186 (2007).
118. Dewaele, A., Torrent, M., Loubeyre, P. & Mezouar, M. Compression curves of transition metals in the Mbar range: Experiments and projector augmented-wave calculations. *Phys. Rev. B* **78**, 104102 (2008).
119. Dewaele, A., Belonoshko, A. B., Garbarino, G., Occelli, F., Bouvier, P., Hanfland, M. & Mezouar, M. High-pressure–high-temperature equation of state of KCl and KBr. *Phys. Rev. B* **85**, 214105 (2012).
120. Boehler, R., Musshoff, H. G., Ditz, R., Aquilanti, G. & Trapananti, a. Portable laser-heating stand for synchrotron applications. *Rev. Sci. Instrum.* **80**, 045103 (2009).
121. Kuppenko, I., Dubrovinsky, L., Dubrovinskaia, N., McCammon, C., Glazyrin, K., Bykova, E., Boffa Ballaran, T., Sinmyo, R., Chumakov, A. I., Potapkin, V., Kantor, I., Rüffer, R., Hanfland, M., Crichton, W. & Merlini, M. Portable double-sided laser-heating system for Mössbauer spectroscopy and X-ray diffraction experiments at synchrotron facilities with diamond anvil cells. *Rev. Sci. Instrum.* **83**, 124501 (2012).

122. Rothkirch, A., Gatta, G. D., Meyer, M., Merkel, S., Merlini, M. & Liermann, H. P. Single-crystal diffraction at the Extreme Conditions beamline P02.2: Procedure for collecting and analyzing high-pressure single-crystal data. *J. Synchrotron Radiat.* **20**, 711–720 (2013).
123. Sørensen, H. O., Schmidt, S., Wright, J. P., Vaughan, G. B. M., Techert, S., Garman, E. F., Oddershede, J., Davaasambuu, J., Paithankar, K. S., Gundlach, C. & Poulsen, H. F. Multigrain crystallography. *Z. Kristallogr.* **227**, 63–78 (2012).
124. Sheldrick, G. M. A short history of SHELX. *Acta Crystallogr. A.* **64**, 112–122 (2008).
125. Petříček, V., Dušek, M. & Palatinus, L. Crystallographic computing system JANA2006: General features. *Z. Kristallogr.* **229**, 345–352 (2014).
126. Higashi, I., Iwasaki, H., Ito, T., Lundstrom, T., Okada, S. & Tergenius, L. E. Single-crystal X-ray-diffraction study of AlB_{31} of the β -rhombohedral boron structure. *J. Solid State Chem.* **82**, 230–238 (1989).
127. Roger, J., Babizhetskyy, V., Halet, J.-F. & Guérin, R. Boron–silicon solid solution: synthesis and crystal structure of a carbon-doped boron-rich SiB_n ($n \sim 30$) compound. *J. Solid State Chem.* **177**, 4167–4174 (2004).
128. Gou, H., Dubrovinskaia, N., Bykova, E., Tsirlin, A. A., Kasinathan, D., Schnelle, W., Richter, A., Merlini, M., Hanfland, M., Abakumov, A. M., Batuk, D., Van Tendeloo, G., Nakajima, Y., Kolmogorov, A. N. & Dubrovinsky, L. Discovery of a superhard iron tetraboride superconductor. *Phys. Rev. Lett.* **111**, 157002 (2013).
129. Occelli, F., Loubeyre, P. & LeToullec, R. Properties of diamond under hydrostatic pressures up to 140 GPa. *Nat. Mater.* **2**, 151–154 (2003).
130. Gou, H., Tsirlin, A. A., Bykova, E., Abakumov, A. M., Van Tendeloo, G., Richter, A., Ovsyannikov, S. V., Kurnosov, A. V., Trots, D. M., Konôpková, Z., Liermann, H.-P., Dubrovinsky, L. & Dubrovinskaia, N. Peierls distortion, magnetism, and high hardness of manganese tetraboride. *Phys. Rev. B* **89**, 064108 (2014).
131. Knappschneider, A., Litterscheid, C., Dzivenko, D., Kurzman, J. A., Seshadri, R., Wagner, N., Beck, J., Riedel, R. & Albert, B. Possible Superhardness of $\text{CrB}(4)$. *Inorg. Chem.* **52**, 540–2 (2013).
132. Brazhkin, V., Dubrovinskaia, N., Nicol, M., Novikov, N., Riedel, R., Solozhenko, V. & Zhao, Y. What does “harder than diamond” mean? *Nat. Mater.* **3**, 576–577 (2004).

133. Bykova, E., Tsirlin, A. A., Gou, H., Dubrovinsky, L. & Dubrovinskaia, N. Novel non-magnetic hard boride Co_5B_{16} synthesized under high pressure. *J. Alloys Compd.* **608**, 69–72 (2014).
134. Andersson, S., Lundström, T., Andresen, A. F. & Pearson, W. B. The crystal structure of CrB_4 . *Acta Chem. Scand.* **22**, 3103–3110 (1968).
135. Nelmes, R., Loveday, J., Allan, D., Besson, J., Hamel, G., Grima, P. & Hull, S. Neutron- and x-ray-diffraction measurements of the bulk modulus of boron. *Phys. Rev. B* **47**, 7668–7673 (1993).
136. Polian, A., Chervin, J. C., Munsch, P. & Gauthier, M. A-boron at very high pressure: structural and vibrational properties. *J. Phys. Conf. Ser.* **121**, 042017 (2008).
137. Sanz, D., Loubeyre, P. & Mezouar, M. Equation of state and pressure induced amorphization of β -boron from X-ray measurements up to 100 GPa. *Phys. Rev. Lett.* **89**, 245501 (2002).
138. Ma, Y., Prewitt, C., Zou, G., Mao, H. & Hemley, R. High-pressure high-temperature X-ray diffraction of β -boron to 30 GPa. *Phys. Rev. B* **67**, 174116 (2003).
139. Zarechnaya, E., Dubrovinskaia, N., Caracas, R., Merlini, M., Hanfland, M., Filinchuk, Y., Chernyshov, D., Dmitriev, V. & Dubrovinsky, L. Pressure-induced isostructural phase transformation in $\gamma\text{-B}_{28}$. *Phys. Rev. B* **82**, 184111 (2010).
140. Friedrich, A., Wilson, D. J., Haussühl, E., Winkler, B., Morgenroth, W., Refson, K., Milman, V. & Haussühl, E. High-pressure properties of diaspore, $\text{AlO}(\text{OH})$. *Phys. Chem. Miner.* **34**, 145–157 (2007).
141. Lavina, B., Dera, P., Kim, E., Meng, Y., Downs, R. T., Weck, P. F., Sutton, S. R. & Zhao, Y. Discovery of the recoverable high-pressure iron oxide Fe_4O_5 . *Proc. Natl. Acad. Sci. USA* **108**, 17281–17285 (2011).
142. Guignard, J. & Crichton, W. a. Synthesis and recovery of bulk Fe_4O_5 from magnetite, Fe_3O_4 . A member of a self-similar series of structures for the lower mantle and transition zone. *Mineral. Mag.* **78**, 361–371 (2014).
143. Perkins, G. L. *Boron: Compounds, Production, and Applications*. 616 p. (Nova Science Publishers, Incorporated, 2011).
144. Braccini, V., Nardelli, D., Penco, R. & Grasso, G. Development of ex situ processed MgB_2 wires and their applications to magnets. *Phys. C* **456**, 209–217 (2007).

145. Mirkovic, D., Grobner, J., Schmid-Fetzer, R., Fabrichnaya, O. & Lukas, H. L. Experimental study and thermodynamic re-assessment of the Al-B system. *J. Alloys Compd.* **384**, 168–174 (2004).
146. Burkhardt, U., Gurin, V., Haarmann, F., Borrmann, H., Schnelle, W., Yaresko, A. & Grin, Y. On the electronic and structural properties of aluminum diboride $\text{Al}_{0.9}\text{B}_2$. *J. Solid State Chem.* **177**, 389–394 (2004).
147. Will, G. Crystal structure analysis of AlB_{10} by the convolution molecule method. *Acta Crystallogr.* **23**, 1071–1079 (1967).
148. Higashi, I., Sakurai, T. & Atoda, T. Crystal-structure of Alpha- AlB_{12} . *J. Solid State Chem.* **20**, 67–77 (1977).
149. Hughes, R. E., Leoniwicz, M. E., Lemley, J. T. & Tai, L. T. Icosahedral boron frameworks - structure of $\gamma\text{-AlB}_{12}$. *J. Am. Chem. Soc.* **99**, 5507–5508 (1977).
150. Geist, D., Kloss, R. & Follner, H. Verfeinerung des β -rhomboedrischen Bors. *Acta Crystallogr. B-Stru.* **26**, 1800–1802 (1970).
151. Callmer, B. An accurate refinement of the β -rhombohedral boron structure. *Acta Crystallogr. B* **33**, 1951–1954 (1977).
152. Slack, G. A., Hejna, C. I., Garbaskas, M. F. & Kasper, J. S. The crystal structure and density of β -rhombohedral boron. *J. Solid State Chem.* **76**, 52–63 (1988).
153. Hoard, J. L., Sullenger, D. B., Kennard, C. H. L. & Hughes, R. E. The structure analysis of β -rhombohedral boron. *J. Solid State Chem.* **1**, 268–277 (1970).
154. Kolakowski, B. Structure of rhombohedral complicated modification of boron. *Acta Phys. Pol.* **22**, 439–440 (1962).
155. Andersson, S. & Lundström, T. The solubility of chromium in β -rhombohedral boron as determined in CrB_{41} by single-crystal diffractometry. *J. Solid State Chem.* **2**, 603–611 (1970).
156. Dubrovinskaia, N., Dubrovinsky, L. & McCammon, C. Iron–magnesium alloying at high pressures and temperatures. *J. Phys. Condens. Matter* **16**, S1143–S1150 (2004).
157. Oxford Diffraction. CrysAlis CCD. (2006).
158. Oxford Diffraction. CrysAlis RED. (2006).

159. Blessing, R. H. DREADD – data reduction and error analysis for single-crystal diffractometer data. *J. Appl. Crystallogr.* **22**, 396–397 (1989).
160. Sheldrick, G. M. SADABS. (2003).
161. Sheldrick, G. M. SHELXL97. (2003).
162. Brandenburg, K. & Putz, H. Diamond - crystal and molecular structure visualization. (1999).
163. Garbaskas, M. F., Kasper, J. S. & Slack, G. A. The incorporation of vanadium in β -rhombohedral boron as determined by single-crystal diffractometry. *J. Solid State Chem.* **63**, 424–430 (1986).
164. Lundström, T., Terenius, L.-E. & Higashi, I. A single-crystal investigation of the solid solution $\text{NiB}_{48.5}$ of β -rhombohedral boron type structure. *Z. Kristallogr.* **167**, 235–246 (1984).
165. Higashi, I., Sakurai, T. & Atoda, T. Crystal-structure of CuB_{23} . *J. Less-common Met.* **45**, 283–292 (1976).
166. Belsky, A., Hellenbrandt, M., Karen, V. L. & Luksch, P. New developments in the Inorganic Crystal Structure Database (ICSD): accessibility in support of materials research and design. *Acta Crystallogr. B* **58**, 364–369 (2002).
167. Gmelin, L., Amberger, E. & Stumpf, W. *Boron Compounds, Elemental Boron and Boron Carbides, Gmelin Handbook of Inorganic Chemistry*. 242 p. (Springer-Verlag, 1981).
168. Balakrishnarajan, M. M. & Hoffmann, R. Electron-deficient bonding in lozenge rhomboid rings. *J. Am. Chem. Soc.* **126**, 13119–13131 (2004).
169. Hermann, A., McSorley, A., Ashcroft, N. W. & Hoffmann, R. From Wade-Mingos to Zintl-Klemm at 100 GPa: binary compounds of boron and lithium. *J. Am. Chem. Soc.* **134**, 18606–18618 (2012).
170. Levine, J. B., Tolbert, S. H. & Kaner, R. B. Advancements in the search for superhard ultra-incompressible metal borides. *Adv. Funct. Mater.* **19**, 3519–3533 (2009).
171. Cumberland, R. W., Weinberger, M. B., Gilman, J. J., Clark, S. M., Tolbert, S. H. & Kaner, R. B. Osmium diboride, an ultra-incompressible, hard material. *J. Am. Chem. Soc.* **127**, 7264–7265 (2005).

172. Chung, H.-Y., Weinberger, M. B., Levine, J. B., Kavner, A., Yang, J.-M., Tolbert, S. H. & Kaner, R. B. Synthesis of ultra-incompressible superhard rhenium diboride at ambient pressure. *Science* **316**, 436–439 (2007).
173. Kaner, R. B., Gilman, J. J. & Tolbert, S. H. Materials science. Designing superhard materials. *Science* **308**, 1268–1269 (2005).
174. Dubrovinskaia, N., Dubrovinsky, L. & Solozhenko, V. L. Comment on “synthesis of ultra-incompressible superhard rhenium diboride at ambient pressure.” *Science* **318**, 1550c (2007).
175. Gu, Q., Krauss, G. G. & Steurer, W. Transition metal borides: superhard versus ultra-incompressible. *Adv. Mater.* **20**, 3620–3626 (2008).
176. Qin, J., He, D., Wang, J., Fang, L., Lei, L., Li, Y., Hu, J., Kou, Z. & Bi, Y. Is rhenium diboride a superhard material? *Adv. Mater.* **20**, 4780–4783 (2008).
177. Knappschneider, A., Litterscheid, C., Dzivenko, D., Kurzman, J. A., Seshadri, R., Wagner, N., Beck, J., Riedel, R. & Albert, B. Possible superhardness of CrB₄. *Inorg. Chem.* **52**, 540–542 (2013).
178. Ito, E. Theory and practice – multianvil cells and high-pressure experimental methods. In *Treatise on Geophysics* (eds. Price, G. D. & Schubert, G.) 197–230 (Elsevier, 2007).
179. Xcalibur/SuperNova CCD system, CrysAlisPro Software system, Version 171.36.32. (2012).
180. Liermann, H.-P., Morgenroth, W., Ehnes, A., Berghäuser, A., Winkler, B., Franz, H. & Weckert, E. The Extreme Conditions Beamline at PETRA III, DESY: Possibilities to conduct time resolved monochromatic diffraction experiments in dynamic and laser heated DAC. *J. Phys. Conf. Ser.* **215**, 012029 (2010).
181. Hammersley, A. P., Svensson, S. O., Hanfland, M., Fitch, A. N. & Hausermann, D. Two-dimensional detector software: From real detector to idealised image or two-theta scan. *High Pressure Res.* **14**, 235–248 (1996).
182. Niu, H., Wang, J., Chen, X.-Q., Li, D., Li, Y., Lazar, P., Podlucky, R. & Kolmogorov, A. N. Structure, bonding, and possible superhardness of CrB₄. *Phys. Rev. B* **85**, 144116 (2012).
183. Orobengoa, D., Capillas, C., Aroyo, M. I. & Perez-Mato, J. M. AMPLIMODES : symmetry-mode analysis on the Bilbao Crystallographic Server. *J. Appl. Crystallogr.* **42**, 820–833 (2009).

184. Perez-Mato, J. M., Orobengoa, D. & Aroyo, M. I. Mode crystallography of distorted structures. *Acta Crystallogr. A* **66**, 558–590 (2010).
185. Litterscheid, C., Knappschneider, A. & Albert, B. Single crystal structure of MnB₄. *Z. Anorg. Allg. Chem.* **638**, 1608–1608 (2012).
186. Petukhov, A., Mazin, I., Chioncel, L. & Lichtenstein, A. Correlated metals and the LDA+U method. *Phys. Rev. B* **67**, 153106 (2003).
187. Yin, W. G., Volja, D. & Ku, W. Orbital ordering in LaMnO₃: Electron-electron versus electron-lattice interactions. *Phys. Rev. Lett.* **96**, 116405 (2006).
188. Kumagai, Y., Belik, A. A., Lilienblum, M., Leo, N., Fiebig, M. & Spaldin, N. A. Observation of persistent centrosymmetry in the hexagonal manganite family. *Phys. Rev. B* **85**, 174422 (2012).
189. Stishov, S., Petrova, A., Khasanov, S., Panova, G., Shikov, A., Lashley, J., Wu, D. & Lograsso, T. Magnetic phase transition in the itinerant helimagnet MnSi: Thermodynamic and transport properties. *Phys. Rev. B* **76**, 52405 (2007).
190. Berlinsky, A. J. One-dimensional metals and charge density wave effects in these materials. *Reports Prog. Phys.* **42**, 1243–1283 (1979).
191. Toriyama, T., Nakao, A., Yamaki, Y., Nakao, H., Murakami, Y., Hasegawa, K., Isobe, M., Ueda, Y., Ushakov, A. V, Khomskii, D. I., Streltsov, S. V, Konishi, T. & Ohta, Y. Peierls mechanism of the metal-insulator transition in ferromagnetic hollandite K₂Cr₈O₁₆. *Phys. Rev. Lett.* **107**, 266402 (2011).
192. Haussermann, U., Bostrom, M., Viklund, P., Rapp, O. & Bjornangen, T. FeGa₃ and RuGa₃: Semiconducting intermetallic compounds. *J. Solid State Chem.* **165**, 94–99 (2002).
193. Isnard, O. & Fruchart, D. Magnetism in Fe-based intermetallics: relationships between local environments and local magnetic moments. *J. Alloys Compd.* **205**, 1–15 (1994).
194. Barbour, L. J. X-Seed - A software tool for supramolecular crystallography. *J. Supramol. Chem.* **1**, 189–191 (2001).
195. Koepnik, K. & Eschrig, H. Full-potential nonorthogonal local-orbital minimum-basis band-structure scheme. *Phys. Rev. B* **59**, 1743–1757 (1999).
196. Perdew, J. P. & Wang, Y. Accurate and simple analytic representation of the electron-gas correlation energy. *Phys. Rev. B* **45**, 13244–13249 (1992).

197. Knappschneider, A., Litterscheid, C., George, N. C., Brgoch, J., Wagner, N., Beck, J., Kurzman, J. A., Seshadri, R. & Albert, B. Peierls-distorted monoclinic MnB_4 with a Mn-Mn bond. *Angew. Chem. Int. Ed. Engl.* **53**, 1684–1688 (2014).
198. König, E. & König, G. *Magnetic Properties of Coordination and Organometallic Transition Metal Compounds*. **11**, p. (Springer-Verlag, 1981).
199. Fruchart, R. Moments magnetiques des borures ferromagnetiques de cobalt Co_3B , Co_2B et du borure de fer FeB . *Cr. Hebd. Acad. Sci.* **256**, 3304–3306 (1963).
200. Lundquist, N., Myers, H. P. & Westin, R. The paramagnetic properties of the monoborides of V, Cr, Mn, Fe, Co and Ni. *Philos. Mag.* **7**, 1187–1195 (1962).
201. Novak, G. A. & Gibbs, G. V. Crystal chemistry of silicate garnets. *Am. Mineral.* **56**, 791–825 (1971).
202. Ottonello, G., Bokreta, M. & Sciuto, P. F. Parameterization of energy and interactions in garnets: End-member properties. *Am. Mineral.* **81**, 429–447 (1996).
203. Milman, V., Akhmatkaya, E. V., Nobes, R. H., Winkler, B., Pickard, C. J. & White, J. A. Systematic ab initio study of the compressibility of silicate garnets. *Acta Crystallogr. B* **57**, 163–177 (2001).
204. Frost, D. J., Poe, B. T., Tronnes, R. G., Liebske, C., Duba, A. & Rubie, D. C. A new large-volume multianvil system. *Phys. Earth Planet. Inter.* **143**, 507–514 (2004).
205. Schmitz, W. *International tables for X-ray crystallography, vol. IV*. 366 p. (Kynock Press, 1974).
206. Oxford Diffraction & Oxford Diffraction. CrysAlis RED. CrysAlis RED. (2006).
207. Andrut, M. & Wildner, M. The crystal chemistry of birefringent natural uvarovites. Part III. Application of the superposition model of crystal fields with a characterization of synthetic cubic uvarovite. *Phys. Chem. Miner.* **29**, 595–608 (2002).
208. McMillan, P., Akaogi, M., Ohtani, E., Williams, Q., Nieman, R. & Sato, R. Cation disorder in garnets along the $\text{Mg}_3\text{Al}_2\text{Si}_3\text{O}_{12}$ - $\text{Mg}_4\text{Si}_4\text{O}_{12}$ join: an infrared, Raman and NMR study. *Phys. Chem. Miner.* **16**, 428–435 (1989).
209. Akaogi, M. & Akimoto, S. Pyroxene-garnet solid-solution equilibria in the systems $\text{Mg}_4\text{Si}_4\text{O}_{12}$ - $\text{Mg}_3\text{Al}_2\text{Si}_3\text{O}_{12}$ and $\text{Fe}_4\text{Si}_4\text{O}_{12}$ - $\text{Fe}_3\text{Al}_2\text{Si}_3\text{O}_{12}$ at high pressures and temperatures. *Phys. Earth Planet. Inter.* **15**, 90–106 (1977).

210. Ono, S. & Yasuda, A. Compositional change of majoritic garnet in a MORB composition from 7 to 17 GPa and 1400 to 1600°C. *Phys. Earth Planet. Inter.* **96**, 171–179 (1996).
211. Keppler, H. & Frost, D. J. Introduction to minerals under extreme conditions. In *Mineral behavior at extreme conditions* (ed. Miletich, R.) 1–30 (European Mineralogical Union, 2005).
212. Potapkin, V., Chumakov, A. I., Smirnov, G. V, Celse, J. P., Rüffer, R., McCammon, C. & Dubrovinsky, L. The ^{57}Fe Synchrotron Mössbauer Source at the ESRF. *J. Synchrotron Radiat.* **19**, 559–569 (2012).
213. Potapkin, V., McCammon, C., Glazyrin, K., Kantor, A., Kuppenko, I., Prescher, C., Sinmyo, R., Smirnov, G. V, Chumakov, A. I., Rüffer, R. & Dubrovinsky, L. Effect of iron oxidation state on the electrical conductivity of the Earth's lower mantle. *Nat. Commun.* **4**, 1427 (2013).
214. Mao, H. K., Hemley, R. J., Fei, Y., Shu, J. F., Chen, L. C., Jephcoat, A. P., Wu, Y. & Bassett, W. A. Effect of pressure, temperature, and composition on lattice parameters and density of (Fe,Mg)SiO₃-perovskites to 30 GPa. *J. Geophys. Res.* **96**, 8069–8079 (1991).
215. Wang, Y., Weidner, D. J., Liebermann, R. C. & Zhao, Y. P-V-T equation of state of (Mg,Fe)SiO₃ perovskite: constraints on composition of the lower mantle. *Phys. Earth Planet. Inter.* **83**, 13–40 (1994).
216. Fei, Y. W., Wang, Y. B. & Finger, L. W. Maximum solubility of FeO in (Mg, Fe)SiO₃-perovskite as a function of temperature at 26 GPa: Implication for FeO content in the lower mantle. *J. Geophys. Res. Earth* **101**, 11525–11530 (1996).
217. Fiquet, G., Andrault, D., Dewaele, A., Charpin, T., Kunz, M. & Hausermann, D. P-V-T equation of state of MgSiO₃ perovskite. *Phys. Earth Planet. Inter.* **105**, 21–31 (1998).
218. Nishio-Hamane, D. Fe³⁺ and Al solubilities in MgSiO₃ perovskite: implication of the Fe³⁺AlO₃ substitution in MgSiO₃ perovskite at the lower mantle condition. *Geophys. Res. Lett.* **32**, L16306 (2005).
219. Tange, Y., Takahashi, E., Nishihara, Y., Funakoshi, K. & Sata, N. Phase relations in the system MgO-FeO-SiO₂ to 50 GPa and 2000 degrees C: An application of experimental techniques using multianvil apparatus with sintered diamond anvils. *J. Geophys. Res. Earth* **114**, B02214 (2009).
220. Ballaran, T. B., Kurnosov, A., Glazyrin, K., Frost, D. J., Merlini, M., Hanfland, M. & Caracas, R. Effect of chemistry on the compressibility of silicate perovskite in the lower mantle. *Earth Planet. Sci. Lett.* **333**, 181–190 (2012).

221. Ito, E. & Yamada, H. Stability relations of silicate spinels, ilmenites and perovskite. In *High pressure research in geophysics* (eds. Akimoto, S. & Manghnani, M. H.) 405–419 (Center for Publications, 1982).
222. Parise, J. B., Wang, Y., Yeganeh-Haeri, A., Cox, D. E. & Fei, Y. Crystal structure and thermal expansion of (Mg,Fe)SiO₃ perovskite. *Geophys. Res. Lett.* **17**, 2089–2092 (1990).
223. Bolfan-Casanova. The distribution of water in the Earth's mantle: an experimental and infrared spectroscopic study. (2000).
224. Kröger, F. A. & Vink, H. H. Relations between the concentrations of imperfections in crystalline solids. In *Solid State Physics, vol. 3* (eds. Sritz, F. & Turnbull, D.) 367–435 (Academic Press, 1956).
225. O'Neill, B. & Jeanloz, R. MgSiO₃-FeSiO₃-Al₂O₃ in the Earth's lower mantle: Perovskite and garnet at 1200 km depth. *J. Geophys. Res. Earth* **99**, 19901–19915 (1994).
226. Nishiyama, N., Yagi, T., Ono, S., Gotou, H., Harada, T. & Kikegawa, T. Effect of incorporation of iron and aluminum on the thermoelastic properties of magnesium silicate perovskite. *Phys. Chem. Miner.* **34**, 131–143 (2007).
227. O'Keeffe, M., Hyde, B. G. & Bovin, J.-O. Contribution to the crystal chemistry of orthorhombic perovskites: MgSiO₃ and NaMgF₃. *Phys. Chem. Miner.* **4**, 299–305 (1979).
228. Mitchell, R. H. *Perovskites: modern and ancient*. 318 p. (Almaz Press Incorporated, 2002).
229. Zhao, Y., Weidner, D. J., Parise, J. B. & Cox, D. E. Critical phenomena and phase transition of perovskite — data for NaMgF₃ perovskite. Part II. *Phys. Earth Planet. Inter.* **76**, 17–34 (1993).
230. Woodley, S. M. & Catlow, R. Crystal structure prediction from first principles. *Nat. Mater.* **7**, 937–946 (2008).
231. Hautier, G., Jain, A. & Ong, S. P. From the computer to the laboratory: materials discovery and design using first-principles calculations. *J. Mater. Sci.* **47**, 7317–7340 (2012).
232. Cohen, M. L. Conceptual progress for explaining and predicting semiconductor properties. *J. Mater. Res.* **26**, 2815–2825 (2011).
233. Lüders, M., Marques, M., Lathiotakis, N., Floris, A., Profeta, G., Fast, L., Continenza, A., Massidda, S. & Gross, E. Ab initio theory of superconductivity. I. Density functional formalism and approximate functionals. *Phys. Rev. B* **72**, 24545 (2005).

234. Kolmogorov, A., Calandra, M. & Curtarolo, S. Thermodynamic stabilities of ternary metal borides: An ab initio guide for synthesizing layered superconductors. *Phys. Rev. B* **78**, 94520 (2008).
235. Chang, K. & Cohen, M. Structural and electronic properties of the high-pressure hexagonal phases of Si. *Phys. Rev. B* **30**, 5376–5378 (1984).
236. Neaton, J. & Ashcroft, N. Pairing in dense lithium. *Nature* **400**, 141–144 (1999).
237. Burke, K. Perspective on density functional theory. *J. Chem. Phys.* **136**, 150901 (2012).
238. Allen, P. B. & Mitrović, B. Theory of Superconducting Tc. *Solid State Phys.* **37**, 1–92 (1983).
239. Shenoy, G. K. Mössbauer study of superconducting LaFe₄P₁₂. *J. Appl. Phys.* **53**, 2628–2631 (1982).
240. Nakai, Y., Ishida, K., Kikuchi, D., Sugawara, H. & Sato, H. Evidence for s -wave superconductivity with antiferromagnetic fluctuations in filled skutterudite LaFe₄P₁₂: ¹³⁹La and ³¹P-NMR studies. *J. Phys. Soc. Japan* **74**, 3370–3374 (2005).
241. Smith, J. L., Lashley, J. C., Volz, H. M., Fisher, R. A. & Riseborough, P. S. Thermodynamics and superconductivity of the Th₇(Fe, Ru, Os, Co, Rh, Ir)₃ system. *Philos. Mag.* **88**, 2847–2850 (2008).
242. Khan, Y., Kneller, E. & Sostarich, M. The phase Fe₃B. *Z. Metallkd.* **73**, 624–626 (1982).
243. Barinov, V. A., Tsurin, V. A., Voronin, V. I., Novikov, S. I. & Surikov, V. T. Mössbauer investigations of the metastable Fe₂₃B₆ phase. *Phys. Met. Metallogr.* **101**, 456–466 (2006).
244. Mühlischlegel, B. Die thermodynamischen Funktionen des Supraleiters. *Z. Physik* **155**, 313–327 (1959).
245. Werthamer, N. R., Helfand, E. & Hohenberg, P. C. Temperature and purity dependence of the superconducting critical field, H_{c2}. III. Electron spin and spin-orbit effects. *Phys. Rev.* **147**, 295–302 (1966).
246. Chandrasekhar, B. S. A note on the maximum critical field of high-field superconductors. *Appl. Phys. Lett.* **1**, 7–8 (1962).
247. James, F. *Materials science and engineering handbook*. 1980 p. (CRC Press, 2000).

-
248. Dubrovinskaia, N., Dub, S. & Dubrovinsky, L. Superior wear resistance of aggregated diamond nanorods. *Nano Lett.* **6**, 824–826 (2006).
249. Haubner, R., Wilhelm, M., Weissenbacher, R. & Lux, B. Boron nitrides — properties, synthesis and applications. In *High performance non-oxide ceramics II* (ed. Jansen, M.) **102**, 1–45 (Springer Berlin Heidelberg, 2002).
250. Dubrovinskaia, N., Wirth, R., Wosnitza, J., Papageorgiou, T., Braun, H. F., Miyajima, N. & Dubrovinsky, L. An insight into what superconducts in polycrystalline boron-doped diamonds based on investigations of microstructure. *Proc. Natl. Acad. Sci. USA* **105**, 11619–11622 (2008).
251. Dubrovinskaia, N., Dubrovinsky, L., Miyajima, N., Langenhorst, F., Crichton, W. A. & F, B. H. High-pressure/high-temperature synthesis and characterization of boron-doped diamond. *Z. Naturforsch.* **61b**, 1561–1565 (2006).
252. Oxford Diffraction & Oxford Diffraction. CrysAlis CCD. CrysAlis CCD. (2006).
253. Syassen, K. Ruby under pressure. *High Pressure Res.* **28**, 75–126 (2008).
254. Oliver, W. C. & Pharr, G. M. An improved technique for determining hardness and elastic modulus using load and displacement sensing indentation experiments. *J. Mater. Res.* **7**, 1564–1583 (2011).
255. Richter, A., Smith, R., Dubrovinskaia, N. & Mcgee, E. Mechanical properties of superhard materials synthesised at various pressure–temperature conditions investigated by nanoindentation. *High Pressure Res.* **26**, 99–109 (2006).
256. Wolf, B. & Richter, A. The concept of differential hardness in depth sensing indentation. *New J. Phys.* **5**, 15 (2003).
257. Cowlam, N. & Carr, G. E. Magnetic and structural properties of Fe-B binary metallic glasses. I. Variation of magnetic moment with composition. *J. Phys. F Met. Phys.* **15**, 1109–1116 (1985).
258. Taylor, J., Duffy, J., Bebb, A., Cooper, M., Dugdale, S., McCarthy, J., Timms, D., Greig, D. & Xu, Y. Magnetic Compton scattering study of the ferromagnetic amorphous alloys $\text{Fe}_{1-x}\text{B}_x$. *Phys. Rev. B* **63**, 220404 (2001).
259. Koch, C. Determination of core structure periodicity and point defect density along dislocations. 214 (2002).
260. Wojdyr, M. Fityk : a general-purpose peak fitting program. *J. Appl. Crystallogr.* **43**, 1126–1128 (2010).

261. Bialon, A. F., Hammerschmidt, T., Drautz, R., Shah, S., Margine, E. R. & Kolmogorov, a. N. Possible routes for synthesis of new boron-rich Fe–B and $\text{Fe}_{1-x}\text{Cr}_x\text{B}_4$ compounds. *Appl. Phys. Lett.* **98**, 081901 (2011).
262. Van Der Geest, A. G. & Kolmogorov, A. N. Stability of 41 metal–boron systems at 0GPa and 30GPa from first principles. *Calphad* **46**, 184–204 (2014).
263. Parakhonskiy, G., Dubrovinskaia, N., Bykova, E., Wirth, R. & Dubrovinsky, L. High pressure synthesis and investigation of single crystals of metastable boron phases. *High Pressure Res.* **33**, 673–683 (2013).
264. Agilent Technologies. CrysAlisPro Software system. (2013).
265. Amberger, E. & Gerster, H. P. Struktur ternärer I-tetragonaler Boride: $(\text{B}_{12})_4\text{C}_2\text{Ti}_{1,86}$ und $(\text{B}_{12})_4\text{C}_2\text{V}_{1,29}$. *Acta Crystallogr. B-Stru.* **36**, 672–675 (1980).
266. Vast, N., Baroni, S., Zerah, G., Besson, J., Polian, A., Grimsditch, M. & Chervin, J. Lattice dynamics of icosahedral α -boron under pressure. *Phys. Rev. Lett.* **78**, 693–696 (1997).
267. Shirai, K., Masago, A. & Katayama-Yoshida, H. High-pressure properties of icosahedron-based solid borons. *Phys. Status Solidi B* **241**, 3161–3167 (2004).
268. Otte, K., Pentcheva, R., Schmahl, W. W. & Rustad, J. R. Pressure-induced structural and electronic transitions in FeOOH from first principles. *Phys. Rev. B* **80**, 1–9 (2009).
269. Bocquet, S., Pollard, R. & Cashion, J. Dynamic magnetic phenomena in fine-particle goethite. *Phys. Rev. B* **46**, 11657–11664 (1992).
270. Peslier, A. H., Woodland, A. B., Bell, D. R. & Lazarov, M. Olivine water contents in the continental lithosphere and the longevity of cratons. *Nature* **467**, 78–81 (2010).
271. Xu, W., Naaman, O., Rozenberg, G., Pasternak, M. & Taylor, R. Pressure-induced breakdown of a correlated system: The progressive collapse of the Mott-Hubbard state in RFeO_3 . *Phys. Rev. B* **64**, 094411 (2001).
272. Hohenberg, P. Inhomogeneous electron gas. *Phys. Rev.* **136**, B864–B871 (1964).
273. Wang, Y. & Perdew, J. Correlation hole of the spin-polarized electron gas, with exact small-wave-vector and high-density scaling. *Phys. Rev. B* **44**, 13298–13307 (1991).
274. Anisimov, V. I., Zaanen, J. & Andersen, O. K. Band theory and Mott insulators: Hubbard U instead of Stoner I. *Phys. Rev. B* **44**, 943–954 (1991).

-
275. Dudarev, S. L., Savrasov, S. Y., Humphreys, C. J. & Sutton, A. P. Electron-energy-loss spectra and the structural stability of nickel oxide: An LSDA+U study. *Phys. Rev. B* **57**, 1505–1509 (1998).
276. Perdew, J. P., Jackson, K. A., Pederson, M. R., Singh, D. J. & Fiolhais, C. Atoms, molecules, solids, and surfaces: Applications of the generalized gradient approximation for exchange and correlation. *Phys. Rev. B* **46**, 6671–6687 (1992).
277. Blöchl, P. E. Projector augmented-wave method. *Phys. Rev. B* **50**, 17953–17979 (1994).
278. Kresse, G. From ultrasoft pseudopotentials to the projector augmented-wave method. *Phys. Rev. B* **59**, 1758–1775 (1999).
279. Kresse, G. & Hafner, J. Ab initio molecular dynamics for liquid metals. *Phys. Rev. B* **47**, 558–561 (1993).
280. Kresse, G. & Hafner, J. Ab initio molecular-dynamics simulation of the liquid-metal–amorphous-semiconductor transition in germanium. *Phys. Rev. B* **49**, 14251–14269 (1994).
281. Kresse, G. & Furthmüller, J. Efficiency of ab-initio total energy calculations for metals and semiconductors using a plane-wave basis set. *Comput. Mater. Sci.* **6**, 15–50 (1996).
282. Kresse, G. & Furthmüller, J. Efficient iterative schemes for ab initio total-energy calculations using a plane-wave basis set. *Phys. Rev. B* **54**, 11169–11186 (1996).
283. Anderson, O. L. *Equations of state of solids for geophysics and ceramic science*. 432 p. (Oxford University Press, 1995).
284. Sata, N., Shen, G., Rivers, M. & Sutton, S. Pressure-volume equation of state of the high-pressure B2 phase of NaCl. *Phys. Rev. B* **65**, 104114 (2002).
285. Sano-Furukawa, A., Yagi, T., Okada, T., Gotou, H. & Kikegawa, T. Compression behaviors of distorted rutile-type hydrous phases, MOOH (M = Ga, In, Cr) and CrOOD. *Phys. Chem. Miner.* **39**, 375–383 (2012).
286. Williams, Q. & Guenther, L. Pressure-induced changes in the bonding and orientation of hydrogen in FeOOH-goethite. *Solid State Commun.* **100**, 105–109 (1996).
287. Brown, I. D. & Altermatt, D. Bond-valence parameters obtained from a systematic analysis of the Inorganic Crystal Structure Database. *Acta Crystallogr. B* **41**, 244–247 (1985).

288. Brown, I. D. *The chemical bond in inorganic chemistry. The bond valence model*. 278 p. (Oxford University Press, 2002).
289. Schouwink, P., Dubrovinsky, L., Glazyrin, K., Merlini, M., Hanfland, M., Pippinger, T. & Miletich, R. High-pressure structural behavior of α -Fe₂O₃ studied by single-crystal X-ray diffraction and synchrotron radiation up to 25 GPa. *Am. Mineral.* **96**, 1781–1786 (2011).
290. Knittle, E. & Jeanloz, R. High-pressure electrical resistivity measurements of Fe₂O₃: comparison of static-compression and shock-wave experiments to 61 GPa. *Solid State Commun.* **58**, 129–131 (1986).
291. Syono, Y., Ito, A., Morimoto, S., Suzuki, T., Yagi, T. & Akimoto, S. Mössbauer study on the high pressure phase of Fe₂O₃. *Solid State Commun.* **50**, 97–100 (1984).
292. Murakami, M., Hirose, K., Kawamura, K., Sata, N. & Ohishi, Y. Post-perovskite phase transition in MgSiO₃. *Science* **304**, 855–858 (2004).
293. Boehler, R. New diamond cell for single-crystal x-ray diffraction. *Rev. Sci. Instrum.* **77**, 115103 (2006).
294. Dubrovinskaia, N., Dubrovinsky, L., Hanfland, M. & Hofmann, M. Diamond anvils with a spherical support designed for X-ray and neutron diffraction experiments in DAC. *High Pressure Res.* **32**, 537–543 (2012).
295. Dera, P. GSE-ADA data analysis program for monochromatic single crystal diffraction with area detector (GeoSoilEnviroCARS, Argonne, IL). (2007).
296. Birch, F. Finite elastic strain of cubic crystals. *Phys. Rev.* **71**, 809–824 (1947).
297. Finger, L. W. & Hazen, R. M. Crystal structure and isothermal compression of Fe₂O₃, Cr₂O₃, and V₂O₃ to 50 kbars. *J. Appl. Phys.* **51**, 5362–5367 (1980).
298. Cox, P. A. *Transition metal oxides: an introduction to their electronic structure and properties*. 284 p. (Oxford University Press, 1992).
299. Dubrovinsky, L. S., Saxena, S. K. & Lazor, P. High-pressure and high-temperature in situ X-ray diffraction study of iron and corundum to 68 GPa using an internally heated diamond anvil cell. *Phys. Chem. Miner.* **25**, 434–441 (1998).
300. Alonso, J. A., Casais, M. T., Martínez-Lope, M. J., Martínez, J. L., Velasco, P., Muñoz, A. & Fernández-Díaz, M. T. Preparation, crystal structure, and magnetic and magnetotransport properties of the double perovskite Ca₂FeMoO₆. *Chem. Mater.* **12**, 161–168 (2000).

301. Muñoz, A., Alonso, J. A., Casais, M. T., Martínez-Lope, M. J. & Fernández-Díaz, M. T. Crystal and magnetic structure of the complex oxides $\text{Sr}_2\text{MnMoO}_6$, Sr_2MnWO_6 and Ca_2MnWO_6 : a neutron diffraction study. *J. Phys. Condens. Matter* **14**, 8817–8830 (2002).
302. Kennedy, B. J., Howard, C. J., Knight, K. S., Zhang, Z. & Zhou, Q. Structures and phase transitions in the ordered double perovskites $\text{Ba}_2\text{Bi}^{\text{III}}\text{Bi}^{\text{V}}\text{O}_6$ and $\text{Ba}_2\text{Bi}^{\text{III}}\text{Sb}^{\text{V}}\text{O}_6$. *Acta Crystallogr. B* **62**, 537–546 (2006).
303. Campbell, B. J., Stokes, H. T., Tanner, D. E. & Hatch, D. M. ISODISPLACE : a web-based tool for exploring structural distortions. *J. Appl. Crystallogr.* **39**, 607–614 (2006).
304. Merlini, M., Hanfland, M., Gemmi, M., Huotari, S., Simonelli, L. & Strobel, P. Fe^{3+} spin transition in CaFe_2O_4 at high pressure. *Am. Mineral.* **95**, 200–203 (2010).
305. Xu, W., Greenberg, E., Rozenberg, G. K., Pasternak, M. P., Bykova, E., Boffa-Ballaran, T., Dubrovinsky, L., Prakapenka, V., Hanfland, M., Vekilova, O. Y., Simak, S. I. & Abrikosov, I. A. Pressure-induced hydrogen bond symmetrization in iron oxyhydroxide. *Phys. Rev. Lett.* **111**, 175501 (2013).
306. Shannon, R. D. & Prewitt, C. T. Synthesis and structure of a new high-pressure form of Rh_2O_3 . *J. Solid State Chem.* **2**, 134–136 (1970).
307. Wang, L., Pan, Y., Ding, Y., Yang, W., Mao, W. L., Sinogeikin, S. V., Meng, Y., Shen, G. & Mao, H. High-pressure induced phase transitions of Y_2O_3 and $\text{Y}_2\text{O}_3\text{:Eu}^{3+}$. *Appl. Phys. Lett.* **94**, 061921 (2009).
308. Yusa, H., Tsuchiya, T., Sata, N. & Ohishi, Y. Dense yttria phase eclipsing the A-type sesquioxide structure: high-pressure experiments and ab initio calculations. *Inorg. Chem.* **49**, 4478–4485 (2010).
309. Yusa, H., Tsuchiya, T., Sata, N. & Ohishi, Y. High-pressure phase transition to the Gd_2S_3 structure in Sc_2O_3 : a new trend in dense structures in sesquioxides. *Inorg. Chem.* **48**, 7537–43 (2009).
310. Nishio-Hamane, D., Katagiri, M., Niwa, K., Sano-Furukawa, A., Okada, T. & Yagi, T. A new high-pressure polymorph of Ti_2O_3 : implication for high-pressure phase transition in sesquioxides. *High Pressure Res.* **29**, 379–388 (2009).
311. Ovsyannikov, S. V, Wu, X., Shchennikov, V. V, Karkin, A. E., Dubrovinskaia, N., Garbarino, G. & Dubrovinsky, L. Structural stability of a golden semiconducting orthorhombic polymorph of Ti_2O_3 under high pressures and high temperatures. *J. Phys. Condens. Matter* **22**, 375402 (2010).

312. Ovsyannikov, S. V, Abakumov, A. M., Tsirlin, A. a, Schnelle, W., Egoavil, R., Verbeeck, J., Van Tendeloo, G., Glazyrin, K. V, Hanfland, M. & Dubrovinsky, L. Perovskite-like Mn_2O_3 : a path to new manganites. *Angew. Chem. Int. Ed. Engl.* **52**, 1494–8 (2013).
313. Shirako, Y., Shi, Y. G., Aimi, A., Mori, D., Kojitani, H., Yamaura, K., Inaguma, Y. & Akaogi, M. High-pressure stability relations, crystal structures, and physical properties of perovskite and post-perovskite of NaNiF_3 . *J. Solid State Chem.* **191**, 167–174 (2012).
314. Ju, S., Cai, T.-Y., Lu, H.-S. & Gong, C.-D. Pressure-induced crystal structure and spin-state transitions in magnetite (Fe_3O_4). *J. Am. Chem. Soc.* **134**, 13780–13786 (2012).
315. Dziewonski, A. M. & Anderson, D. L. Preliminary reference Earth model. *Phys. Earth Planet. Inter.* **25**, 297–356 (1981).
316. Katsura, T., Yoneda, A., Yamazaki, D., Yoshino, T. & Ito, E. Adiabatic temperature profile in the mantle. *Phys. Earth Planet. Inter.* **183**, 212–218 (2010).
317. Mizusaki, J., Yamauchi, S., Fueki, K. & Ishikawa, A. Nonstoichiometry of the perovskite-type oxide $\text{La}_{1-x}\text{Sr}_x\text{CrO}_{3-\delta}$. *Solid State Ionics* **12**, 119–124 (1984).
318. Brazhkin, V. V, Voloshin, R. N., Lyapin, a G. & Popova, S. V. Phase equilibria in partially open systems under pressure: the decomposition of stoichiometric GeO_2 oxide. *Physics-Uspekhi* **46**, 1283–1289 (2003).
319. Litasov, K. D., Goncharov, A. F. & Hemley, R. J. Crossover from melting to dissociation of CO_2 under pressure: Implications for the lower mantle. *Earth Planet. Sci. Lett.* **309**, 318–323 (2011).
320. Freiman, Y. A. & Jodl, H. J. Solid oxygen. *Phys. Rep.* **401**, 1–228 (2004).
321. Frost, D. J., Liebske, C., Langenhorst, F., McCammon, C. A., Trønnes, R. G. & Rubie, D. C. Experimental evidence for the existence of iron-rich metal in the Earth's lower mantle. *Nature* **428**, 409–412 (2004).
322. Rohrbach, A. & Schmidt, M. W. Redox freezing and melting in the Earth's deep mantle resulting from carbon-iron redox coupling. *Nature* **472**, 209–212 (2011).
323. Stagno, V., Ojwang, D. O., McCammon, C. A. & Frost, D. J. The oxidation state of the mantle and the extraction of carbon from Earth's interior. *Nature* **493**, 84–88 (2013).
324. Okamoto, S. Structure of the new $\delta\text{-Fe}_2\text{O}_3$ (hydrate). *J. Am. Ceram. Soc.* **51**, 54 (1968).

(Eidesstattliche) Versicherungen und Erklärungen

(§ 8 S. 2 Nr. 6 PromO)

Hiermit erkläre ich mich damit einverstanden, dass die elektronische Fassung meiner Dissertation unter Wahrung meiner Urheberrechte und des Datenschutzes einer gesonderten Überprüfung hinsichtlich der eigenständigen Anfertigung der Dissertation unterzogen werden kann.

(§ 8 S. 2 Nr. 8 PromO)

Hiermit erkläre ich eidesstattlich, dass ich die Dissertation selbständig verfasst und keine anderen als die von mir angegebenen Quellen und Hilfsmittel benutzt habe.

(§ 8 S. 2 Nr. 9 PromO)

Ich habe die Dissertation nicht bereits zur Erlangung eines akademischen Grades anderweitig eingereicht und habe auch nicht bereits diese oder eine gleichartige Doktorprüfung endgültig nicht bestanden.

(§ 8 S. 2 Nr. 10 PromO)

Hiermit erkläre ich, dass ich keine Hilfe von gewerbliche Promotionsberatern bzw. -vermittlern in Anspruch genommen habe und auch künftig nicht nehmen werde.

.....
Ort, Datum, Unterschrift